Report on the effect of Thermal, Hydraulic, Mechanical and Chemical coupled processes on caprock integrity from analogue analysis

MUSTANG

A MUltiple Space and Time scale Approach for the quaNtification of deep saline formations for CO2 storaGe

Project Number:227286

Work-Package: *WP4*

WP Title
Laboratory Experiments

Deliverable *D045*
Report on the effect of Thermal, Hydraulic, Mechanical and Chemical coupled processes on caprock integrity from analogue analysis.

The research leading to these results has received funding from the European Community's Seventh Framework Programme [FP7/20072013) under grant agreement n° [227286]

Date 30.07.2012

MUSTANG

A MUltiple Space and Time scale Approach for the quaNtification of deep saline formations for CO2 storaGe

Project Number:227286

Work-Package: *WP4*

WP Title
Laboratory Experiments

Deliverable *D045*
Report on the effect of Thermal, Hydraulic, Mechanical and Chemical coupled processes on caprock integrity from analogue analysis.

Status	FINAL
Version	1.01
Review level	SIRAB
Planned delivery date	Month 36
Actual delivery date	Month 38
Leading participant	Dr. habil. C.I.McDermott
Contributing participants	Prof. Dr. S. Haszeldine, Dr. K. Edlmann, Dr. M. Edwards, B. Robbins, A. De la Rosa Illescas

Dissemination Level

PU	Public	**X**
RE	Restricted to the consortium members, the SIRAB, the end-users and the EU officers	
CO	Confidential (only the consortium and the EU officers)	

Deliverable number	**D045**
Deliverable name	**Report on the effect of Thermal, Hydraulic, Mechanical and Chemical coupled processes on caprock integrity from analogue analysis.**
Work-package	**WP4**
Lead participant	**Dr. habil. C. I. McDermott**

Version	Submitted by	Review level	Submitted	Reviewed
1.00	UEDIN	WP, PSC, SIRAB, EU, ALL	Date 30.06.2012	Date 25.07.2012
1.01	UEDIN	SIRAB	30.07.2012	
..				
..				

Editors		
Name	**Participant**	**email**

Executive summary

Experimental, analogue and numerical investigation of coupled thermal, hydraulic, mechanical and chemical processes has been undertaken. Experimentally a wide range of analogue caprocks and some reservoir rocks were investigated using new equipment developed at the university of Edinburgh to replicate in situ conditions of temperature, pressure and chemistry. A number of natural analogues were considered to demonstrate the long term impact of CO2 storage. The natural analogues provided both samples for the experimental work and large scale data relating to the impacts of coupled processes under reservoir conditions. Numerically key observations of the experimental work and analogue work informed new model development. A holistic approach relating the depositional environment to key storage location characteristics was attempted.

Section 1 :Introduction and Overview
Section 2: Experimental Investigation of Analogue Samples
Section 3: Natural analogues
Section 4: Numerical Investigation of Experimental and Analogue Results
Section 5: Preliminary work on Geo-mechanical facies

Scientific Highlights

- a large amount of experimental data relating to the flow and impact of supercritical CO2 on several caprocks including caprock core drilled from analogue fields at a depth of circa 4km, and Heletz (MUSTANG Project) caprock

- unique experimental results on the behaviour of supercritical and gaseous CO2 through naturally fractured caprock.
- chemical effects of CO2 on Heletz caprock leading to the development of micro-fissures.
- a study of several analogues for CO2 storage with a focus on the identification of coupled processes // positive feedback processes which may lead to failure of the storage system.
- a caprock model of the East Brae field, subdivided into genetic units based on the analysis of some 38 wells.
- a new numerical method and modelling study on the effects of heterogeneities on the migration of supercritical CO2 in a two phase brine CO2 system.
- a new conceptual approach coupled with a modelling approach for natural fluid fracking, and relate this to analogue field observations. Directly applicable to the effect of increasing reservoir fluid pressure due to fluid injection.
- Initial application of a geomechanical facies approach to considering key risk scenarios based on the consideration of THMC processes operating under generic, but distinctive in terms of deposition environment and tectonics, proposed storage sites.

Keywords	

Table of contents

Scientific highlights....14
Introduction and Overview....16
1.1 Definition of the Processes described as Thermal, Hydraulic, Mechanical and Chemical....16
1.2 The effects of THMC Coupling....17
1.3 Geomechanical facies as holistic approach to the analysis of the integrity of CO2 storage systems....19
1.4 Structure of report....20
1.5 Acknowledgments....21
1.6 References to Introduction....21
2 Experimental Investigation of Analogue Samples....24
2.1 Summary of the experimental samples obtained....24
2.1.1 MUSTANG test sites....24
2.1.2 UEDIN analogue sites....24
2.1.3 Additional UK North Sea Caprock....24
2.1.4 Summary of the experimental samples obtained for THMC testing....25
2.1.5 Laboratory experiments undertaken....27
2.1.6 Bench Experiment Type A - ambient pressure / in-situ temperature....27
2.1.7 Bench Experiment Type B - high pressure / high temperature....28
2.1.8 High pressure and temperature CO2 flow rig....28
2.2 Analysis techniques....31
2.2.1 Scanning Electron Microscope (SEM) imaging....31
2.2.2 EDS (energy dispersive) X-ray analysis....31
2.2.3 X-Ray Diffraction (XRD) analysis....31
2.2.4 X-Ray CT (Computed Tomography)....31
2.3 THMC experimental summary....32
2.4 THMC experimental results....34
2.4.1 St Ninian's Shale caprock....34
2.4.2 Heletz Caprock....36
2.4.3 Kimmeridge Clay - Miller Field caprock....47
2.4.4 Kimmeridge Clay – East Brae Field Caprock .. (non fractured and naturally fractured samples)....57
2.4.5 Evaporite caprock....69
2.4.6 Clashach reservoir sandstone....71
2.4.7 Stuben reservoir sandstone....74
2.5 Summary of the experimental investigation into the effect of thermal, hydraulic, mechanical and chemical coupled processes on caprock and reservoir rock....77
2.6 References....80
3 Natural Analogues....81
3.1 Objectives....81
3.2 Initial Efforts....81
3.3 Motivation for the main analogue targets....81
3.3.1 Black Devonian "shales" in NE USA....82
3.3.2 Kimmeridge Clay Formation....82
3.3.3 Rationale....82
3.3.4 Analogue targets deselected or rejected....83
3.4 W. New York Devonian Black Shales....84
3.4.1 Natural hydraulic fractures arrested by Dunkirk Black Shale....86
3.5 Initial Steps for the Evaluation of the Marcellus Fractures....87
3.5.1 Marcellus potential....87
3.6 Analysis of the fractures in shales of the lake Ontario shore near Dunkirk, NY....90
3.6.1 Method....90
3.6.2 Calculations....91

3.6.3 Dunkirk shale fractures – spacing analysis 92
3.7 Kimmeridge Clay Formation 97
3.7.1 Motivation 97
3.7.2 Initial onshore screening for suitable KCF 97
3.7.3 The Brae Hydrocarbon Field, North Sea, UK sector 101
3.7.4 Initial requests to Marathon UK 101
3.7.5 East Brae geological background 101
3.8 Development of a caprock model 103
3.8.1 Model build 103
3.8.2 Geological Setting 103
3.8.3 Data distribution 104
3.8.4 Core characterisation and sampling methods 104
3.8.5 Microfacies 106
3.8.6 Laboratory analyses for caprock model 107
3.8.7 Well Correlation Methodology 107
3.8.8 Discriminating the genetic units 108
3.8.9 Initial correlations 111
3.8.10 Secondary Seal Discrimination 112
3.8.11 Model Conceptualisation 113
3.8.12 Petrel Software 114
3.8.13 Stages 1 & 2 modelling, data density impact 114
3.8.14 Data Loading 115
3.8.15 Data Preparation 117
3.8.16 Generating surfaces and boundary polygons 117
3.8.17 Generating isochore surfaces for GU 1 – 3 and smoothing 2D surfaces 118
3.8.18 Structural Modelling 122
3.8.19 Fault Modelling 122
3.8.20 Pillar Gridding 122
3.8.21 Vertical Layering 122
3.8.22 Structural modelling Workflow 123
3.8.23 Results: Final 38 well Model 124
3.8.24 Data Sensitivity of the model 125
3.9 Model Analysis 132
3.9.1 Limitations 134
3.9.2 Quality of stage 1 interpretation 134
3.9.3 Fault geometry 134
3.9.4 Accuracy of the 3D geometry of the model 134
3.10 Future work 134
3.11 Concluding Remarks to Caprock Model 135
3.12 Discussion on proxies for mechanical behaviour 136
3.13 Acknowledgements 138
3.14 Appendices to Analogue Section 139
3.14.1 Appendix 1 Common Data Access 139
3.14.2 Appendix 2: Database from interpreted Kimmeridge Clay Formation Genetic Units and Secondary Seal 141
3.14.3 Appendix 3: Caprock Cross Sections 150
3.14.4 Kimmeridge Clay Formation Core Samples 155
3.14.5 List of websites or sources checked for W. New York sate satellite imagery 157
3.14.6 Mustang caprock sampling strategies notes 160
3.14.7 Contact Addresses and Locations of selected collaborators outwith main Mustang group 160
4 Numerical Investigation of Experimental and Analogue Results 162
4.1 Overview 162
4.2 Discussion 162

4.3 Paper: Front Tracking using a Hybrid Analytical Finite Element Approach for Two Phase Flow Applied to Supercritical CO2 Replacing Brine in a Heterogeneous Reservoir and Caprock....166
4.4 Paper: Predicting hydraulic tensile-fracture spacing in strata-bound systems. 199
5 Geomechancial Facies Approach 162
5.1 Introduction and Overview....216
5.2 Paper : Appraisal of caprock security in commercial CO2 storage; a thermo-hydro-mechanical-chemical coupled processes and geomechanical facies approach....217

List of Figures

Figure 1 Coupled Processes 18
Figure 2 Geomechanical facies as a basis for holistic multi-scale coupled process investigation ..20
Figure 3 Bench Experiment - Type A equipment. 27
Figure 4 Bench Experiment Type B equipment..... 28
Figure 5 Image of the experimental rig capable of reproducing in-situ reservoir and CO_2 injection conditions..... 29
Figure 6 Flow path sketch of the experimental rig in the Edinburgh University CO_2 Lab 30
Figure 7 St Ninian's caprock in outcrop - Kelty Quarry, Fife UK..... 34
Figure 8 St Ninian's caprock experimental samples. 35
Figure 9 Heletz caprock experimental samples. 36
Figure 10 Average SEM image of the surface of the Heletz cap rock. 37
Figure 11 Average elemental composition of the Heletz cap rock matrix. 37
Figure 12 SEM image and elemental analysis of Heletz cap rock. 38
Figure 13 Further SEM image and elemental analysis of Heletz cap rock..... 39
Figure 14 Matrix compositions at beginning of experiment and after 3 months. 40
Figure 15 Heletz cap rock matrix at beginning of experiment (A) and after 3 months (B). 41
Figure 16 Detail of the Heletz cap rock matrix at beginning of experiment and after 3 months, indicating that the matrix clay material becomes less defined and the edges are broken down over time and exposure to CO_2 (B) as opposed to the more defined edges of the sample exposed to heat and brine only (A)..... 41
Figure 17 delicate bridging structures are preserved in the samples not exposed to CO2 over time (this sample has been in the batch experiment with heat and brine but without CO2 for 2 months 23 days). 42
Figure 18 Ca crystals evident in samples exposed to brine and heat only after 3 months. 43
Figure 19 Evidence of micro fracturing that is not seen in the samples not exposed to CO_2. 43
Figure 20 Typical appearance of Pyrite in Heletz cap rock samples. 44
Figure 21 Backscattered electron image of two Heletz cap rock samples, one exposed to CO_2, heat and brine (A) the other heat and brine only (B). The pyrite shows up as the brightest spots. It is possible that the distribution of pyrite increases over time and with exposure to CO_2. .44
Figure 22 Typical quartz crystals in Heletz cap rock samples after exposure to heat and brine only (A) and heat, brine and CO_2 (B) for 3 months. 45
Figure 23 Visual section of Kimmeridge clay in well 9/28b-17 47
Figure 24 Kimmeridge Clay - Miller Field caprock experimental samples. 48
Figure 25 Mineral compositions of shale samples plotted against a lithologic column, well 9/28b-17. Little dots on the column indicate sample positions. Reservoir crest is marked. Note that the profile is not continuous with depth (Jiemin Lu Ph.D. 2008). 49
Figure 26 SEM image and X-ray analysis of sample matrix (Sample 1 starting sample Kimmeridge Clay 5mm chip) 51
Figure 27 SEM detail and x-ray analysis of pyrite (iron sulpide) on Sample 2 - starting sample Kimmeridge Clay 5mm chip..... 51
Figure 28 SEM detail and X-ray analysis of an Aluminium silicate with composition Si, Al, O, K and Fe in sample on Sample 2 - starting sample Kimmeridge Clay 5mm chip. 52
Figure 29 SEM image and X-ray analysis of matrix of Sample 17 - Kimmeridge clay sample exposed to NaCl brine only at 80°C for 80 days 52
Figure 30 SEM image and X-ray analysis of matrix of Sample 18 - Kimmeridge clay sample exposed to NaCl brine and CO_2 at 80°C for 80 days..... 53
Figure 31 SEM image and X-ray analysis of flakes within matrix of Sample 18 - Kimmeridge clay sample exposed to NaCl brine and CO_2 at 80°C for 70 days. 53
Figure 32 SEM image and X-ray analysis of quartz from Sample 17 - Kimmeridge clay sample exposed to NaCl brine only at 80°C for 80 days 53
Figure 33 Slices through un-reacted sample – yellow dots are pyrite, Sample is 3mm across and 5mm long. 54
Figure 34 Reacted Sample (120 days in 70,000ppm NaCl at 80°C saturated in CO_2) – yellow dots are pyrite, Sample is 3mm across and 5mm long..... 56
Figure 35 Images of the two 38mm diameter core samples of naturally fractured caprock from East Brae. 58
Figure 36 The % mineral abundances for caprock sample 16/3a-E1. 58

Figure 37 SEM backscatter images of the East Brae Kimmeridge Clay caprock showing depositional fabric (A) and quartz and pyrite crystals (B) 59
Figure 38 The % mineral abundances for the unfractured and fractured caprock samples from Well 16/3a-E1. 59
Figure 39 Image of the 38mm diameter core non fractured caprock sample, B-c from the North Sea Brae field. 63
Figure 40 SEM image of the transect and the mineral weight percent of the common minerals for both the fracture face exposed to CO2 and the original fracture face. 65
Figure 41 Mineral weight percent of the common minerals for both the fracture face exposed to CO_2 and the original fracture face 65
Figure 42 Average mineral weight percent from the SEM and Spirit Elemental analysis software data of the fracture face before and after CO_2 exposure. 66
Figure 43 SEM image and mineral weight percent of the common minerals on the line of transect along the bedding parallel microcracks 67
Figure 44 Boulby evaporites samples. 69
Figure 45 Image of the 38mm diameter Clashach sandstone core. 71
Figure 46 Effect of scCO2 flow rate through the Clashach reservoir sandstone at 40°C and a back pressure set to 10MPa 72
Figure 47 Differential pressures across the Clashach sandstone at a 3g/min flow rate at 10MPa, 20MPa and 30MPa fluid (back pressure) pressures at 40°C 73
Figure 48 Image of the 38mm diameter Stuben sandstone core – the sample length is 43mm. ..74
Figure 49 Measured average differential pressure and average permeability across the Stuben sandstone under flow experiments at 40°C, with flow rate held at 1g/min, the back pressure held at 9MPa, confining pressure was then increased from 20-30-40-50-60-70MPa. 75
Figure 50 Visual degradation in the surface of the Stuben sandstone even at low temperature, pressure and flow rate exposure to scCO2 76
Figure 51 Pease Bay Location 83
Figure 52 Straiths 84
Figure 53 Location maps of outcrop region for analogue case-study in western New York (NY). Red square is location of inset-in-inset showing New York State. Red dot in main fig shows approximate realm of central New York outcrop and borehole areas for Marcellus. Area labelled A on Lake Erie inset is Point Gratiot shoreline outcrop sequence of Dunkirk Black Shale. (External sources: Google Maps; Lash & Blood 2004) 85
Figure 54 Overview of NYS Devonian Catskill Delta (both images after Smith et al. date - AAPG, etc) 86
Figure 55 Tracing of Gratiot Pt Fractures on Corel georeferenced base map 88
Figure 56 Marcellus at NY rt20 road 89
Figure 57 Marcellus Western NYS 89
Figure 58 Satellite image of analogue fractures 90
Figure 59 Fractures picked for analysis 90
Figure 60 Division of area into sections 91
Figure 61 Length distribution of all fractures measured 93
Figure 62 Azimuth of all fractures measured 94
Figure 63 Length of fractures in section 0 94
Figure 64 Azimuth of all fractures in section 0 94
Figure 65 Length of all fractures in section 1 95
Figure 66 Azimuth of all fractures in section 1 95
Figure 67 Azimuth of all fractures in section 2 96
Figure 68 Length of all fractures in section 3 96
Figure 69 Azimuth of all fractures in section 3 96
Figure 70 Length of all fractures in section 4 97
Figure 71 Azimuth of all fractures in section 4 97
Figure 72 Kimmeridge Bay, Dorset 98
Figure 73 North Skye 99
Figure 74 Helmsdale, Sutherland 99
Figure 75 Conceptual cross section of South Viking Graben 100
Figure 76 Location of selected North Sea hydrocarbon fields highlighting Marathon's operations, Source: www.marathon.com/content/inline-images/marathon_com/maps/brae_2010.jpg ..102
Figure 77 Geologic cross section across Viking Graben north of Brae. Source: www.marathon.com 103

Figure 78 Geologic cross section across East Brae. Source: www.marathon.com 103
Figure 79 Map of the East Brae Field, UKCNS. (left) shows the number of wells (purple) used to discriminate the genetic units (GU's) within the KCF, (right) shows the well locations (green) used to map the secondary seal, Major Faults N1 – N3 are labelled in grey. (courtesy of Marathon Oil). 104
Figure 80 Each thin section is 20 mm wide. Microfacies classes shown are 1 to 5 left to right. Note banding frequency and distribution. 107
Figure 81 XRD results for different micro-facies within the East Brea Caprock 107
Figure 82 Well 16/03a-E2. Shows good quality wireline log displaying the 3 GU units; GU 1(red), GU 2 (orange), and GU 3 (yellow) based on the gamma ray and resistivity response. Note the difference in resistivity between GU 2 and GU 3. 109
Figure 83 Well 16/03a-E3 shows GU 3 is missing; hence the section has been interpreted as two genetic units only. The separation between the resistivity curves marks the difference between interpreting the lower section as GU 2. 110
Figure 84 Well 16/03a-E10. Where available in composite logs, neutron-density curves (green) were used to discriminate GU 2 (orange). In this well, the gamma ray log shows the contrast between the coarsening upward trend on GU 1 (red) and a more serrated pattern observed in GU 2. 110
Once the caprock and genetic units were interpreted, three correlation transects (Figure 85 & Figure 86) preceding the 3D model were built in Ed-Excel, illustrating the dome geometry of the KCF Caprock and the genetic units as conformable layers. From the 38 wells analysed, only the marginal well 16/03a-E16 was not conformable having repeating cycles of GU 1 and GU 2, thus there is no correlation with nearby wells that display a conformable trend. The thickness of the KCF varies significantly through the field, from 6m closer to the domal tip, to 80m at the far margins. 111
Figure 86 Map view illustrating three correlation transects: A-A' (green), B-B' (purple), C-C' (blue) across the Brae Formation. Note the presence of the ESE - WNW trending faults, major faults N1 – N3 (grey) are also shown. 111
Figure 87 Series of correlations were created in excel to give a first impression of the overall caprock geometry. Transects A-A' (top) and C-C' (bottom) illustrate the anticlinal structure. In A-A' Well E25 does not have GU 3, interpreted as a pinch out towards the domal tip. Transect B-B' crosses the E. Brae field N-S showing GU 3 (yellow) is missing in wells E12 and E14, interpreted as nearby fault related events. 112
Figure 88 Well 16/03a-2Z. Composite log depicting the secondary seal overlying the KCF caprock. The Valhall was interpreted as a marl unit for most of the 18 wells across the E. Brae field based on a consistent low, blocky gamma ray pattern. 113
Figure 89 shows the lateral distribution of the 38 wells throughout the study area. The complete data set comprises of the original wells (red) and new downloaded wells from CDA (blue). The position of Well 16/03-E16 that shows non-chronological GU interpretation is outlined (green box). (Compliments of Marathon Oil) 114
Figure 90 shows a 2D map view in Petrel contrasting the stage 1 "previous" data set (left) and the stage 2 "updated" data set (right). It shows the geographic position of the Brae Field (Cream with red boarder), Study Area (Purple box), spatial distribution of the wells (green dots) within UK North Sea block 16/03a – b. (compliments of DECC Open Government Licence V.1.0.) 115
Figure 91 shows the vertical distribution of the caprock using Matlab software. This approach, however, did not image the 3D architecture of the GU's and their lateral distribution. (Stage 1 3D Visual) 115
Figure 92 shows a 3D perspective of both (left) deviated and (right) Vertical well paths (multi-coloured lines) intersecting the top KCF surface. 116
Figure 93 Shows the extent of the deviated well paths in 2D Map view. 116
Figure 94 Petrels 2D map view of the presence of well top markers for (a) KCF top, (b) GU 1, (c) GU 2, (d) GU 3. GU 1 & 3 polygons (Purple) have been created based on their associated well top availability 118
Figure 95 shows thickness maps for VF, before (above) and after (below) Petrels smoothing 119
Figure 96 a & b 120
Figure 97 showing a Flowchart detailing Petrel workflow for a faulted Caprock, starting with a fault model and finishing with the vertical layering within the model. (Modified from: Slb, 2010) 122

Figure 98 Flowchart detailing Petrel workflow for Structural Modelling of the faulted KCF Caprock in stages from (1) Un-faulted model, (2) Fault modelling, (3) Pillar Gridding, (4) New 3D Skeleton Grid creation, (5) Vertical Layering make horizons to (6) the final model to include zones. 123
Figure 99 shows a progressive build up of the structural KCF caprock model in stratigraphic sequence (1) KCF bottom; (2) GU3 top; (3) GU2 top; (4) GU1 top; (5) Valhall Formation top; and, the distribution of major faults in the study area. 124
Figure 100 shows the regular grid intersections across the study area displayed relating to the 2Dviews in Appendix a – d. Both N-S and E-W intersections are spaced at 0.5km. Additionally, the high confidence zone < 650m is highlighted in light green and generally follows the Brae Field Limits. 125
Figure 101 shows the HC locations (light red) within a moderate data area (20 wells). Well positions displayed in 20 well caprock cross sections (Figure 39 -40) 126
Figure 102 shows the HC locations (light red) within a data poor area based on 6 wells. Well positions displayed in 6 well caprock cross sections (Figure 39 -40) 126
Figure 106 Comparison of finite element with front tracking and a finite volume approach for CO2 spreading in a heterogeneous reservoir. 163
Figure 107 Model predicting tensile fracturing of layered sedimentary sequences during fluid injection 164
Figure 108 Illustration of a caprock fracturing during fluid pressure increase, sedimentary section of cyclical sequence after Kassi et al. 2004, from the lower Carboniferous of Scotland. 165
Figure 109 Analytical solution for two phase flow 192
Figure 110 Two phase flow surface is approximated by a polynomial expression. 192
Figure 111 Extra input code to trigger and describe the HAN method in OpenGeoSys 193
Figure 112 The front has passed one node in the element 193
Figure 113 The front has passed two nodes in an element. 194
Figure 114 Two phase flow front has passed an element 194
Figure 115 Two phase flow front has not yet reached the element 195
Figure 116 Model for injection of supercritical CO_2 at the base of homogeneous caprock, application of front tracking method. 195
Figure 117 Relative permeabilities functions from *Buckley and Leverett* [1941] 196
Figure 118 Comparison of the analytical solution to volumetric method, the analytical method with and without mass distribution and the estimation of the front tracking method. 196
Figure 119 Comparison of radial solutions using the FUG-FE and the FUG-a approaches. 196
Figure 120 Low permeability layer just above the injection front, comparison of FUG and FUG-vT model performance, 40.5 days after start of forced injection 197
Figure 121 Injection into a heterogeneous field 197
Figure 122 Front tracking provides sub element scale information on the location of the saturation front in a heterogeneous field. 198
Figure 123 Comparison of well injection of supercritical CO_2 in a heterogeneous reservoir rock with front tracking, then without front tracking and continuous colouring for FUG-vT and a Finite volume solution. 198
Figure 124 Stack of sedimentary deposits 212
Figure 125 Generic sedimentary sequence 212
Figure 126 Standard elastic strip solution on a semi–infinite layer 213
Figure 127 Elastic solutions for a rough strip foundation underlayen by a rigid base 213
Figure 128 Standard relationship for tensile fracturing conditions 213
Figure 129 Natural hydraulic fracturing conditions, impact of Poisson's ratio (u in figure) 214
Figure 130 Development of five fracture sets 214
Figure 131 Sedimentary sequence and hydro-fracturing 215
Figure 132 Tetrahedron (3-simplex) plot of the four nodes of the THMC coupling processes and the potential spectrum of reciprocal interaction and feedback amongst these processes. ... 240
Figure 133 Conceptual model of fracture and scale issues in modelling. Shown is variation in co-efficient of restraint for thermal stress considerations of density of fracture in a single geological media. 241
Figure 134 Effects of pore fluid pressure on effective. 3a, stress a Mohr circle for the two dimensional stress tensor allows graphical resolution of shear and normal stress values to be resolved on a fault (new fracture &/or dynamic rupture) and a pre-existing fault (frictional shear slip) before and after an increase in fluid pressure. Angles and magnitudes

intensionally unspecified. 3b, example of fracture population disrtibuition with respect to an prevailing stress field with calculations of pore fluid pressure contoured for isobaric values for changing σ_1/σ_3 ratios. **241**
Figure 135 Tectonic settings of basin types for reservoirs. 4a, basin type classification based upon plate tectonic kinematics. 4b, summary of media types that may be present and respective dominant reservoir flow characteristics **242**
Figure 136 Schematic illustration of basin setting architecture of the upper lithosphere for extensional systems **242**
Figure 137 Schematic illustration of basin setting architecture of the upper lithosphere for convergent systems **243**
Figure 138 Schematic illustration of basin setting architecture of the upper lithosphere for Strike-Slip Systems **243**
Figure 139 The relationship between permeability and pressure in three kinds of rock (Datapoints after: Brace et al., 1968; Kilmer et al., 1987; Neuzil, 1986; Rutqvist and Stephanson, 2003) **244**
Figure 140 Schematic cross section of the Miller CO_2 storage site (after Lu 2008) **245**

List of tables

Table 1 Caprock availability from the MUSTANG test sites. 24
Table 2 A summary of the primary North Sea caprock types. 25
Table 3 Outline of each experimental rock type. 26
Table 4 The THMC parameters measured for each rock type 32
Table 5 THMC coupled process investigations conducted through the experimental program for each of the rock samples. 33
Table 6 THMC investigations undertaken on the St Ninian's caprock in bench experiment type A equipment. 35
Table 7 THMC investigations undertaken on the Heletz caprock in bench experiment type A equipment. 40
Table 8 THMC investigations undertaken on the Miller Field Kimmeridge clay caprock in bench experiment A equipment. 50
Table 9 THMC investigations undertaken on the East Brae naturally fractured Kimmeridge Clay caprock in the high pressure and temperature CO2 flow rig. 60
Table 10 Experimental program run during the investigation into multiphase flow of CO_2 in fractured caprock. 61
Table 11 Maximum differential pressures at each confining pressure stage for the phase 1 supercritical CO_2 flow experiment on samples B-a and B-b. 62
Table 12 Maximum differential pressures at each confining pressure stage for the phase 2 supercritical CO_2 flow experiment on samples B-a and B-b. 63
Table 13 Maximum differential pressures for the non fractured sample B-c under the scCO_2 experiment. 64
Table 14 THMC investigations undertaken on the Evaporite caprock in bench experiment B equipment. 70
Table 15 THMC investigations undertaken on the Clashach reservoir sandstone using the high pressure and temperature supercritical CO2 flow rig at in-situ temperature and pressure with scCO2 flow 72
Table 16 THMC investigations undertaken on the Stuben reservoir sandstone using the high pressure and temperature supercritical CO2 flow rig at in-situ temperature and pressure with scCO2 flow 75
Table 17 Summary of the key results from the full suite of THMC investigations conducted through the experimental testing on shale, claystone and evaporate caprock types and reservoir sandstones. 79
Table 18 Fracture statistics 93
Table 19 Three reservoir-wide genetic units were interpreted by analysing discriminable, repeating patterns in the wireline log signals. 108
Table 20 shows a summary of real thickness values against modelled data for models based on a) 6 wells, b) 20 wells and c) 38 wells. The model match good (green), medium (orange) and bad (red) is outlined. 133
Table 21 Fluid properties, models 1,2 & 3 191
Table 22 Material parameters, model 1&3 191
Table 23 Material parameters model 4 & 5. 191
Table 24 Basin type and susceptibility to problems relating to CO2 storage 216
Table 25 Overview of basin types susceptible to problems or unsuitable for geomechanical facies type classification 246
Table 26 General properties of the Utsira Sand 247
Table 27 General properties of the Utsira Caprock 247

Scientific highlights

Included in this report is

- a large amount of experimental data relating to the flow and impact of supercritical CO2 on several caprocks including caprock core drilled from analogue fields at a depth of circa 4km, and Heletz (MUSTANG Project) caprock

- unique experimental results on the behaviour of supercritical and gaseous CO2 through naturally fractured caprock.

- chemical effects of CO2 on Heletz caprock leading to the development of micro-fissures.

- a study of several analogues for CO2 storage with a focus on the identification of coupled processes // positive feedback processes which may lead to failure of the storage system.

- a caprock model of the East Brae field, subdivided into genetic units based on the analysis of some 38 wells.

- a new numerical method and modelling study on the effects of heterogeneities on the migration of supercritical CO2 in a two phase brine CO2 system.

- a new conceptual approach coupled with a modelling approach for natural fluid fracking, and relate this to analogue field observations. Directly applicable to the effect of increasing reservoir fluid pressure due to fluid injection.

- Initial application of a geomechanical facies approach to considering key risk scenarios based on the consideration of THMC processes operating under generic, but distinctive in terms of deposition environment and tectonics, proposed storage sites.

Nomenclature

c	Heat capacity (J/kg K)
C	Chemical concentration (Kg/m^3)
D_C	Chemical diffusion dispersion tensor (m^2 / s)
D_T	Heat diffusion dispersion tensor (J/K m s)
E	Young's modulus (Pa)
μ	Dynamic viscosity (Pa s)
g	Acceleration of gravity (m²/s)
ρ	Density (kg/m³)
ρ_b	Density of solids (kg/m³)
σ	*S*tress (Pa)
k	Intrinsic permeability (m²)
K_d	Solute distribution coefficient (m^3 / Kg)
n	Porosity
p	Fluid pressure (Pa)
Q	Flow rate (m^{3}s^{-1})
Q_T	Heat source (J/kg K)
Q_{rxn}	Chemical species source due to reactions (Kg/m^3)
S_s	Specific storage (Pa^{-1})
t	Time (s)
T	Temperature (K), unless otherwise specified
m	Equivalent value for porous medium
w	Water
q	Velocity (m/s)
z	Height above datum (m)

Introduction and Overview

Geological sequestration of Carbon dioxide requires both a suitable host reservoir formation comprising high accessible porosity for storage and a low permeability barrier (Caprock) to prevent the CO_2 returning to the surface. In this report we present the results of work done at the University of Edinburgh on factors relating to Thermal, Hydraulic, Mechanical and Chemical (THMC) processes significantly influencing the ability of the caprock to restrain the return of CO_2 to the surface for a period of at least 1000 years. After 1000 years it is assumed that technology will have so further developed as to make the escape of stored CO_2 into the atmosphere of minor environmental impact. In the literature there is much work on individual combinations of these processes, e.g. (Angeli et al., 2009; Bildstein et al., 2010; Ferronato et al., 2010; Hangx et al., 2010a; Hangx et al., 2010b; Jensen et al., 2009; McDermott et al., 2011; Quattrocchi et al., 2009; Rutqvist et al., 2007; Selvadurai, 2009; Seyedi et al., 2009; Verdon et al., 2011; Vilarrasa et al., 2010; Wollenweber et al., 2010), and an overall review of the issues surrounding caprock integrity is presented by (Shukla et al., 2010; Shukla et al., 2011). Our work focuses on elements identified as research gaps and required future work.

We have focused our investigation on the integrity of the Caprock by using

1. small scale experimental investigation of naturally fractures and intact analogue material under in situ conditions of temperature, pressure and geochemistry,
2. the investigation of large scale analogues
3. the development of new numerical models and concepts to explain observed phenomena.

Two key analogue sites have been chosen representing a likely future storage repository caprock, The Kimmeridge Clay caprock of the Brea-Millar field in the North Sea and an increasingly researched shale where we contend that a clear example of hydro-mechanical fracturing is apparent and from which clear lessons about caprock behaviour can be derived, the Marceleous Shale.

1.1 Definition of the Processes described as Thermal, Hydraulic, Mechanical and Chemical

In Deliverable D0502, PROCESS MODELS FOR FLOW, TRANSPORT and GEOCHEMICAL PROCESSES, key processes are described impacting the behaviour of CO2 in the subsurface. In this current document we define a process as being described by a mass or energy balance equation. In other words there is a separate mass or energy balance equation which describes the behaviour of the temperature (T), fluid pressure (H), stress (M) or geochemistry (C).

These individual processes interact with each other, hence the term coupled. This interaction may amplify the effect of a certain process, or diminish it through a feedback mechanism. The interaction of the processes with each other is through material behaviour. For instance temperature impacts fluid flow through viscosity, increased temperature leads to lower viscosity which leads to increased fluid flow which leads to an increased impact of the fluid on the system. To try to investigate a system by only considering one of the processes leads to an oversimplified representation.

The key balance equations for these processes are described below. There are many different ways of solving these equations and their coupling but this aspect is beyond the remit of this report.

For heat transport (T) this is given by equation (1).

$$D_T \Delta T - c^w \rho^w \nabla \cdot qT - \rho Q_T = c^m \rho^m \frac{\partial T}{\partial t} \quad (1)$$

Equation (1) represents the change in the amount of energy in a continuum at a discrete location in a unit volume as a consequence of heat entering, leaving or being stored in the discrete unit volume either through conduction, radiation diffusion or convection. Here an energy balance equation is used, and the energy at any location is expressed as temperature.

For fluid flow (H), the hydraulic process is similarly described as being the change in the mass of fluid in a continuum at a discrete location as a consequence of fluid entering, leaving or being stored the discrete unit volume either through advection, or addition / removal through a source term.

$$S_s \frac{\partial p}{\partial t} - \nabla \cdot \left(\frac{k}{\mu} \left(\nabla \cdot p + \rho g \nabla \cdot z \right) \right) = Q \quad (2)$$

For mechanical processes (M), we again describe the deformation of a continuum as a function of the stress applied, which can be shown to be an energy balance equation. Again the basis for the analysis is that of the energy balance in a continuum at a discrete location as a consequence of stress and deformation changes within a discrete unit volume.

$$\nabla \sigma - \rho g = 0 \quad (3)$$

Chemical transport (C) is described as being the change in the mass of a chemical species in a continuum at a discrete location as a consequence of fluid that species entering, leaving, being stored or being removed from the discrete unit volume either through advection, diffusion, sorption, or addition / removal through reactivity, usually represented as a source term.

$$nD_C \Delta C - \nabla \cdot qC - N_{rxn} = \frac{\partial \left(nC + \rho_b K_d C \right)}{\partial t} \quad (4)$$

Generally there will be one thermal process (T), one mechanical process (M), one, two or in some cases three fluid flow processes (H, H^2, H^3) depending on how multi phase flow is dealt with and (n) Chemical processes considered depending on the number of chemical species considered, typically n > 6.

1.2 The effects of THMC Coupling

Several researchers have described a number of interacting physical phenomena as a result of THMC processes interacting with one another, a key paper being (Tsang, 1991). Since then there have been several hundreds of publications. The interaction of coupled processes is illustrated in Figure 1. In this diagram we illustrate the fact that all the key processes listed above are linked via material behaviour coupled in someway. This behaviour is also influenced in the storage settings we are considering by a complex three dimensional heterogeneous

geology, describing the distribution of the different facies present and their associated material parameters. We can expect that all of these physical phenomena illustrated here (none exclusive list), will be operating in a caprock during storage.

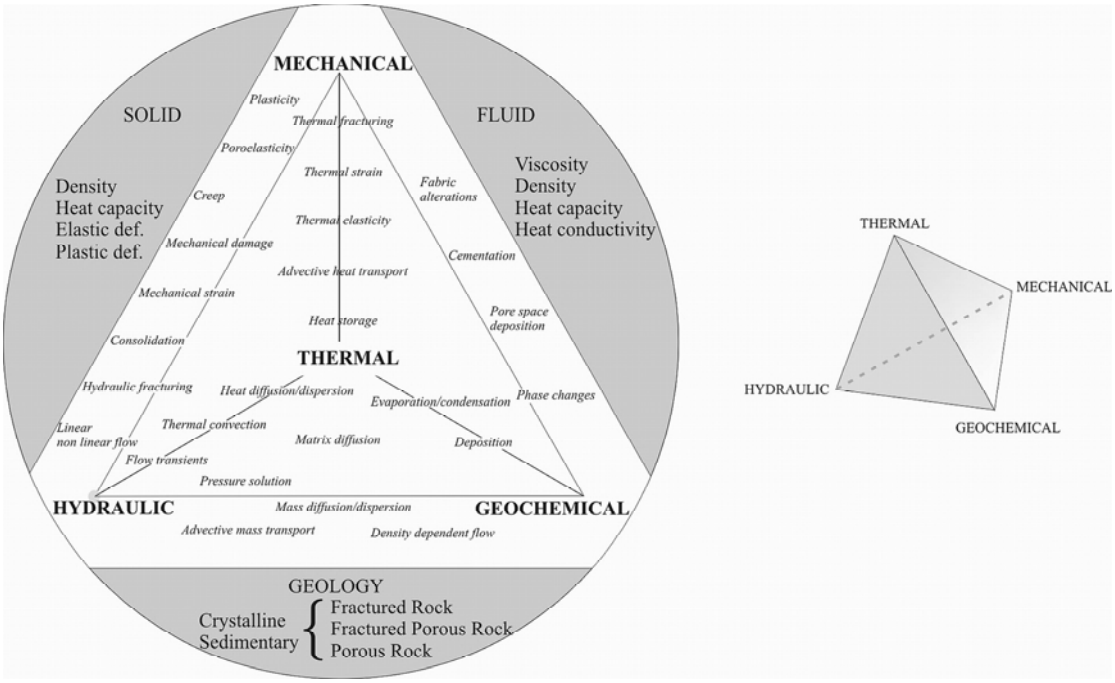

Figure 1 Coupled Processes

To demonstrate this, if we take the example of a fracture in a caprock, the impact of several coupled processes as a consequence of CO_2 injection on the system can be illustrated. On the event that CO_2 is injected in a reservoir beneath the caprock (H^2), the caprock will see an increase in vertical stress (M) due to the displacement of the fluids already present in the reservoir. These fluids will be moving from one chemical environment to another, and therefore there will be a change in local geochemical gradients (nC). In addition the temperature (T) of the injected fluid, the formation fluid and the reservoir host rock will be different, and therefore there will be a change in the local temperature gradients related to the conduction of the medium, the advection of fluids and any radiative effects. The fluid pressure increase and the change in temperature will have a mechanical impact on the fluid flow properties of the caprock, which in turn will be being impacted by the geochemical alterations described. Changes will be focussed on certain areas in the reservoir and caprock due to the inherent geological structure present and heterogeneity.

The interaction of coupled processes will lead to positive or negative feedback loops. By a positive feedback loop we understand that a particular phenomenon when considered only in one of the processes described above would come to a certain state equilibrium, however through coupling to another process the phenomenon reaches a different state of equilibrium. An example would be the advective flow of a cold fluid through a warm fractured caprock. As the cold fluid flows through the rock so the rock experiences cooling, the cooling leads to a thermal change in the volume of the rock which is expressed in a change in fracture aperture and a change in the thermal stress footprint in the system. Under most mechanical conditions a cooling will lead to a reduction in stress across the fracture, which will lead to an increase in the permeability of the

fracture so more cold fluid can pass through (Thermal stress can be shown to have more of an impact than tectonic stress depending on the restraint of the rock mass system). If this process had only been considered either as a hydraulic or as a thermal process then the modelling of the system would have been an oversimplification, and the results a poor representation of what was occurring. By including the coupling, although the model is getting more complex, there is more confidence that key processes and phenomena are being represented.

1.3 Geomechanical facies as holistic approach to the analysis of the integrity of CO2 storage systems

In this report we start to address the identification and quantification of coupled THMC processes particularly effecting caprock type strata during CO2 injection. Inherent in the work is the concept that the subsurface is divided into "Phenomenological" units rather than geological units. This approach means we group together deposits, and our investigation of the deposits according to their behaviour for the different THMC processes described above in an attempt to represent subsurface structures and also to provide fundamental building blocks for our experimental, modelling and analogue comparisons. To do this we use the "Geomechanical facies" approach (McDermott et al., 2006; McDermott et al., 2007; Tenzer et al., 2010).

A Geomechanical facies (GM facies) is considered as being constructed of one or more portable genetic units and having similar behaviour for specific processes. The GM facies form a conceptual building block for the subsurface, whereby the coupled process behaviour of the deposits are captured in the GM facies descriptions. Several different scales of data are used to define the parametrical responses of the GM facies, which allows the combination of different scales of investigation and interpretation. In addition the GM facies form the "conceptual geometrical and parameter related building blocks" (see McDermott et al. 2007) for construction of numerical models and the investigation of positive feedback loops in the coupling of processes.

The subsurface is not just a random collection of deposits, rather there is a clear depositional (energy of deposition) structural (stress history) and diagenetic (burial and fluid circulation) control on the characteristics of the deposits. Therefore under similar conditions similar types of deposits can be expected. Hence by understanding the typical characteristics of the GM facies which can be expected to be present dependent on the tectonic settings and depositional influence, it is possible to use the GM facies approach as a means of comparing the characteristics of different storage sites. This leads to the ability to be able to develop a risk type assessment based on expected storage site characteristics, as a function of the key controls to the development of the different GM facies and their sequence.

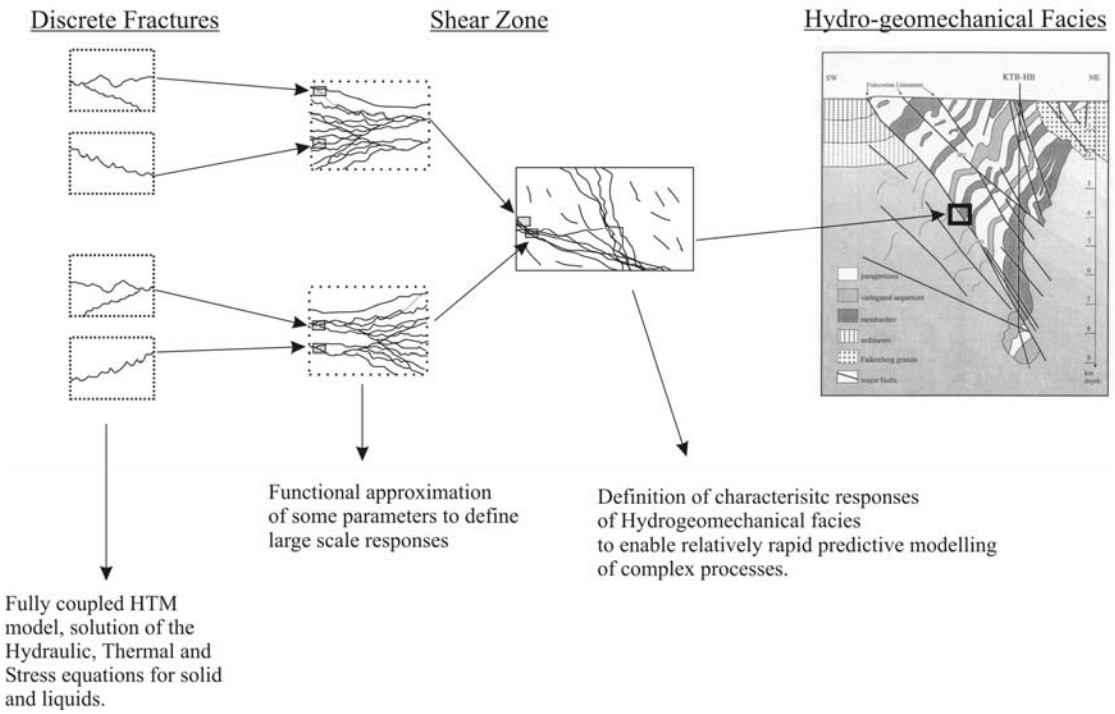

Figure 2 Geomechanical facies as a basis for holistic multi-scale coupled process investigation

1.4 Structure of report

Section 2) Experimental Investigation of Analogue Samples
A laboratory scale where under a controlled environment, in situ conditions of fluid pressure (to 60MPa), mechanical restraint, temperature (to 80 Celcius) and chemistry (concentrated brines) are replicated as closely as possible on samples of analogue caprock. New laboratory equipment was designed and built to examine flow, temperature and chemical phenomena of caprock samples, some of which were recovered from a depth of over 4km containing natural fractures.

Section 3) Large Scale Analogue Investigation
Field scale investigation using field observations of analogue strata where certain THMC processes considered important for caprock behaviour under storage conditions are described. Several analogue outcrops are described from which two analogues are investigated in more detail. The main analogue investigated is the Millar-Brae. It is identified as having effectively stored CO2 for a significant period of time, in addition much data is available and we were able to gain ready access to core samples. Secondly the Marcellous shale is also identified as providing information on key HM process'. We consider these processes vital for the integrity of caprocks where the pressure of fluids confined by the caprock is being artificially increased. A caprock facies model is constructed for the Millar Brae field based on genetic units, which in turn combines to allow a consideration of the geo-mechanical facies present, exportable to most numerical codes.

Section 4) Development of Modelling Tools describing CO2 replacement in heterogeneous media and caprock fluid pressure-fracturing due to CO2 emplacement

In this section tools which were specifically designed in conjunction with the experimental and analogue work are presented. More details on the general modelling tools developed in MUSTANG can be found in work package 5, 6 and 7.

Modelling tools were used to identify key processes operating under the conditions to be expected during the normal operation of the engineered geosystems storing CO_2. Particularly the possible impact of the heterogeneities in caprocks was investigated for two phase flow (CO_2/Brine) using a new hybrid finite element and analytical technique for solving the multiphase fluid transport equations developed as part of this project (McDermott et al., 2011), section 4:1. In addition a further new HM model was developed to describe the development of strata bound fracturing in a layered stratagraphical sequence, typical of most caprock sequences. This model matches fractured data and literature well, uses fluid pressure and tensile strength relationships as well as permeabilities of the layers to describe the build up of pore pressure as a function of an external forcing (e.g. burial leading to the increase of pressure or fluid injection such as in hydrofracing operations of CO_2 storage operations) section 4:2

Section 5) Integrating Field Scale, Lab Scale and Numerical Analysis
Geomechanical facies analysis provides the basis for an overall comparison of the setting of different storage sites and the identification of "critical pathways" for storage failure. A critical pathway comprises the development of positive feedback loops between processes leading to detrimental effects on the integrity of the storage system. This is dependent on the combination of the field variables (THMC) as well as the depositional and structural history of a deposit (Geomechanical facies section 5). In addition this type of analysis also provides the basis for an assessment of the risk of a storage system not performing as predicted during the CO2 storage lifetime.

1.5 Acknowledgments

The research leading to these results has received funding from the European Community's Seventh framework Programme FP7/2007-2013 under the grant agreement No. 227286 as part of the MUSTANG project and from the Scottish Funding Council for the Joint Research Institute with the Heriot-Watt University which is part of the Edinburgh Research Partnership in Engineering and mathematics (ERPem).

1.6 References to Introduction

Angeli, M., Soldal, M., Skurtveit, E., and Aker, E., 2009, Experimental percolation of supercritical CO(2) through a caprock, Greenhouse Gas Control Technologies 9, Volume 1: Energy Procedia, p. 3351-3358.

Bildstein, O., Kervevan, C., Lagneau, V., Delaplace, P., Credoz, A., Audigane, P., Perfetti, E., Jacquemet, N., and Jullien, M., 2010, Integrative Modeling of Caprock Integrity in the Context of CO(2) Storage: Evolution of Transport and Geochemical Properties and Impact on Performance and Safety Assessment: Oil & Gas Science and Technology-Revue De L Institut Francais Du Petrole, v. 65, p. 485-502.

Ferronato, M., Gambolati, G., Janna, C., and Teatini, P., 2010, Geomechanical issues of anthropogenic CO(2) sequestration in exploited gas fields: Energy Conversion and Management, v. 51, p. 1918-1928.

Hangx, S.J.T., Spiers, C.J., and Peach, C.J., 2010a, The effect of deformation on permeability development in anhydrite and implications for caprock integrity during geological storage of CO(2): Geofluids, v. 10, p. 369-387.

—, 2010b, Mechanical behavior of anhydrite caprock and implications for CO(2) sealing capacity: Journal of Geophysical Research-Solid Earth, v. 115.

Jensen, G.K.S., Nickel, E.H., Whittaker, S., and Rostron, B.J., 2009, Geological model and hydrogeological framework of an active CO(2) sequestration project in the Weyburn-Midale area, Saskatchewan: Leading to a further understanding of possible CO(2) migration, Greenhouse Gas Control Technologies 9, Volume 1: Energy Procedia, p. 2983-2989.

McDermott, C.I., Bond, A.E., Wang, W., and Kolditz, O., 2011, Front Tracking Using a Hybrid Analytical Finite Element Approach for Two-Phase Flow Applied to Supercritical CO(2) Replacing Brine in a Heterogeneous Reservoir and Caprock: Transport in Porous Media, v. 90, p. 545-573.

McDermott, C.I., Lodemann, M., Ghergut, I., Tenzer, H., Sauter, M., and Kolditz, O., 2006, Investigation of coupled hydraulic-geomechanical processes at the KTB site: pressure-dependent characteristics of a long-term pump test and elastic interpretation using a geomechanical facies model: Geofluids, v. 6, p. 67-81.

McDermott, C.I., Xie, M., Kosakowski, G., Mettier, R., Moog, H., and Kolditz, O., 2007, Geomechanical Facies Concept and the Application of Hybrid Numerical and Analytical Techniques for the Description of HTMC Coupled Transport in Fractured Systems, PROCEEDINGS, Thirty-Second Workshop on Geothermal Reservoir Engineering, Stanford University, Stanford, California, January 22-24, 2007, SGP-TR-183.

Quattrocchi, F., Cantucci, B., Cinti, D., Galli, G., Pizzino, L., Sciarra, A., and Voltattorni, N., 2009, Continuous/discrete geochemical monitoring of CO(2) Natural Analogues and of Diffuse Degassing Structures (DDS): hints for CO(2) storage sites geochemical monitoring protocol, Greenhouse Gas Control Technologies 9, Volume 1: Energy Procedia, p. 2135-2142.

Rutqvist, J., Birkholzer, J., Cappa, F., and Tsang, C.F., 2007, Estimating maximum sustainable injection pressure during geological sequestration of CO2 using coupled fluid flow and geomechanical fault-slip analysis: Energy Conversion and Management, v. 48, p. 1798-1807.

Selvadurai, A.P.S., 2009, Heave of a surficial rock layer due to pressures generated by injected fluids: Geophysical Research Letters, v. 36.

Seyedi, D., Ducellier, A., Foerster, E., Guy, N., Hild, F., and Rohmer, J., 2009, Coupled hydromechanical modeling to study the integrity and safety of geological storage of CO(2), Greenhouse Gas Control Technologies 9, Volume 1: Energy Procedia, p. 2541-2548.

Shukla, R., Ranjith, P., Haque, A., and Choi, X., 2010, A review of studies on CO(2) sequestration and caprock integrity: Fuel, v. 89, p. 2651-2664.

Shukla, R., Ranjith, P.G., Choi, S.K., and Haque, A., 2011, Study of Caprock Integrity in Geosequestration of Carbon Dioxide: International Journal of Geomechanics, v. 11, p. 294-301.

Tenzer, H., Park, C.-H., Kolditz, O., and McDermott, C.I., 2010, Application of the geomechanical facies approach and comparison of exploration and evaluation methods used at Soultz-sous-Forts (France) and Spa Urach (Germany) geothermal sites: Environmental Earth Sciences, v. 61, p. 853-880.

Tsang, C.-F., 1991, Coupled hydromechanical-thermochemical processes in rock fractures: Rev. Geophys., v. 29, p. 537 - 552.

Verdon, J.P., Kendall, J.M., White, D.J., and Angus, D.A., 2011, Linking microseismic event observations with geomechanical models to minimise the risks of storing CO(2) in geological formations: Earth and Planetary Science Letters, v. 305, p. 143-152.

Vilarrasa, V., Bolster, D., Olivella, S., and Carrera, J., 2010, Coupled hydromechanical modeling of CO(2) sequestration in deep saline aquifers: International Journal of Greenhouse Gas Control, v. 4, p. 910-919.

Wollenweber, J., Alles, S., Busch, A., Krooss, B.M., Stanjek, H., and Littke, R., 2010, Experimental investigation of the CO(2) sealing efficiency of caprocks: International Journal of Greenhouse Gas Control, v. 4, p. 231-241.

2 Experimental Investigation of Analogue Samples

A laboratory scale where under a controlled environment of in situ conditions of fluid pressure (to 60MPa), mechanical restraint, temperature (to 80 Celsius) and chemistry (concentrated brines) are replicated as closely as possible on samples of analogue caprock. New laboratory equipment was designed and built to examine flow, temperature and chemical phenomena of caprock samples, some of which were recovered from a depth of over 4km containing natural fractures.

2.1 Summary of the experimental samples obtained

Accessibility proved to be the deciding factor in sample collection. Three sources of caprock samples were investigated:
MUSTANG test sites
UEDIN analogue sites
Additional UK North Sea Caprock

2.1.1 MUSTANG test sites

The MUSTANG partners were approached for caprock samples from each of the test sites, Table 1. Limited caprock core was available and collected from Heletz and there was no caprock was cored or available from any of the other test sites. Caprock core will become available when the new Heletz well is cored.

Test Site	Cap rock core availability
Heletz (Israel)	Limited small fragments of cap rock core available and collected. Cap rock will be provided from newly drilled well mid 2012.
Horstberg (Germany)	No core for Horstberg, small possibility from nearby wells but will take time to identify if there is cap rock core.
Valcele (Romania)	No cap rock core.
Northern Spain	No cap rock core.
South Scania (Sweden)	No cap rock core on first look.
Maguelone (Languedoc, France)	No cap rock core.

Table 1 Caprock availability from the MUSTANG test sites.

2.1.2 UEDIN analogue sites

In addition to the MUSTANG test sites, the aim was to obtain caprock core from the two CO2 natural analogue sites of St Johns and UK North Sea (East Brae field was chosen, see Chapter 1 for detailed information on the East Brae caprock properties and distribution). Limited outcrop rock samples of the St Johns caprock, the Marcellus Shale was obtained. For the East Brae caprock (Kimmeridge Clay) downhole core was obtained from depths of 4km where 6m of Kimmeridge clay core was provided by Marathon.

2.1.3 Additional UK North Sea Caprock

To fully categorise the THMC controls on caprock it is important to test the full range of caprock types. Caprock is any rock with low porosity and permeability

that impedes the escape of fluids from the porous and permeable reservoir rock. The evolving depositional environment of the North Sea basin and its subsequent structural history has lead to a number of different caprock types including shales, evaporites and chalks. Table 2 provides a summary of the North Sea caprock types. The Zechstein evaporites are a major seal of the Southern North Sea and is the caprock for the Fizzy field and other CO2 rich gas fields which are very useful CO2 storage analogues.

Geological Period	Location	Example Reservoir	Caprock type
Cenozoic	Central and Northern North Sea	Frigg	Middle Eocene marine mudstones
Upper Cretaceous	Southern North Sea	Dan, Ekofisk	Chalk
Cretaceous	Outer Moray Firth	Northern Claymore field	Aptain marls, Cromer knoll marls Campanian marls
Jurassic	Viking Grabben, East Shetland Basin	Brent, Magnus, Brae	Kimmeridge clay
Upper Triassic / lower Jurassic	East Shetland Basin	Statford sandstones	Dunlin shale
Triassic	Southern and Central North Sea	Bunter, Cormorant	Keuper halite Bunter shale
Permian	Southern Permian Basin	Rotliegends	Zechstein halite / anhydrite Rotliegend shale
Carboniferous	Southern North Sea Basin	Silverpit, Barren red	Westphallian shales

Table 2 A summary of the primary North Sea caprock types.

For the MUSTANG experiments, in addition to the East Brae Kimmeridge Clay caprock and the Heletz caprock, the following UK North Sea caprock types were obtained:
Permian / Triassic evaporites from the Boulby Potash mine
Carboniferous shales from St Ninian's Quarry, Fife
Jurassic Kimmeridge Clay from the UK North Sea Miller field

2.1.4 Summary of the experimental samples obtained for THMC testing

The caprock types and reservoir rocks collected for the MUSTANG THMC experimental testing are as follows:
St Ninian's shale
Heletz caprock
Kimmeridge Clay – UK North Sea Miller Field caprock
Kimmeridge Clay - UK North Sea East Brae Field caprock
Boulby mine evaporite
Clashach sandstone
Stuben sandstone

A brief outline of each caprock type is presented in Table 3, which provides a summary of each caprock tested including location, sample description and mineralogy along with formation brine composition and reservoir temperature if relevant. More details of the individual caprock types will be given in section 2.4 when the THMC responses to CO2 are discussed.

Sample location	Sample description	Formation water composition	Reservoir Temp	Bulk mineralogy
St Ninian's Shale – from St Ninian's Quarry, Fife, Scotland UK	Carboniferous rocks of Midland Valley of Scotland. St Ninan's shale is in the Limestone Coal formation formed under fluvial deltaic high frequency cyclical deposits.	70,000 NaCl eq. ppm	80°C	Awaiting XRD results – will be presented in Deliverable 045, due month 36
Heletz cap rock – from Well H-2, C#18, Bx-1. Heletz, Israel	Heletz is Lower Cretaceous encompassing: alluvial braidplain, tidal flat, tidal marsh-costal swamp, inner shelf and meandering river and are a sequences of repeated regressive – transgressive (fluvial – marine) depositional sequences.	35,000 NaCl eq. ppm	55°C	Matrix: Silicon (Si), Oxygen (O) and Aluminium (Al) with minor Iron (Fe), Potassium (K) and Magnesium (Mg) (predominantly illite). Discrete crystals of: Pyrite, Titanuim-Iron oxide (Ti-Fe) and Iron-Sulphur oxide (Fe-S) along with Calcite ($CaCO_3$) and Quartz (Si-O)
Kimmeridge Clay – from Miller Field, Well 16/7b-20. UK North Sea	The Kimmeridge Clay was deposited during the Jurassic in a deep water anoxic environment mainly consists of organic-rich 'black' shales interbedded with thin sand/silt beds.	70,000 NaCl eq. ppm	80°C	Matrix: Silicon (Si), Oxygen (O) and Aluminium (Al) with minor Iron (Fe), Potassium (K) and Magnesium (Mg) (predominantly illite with minor kaolinite) Discrete crystals of: Quartz, K-feldspar, pyrite with minor sodium plagioclase (albite), Calcite and dolomite.
Kimmeridge Clay – from East Brae Field, Well 16/3a-E1. UK North Sea	The Jurassic Kimmeridge Clay was deposited in a deep water anoxic environment. Organic-rich 'black' shales interbedded with thin sand/silt beds. Interpreted as basin floor lateral equivalents of the North Brae feeder system to the SW.	45,000 – 72,000 NaCl eq. ppm	120°C	Matrix: a typical illite clay rich matrix chemistry and morphology - primarily Si with O, Al and some K and Fe. Discrete crystals of: Quartz, K-feldspar, pyrite with minor sodium plagioclase (albite), Calcite and dolomite.
Boulby Mine evaporite	Permian / Triassic evaporite sequence deposited from the Zechstien Sea	NA	NA	Salts deposited include anhydrite (Calcium sulphate) and gypsum, then halite (NaCl) and sylvinite (KCl). Awaiting XRD results – will be presented in Deliverable 045, due month 36
Clashach Sandstone	Aeolian New Red Sandstone from the Permian age. Deposited as sand dunes formed in a desert environment.	NA	NA	Clashach is a medium grained sandstone with average: 16% porosity, 1150mD permeability, 2.16 g/cm3 bulk density and 0.2mm grain diameter. It is composed of 95% quartz, 3% k-feldspar, <0.5 clays, <0.5 ankerite and < 1% others. Awaiting XRD results – will be presented in Deliverable 045, due month 36
Stuben Sandstone	Triassic terminal alluvial plain of the South German Keuper Basin	NA	NA	16 % porosity, primarily quartz with relatively high feldspar content. Awaiting XRD results – will be presented in Deliverable 045, due month 36

Table 3 Outline of each experimental rock type.

2.1.5 Laboratory experiments undertaken

Three different laboratory experimental set-ups have been used to investigate the THMC properties of caprock:

1. **Bench experiment - Type A**
   Ambient pressure / in-situ temperature / in-situ formation fluids / no flow: Heated glass flask with 5mm rock chips submerged in CO_2 saturated formation fluid brine at in-situ temperature and ambient pressure.

2. **Bench experiment - Type B**
   In-situ pressure / in-situ temperature / in-situ formation fluids / no flow: 316 stainless steel pressure vessel with 5mm rock chips or powdered rock at in-situ temperatures, pressure, formation fluid salinity and supercritical CO_2.

3. **High pressure and temperature CO_2 flow rig**
   In-situ pressure / in-situ temperature / in-situ formation fluids / single and multiphase scCO_2 and brine flow: Pressure vessel with confining pressure up to 69MPa (10,000psi), fluid pressures up to 69MPa (10,000psi), fluid and rock temperatures up to 80°C, supercritical CO_2 fluid flow, multiphase CO_2 and brine flow and high salinity wetting fluids.

2.1.6 Bench Experiment Type A - ambient pressure / in-situ temperature

Bench Experiment - Type A comprises a 3 arm conical flask, Ludwig condenser and heating mantle, thermometer and CO2 inlet, Figure 3.

The experiments are run with 5mm (average) rock chips held in brine made to in-situ formation water salinity. They are heated to the required temperature, up to 120°C maximum. CO2 was bubbled through the brine and the pH monitored to ensure that full CO2 saturation was obtained. Another bench experiment - Type A is run in tandem without the CO2 for comparison.

Figure 3 Bench Experiment - Type A equipment.

Rock and fluid samples are taken at weekly intervals from both the CO2 and non-CO2 exposed vessels throughout the duration of the experiment.

2.1.7 Bench Experiment Type B - high pressure / high temperature

Bench Experiment Type B comprises a 1/4inch 10cm long 316 stainless steel tube, heating tape and thermostat, CO2 inlet with close off valve, a 60micron filter and a pressure release valve set at 20MPa crack pressure, Figure 4.

The experiments are run with powdered rock samples (ground to a powder in an agate pestle and mortar) to provide the maximum surface area for reaction. The powdered rock is held in a 316 stainless steel pressure vessel, heated with heating tape or held in an oven at the required temperature (up to 80oC maximum) and charged with supercritical CO2 and NaCl brine (made to in-situ formation water salinity) as required. Another bench experiment type B is run in tandem without the CO2 for comparison. The sealing pressures are monitored and maintained. After a set time the samples are depressurised.

Figure 4 Bench Experiment Type B equipment

The powered rock samples are subjected to XRD analysis before and after the experiment to identify any mineralogical changes.

2.1.8 High pressure and temperature CO2 flow rig

The high pressure and temperature supercritical CO2 flow rig has been designed specifically for the MUSTANG project to offer robust and flexible multi-phase flow of supercritical CO_2 through 38mm diameter cylindrical rock samples over a range of temperatures, fluid types, fluid pressure and confining stress, thereby facilitating a true investigation of the effect of coupled THMC processes on caprock integrity. It also facilitates the injection of tracers and other such markers along with fluid and gas sample collection post rock contact.

A schematic and image of the experimental apparatus can be seen in Figures 3 and 4 respectively.

In summary the equipment consists of a Hassler-type high pressure cell (pressure vessel) which holds cylindrical rock samples of 38mm diameter and up to 75mm in length. The fluid pumps (both brine and CO2) are designed for high temperature, pressure and supercritical CO2 conditions and all wetting parts within the system are in 316 stainless steel or PEEK to limit corrosion on exposure to brine and supercritical CO2.

The system can provide in-situ and scalable measurements at a range of pressures, temperatures, rock types and fluid types to provide insight into characterising the thermo - hydro - mechanical and chemical processes associated with the flow of supercritical and dissolved CO_2 through the reservoir, aquifer and cap rocks.

The experimental equipment is rated to provide:

Up to 69MPa (10,000psi) confining and fluid pressure.
Up to 80°C fluid and rock temperature.
Supercritical CO_2 and brine fluid flow (both single and multi-phase).
Upstream and downstream pressure measurement along with the differential pressure.

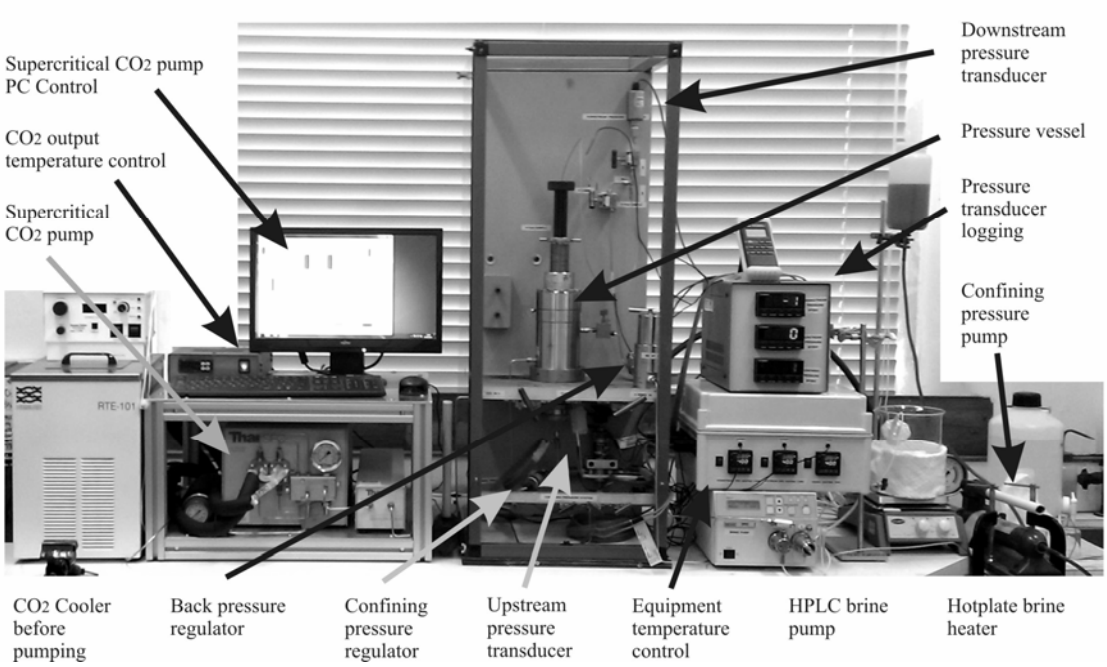

Figure 5 Image of the experimental rig capable of reproducing in-situ reservoir and CO_2 injection conditions.

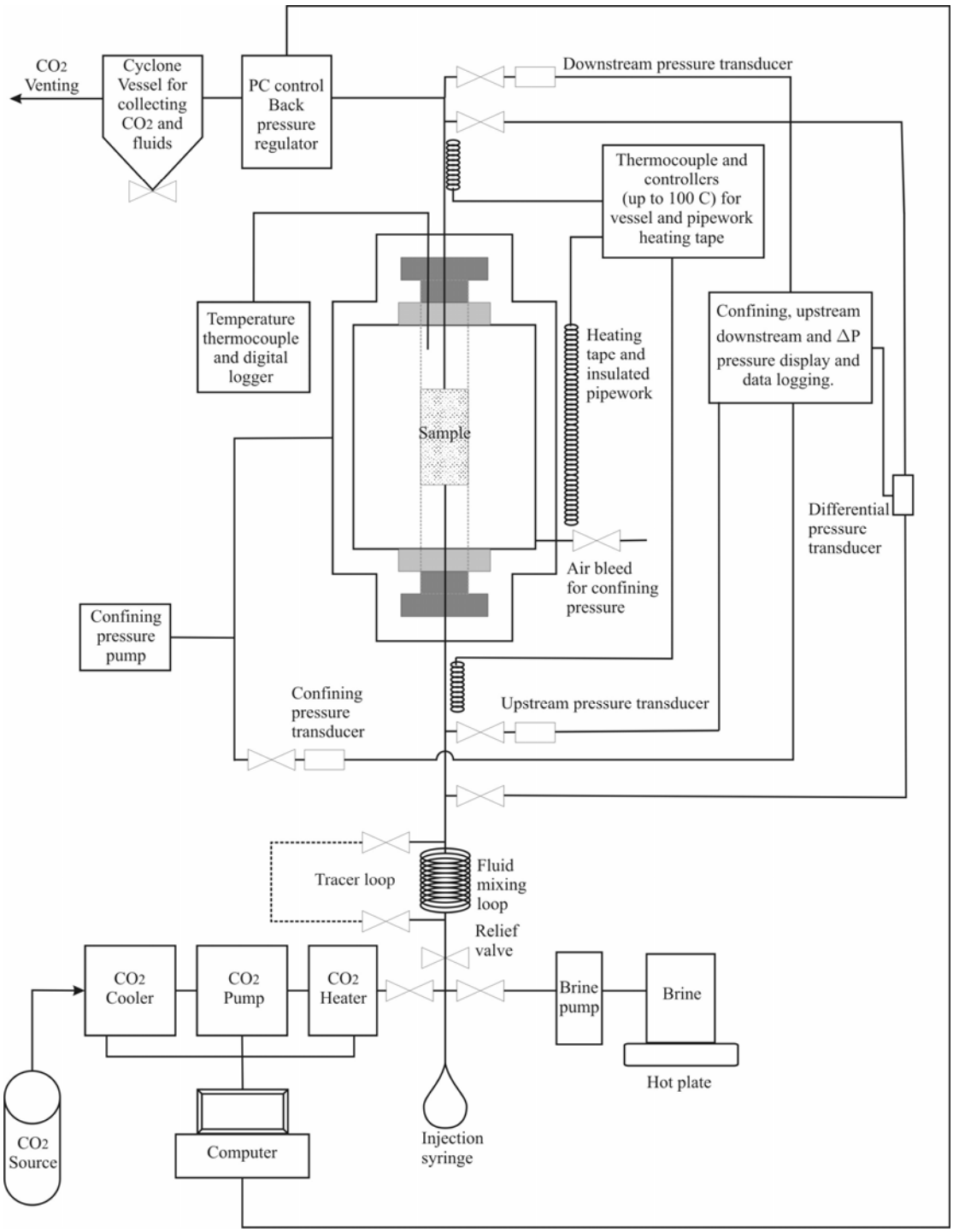

Figure 6 Flow path sketch of the experimental rig in the Edinburgh University CO_2 Lab

2.2 Analysis techniques

Before, during and after experimentation the rock samples were subjected to a range of experimental techniques to fully investigate the THMC processes affecting the caprock including:
Scanning Electron Microscope (SEM) imaging
EDS (energy dispersive) X-ray analysis
X-Ray Diffraction (XRD) analysis
X-Ray CT (Computed Tomography)

2.2.1 Scanning Electron Microscope (SEM) imaging

A tungsten filament source produces a stable and high current electron beam. When the electron beam interacts with the sample, the electrons lose energy by repeated random scattering and absorption within a teardrop-shaped volume of the specimen known as the interaction volume. The size of the interaction volume depends on the electron's landing energy, the atomic number of the specimen and the specimen's density.

2.2.2 EDS (energy dispersive) X-ray analysis

The PGT Spirit EDS X-ray analysis system allows qualitative and quantitative mineral analysis as well as X-ray imaging of samples. The number and energy of the X-rays emitted from a specimen are measured by an energy-dispersive spectrometer. As the energy of the X-rays are characteristic of the difference in energy between the two shells, and of the atomic structure of the element from which they were emitted, this allows the elemental composition of the specimen to be measured.

2.2.3 X-Ray Diffraction (XRD) analysis

XRD measurements are based on observing the scattered intensity of an X-ray beam hitting a sample as a function of incident and scattered angle, polarization, and wavelength or energy. X-Ray Powder diffraction facilitates qualitative identification of minerals in all rock types.

2.2.4 X-Ray CT (Computed Tomography)

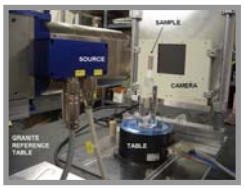

X-Ray Computed Tomography (CT) is a non-destructive technique for visualizing interior features within solid objects, and for obtaining digital information on their 3-D geometries and properties. X-ray attenuation is primarily a function of X-ray energy and the density and atomic number of the material being imaged. A CT image is created by directing X-rays through the slice plane from multiple orientations and measuring their resultant decrease in intensity. A specialized algorithm is then used to reconstruct the distribution of X-ray attenuation in the slice plane. By acquiring a stacked, contiguous series of CT images, data describing an entire volume can be obtained and visualised.

2.3 THMC experimental summary

The effect of THMC processes on the 7 caprock and reservoir rock types were investigated by one of the 3 different experimental methods.

This facilitated the following Temperature, Hydraulic (flow rate) and Mechanical (pressure) parameters to be controlled experimentally for each rock type, Table 4. Chemical changes were determined before and after experimental testing using the techniques described in the section following.

Rock type	Experiment type	Temperature (°C)	Flow rate (g/min)	Pressure (MPa)
St Ninian's shale caprock	bench experiment type A.	30 / 80	0	0
Heletz claystone caprock	bench experiment type A	55	0	0
Miller Kimmeridge Clay caprock	bench experiment type A	40 / 80	0	0
East Brae Kimmeridge Clay caprock	high pressure / temperature flow rig.	20 / 40	1 / 2 / 3 / 4 / 5	20 / 30 / 40 / 50
Boulby Evaporite	bench experiment type B	35 / 50	0	0 / 20
Clashach Sandstone	high pressure / temperature flow rig	40 / 60	1 / 2 / 3 / 4 / 5	20 / 30 / 40 / 50
Stuben sandstone	high pressure / temperature flow rig	40	1	20 / 30 / 40 / 50

Table 4 The THMC parameters measured for each rock type.

Table 5 presents the full suite of THMC coupled process investigations conducted through the experimental program for each of the rock samples.

	T	H	M	C
T		Naturally fractured East Brae Kimmeridge Clay caprock at 20°C & 40°C and flow rates of 1 / 2 / 3 / 4 & 5 g/min Clashach reservoir sandstone at 40°C & 60°C and flow rates of 1 / 2 / 3 / 4 & 5 g/min. Stuben reservoir sandstone at 40°C and flow rate of 1 g/min	Naturally fractured East Brae Kimmeridge Clay caprock at 20°C & 40°C and confining and fluid pressures of 20 / 30 / 40 & 50 MPa Evaporite caprock at 35 °C & 50 °C at ambient and 20MPa pressures. Clashach reservoir sandstone at 20°C / 40°C & 60°C and confining & fluid pressures of 20 / 30 / 40 & 50 MPa Stuben reservoir sandstone at 40°C and confining & fluid pressures of 20, 30, 40 & 50 MPa	St Ninian's Shale at 30 °C & 80 °C Heletz caprock at 55 °C Miller Kimmeridge Clay caprock at 40°C & 80°C East Brae Kimmeridge Clay caprock at 20°C & 40°C Evaporite caprock at 35 °C & 50 °C Clashach reservoir Sandstone at 40°C & 60°C Stuben reservoir sandstone at 40°C
H			Naturally fractured East Brae Kimmeridge Clay caprock at flow rates of 1 / 2 / 3 / 4 & 5 g/min and confining & fluid pressures of 20 / 30 / 40 & 50 MPa Clashach reservoir sandstone at Sandstone at flow rates of 1 / 2 / 3 / 4 & 5 g/min and confining & fluid pressures of 20 / 30 / 40 & 50 MPa Stuben reservoir sandstone at Sandstone at flow rate of 1 g/min and confining & fluid pressures of 20 / 30 / 40 & 50 MPa	Naturally fractured east Brae Kimmeridge Clay caprock at flow rates of 1 / 2 / 3 / 4 & 5 g/min Clashach reservoir sandstone at flow rates of 1 / 2 / 3 / 4 & 5 g/min. Stuben reservoir sandstone at flow rates of 1 g/min
M				St Ninian's Shale at ambient pressure Heletz caprock at ambient pressure Miller Kimmeridge Clay caprock at ambient pressure East Brae Kimmeridge Clay caprock at confining and fluid pressures of 20 / 30 / 40 & 50 MPa Evaporite caprock at ambient and 20MPa pressures. Clashach reservoir sandstone at confining & fluid pressures of 20 / 30 / 40 & 50 MPa Stuben reservoir sandstone at confining & fluid pressures of 20 / 30 / 40 & 50 MPa
C				

Table 5 THMC coupled process investigations conducted through the experimental program for each of the rock samples.

2.4 THMC experimental results

For each individual rock type tested the following information (if available) will be presented:
Sample location and lithology
Reservoir in-situ temperature, pressure and salinity information.
Experimental sample description
Sample mineralogy.
Summary of the THMC properties experimentally investigated and
THMC results summary.

This will then be summarised in an overview of the effect of thermal, hydraulic, mechanical and chemical processes on caprock integrity.

2.4.1 St Ninian's Shale caprock

THMC processes effecting St Ninian's shale caprock were investigated using bench experiment - Type A. The experiments were conducted at ambient pressure, temperatures of 30^{o}C and 80^{0}C with no flow.

St Ninian's shale location and lithology

St Ninian's Shale caprock samples were taken from a depth of 500m from the Kelty Quarry in Fife, UK. Figure 7.

Figure 7 St Ninian's caprock in outcrop - Kelty Quarry, Fife UK

St Ninian's shale in-situ temperature, pressure and salinity information

The literature indicates a formation fluid salinity of 70,000 NaCl eq ppm and an in-situ temperature of 80oC for the Carboniferous Limestone Coal formations.

St Ninian's shale experimental sample description

5mm chips of St Ninian's caprock were obtained (Figure 8) and placed in bench experiment - Type A at temperatures of 30oC and 80oC in a 70,000 NaCl eq. ppm. Brine. CO2 was bubbled through the brine and pH monitored to ensure that full CO2 saturation of the brine was obtained.

Figure 8 St Ninian's caprock experimental samples.

St Ninian's shale mineralogy.

Awaiting results of the XRD mineralogy on St Ninian's shale – will be presented in Deliverable 046, due month 44.

St Ninian's shale THMC properties experimentally investigated

Table 1 presents the THMC investigations undertaken on the St Ninian's shale caprock using bench experiment type A equipment.

	T	H	M	C
T		30°C & 80°C No flow	30°C & 80°C Ambient pressure	30°C & 80°C CO_2 saturated formation brine
H			No flow Ambient pressure	No flow CO_2 saturated formation brine
M				Ambient pressure CO_2 saturated formation brine
C				

Table 6 THMC investigations undertaken on the St Ninian's caprock in bench experiment type A equipment.

St Ninian's shale THMC results

Awaiting XRD results from before and after CO2 exposure at 30oC and 80oC of St Ninian's chips to look at effect of CO2 exposure and temperature on the chemistry of the St Ninian's shale caprock integrity – will be presented in Deliverable 046, due month 44.

2.4.2 Heletz Caprock

THMC processes effecting Heletz caprock were investigated using bench experiment - Type A. The experiments were conducted at ambient pressure, in-situ temperatures of 55°Cwith no flow.

Heletz shale location and lithology

Three sample bags containing core samples were received by Edinburgh University from the Heletz Field from Wells H-2, H-9 and H-14. The Heletz caprock is contained within Lower Cretaceous rocks which encompass five depositional environments: alluvial braidplain, tidal flat, tidal marsh-costal swamp, inner shelf and meandering river and are a sequences of repeated regressive – transgressive (fluvial – marine) depositional sequences.

Heletz in-situ temperature, pressure and salinity information

The following information was available on the Heletz reservoir which was used to set the experimental testing conditions.

- **Salinity:** The MUSTANG report (2008) provides salinity from well H-38 defined by DST of 35,000 – 40,000ppm at 1050m depth and 22,113ppm Cl at 1555m. A salinity of 35,000ppm NaCl will be used for the batch experiments.
- **Temperature;** Satrinsky (1974) indicates maximum temperatures of 50-60oC at the depth of brines at 1500-1800m and no evidence that they have been subjected to higher temperatures in the past. A temperature of 55oC will be used in the batch experiments.
- **Reservoir Pressure:** Ran Calvo & Zohar Gvirtzman allude to a reservoir pressure of 2000psi (13.8MPa / 138bar) but there is limited data available.

Heletz experimental sample description

Samples from Heletz well H-2, C#18, Bx-1 were used to conduct experiments on the interaction between brine saturated CO2 and the Heletz cap rock. The chips are 95% mudstone grains and with some concretions. 12g of chips were weighed out for the CO2 and non CO2 exposed bench experiments. 5mm chips of Heletz caprock were produced (Figure 7) and were placed in bench experiment type A at temperatures of 55oC in a brine of composition 35,000 NaCl eq. ppm. CO2 was bubbled through the brine and the pH monitored to ensure that full CO2 saturation was obtained.

Figure 9 Heletz caprock experimental samples.

Heletz caprock mineralogy.

In summary the Heletz cap rock is relatively homogeneous. Figure 10 shows a typical cap rock fragment surface. The matrix material, Figure 11, is mainly Si, O and Al with iron and minor potassium and magnesium. This classifies the Heletz cap rock matrix material as a silicate clay and as there is no evidence of swelling throughout the duration of the experiment it is most likely to be illite.

Within the matrix material there are a small number of discrete crystals of Titanuim-Iron oxide (Ti-Fe) and Iron-Sulphur oxide (Fe-S) – (Figure 12) along with Calcite (Ca) and Quartz (Si-O) – (Figure 13). All other discrete crystal observed on the surface have the same composition as the matrix.

This indicates that there are very few minerals in the Heletz caprock available for any reaction with CO2 or brine.

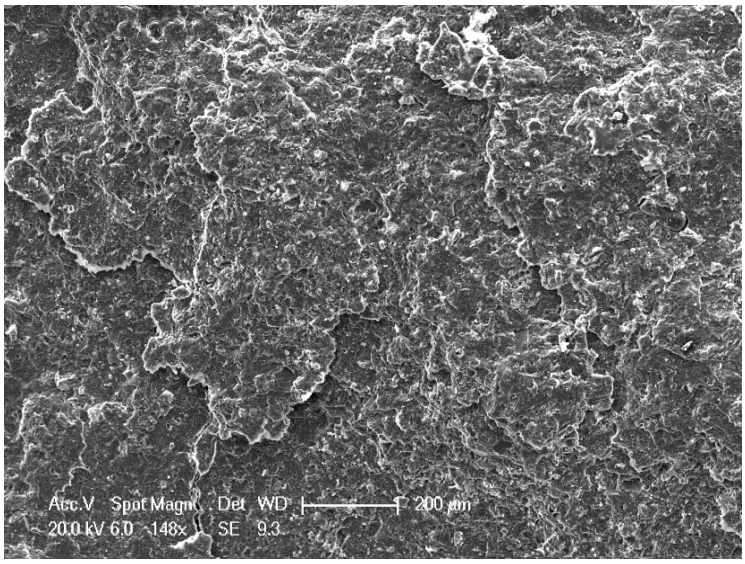

Figure 10 Average SEM image of the surface of the Heletz cap rock.

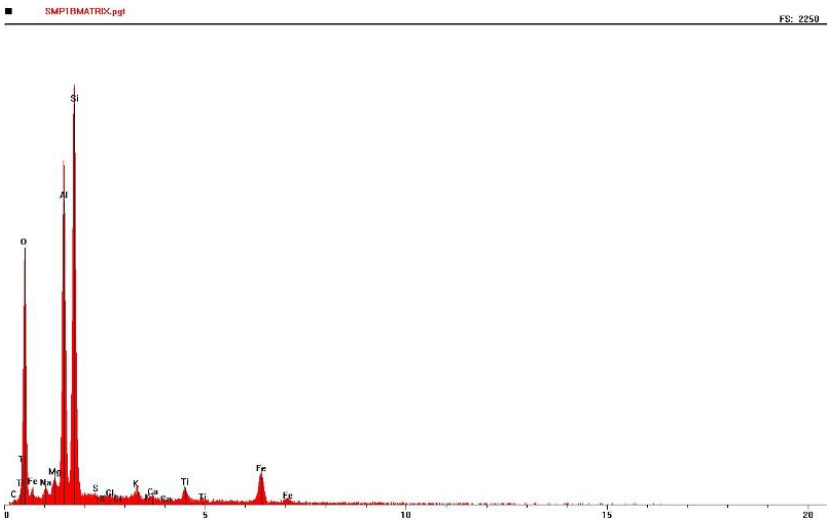

Figure 11 Average elemental composition of the Heletz cap rock matrix.

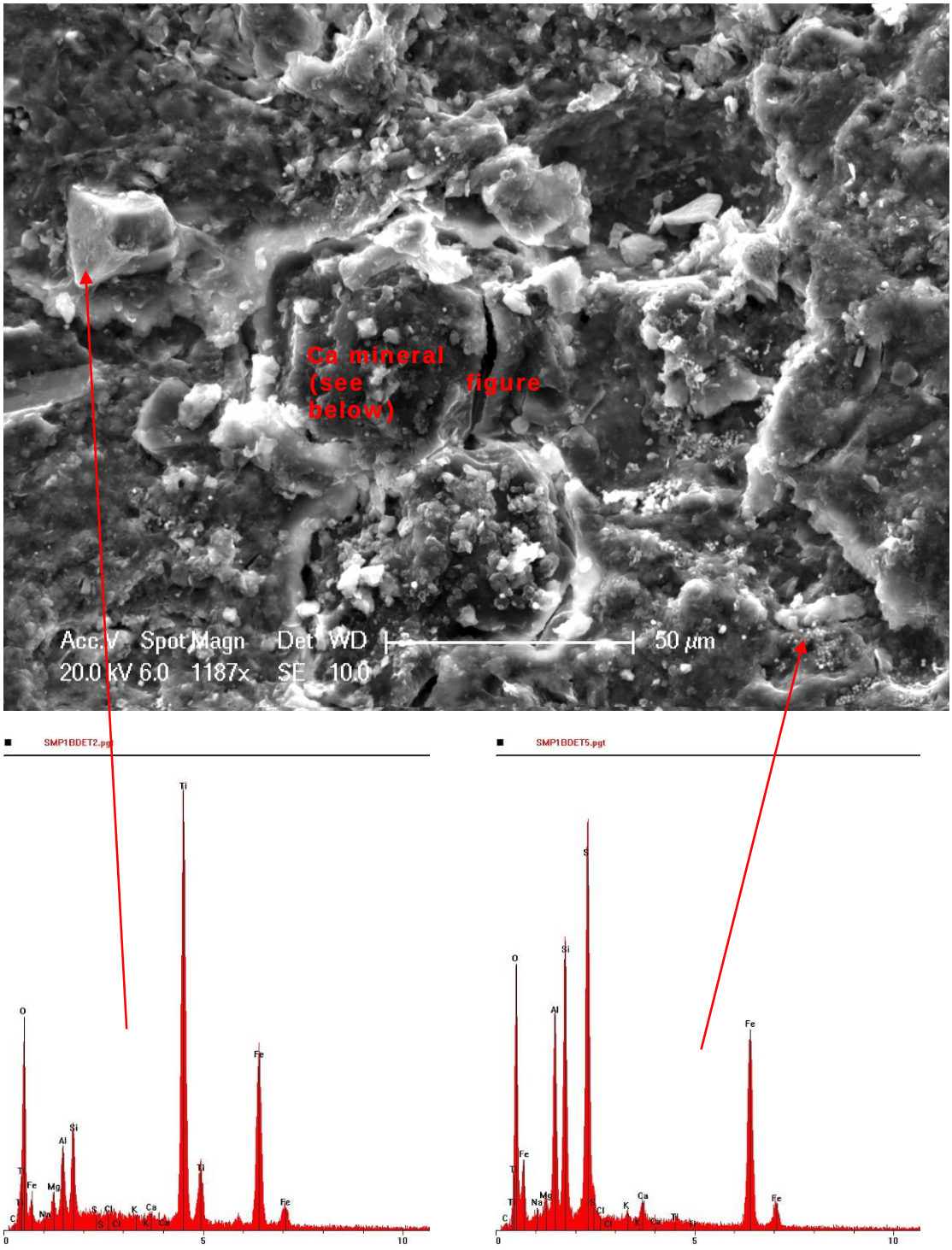

Ti-Fe oxide – weathering into haematite, pyrite and titanium oxides

Iron / Sulphur – Pyrite in granular / globular form.

Figure 12 SEM image and elemental analysis of Heletz cap rock.

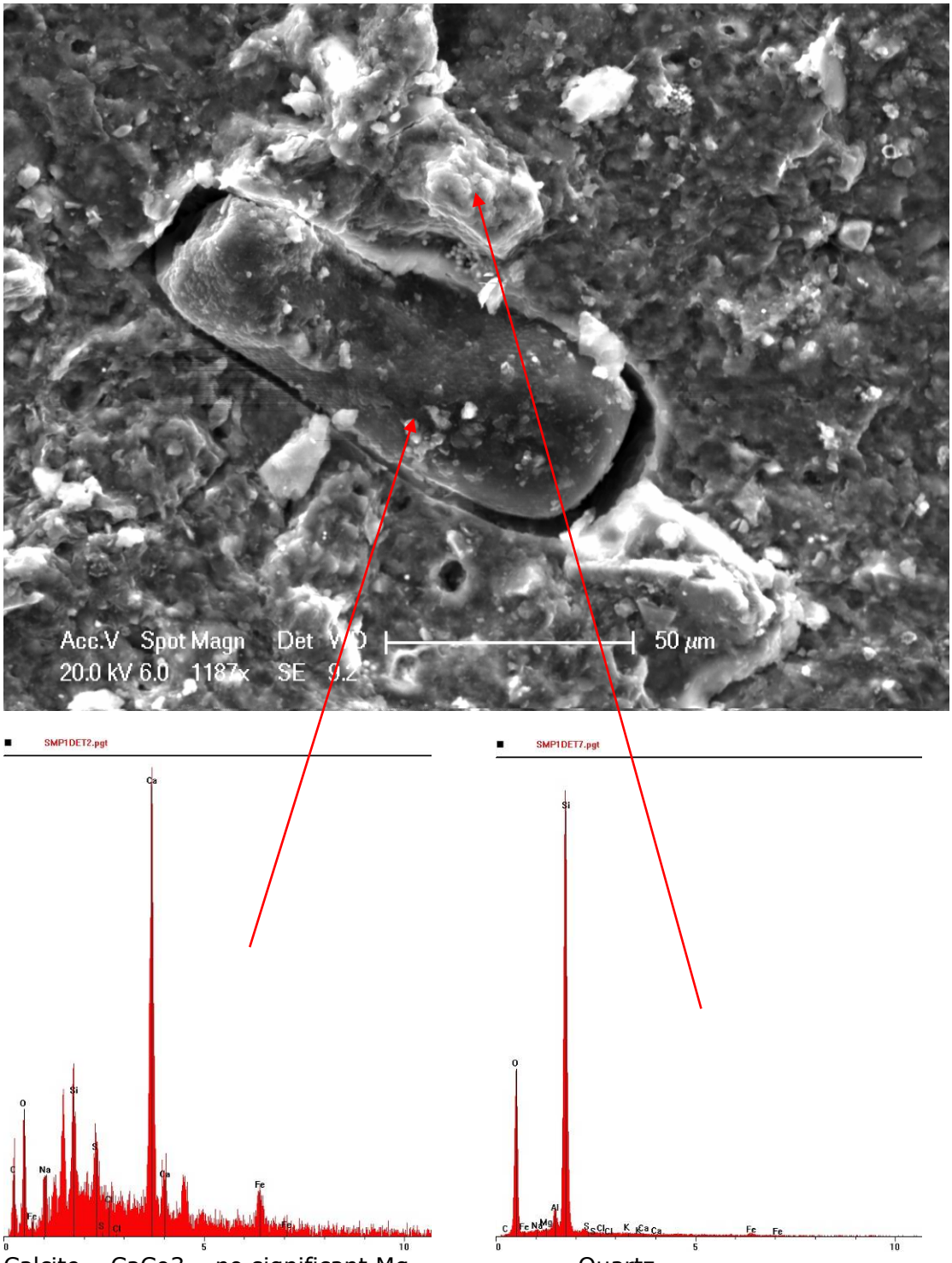

Calcite – CaCo3 – no significant Mg Content - not undergone dolomitisation?

Quartz

Figure 13 Further SEM image and elemental analysis of Heletz cap rock.

Heletz THMC properties experimentally investigated

Table 7 presents the THMC investigations undertaken on the Heletz caprock using bench experiment type A equipment.

	T	H	M	C
T		55°C No flow	55°C Ambient pressure	55°C CO_2 saturated formation brine
H			No flow Ambient pressure	No flow CO_2 saturated formation brine
M				Ambient pressure CO_2 saturated formation brine
C				

Table 7 THMC investigations undertaken on the Heletz caprock in bench experiment type A equipment.

Heletz THMC results

Matrix Material

The matrix composition remains unchanged, Figure 14. However it can be seen that the gross surface of the sample becomes more amorphous with the surface rugosity reduced and the surface texture evened out by finer matrix material breaking up, Figure 15.

This is also confirmed when the matrix is looked at in detail where we see that the matrix clay material becomes less defined and the edges are broken down over time and exposure to CO_2. The matrix material of samples only exposed to brine and heat retain well defined edges, Figure 16.

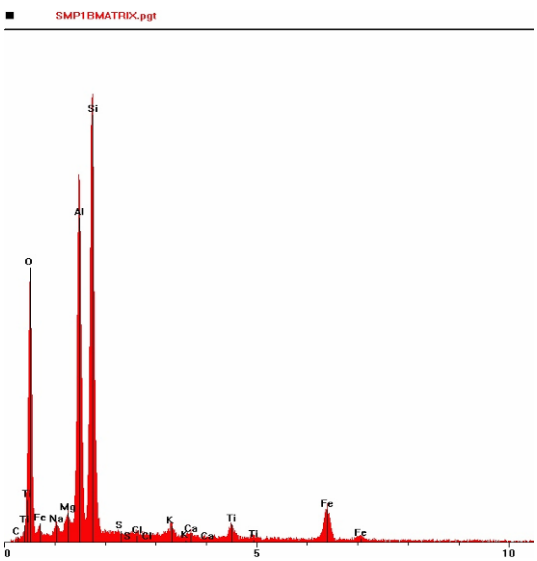

(A) Matrix composition at start of Exp

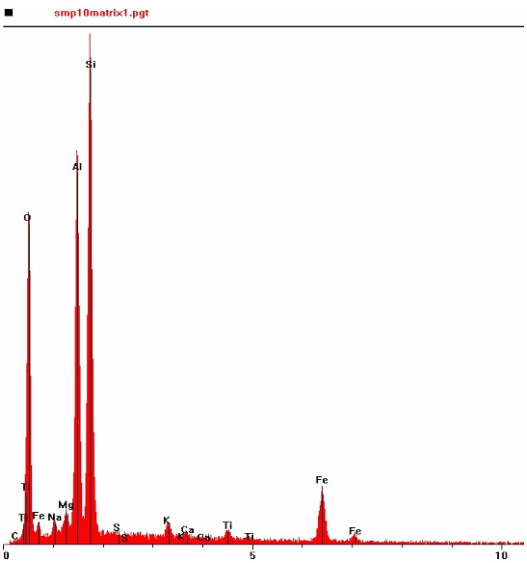

(B) Matrix composition after 3 months

Figure 14 Matrix compositions at beginning of experiment and after 3 months.

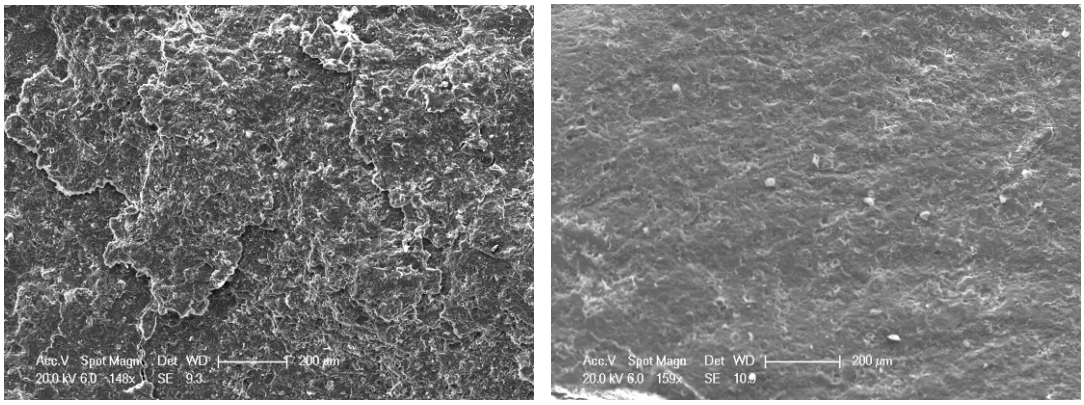

(A) Matrix surface at start of Exp (B) Matrix surface after 3 months of Exp

Figure 15 Heletz cap rock matrix at beginning of experiment (A) and after 3 months (B).

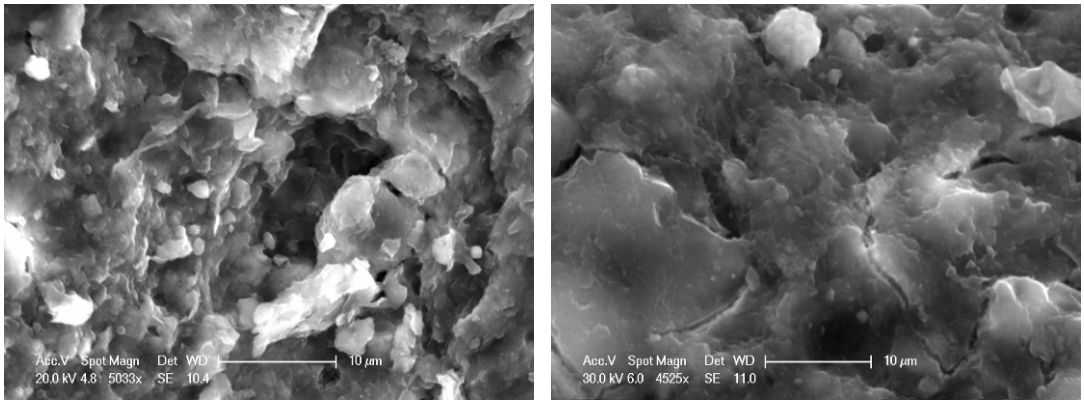

(A) Exposed to brine and heat only (B) Exposed to CO_2, brine and heat

Figure 16 Detail of the Heletz cap rock matrix at beginning of experiment and after 3 months, indicating that the matrix clay material becomes less defined and the edges are broken down over time and exposure to CO_2 (B) as opposed to the more defined edges of the sample exposed to heat and brine only (A)

Even delicate bridging structures are not broken down in the samples that are exposed to heat and brine, Figure 17.

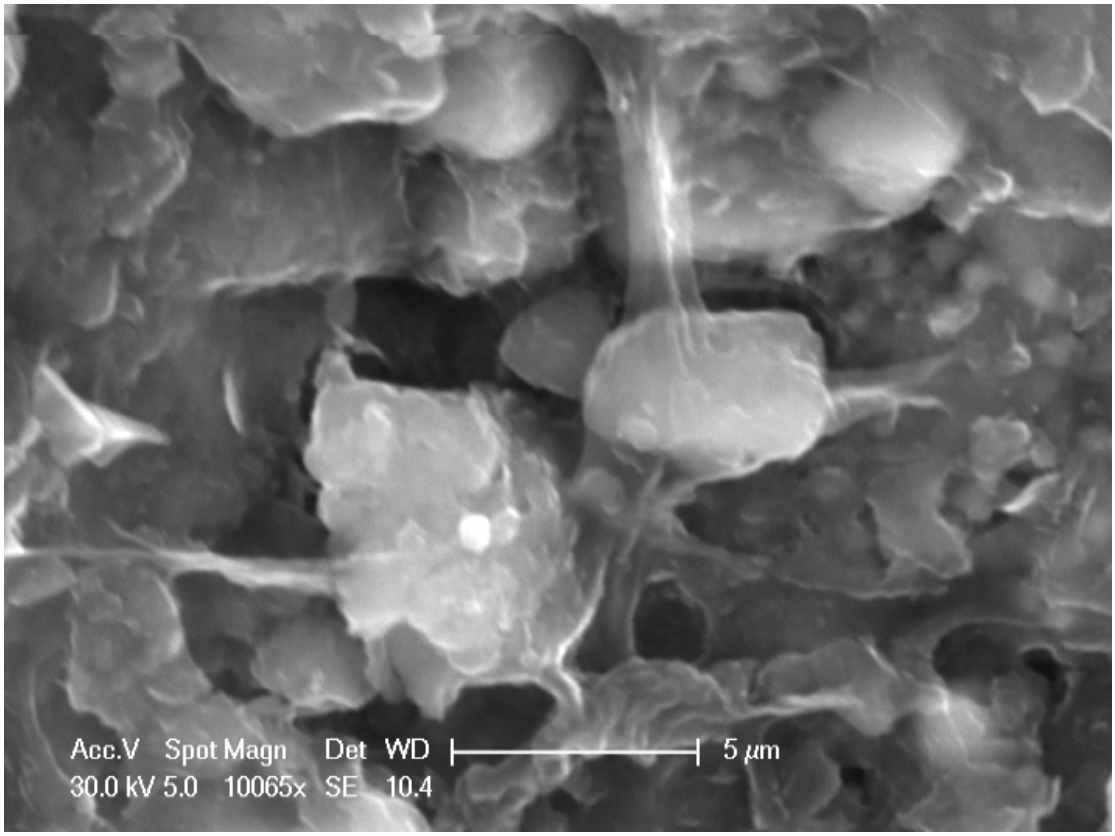

Figure 17 delicate bridging structures are preserved in the samples not exposed to CO2 over time (this sample has been in the batch experiment with heat and brine but without CO2 for 2 months 23 days).

Other Materials
The bench experiments indicate a number of possible minor effects of exposure of cap rock to CO_2 over time including the following:

Ca minerals may be dissolved in the samples exposed to CO_2 over the duration of the experiment. Figure 18 shows a Ca crystal in a cap rock sample exposed to brine and heat only for 3 months. No such crystals could be found in the cap rock samples analysed that had been exposed to CO_2, brine and heat after 3 months.

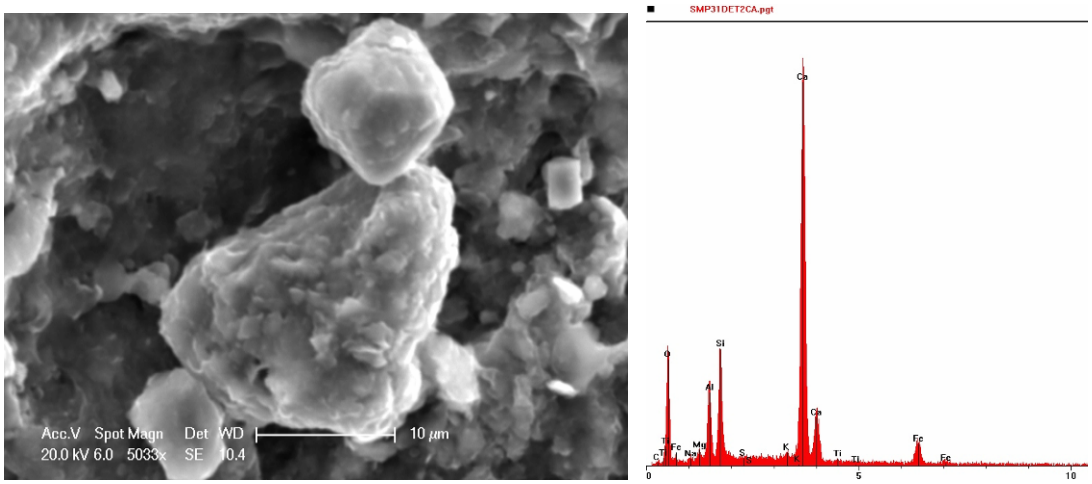

Figure 18 Ca crystals evident in samples exposed to brine and heat only after 3 months.

There is also evidence for the appearance of micro fractures both within the matrix and the discrete crystals in the samples exposed to CO_2, the same degree of micro fracturing is not see in the samples only exposed to brine and heat, Figure 19shows evidence of micro fracturing that is not seen in the samples not exposed to CO_2.

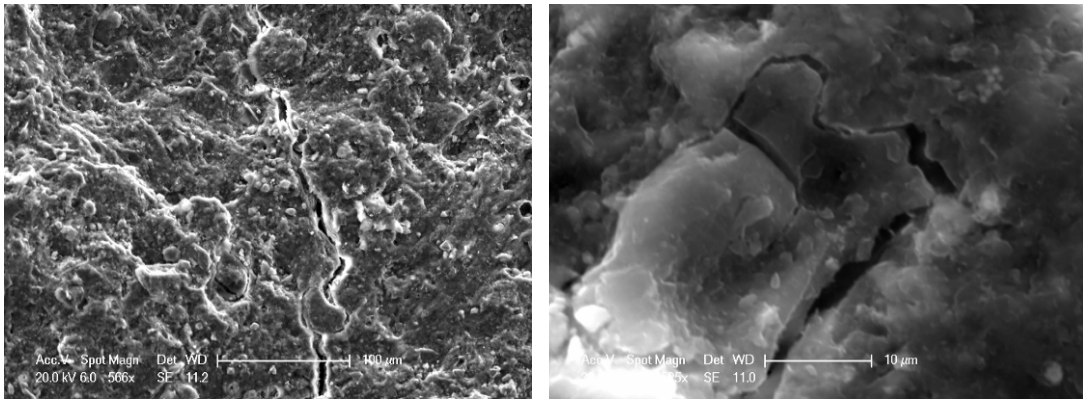

Figure 19 Evidence of micro fracturing that is not seen in the samples not exposed to CO_2.

Within the matrix material there are discrete crystals of Titanuim-Iron oxide (Ti-Fe) and Iron-Sulphur oxide (Fe-S), (refer back to Figure 10) The Ti-Fe minerals are likely to be a weathering product and may lead to the deposit of haematite, pyrite and titanium oxides – all of which are seem within the cap rock fragments. The Fe-S (pyrite) occurs in a granular / globular form on all samples, Figure 20.

The distribution of Fe with exposure to CO_2 can be seen in Figure 21 which shows a backscattered electron image of two Heletz cap rock samples, one exposed to CO2, heat and brine (A) the other heat and brine only (B), the pyrite shows up as the brightest spots. The results indicate that the distribution of pyrite does increase over the duration of the experiment. This could be due to the breaking down and re-distribution of existing pyrite. There is also the possibility that the increased breakdown of the crystals of Titanuim-Iron oxide (Ti-Fe) provides Fe into the system which then reacts with any sulphides to form new pyrite crystals.

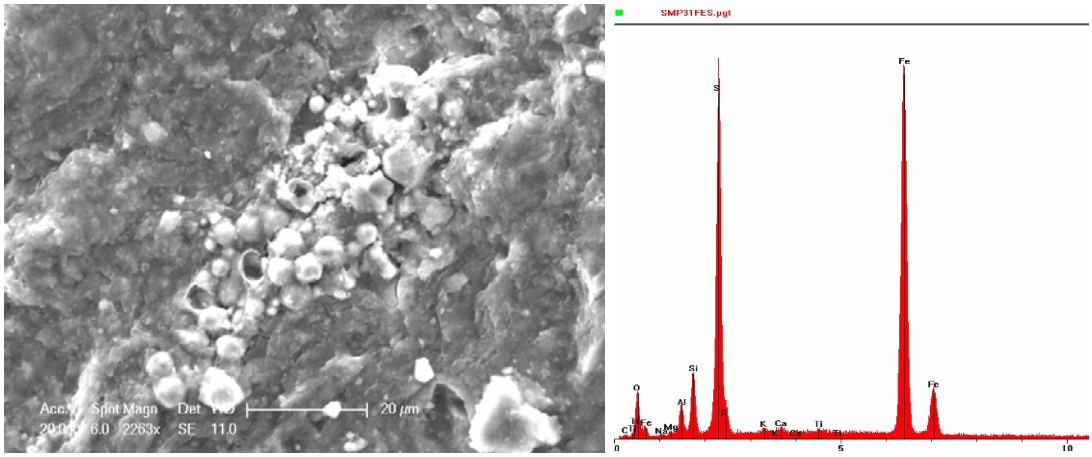

Figure 20 Typical appearance of Pyrite in Heletz cap rock samples.

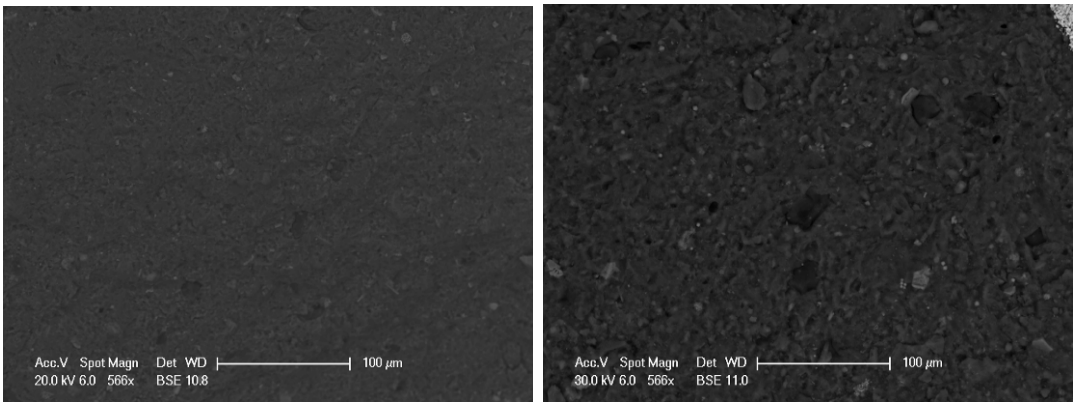

(A) Exposed to heat and brine only (B) Exposed to heat, brine and CO_2

Figure 21 Backscattered electron image of two Heletz cap rock samples, one exposed to CO_2, heat and brine (A) the other heat and brine only (B). The pyrite shows up as the brightest spots. It is possible that the distribution of pyrite increases over time and with exposure to CO_2.

There is little evidence for any surface changes on the quartz crystals. There do not seem to be any changes in the angles of the edges or in any pits with time or exposure to CO_2, Figure 22. However it is worth noting that the Quartz crystals in the Heletz cap rock samples were quite well eroded to start with.

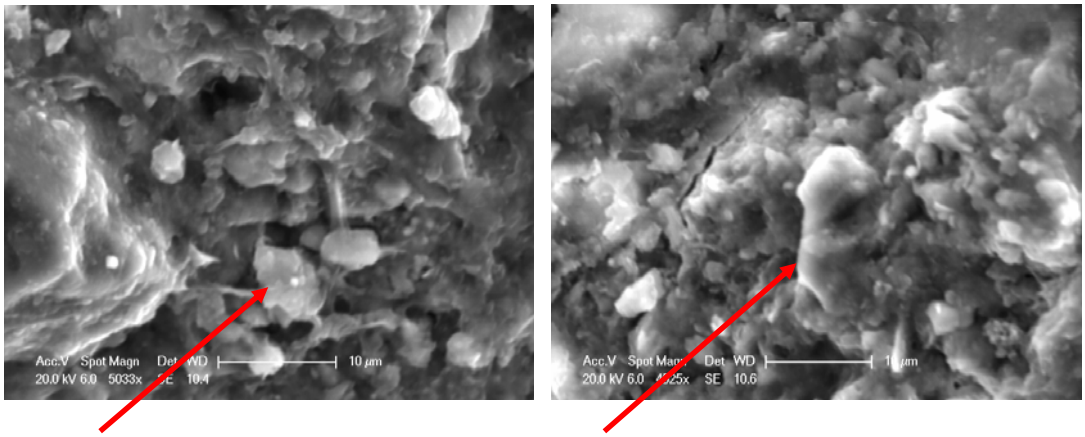

(A) Qtz exposed to heat and brine only (B) Qtz exposed to heat, brine and CO_2

Figure 22 Typical quartz crystals in Heletz cap rock samples after exposure to heat and brine only (A) and heat, brine and CO_2 (B) for 3 months.

There does not seem to be the appearance of any new minerals that may have been precipitated during CO_2, brine or heat exposure in the Heletz cap rock samples. The chemistry of the Heletz cap rock is relatively limited so scope for dissolution and re-mineralisation is limited.

For the Heletz caprock the addition of CO2 to the brine rock system will exert changes over the thermo, hydro, mechanical and chemical processes. It is likely to drive more fluid dominated reactions. The fluid becomes more acid increasing reactions and the solubility of metals and other minerals.

The Heletz cap rock samples have a relatively simple chemical composition. The matrix material is mainly Si, O and Al with iron and minor potassium and magnesium. This classifies the Heletz cap rock matrix material as a silicate clay and as there is no evidence of swelling throughout the duration of the experiment it is most likely to be illite. Further analysis would be required to identify if there is any Kaolinite or smectites in the Heletz matrix. Within the matrix material there are discrete crystals of Titanuim-Iron oxide (Ti-Fe) and Iron-Sulphur oxide (Fe-S) along with Calcite (Ca) and Quartz (Si-O). All other discrete crystal observed on the surface have the same composition as the matrix.

This means there is very little available for reactions with the brine and CO_2 but a number of observations were made and conclusions drawn:

The matrix composition remains unchanged throughout the duration of the experiment for both the samples exposed to heat, brine and CO_2 and those samples exposed to heat and brine only.
However it can be seen that the matrix surface of the sample becomes more amorphous with the surface rugosity reduced and the matrix texture evened out by finer matrix material breaking up on exposure to CO_2. This is most likely an effect of surface chemical weathering of the minerals over the duration of the experiment.

Ca minerals may be broken down in the Heletz caprock if it is exposed to CO_2 over a timescale in excess of 3 months.
There is also evidence for the appearance of micro fractures both within the matrix and the discrete crystals in the samples exposed to CO_2 only.
The distribution of pyrite is observed to increases over time and with exposure to CO_2 . This could be due to the breaking down and re-distribution of existing

pyrite. There is also the possibility that the increased breakdown of the crystals of Titanuim-Iron oxide (Ti-Fe) provides Fe into the system which then reacts with any sulphides to form new pyrite crystals.

There is little evidence for any surface changes on the quartz crystals.
No new minerals are observed to have been precipitated during CO_2, brine or heat exposure in the Heletz cap rock samples.
The current observations conclude that there is the possibility of an increase in permeability through the opening of a micro fracture network that could influence CO_2 migration thorough the cap rock and the possible dissolution of Ca minerals.

A full report on the Heletz caprock experimental results are available on the MUSTANG website, in the file sharing area of WP4, titles Heletzsamplereport.pdf.

2.4.3 Kimmeridge Clay - Miller Field caprock

THMC processes affecting the Miller Field Kimmeridge Clay caprock were investigated using bench experiment type A. The experiments were conducted at ambient pressure, temperatures of 40°C and 80°C with no flow.

Kimmeridge Clay - Miller Field caprock location and lithology

The Miller Field Kimmeridge Clay Formation was deposited in a deep water anoxic environment during regional rifting and subsidence in the latest Jurassic (Ziegler, 1982). The Kimmeridge Clay Formation mainly consists of organic-rich 'black' shales interbedded with thin sand/silt beds.

The core from Well 9/28b-17 show typical 'tiger stripes', which are lithologic alternations between black shales and grey silt/sand beds (Figure 21).

Figure 23 Visual section of Kimmeridge clay in well 9/28b-17

Kimmeridge Clay - Miller Field in-situ temperature, pressure and salinity

The literature indicates a formation fluid salinity of 70,000 NaCl eq ppm and an in-situ temperature of 80oC for the Miller Field Kimmeridge Clay caprock.

Kimmeridge Clay - Miller Field caprock experimental sample description

BGS Edinburgh provided 5 rock samples from well 9/28b-17, the samples were taken from depths:

14761.3 – 14761.4m **– SAMPLE A**
14762.8 – 14762.9 m **– SAMPLE B**
14771.9 -14772 m **– SAMPLE C**
14799.7 – 14799.9 m **– SAMPLE D**
14836.25 – 14836.35 m **– SAMPLE E**

5mm (average) Kimmeridge clay chips from **SAMPLE B and D** (Figure 24) were run in Batch Experiment type A at a temperature of 40°C and 80°C and brine composition of 70,000ppm NaCl eq CO2 saturated brine at ambient pressure. CO2 was bubbled through the brine and the pH monitored to ensure that full CO2 saturation was obtained.

Figure 24 Kimmeridge Clay - Miller Field caprock experimental samples.

Kimmeridge Clay - Miller Field caprock mineralogy

A full mineralogical profile of well 9/28b-17 can be seen in Figure 25, (Jiemin Lu Ph.D. 2008). Interpretation of the X-ray diffraction patterns shows that the shale almost entirely consists of five minerals: quartz, illite, kaolinite, K-feldspar and pyrite. Quartz is the most abundant clastic component at around 50%. K-feldspar is mostly under 5%. It is the most abundant feldspar mineral present. There is small amount of sodium plagioclase (albite) in some of the samples.

Illite is the dominant clay mineral, making up about 20%. Kaolinite is the only other clay mineral identified; it makes up round 5% of the shale. Pyrite is also among the most abundant minerals at an average of 5%. Calcite and dolomite are the main carbonate minerals; however the total concentration of carbonates is negligible in rocks from this well.

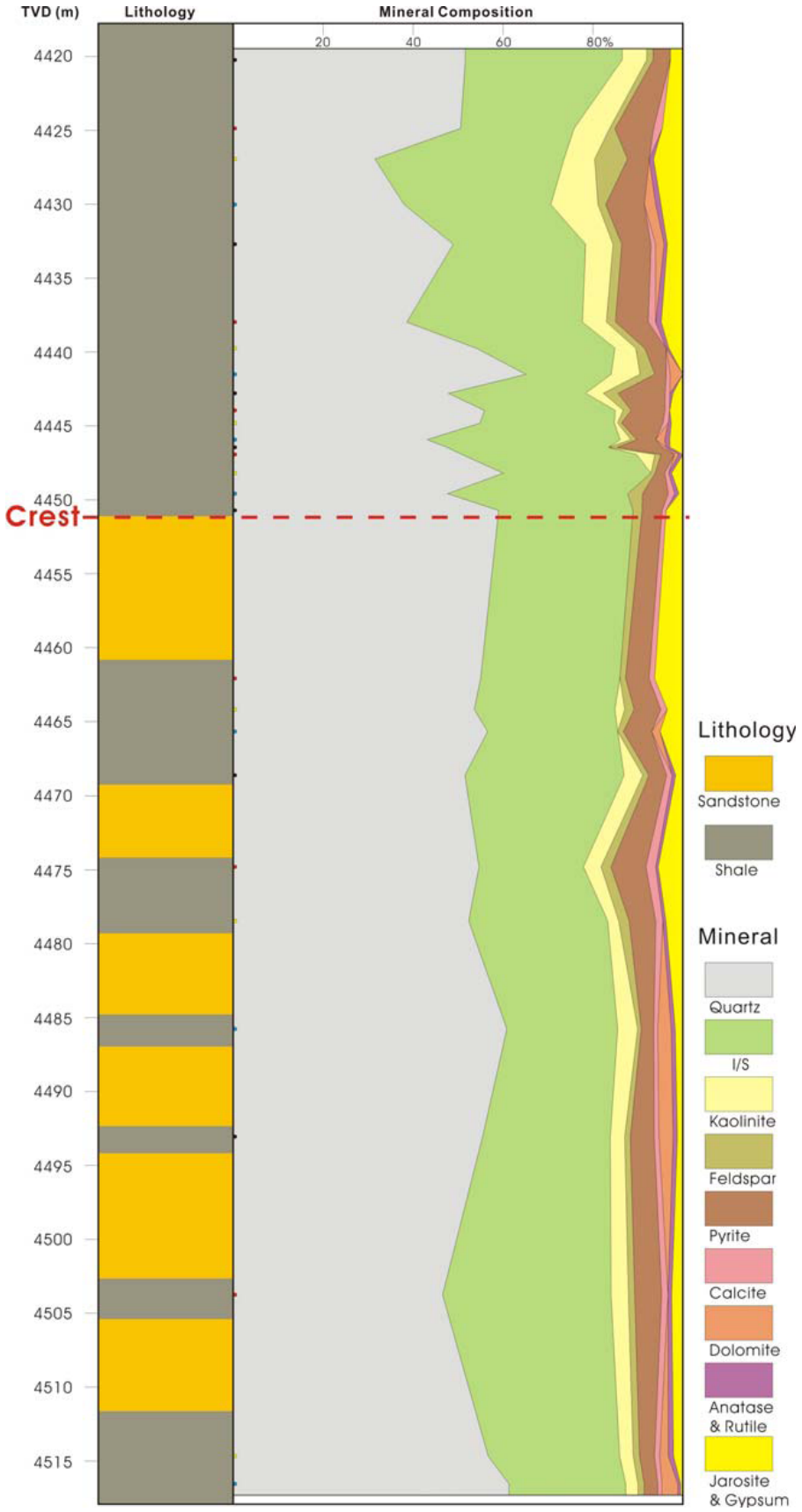

Figure 25 Mineral compositions of shale samples plotted against a lithologic column, well 9/28b-17. Little dots on the column indicate sample positions. Reservoir crest is marked. Note that the profile is not continuous with depth (Jiemin Lu Ph.D. 2008).

Mineral analysis from the SEM are line with the X-ray diffraction analysis.
That even though the small scale (sub mm) pale and dark bands are quite distinct visually, the mineralogy of these all bands is quite similar.
There is a significant amount of pyrite in the sample at around 5%
There are occasional apatite crystals

THMC properties experimentally investigated

Table 8 presents the THMC investigations undertaken on the Miller Field Kimmeridge clay caprock in bench experiment type A equipment.

	T	H	M	C
T		40°C & 80°C No flow	40°C & 80°C Ambient pressure	40°C & 80°C CO_2 saturated formation brine
H			No flow Ambient pressure	No flow CO_2 saturated formation brine
M				Ambient pressure CO_2 saturated formation brine
C				

Table 8 THMC investigations undertaken on the Miller Field Kimmeridge clay caprock in bench experiment A equipment.

Kimmeridge Clay - Miller Field caprock THMC results

Observations from the SEM analysis of the interaction of CO2, brine and Kimmeridge Clay.

The matrix material is primarily Si with O, Al and some K and Fe – Illite? And remains like this for the whole experimental duration.
Matrix material does not show significant alteration and seems relatively amorphous – no fractures or vugs appear
Samples initially have high degree of needle like crystals of composition S, Ca, O, Si – the evaporites Gypsum and/or Anhydrite – this is most likely to be a storage artefact from dehydration of the formation and the drilling fluids as they are only on the surface of the initial sample. As soon as the samples are exposed to both the brine and the CO_2 the needle like evaporites begin to break down (dissolve) throughout the duration of the experiment.
Surface flakes forming during breakdown of the matrix material during experimentation are of the same composition as the matrix material, a surface chemical weathering effect.
There does not seem to be any significant degradation of organic material or distinct quartz crystals during the experimental timescale and conditions for both samples exposed to brine only and brine with CO_2

Investigations using X-ray analysis shows that the sample matrix is primarily Si with O, Al (with trace K and Fe)- Most likely to be Illite, Figure 26. The starting samples also contain pyrite (iron sulphate), Figure 27 along with aluminium silicate and Apatite, Figure 28 in varying amounts and distribution.

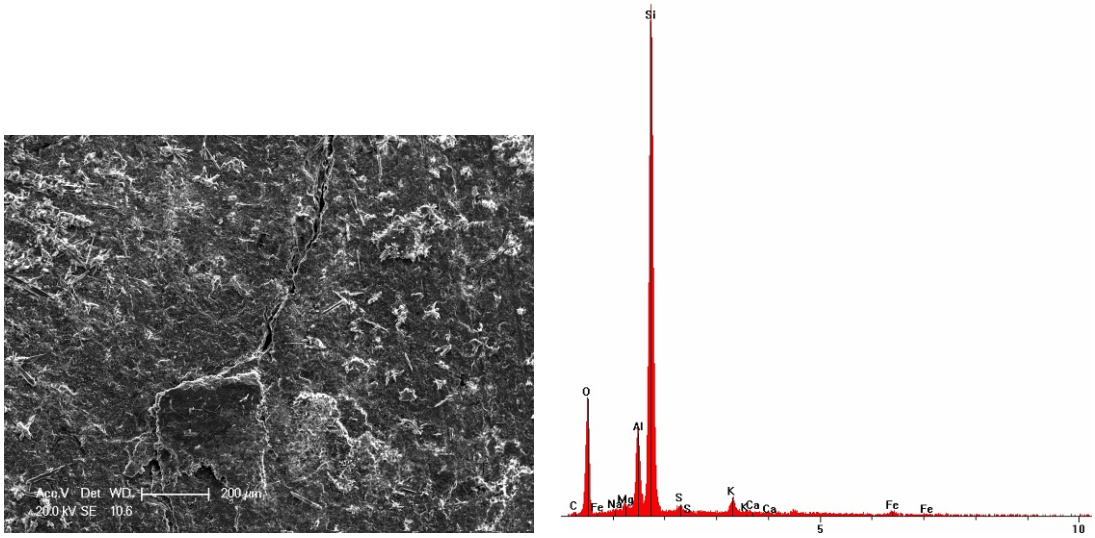

Figure 26 SEM image and X-ray analysis of sample matrix (Sample 1 starting sample Kimmeridge Clay 5mm chip)

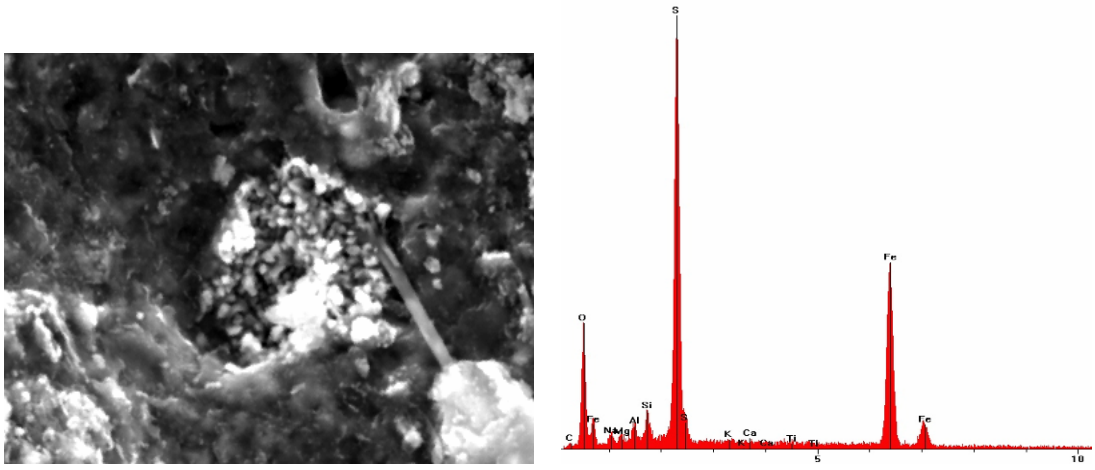

Figure 27 SEM detail and x-ray analysis of pyrite (iron sulpide) on Sample 2 - starting sample Kimmeridge Clay 5mm chip.

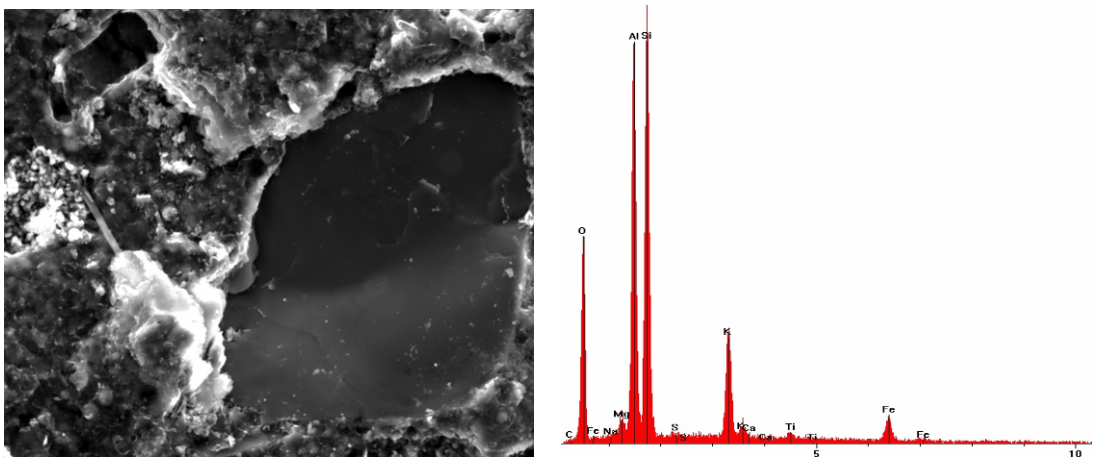

Figure 28 SEM detail and X-ray analysis of an Aluminium silicate with composition Si, Al, O, K and Fe in sample on Sample 2 - starting sample Kimmeridge Clay 5mm chip.

After 80 days experimental exposure

Investigations using X-ray analysis shows that the sample matrix remains primarily Si, Al, O with K and some Fe.
The flakes seen on the sample 18 surface (created during surface chemical weathering) have same chemical composition as amorphous matrix, Figure 30 & Figure 31.
Quartz crystals remain distinct and unaltered in sample 17, Figure 29 and Figure 32.

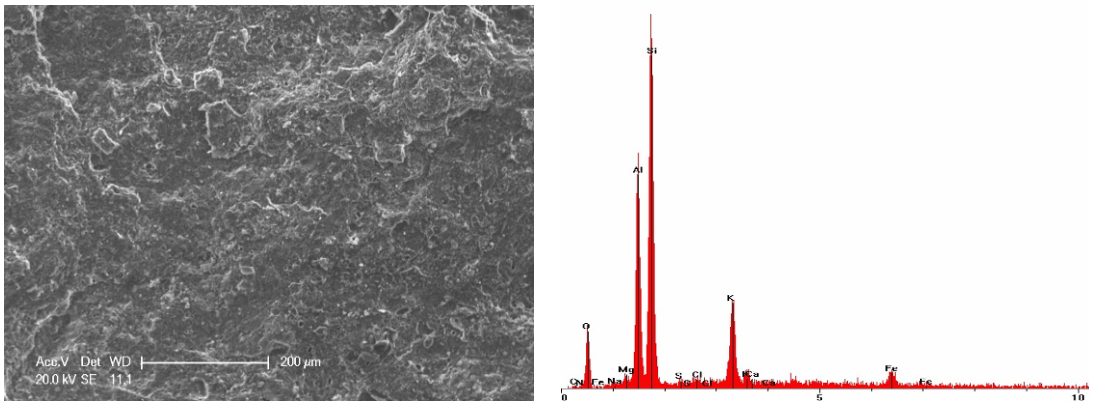

Figure 29 SEM image and X-ray analysis of matrix of Sample 17 - Kimmeridge clay sample exposed to NaCl brine only at 80^{o}C for 80 days

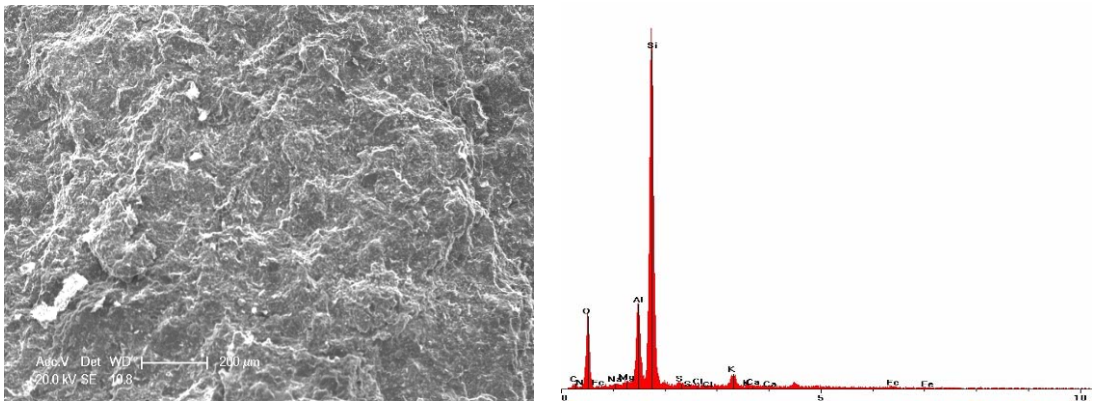

Figure 30 SEM image and X-ray analysis of matrix of Sample 18 - Kimmeridge clay sample exposed to NaCl brine and CO_2 at 80°C for 80 days

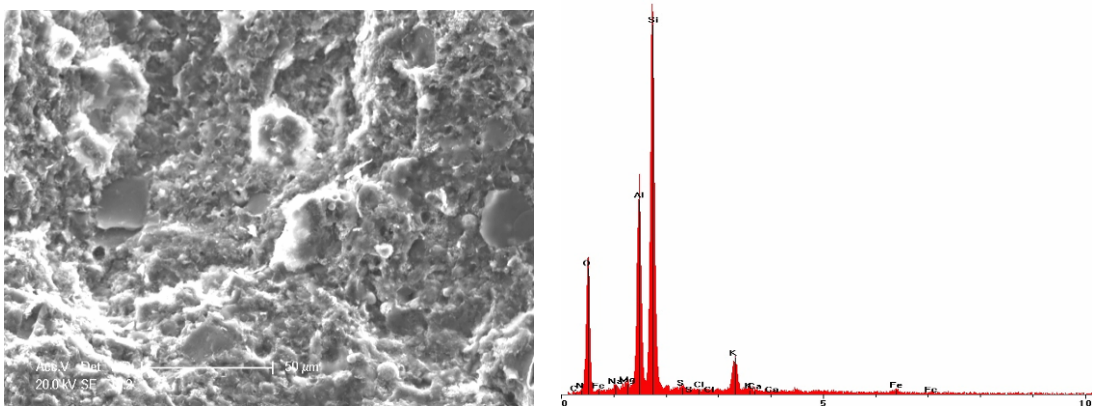

Figure 31 SEM image and X-ray analysis of flakes within matrix of Sample 18 - Kimmeridge clay sample exposed to NaCl brine and CO_2 at 80°C for 70 days.

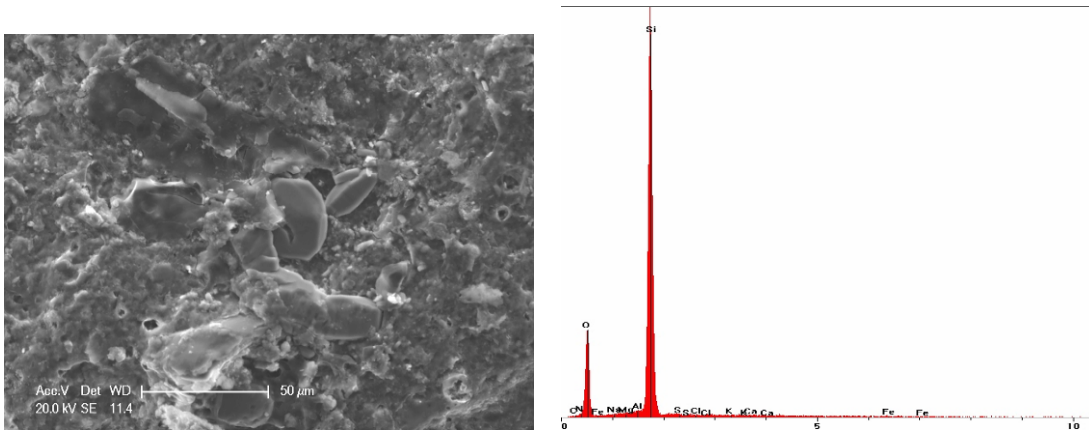

Figure 32 SEM image and X-ray analysis of quartz from Sample 17 - Kimmeridge clay sample exposed to NaCl brine only at 80°C for 80 days

Two chips were analysed using the X-Ray CT (Computed Tomograph) analysis of cap-rock samples before and after 120 days exposure to brine and CO_2. Figure 33shows the shows the X-Ray CT (Computed Tomograph) results from the unreacted Kimmeridge Clay rock chip and Figure 34 from the chip that has been 120 days in 70,000ppm NaCl at 80^{o}C saturated in CO_2.

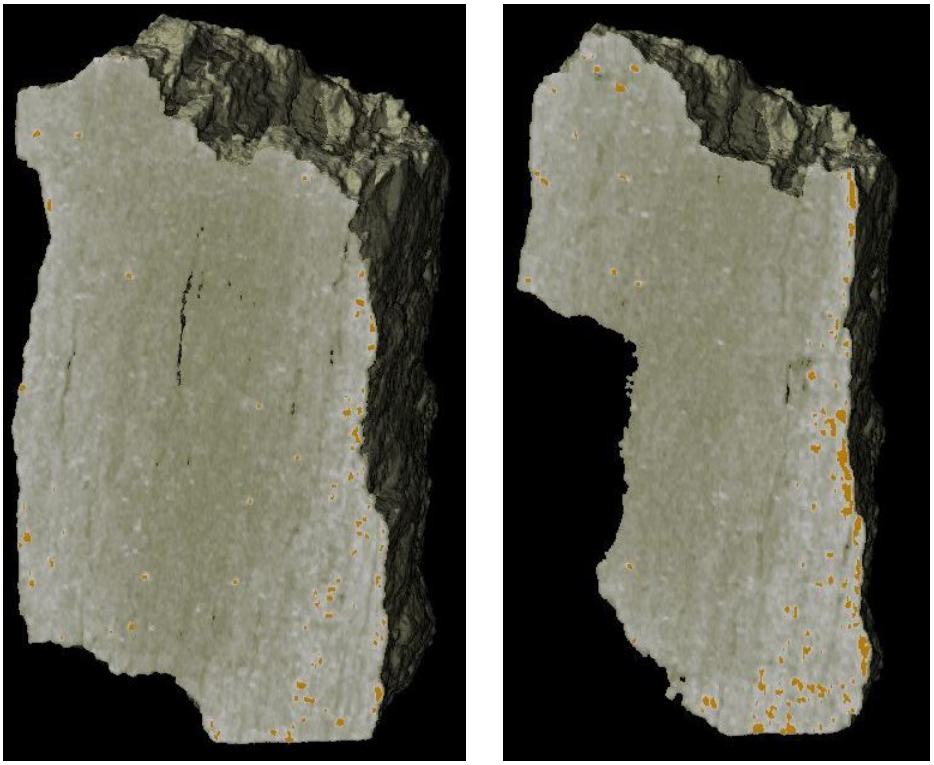

Figure 33 Slices through un-reacted sample – yellow dots are pyrite, Sample is 3mm across and 5mm long.

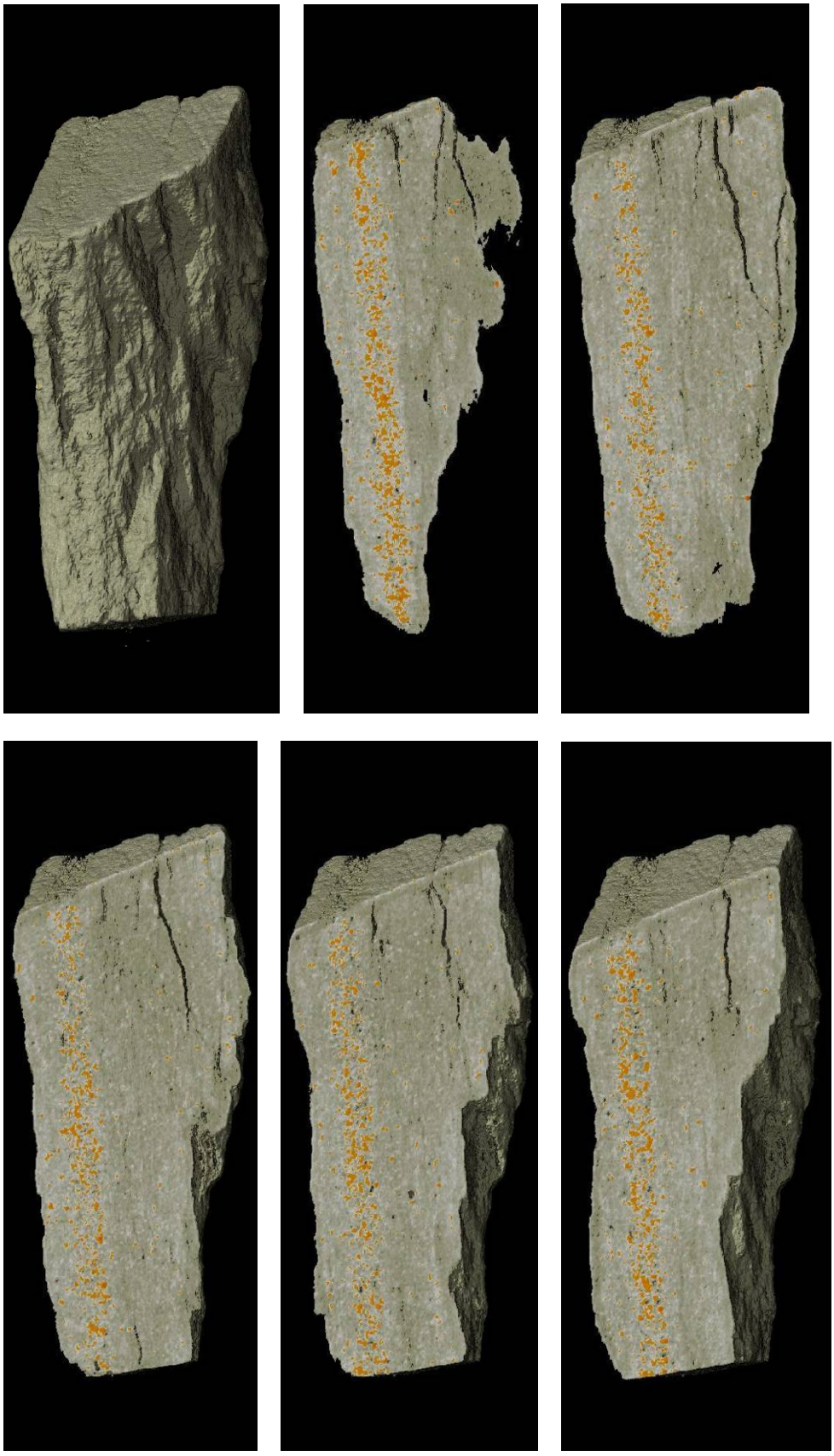

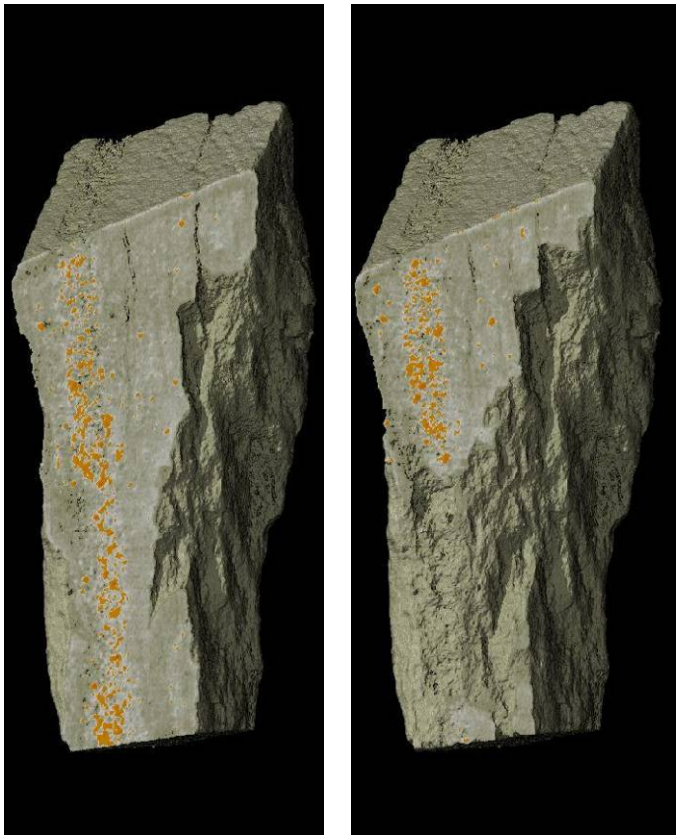

Figure 34 Reacted Sample (120 days in 70,000ppm NaCl at 80^{o}C saturated in CO_2) – yellow dots are pyrite, Sample is 3mm across and 5mm long.

The results show that slight changes are occurring within the samples such as pyrite dissolution, evaporite dissolution and precipitation which need further investigation however in general the sample matrix remains unaltered consisting primarily of Si, Al, O with K and some Fe even after 120 days exposure to brine and CO2. This indicates that there will be few mineral reactions in the Miller type Kimmerdge Clay caprock even in the presence of CO2 and oxygenated formation fluids.

A full report on the Miller Kimmeridge Clay caprock experimental results are available on the MUSTANG website, in the file sharing area of WP4, titles edlmann_intern_rport-to-BGS.pdf.

2.4.4 Kimmeridge Clay – East Brae Field Caprock .. (non fractured and naturally fractured samples)

THMC processes affecting the East Brae Field Kimmeridge Clay caprock (non fractured and naturally fractured samples) were investigated using the high pressure and temperature supercritical CO2 flow rig. The experiments were conducted at a range of pressures, temperatures and flow rates.

Kimmeridge Clay – East Brae Field location and lithology

The Kimmeridge clay caprock is from the North Sea East Brae Field, which lies at the western margin of the South Viking Graben and is operated by Marathon Oil PLC. The East Brae field is an Upper Jurassic gas condensate reservoir, interpreted as a basin floor turbidite sediment enclosed by Kimmeridge Clay. The Kimmeridge Clay is a clay rich siltstone with micaceous laminae with porosities ranging between 20% to 5%, decreasing with depth, permeabilities in the region of 4nD to 0.09nD and pore sizes from 11nm to 6nm (Okiongbo 2011). Wellbore core samples of Kimmeridge clay caprock were obtained from Well 16/3a-E1 from depths 3910m to 3918m for sampling.

Kimmeridge Clay – East Brae Field caprock in-situ temperature, pressure and salinity information

The East Brae reservoir conditions (Branter 2003) are:
Reservoir Salinity of 45,000-72,000 NaCl eq. ppm
Reservoir Temperature of 123.7^{o}C (254.7oF)
Reservoir Initial Pressure of 51MPa

Kimmeridge Clay – East Brae Field caprock experimental sample description

A naturally fractured caprock core was obtained from the East Brae Well 16/3a-E1

The fractured caprock core was drilled and the ends trimmed to provide two intact 38mm diameter cylindrical samples of naturally fractured caprock, Figure 35.

Both samples were vacuum saturated in deionised water for 2 weeks and constantly weighed to ensure maximum saturation was reached.
Sample B-a has a diameter of 38.1mm, a length of 49.6mm and a water saturated weight of 132.3g.
Sample B-b has a diameter of 37.9mm, a length of 54.1mm and a water saturated weight of 144.5g.

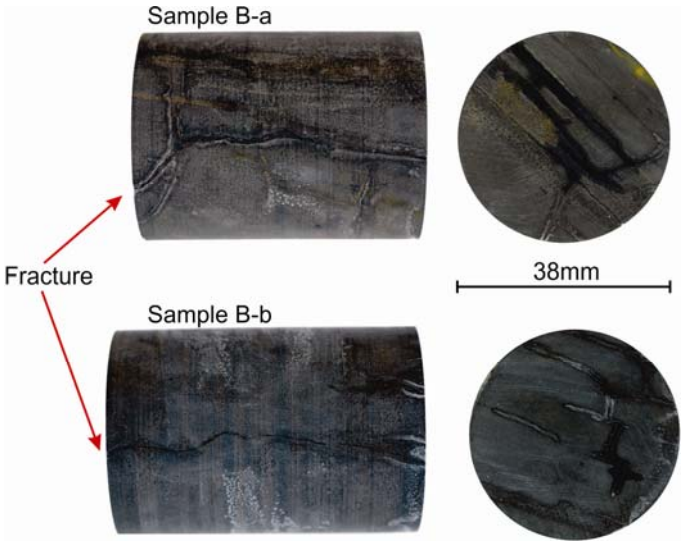

Figure 35 Images of the two 38mm diameter core samples of naturally fractured caprock from East Brae.

Kimmeridge Clay – East Brae Field caprock mineralogy.

X-Ray Diffraction investigations show that quartz and illite are the primary minerals that make up the Kimmeridge clay caprock, Figure 36. SEM images of the Kimmeridge Clay caprock microstructure show that quartz grains of up to 10μm are disseminated in the clay matrix. There is a definite bedding orientation of the matrix material (Figure 37A) with discrete quartz and pyrite crystals (Figure 37B)

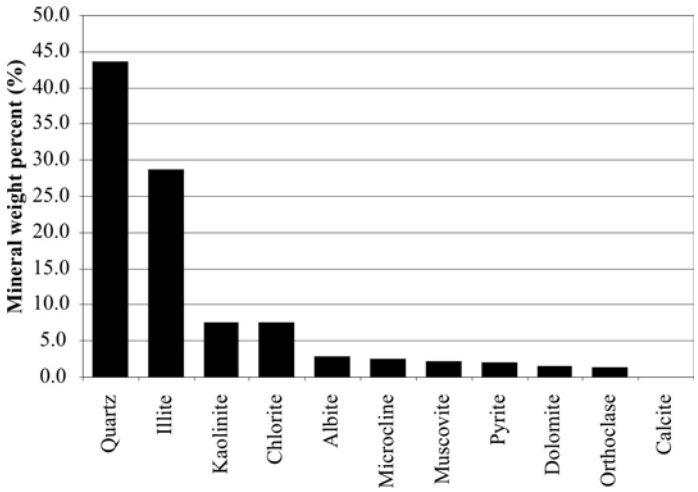

Figure 36 The % mineral abundances for caprock sample 16/3a-E1.

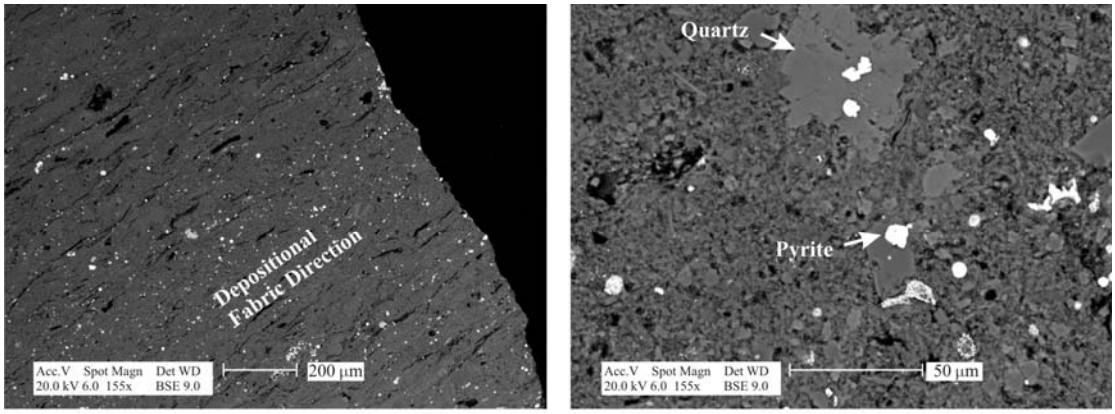

(A) Depositional Fabric (B) Quartz and pyrite crystals

Figure 37 SEM backscatter images of the East Brae Kimmeridge Clay caprock showing depositional fabric (A) and quartz and pyrite crystals (B)

The mineral composition varies slightly in the fractured caprock sample, with the appearance of calcite and a higher percentage of dolomite along with a decrease in illite and to a lesser extent kaolinite and chlorite. This is a result of diagenesis along the fracture surface, indicating historical fluid flow along the fracture. This is also bourn out by the % of illite being greater than muscovite and the % of kaolinite being higher than that of orthoclase indicating diagenesis of the matrix and fracture surface is underway. Figure 38 shows the % mineral abundances for the matrix and fractured samples prior to CO_2 exposure.

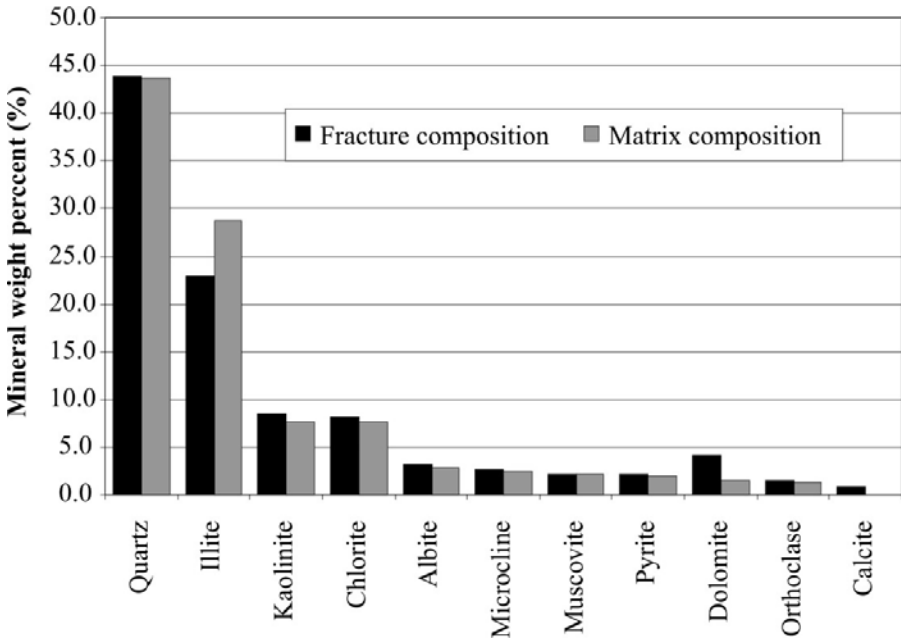

Figure 38 The % mineral abundances for the unfractured and fractured caprock samples from Well 16/3a-E1.

Kimmeridge Clay – East Brae Field caprock THMC properties experimentally investigated

Naturally fractured cores of East Brae Kimmeridge clay were subjected to flow in the high pressure and temperature scCO2 flow rig to fully investigate the influences of THMC properties on naturally fractured caprock. Table 9 presents the THMC investigations undertaken on the East Brae naturally fractured Kimmeridge Clay caprock in the high pressure and temperature CO2 flow rig.

	T	H	M	C
T		20°C & 40°C 1 / 2 / 3 / 4 / 5 g/min flow rates	20°C & 40°C 20 / 30 / 40 / 50 MPa fluid and confining pressures	20°C & 40°C scCO2 / gas phase CO2
H			1 / 2 / 3 / 4 / 5 g/min flow rates 20 / 30 / 40 / 50 MPa fluid and confining pressures	1 / 2 / 3 / 4 / 5 g/min flow rates scCO2 / gas phase CO2
M				20 / 30 / 40 / 50 MPa fluid and confining pressures scCO2 / gas phase CO2
C				

Table 9 THMC investigations undertaken on the East Brae naturally fractured Kimmeridge Clay caprock in the high pressure and temperature CO2 flow rig.

Table 10 lists the THMC experiments carried out during investigation into multiphase flow of $scCO_2$ for the fractured caprock samples presented in this paper. Both samples were vacuum saturated in deionised water prior to experimentation.

Experiment	Comments
Phase 1 Multiphase flow of sc CO_2 experiment of fractured caprock, Samples B-a and B-b	The 38mm caprock sample was held in the pressure vessel and the scCO_2 pump set at a constant flow rate of 1g/min. The temperature of the fluid and rock was maintained at 40°C and the confining pressure was increased in 10MPa increments from 20MPa to 50MPa. After the maximum confining pressure was reached the samples were then held constant for 5 days at 20MPa confining pressure, 40°C and 9MPa fluid pressure, just above the supercritical point.
Phase 2 Gaseous CO_2 exposure to naturally fractured caprock, Sample B-a	Upstream fluid pressure and rock and fluid temperature were dropped below the critical point, Temperature at 20°C, confining pressure at 5MPa. It was noted that gaseous CO_2 did flow through the naturally fractured caprock sample. This situation was left for 30 days to see if the wettability of the fracture surface could be influenced and allow scCO_2 flow if the flow experiment was re-run.
Phase 3 Multiphase flow of scCO_2 experiment of fractured caprock, Sample B-a	The scCO_2 pump was once again set at a constant flow rate of 1g/min with temperature maintained at 40°C and confining pressure increased in 10MPa increments from 20MPa to 50MPa
Phase 4 Supercritical and gaseous CO_2 leak test using a control sample (solid non porous steel cylinder), Samples B-a and B-b	This was conducted immediately after the experimental program to ensure that there was no leakage of gaseous or scCO_2 along the side of the sample and the membrane, thereby increasing confidence that all measurements were directly related to the caprock fracture.
Phase 5 Supercritical and gaseous CO_2 leak test using a non fractured caprock, Sample B-c	This was conducted after the experimental program to ensure that there was no leakage of gaseous CO_2 through the caprock pore network. This ensured that all measurements were directly related to the caprock fracture.

Table 10 Experimental program run during the investigation into multiphase flow of CO_2 in fractured caprock.

Kimmeridge Clay – East Brae Field caprock THMC results

Phase 1: Supercritical CO_2 flow experiment results

There was no detectable flow of scCO2 measured across both fractured samples, even at an upstream pressure of 43MPa and 51MPa, a pressure differential of 43MPa and 51MPa and a pressure gradient of 866MPa/m and 942MPa/m for samples B-a and B-b respectively. These maximum states for each confining pressure increment were held constant under pump pressure control for 4 hours to ensure flow equilibrium was reached. A summary of the differential pressures at each confining pressure are presented in Table 11.

Confining Pressure (MPa)	Upstream Pressure (MPa)	Downstream Pressure (MPa)	Differential Pressure (MPa)
Sample B-a			
21.118	17.257	0	17.257
30.199	24.269	0	24.269
40.065	36.362	0	36.362
48.125	42.954	0	42.954
Sample B-b			
29.916	26.227	0	26.227
40.382	36.438	0	36.438
50.476	46.008	0	46.008
55.240	50.504	0	50.504

Table 11 Maximum differential pressures at each confining pressure stage for the phase 1 supercritical CO_2 flow experiment on samples B-a and B-b.

Each sample was then held at a confining pressure of 20MPa, temperature of 40°C and locked in at fluid pressure of 9MPa (in the critical phase) for 5 days. There was absolutely no supercritical flow measured.

Phase 2: Exposure of gaseous CO_2 below $scCO_2$ phase envelope along the naturally fractured caprock results

At the end of the first $scCO_2$ flow experiment the fluid pressure and temperature were dropped to below the CO_2 critical point (31.1°C and 7.38MPa) and the CO_2 entered its gas phase. Confining pressures were held at 20MPa. Flow of CO_2 in the gas phase was detected and measured across both fractured caprock samples.

For Sample B-a this exposure of the fracture face to gas phase CO_2 was left for 30 days to see if the wettability and capillary entry pressures of the fracture surface could be influenced by exposure to gaseous CO_2 and allow subsequent $scCO_2$ flow across the fracture.

Phase 3: Multiphase $scCO_2$ flow in naturally fractured caprock experiment results

After the fractured sample B-a had been exposed to CO_2 gas for 30 days the initial multiphase supercritical CO_2 flow experiment (see Phase 1) was repeated to see if the wettability and capillary entry pressures of the fractured caprock would be affected by CO_2 exposure and allow $scCO_2$ flow through the fractured caprock. The sample was once again subjected to supercritical CO_2 set at a constant pump flow rate of 1g/min with the temperature of the fluid and rock maintained at 40°C and the confining pressure increased in 10MPa increments from 20MPa to 50MPa.

There was absolutely no flow of supercritical CO_2 measured across the naturally fractured caprock samples, even at confining pressures of 50MPa and upstream fluid pressure of 41MPa, and a pressure differential across the fractured sample of 41MPa. These maximum states for each confining pressure increment were held constant under pump pressure control for 4 hours to ensure equilibrium was reached.

A summary of the maximum differential pressures at each confining pressure stage for the second phase $scCO_2$ flow experiment are presented in Table 12.

Confining Pressure (MPa)	Upstream Pressure (MPa)	Downstream Pressure (MPa)	Differential Pressure (MPa)
20.670	17.974	0	17.975
30.557	28.489	0	28.489
40.327	37.686	0	37.686
50.248	41.120	0	41.120

Table 12 Maximum differential pressures at each confining pressure stage for the phase 2 supercritical CO_2 flow experiment on samples B-a and B-b.

It is interesting to note that gaseous CO_2 flow was detected and measured once the pressure and temperature were dropped back below the critical point for CO_2.

Phase 4: Steel control sample $scCO_2$ flow experiment results

The solid, non porous steel cylinder control sample $scCO_2$ flow experiment was conducted immediately after the main experimental program to ensure that there was no leakage of gaseous or supercritical CO_2 along the side of the sample, between the sample and the confining rubber sleeve of the pressure vessel. This ensured that all pressure and flow measurements were directly related to the caprock fracture.

There was absolutely no flow measured across the steel block sample under both experimental stages. Therefore there is no leakage of supercritical or gaseous CO_2 occurring along the along the side of the sample, between the sample and the confining rubber sleeve of the pressure vessel.

Phase 5: Non Fractured caprock control sample $scCO_2$ flow experiment results

A non fractured caprock sample, B-c (see Figure 39) was subjected to the same $scCO_2$ experiment as the fractured samples. Sample B-c has a diameter of 38.1mm, a length of 60.5mm and a water saturated weight of 173.1g.

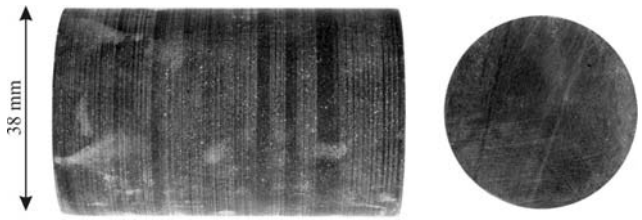

Figure 39 Image of the 38mm diameter core non fractured caprock sample, B-c from the North Sea Brae field.

There was absolutely no flow measured across the non fractured caprock sample under both supercritical and gas phase CO_2 experimental stages, therefore no leakage of supercritical or gaseous CO_2 occurs through the caprock pore network, Table 13.

Confining Pressure (MPa)	Upstream Pressure (MPa)	Downstream Pressure (MPa)	Differential Pressure (MPa)
20.311	19.153	0	19.153
30.736	28.420	0	28.420
40.451	37.934	0	37.934
Dropped below fluid pressure and temperature critical point (held for 10 days)			
14.017	5.791	0	5.791

Table 13 Maximum differential pressures for the non fractured sample B-c under the $scCO_2$ experiment.

These results indicate the possibility that there is a threshold of fracture spacing which allows gas flow but not supercritical CO_2 flow under in-situ conditions.

Mineralogical and petrophysical investigation into the effect of exposure to CO_2 on naturally fractured caprocks

At ambient temperature and CO_2 levels the carbonation of metal oxide bearing minerals occurs within geological time scales (Lasaga and Berner, 1998). When CO_2 reacts with metal oxides (indicated here as MO, where M is a divalent metal, e.g., calcium, magnesium, or iron) its carbonate is formed according to the following chemical reaction:

$$MO + CO_2 \rightarrow MCO_3 \ (+ \text{heat})$$

Two thin sections of the fractured caprock were made from Sample B-a, both from the edge of the fracture face into the caprock matrix, one before experimentation with no $scCO_2$ exposure, the second after the experiment and exposure to $scCO_2$ (note the thin section was taken from the upstream sample face exposed to $scCO_2$). Both were subjected to SEM and X-Ray analysis.

Mineralogical investigation into the effect of CO_2 exposure to naturally fractured caprocks

Average geochemical compositions were measured over a 10µm by 10µm square along a transect line in from the fracture face using the SEM and Spirit Elemental analysis software. Figure 40 presents a SEM image of the transect lines and the associated average mineral weight percent of the common minerals for each 10µm by 10µm square into the matrix from the fracture face for both the original sample and the sample exposed to CO2. Figure 41 shows the graph of the mineral weight percent of the two samples plotted against each other. Figure 42 presents an average mineral weight percent from the SEM and Spirit Elemental analysis software data of the fracture face before and after CO_2 exposure.

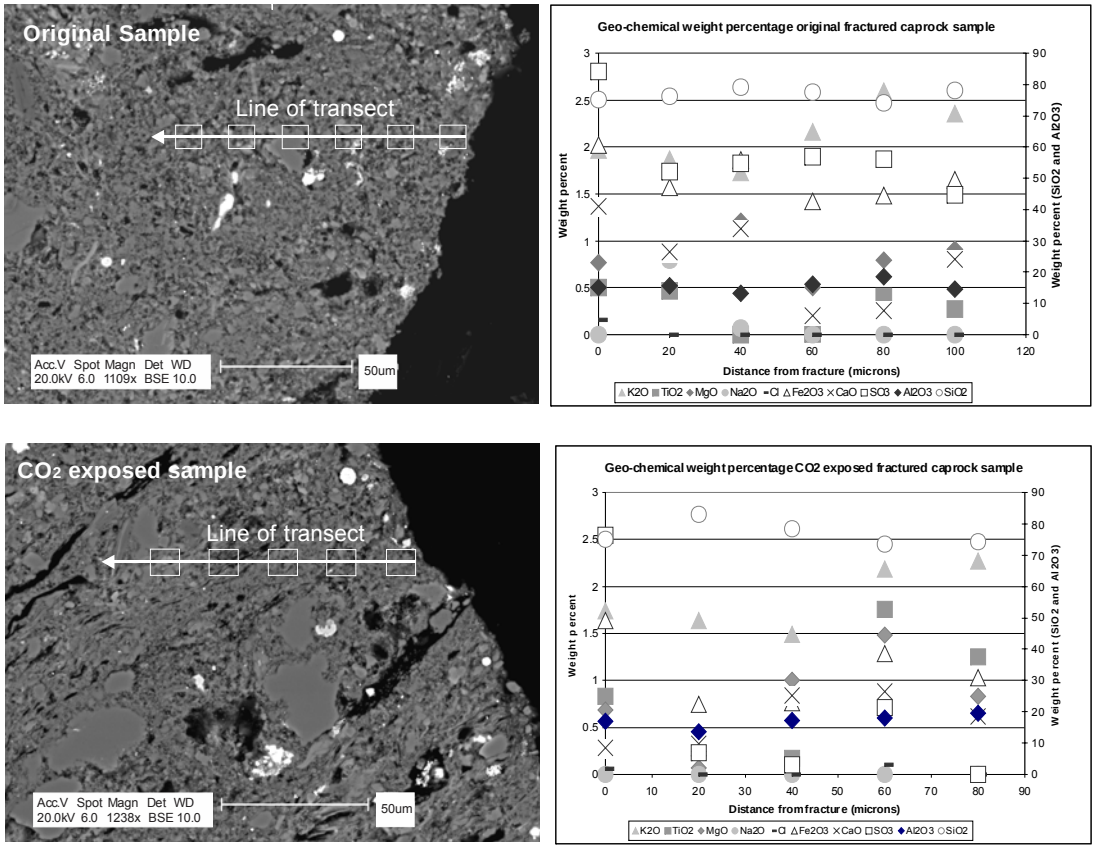

Figure 40 SEM image of the transect and the mineral weight percent of the common minerals for both the fracture face exposed to CO2 and the original fracture face.

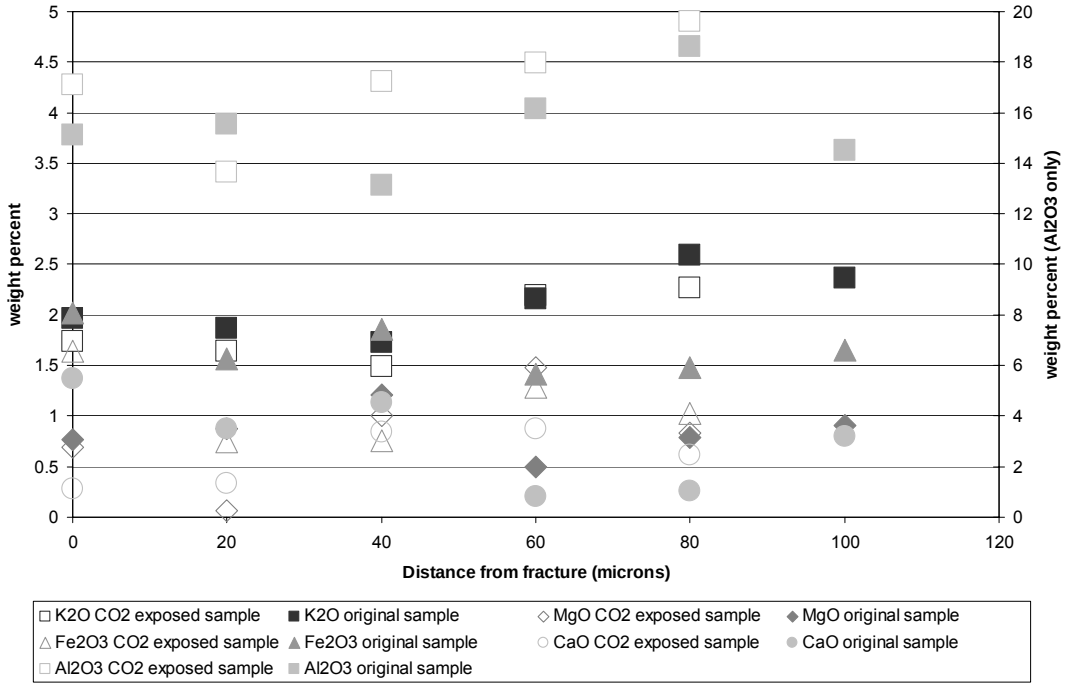

Figure 41 Mineral weight percent of the common minerals for both the fracture face exposed to CO_2 and the original fracture face

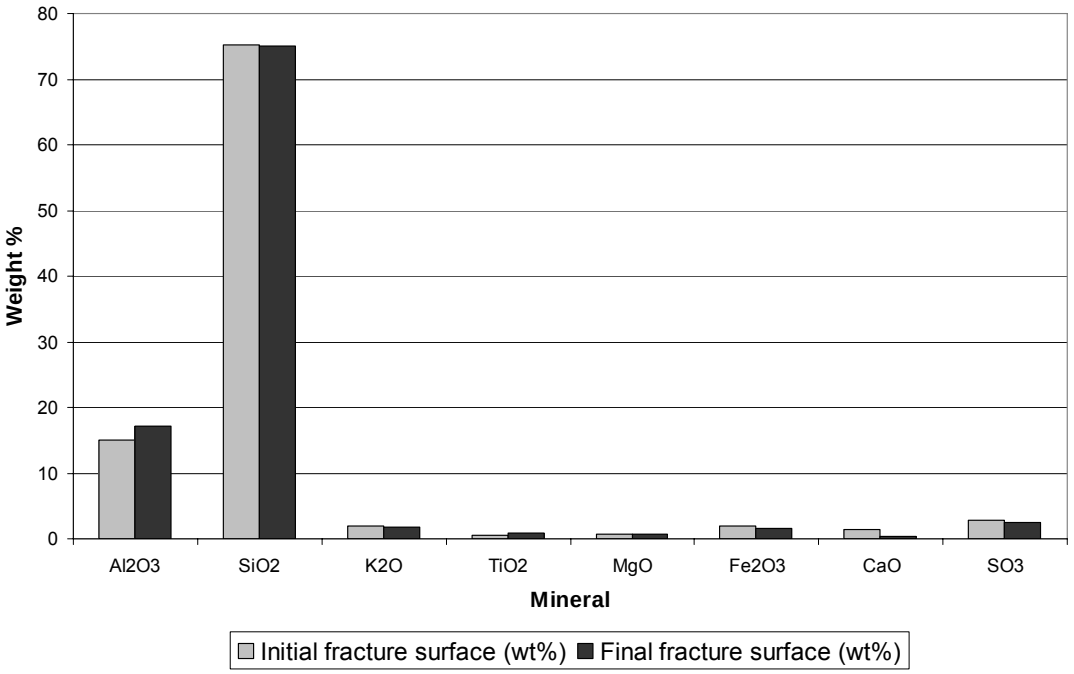

Figure 42 Average mineral weight percent from the SEM and Spirit Elemental analysis software data of the fracture face before and after CO_2 exposure.

Initial results of the mineralogical investigation of the effect of CO_2 exposure on a caprock fracture face indicate that:

In decreasing weight percent the average Kimmeridge clay has 77% SiO_2, 16% Al_2O_3, 2% K_2O_3, 1.5% Fe_2O_3, 1.5% SO_3, 1% MgO, 0.5% CaO and 0.5% TiO. This indicates that there are some limited metal oxides (1% MgO, 0.5% CaO and 0.5% TiO) available for reaction with the CO_2 facilitating the formation of a corresponding carbonate.
The results (figure 10) show that the geochemistry of the average matrix material is unchanged moving into the sample from the fracture face for both the original and the gas phase CO_2 exposed sample.
Looking at more detail at the metal oxides (figure 11) which are the most likely to react with CO_2; the CaO and MgO do not show a weight percent decrease on exposure to CO_2.
For K_2O, Fe_2O_3 and Al_2O_3 both original and CO_2 exposed samples (figure 10) follow a similar linear and unchanging mineral weight percentage trend and the spacing between the two different samples remains constant, any deviations are likely to be a result of the analysis area encountered an anomalously high mineral.
These results indicate that under the experimental timescales the mineralogy along the naturally fractured caprock face remains relatively unchanged on exposure to CO_2.

Mineralogical investigation into the effect of flow of gas phase CO_2 into bedding parallel microcracks within the Kimmeridge clay caprocks

Bedding parallel microcracks (which lie perpendicular to the naturally fractured face) are prevalent in the Kimmeridge clay caprock samples. SEM investigations were conducted to identify whether the CO_2 gas flowing along the fracture had penetrated these microcracks and caused any changes in the microcrack face mineralogy.

Average geochemical compositions were measured over 10micron by 10micron squares in a transect line in from the fracture face using the SEM and Spirit elemental analysis software, Figure 43.

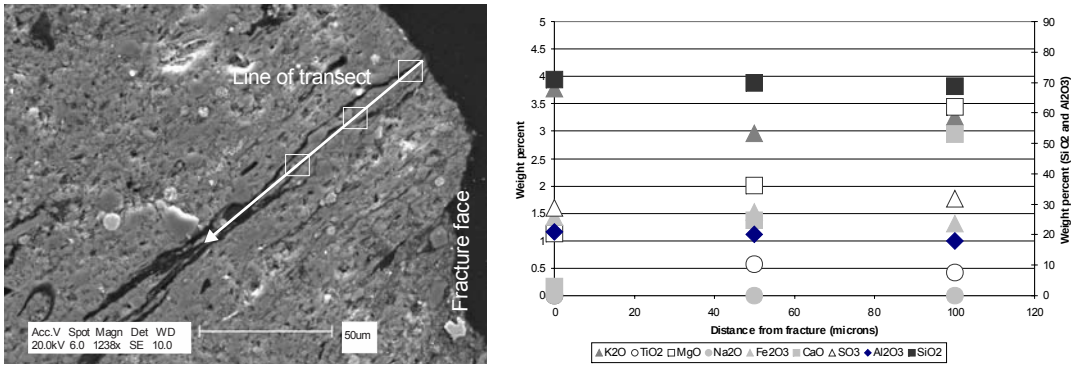

Figure 43 SEM image and mineral weight percent of the common minerals on the line of transect along the bedding parallel microcracks

Geochemical analysis of the weight percent of SiO_2, Al_2O_3, K_2O, TiO, SO_3, Fe_2O_3 and Na_2O experience no significant changes in the geochemistry along these microcracks will have been exposed to the gas phase CO_2 flowing along the fracture and entering into the microcracks.
Looking at more detail at the metal oxides (the most likely to react with CO_2) CaO and MgO do show a weight percent increase in distance along the microcrack away from the fracture face. Whether this is a natural variation or due to carbonates being formed needs further investigation.
These results indicate that under the experimental timescales the general mineralogy along the microcracks do not experience any mineralogical changes on exposure to gas phase CO_2

Under the in-situ pressure and conditions that are experienced during deep geological storage, CO_2 is expected to exist in its supercritical state. Our initial experiments on exposure of supercritical CO_2 to naturally fractured caprocks under geological storage conditions show that there is no flow of supercritical flow across the caprock fracture. This is even with a pressure differential of 43MPa and 51MPa and a pressure gradient of 866MPa/m and 942MPa/m for samples B-a and B-b respectively. When the temperature and fluid pressure are reduced to below the CO_2 phase change boundary and CO_2 enters its gas phase, flow of CO_2 was observed and measured across the fracture. These results indicate a threshold of fracture spacing which allows gas flow but not supercritical CO_2 under in-situ conditions.

After 30 days of gas phase CO_2 flow along the caprock fracture the temperature and pressure were increased back to in-situ conditions and supercritical flow was instigated. Once again no flow of supercritical flow across the caprock fracture was measured. Indicating that under the experimental conditions capillary entry pressures and wettability of the fracture face were not influenced by exposure to gaseous CO_2.

These results indicate the possibility that there is a threshold of fracture spacing which allows gas flow but not supercritical CO_2 under in-situ conditions.

Geochemical investigations into the caprock mineralogy indicate that under the experimental timescales the general mineralogy along the fracture face, caprock matrix and fabric microcracks do not experience any mineralogical changes on exposure to gas phase CO_2.

The implications of these results suggest that if supercritical CO_2 does migrate from the storage site and travels towards the surface, leakage will be restrained until the in-situ conditions of pressure and temperature go below the critical point of 7.35MPa and 31^{o}C (the equivalent of around 840m depth assuming a geothermal gradient of 25°C/km) when there is likely to be leakage through caprock fractures of CO_2 in its gaseous phase.

We note at this stage that the experimental observation tie in with field observations of CO_2 leakage sites in Italy where current field analogue research indicates that there is no CO_2 leakage from deep CO_2 storage reservoirs however there is CO_2 gas leakage from the shallower reservoirs.

2.4.5 Evaporite caprock

THMC processes affecting the evaporite caprock were investigated using bench experiment type B. The experiments were conducted at 20MPa, temperatures of 35°C and 50°C with no flow.

Evaporite caprock location and lithology

The Boulby evaporates are a Permian / Triassic evaporite sequence deposited from the landlocked Zechstien Sea as it was drying up, leaving salt flats. The salts deposited include anhydrite (calcium sulphate) and gypsum, then halite (NaCl) and sylvinite (KCl).

Evaporite caprock in-situ temperature, pressure and salinity information

The Boulby mine is at 1.35 km depth and the temperature is 45°C.

Evaporite caprock experimental sample description

Two samples of Boulby evaporites were available for testing, Figure 33. 5g of each evaporate type were ground to a fine powder in a pestle and mortar. They were sieved to ensure a maximum grain size of 1mm.

Figure 44 Boulby evaporites samples.

Evaporite caprock mineralogy.

Awaiting results of the XRD mineralogy – will be presented in Deliverable 046, due month 44.

Evaporite caprock THMC properties experimentally investigated

Table 14 presents the THMC investigations undertaken on the evaporite caprock and in bench experiment type B equipment.

	T	H	M	C
T		35°C & 50°C No flow	35°C & 50°C Ambient pressure & 20MPa	35°C & 50°C CO_2 saturated formation brine
H			No flow Ambient pressure & 20MPa	No flow CO_2 saturated formation brine
M				Ambient pressure & 20MPa CO_2 saturated formation brine
C				

Table 14 THMC investigations undertaken on the Evaporite caprock in bench experiment B equipment.

Boulby evaporite caprock THMC results

Awaiting XRD results of before and after scCO2 exposure – will be presented in Deliverable 046, due month 44.

2.4.6 Clashach reservoir sandstone

THMC processes affecting the Clashach reservoir sandstone was investigated using the high pressure and temperature supercritical CO2 flow rig. The experiments were conducted at a range of pressures, temperatures and flow rates.

Clashach reservoir sandstone location and lithology

The Clashach sandstone is a Permo-Triassic rock from Elgin, Scotland. It is a well cemented sandstone with silica cement. The grains are well sorted and include well rounded grains and are interpreted as an aeolian dune deposition. Grain size is consistently fine to medium (250-450 microns), average porosity is 18% and the permeability range is approximately 1.2-1.5 Darcies.

Clashach reservoir sandstone experimental sample description

Figure 45 Image of the 38mm diameter Clashach sandstone core.

Clashach reservoir sandstone mineralogy.

Awaiting results of the XRD mineralogy – will be presented in Deliverable 046, due month 44.

Clashach reservoir sandstone in-situ temperature, pressure and salinity information

Relevant data not available.

Clashach reservoir sandstone THMC properties experimentally investigated

Table 15 presents the THMC investigations undertaken on the Clashach reservoir sandstone using the high pressure and temperature supercritical CO2 flow rig at in-situ temperature and pressure with scCO2 flow

	T	H	M	C
T		40°C & 60°C 1 / 2 / 3 / 4 / 5 g/min flow rates	40°C & 60°C 20 / 30 / 40 / 50 MPa fluid and confining pressures	40°C & 60°C scCO2
H			1 / 2 / 3 / 4 / 5 g/min flow rates 20 / 30 / 40 / 50 MPa fluid and confining pressures	1 / 2 / 3 / 4 / 5 g/min flow rates scCO2
M				20 / 30 / 40 / 50 MPa fluid and confining pressures scCO2
C				

Table 15 THMC investigations undertaken on the Clashach reservoir sandstone using the high pressure and temperature supercritical CO2 flow rig at in-situ temperature and pressure with scCO2 flow

Clashach reservoir sandstone THMC results

Looking first at the effect of flow rate of the differential pressure across the sample, Figure 43. It is revealed that there is no strong relationship between rate of flow and differential pressure through the Clashach reservoir sandstone at 40oC and a back pressure (fluid pressure) set to 10MPa.

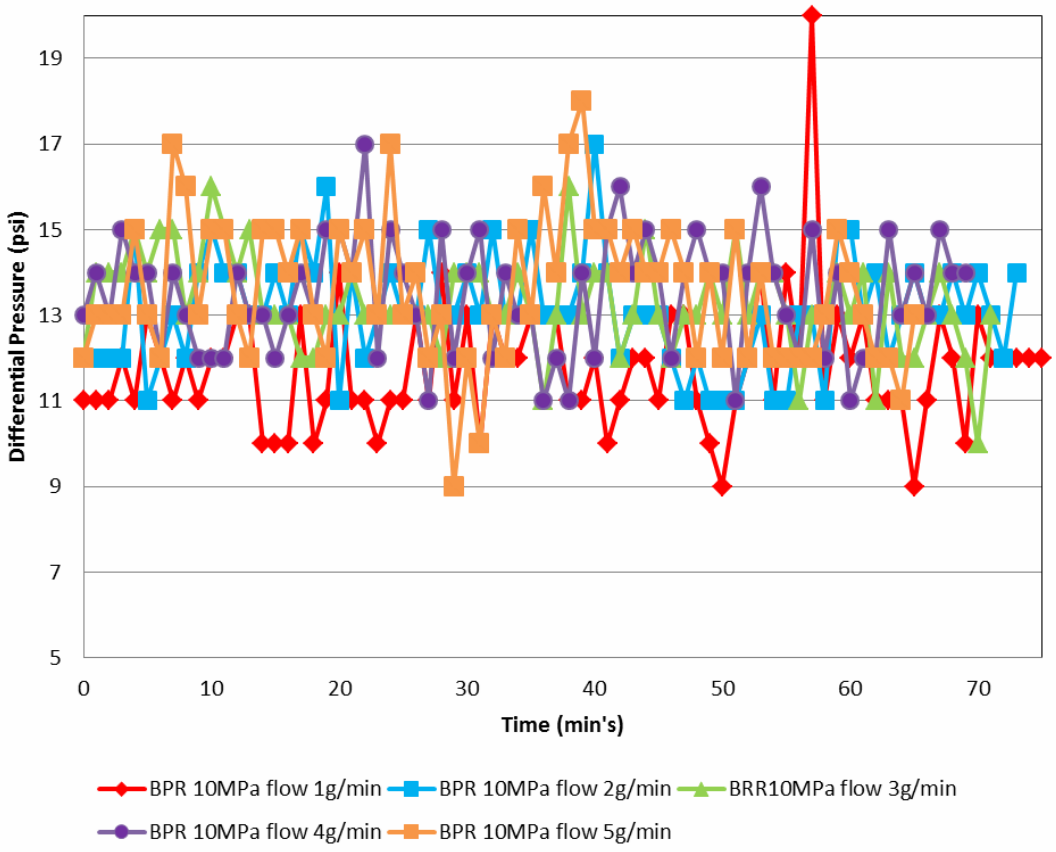

Figure 46 Effect of scCO2 flow rate through the Clashach reservoir sandstone at 40°C and a back pressure set to 10MPa

Looking at the effect of fluid pressure on the flow of scCO2 through the Clashach reservoir sandstone at 40oC, Figure 47 shows the differential pressures at a

3g/min flow rate at 3 different fluid (back pressure) pressures. It can be seen that there is a slight overall increase in the differential pressure across the sample as the fluid pressure increases.

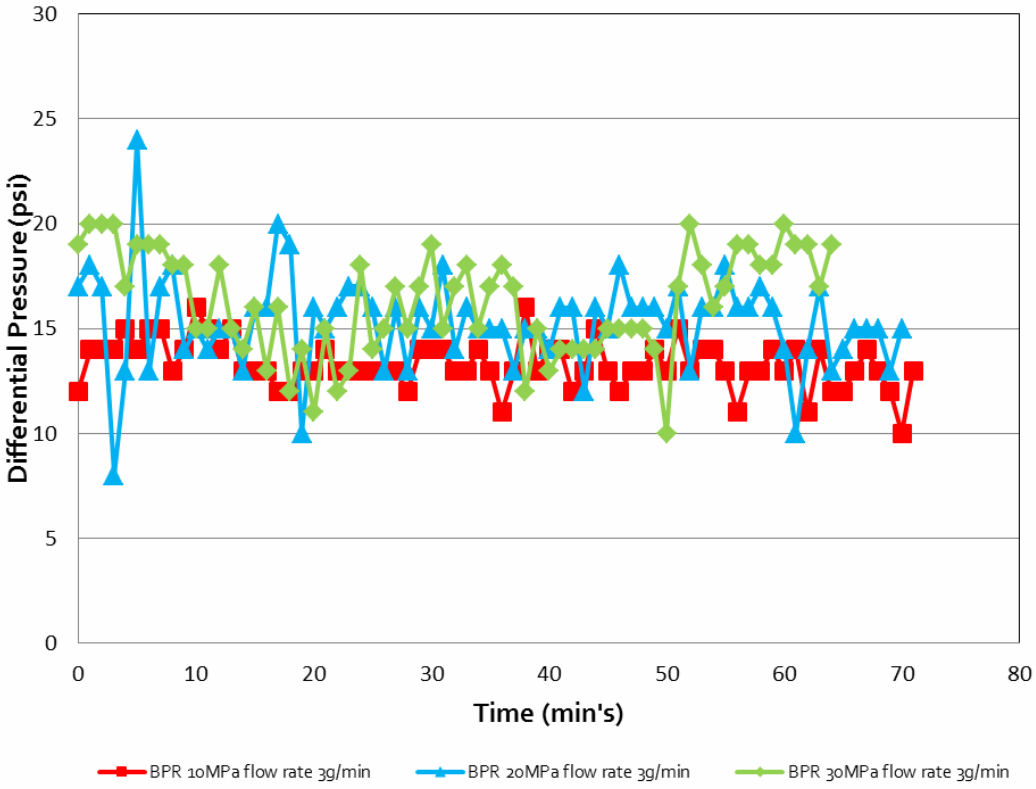

Figure 47 Differential pressures across the Clashach sandstone at a 3g/min flow rate at 10MPa, 20MPa and 30MPa fluid (back pressure) pressures at 40°C

Awaiting experimental results at 60°C to investigate the effect of temperature on the differential pressure across the Clashach sandstone – will be presented in Deliverable 046, due month 44.

Awaiting XRD results of before and after scCO2 exposure – will be presented in Deliverable 046, due month 44.

2.4.7 Stuben reservoir sandstone

THMC processes affecting the Stuben reservoir sandstone was investigated using the high pressure and temperature supercritical CO2 flow rig. The experiments were conducted at a range of pressures, temperatures and flow rates. The Stuben sandstone sample was saturated with 70,000ppm brine then supercritical CO2 pumped in at 1g/min. Flow rate was held at 1g/min the back pressure held at 9MPa (90atm, 90bar, 1305psi) and temperature held constant at 40oC. The confining pressure was increased from 20-30-40-50-60-70MPa.

Stuben reservoir sandstone location and lithology

The late Triassic Stuben sandstone of South West Germany is interpreted as a terminal alluvial plain systems deposited in an arid to semiarid climate. The fine to coarse grained clastic sediments of the Stuben sandstone are mostly arkosic arenites.

Stuben reservoir sandstone experimental sample description

Figure 48 Image of the 38mm diameter Stuben sandstone core – the sample length is 43mm.

Stuben reservoir sandstone mineralogy.

Awaiting results of the XRD mineralogy – will be presented in Deliverable 046, due month 44.

Stuben reservoir sandstone in-situ temperature, pressure and salinity information

Relevant data not available.

Stuben reservoir sandstone THMC properties experimentally investigated

Table 16 presents the THMC investigations undertaken on the Stuben reservoir sandstone using the high pressure and temperature supercritical CO2 flow rig at in-situ temperature and pressure with scCO2 flow

	T	H	M	C
T		40°C 1 g/min flow rates	40°C 20 / 30 / 40 & 50 MPa fluid and confining pressures	40°C scCO2
H	40°C 1 g/min flow rates		1 g/min flow rates 20 / 30 / 40 & 50 MPa fluid and confining pressures	1 g/min flow rates scCO2
M				20 / 30 / 40 & 50 MPa fluid and confining pressures scCO2
C				

Table 16 THMC investigations undertaken on the Stuben reservoir sandstone using the high pressure and temperature supercritical CO2 flow rig at in-situ temperature and pressure with scCO2 flow

Stuben reservoir sandstone THMC results

The Stuben sandstone sample was saturated with 70,000ppm brine then supercritical CO2 pumped in at 1g/min. Flow rate was held at 1g/min, the back pressure (fluid pressure) held at 9MPa (90atm, 90bar, 1305psi) and temperature held constant at 40oC. The confining pressure was then increased from 20-30-40-50-60-70MPa.

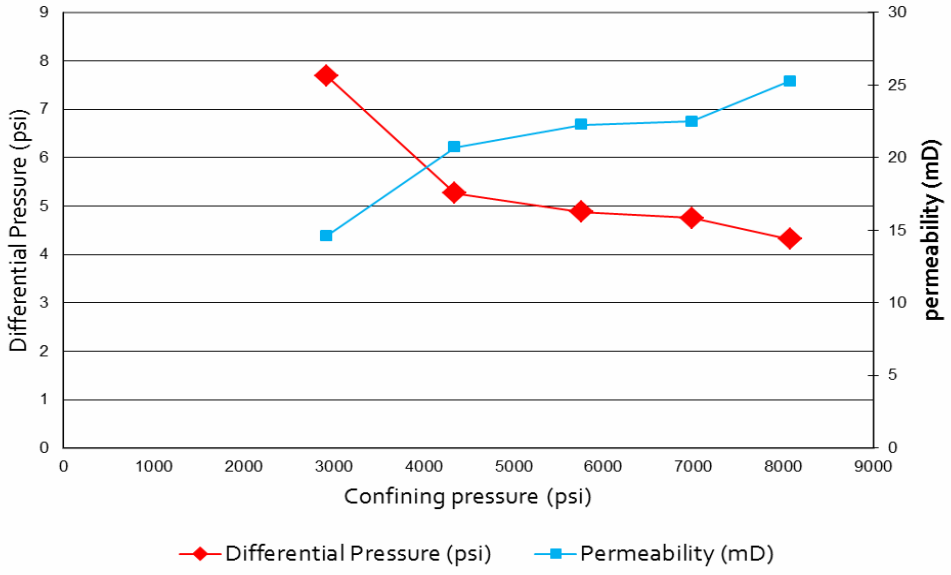

Figure 49 Measured average differential pressure and average permeability across the Stuben sandstone under flow experiments at 40°C, with flow rate held at 1g/min, the back pressure held at 9MPa, confining pressure was then increased from 20-30-40-50-60-70MPa.

The differential pressure across the Stuben sandstone sample is noted to decrease as the confining pressure is increased, and the permeability increased. This indicates that flow of scCO2 becomes easier, i.e. increase in permeability to scCO2 as confining pressure increases. There was a visual degradation in the surface of the Stuben sandstone even at low temperature, pressure and flow rate exposure to scCO2, Figure 50which could explain the increase in ease of flow.

Figure 50 Visual degradation in the surface of the Stuben sandstone even at low temperature, pressure and flow rate exposure to scCO2

Awaiting XRD results of before and after scCO2 exposure to identify if this is due to a change in mineralogy / dehydration? – will be presented in Deliverable 046, due month 44.

2.5 Summary of the experimental investigation into the effect of thermal, hydraulic, mechanical and chemical coupled processes on caprock and reservoir rock.

Table 17 presents a summary of the results from the full suite of THMC investigations conducted through the experimental testing on shale, claystone and evaporite caprock types and reservoir sandstones.

For the experiments undertaken so far we can conclude that for the caprocks investigated there is significant chemical stability. There are some changes, namely; the dissolution of Calcite, surface flaking (through surface chemical weathering), pyrite alteration (possibly due to oxidation in oxygenated waters) and the development of micro cracks (possible dehydration reactions).

The main THMC summary points are:
The effect of temperature and pressure on the phase of CO2 exerts a significant influence on caprock integrity of naturally fractured Kimmeridge clay caprock – **If the temperature and pressure of the system drops below the CO2 critical point and CO2 enters its gas phase then CO2 will flow along natural fractures** that were previously impermeable to scCO2, even at differential pressures in excess of 50MPa across the fracture.
The **clay matrix remains unchanged** in in Heletz, St Ninians, Miller Kimmeridge clay, East Brae Kimmeridge clay and boulby mine evaporites under all experimental pressure, temperature and CO2 exposure conditions.
No new minerals were precipitated in Heletz, St Ninians, Miller Kimmeridge clay, East Brae Kimmeridge clay and Boulby mine evaporites under all experimental pressures, temperatures and CO2 exposure conditions.
Minor **Calcite and Pyrite dissolution** is observed in Heletz, St Ninian's, East Brae Kimmeridge clay and Miller Kimmeridge clay caprock samples under all experimental temperatures, pressures and CO2 exposure conditions.
Looking at more detail at the metal oxides (the most likely to react with CO_2) CaO, MgO, K_2O, Fe_2O_3 and Al_2O_3 follow a linear and unchanging mineral weight percentage trend for the kimmeridge clay and Heletz caprock samples at all rages of temperature, pressure and flow rates.
These results indicate that **under the experimental timescales the general mineralogy along the caprock fractures and microcracks do not experience any mineralogical changes** on exposure to gas phase CO2.
It can be seen that there is a slight overall increase in the differential pressure across the Clashach reservoir sandstone sample as the fluid pressure increases.
The differential pressure across the Stuben sandstone sample is noted to decrease as the confining pressure is increased. This indicates that flow of scCO2 becomes easier, i.e. increase in permeability to scCO2 as confining pressure increases. There was a visual degradation in the surface of the Stuben sandstone which could explain the increase in ease of flow.

	T	H	M	C
T		There is no supercritical flow across the **East Brae Kimmeridge clay** natural fracture at both 40°C and 60°C at all flow rates. When the temperature (and pressure) in the naturally fractured East Brae Kimmeridge Clay caprock was dropped to 200C, below the critical point, gas CO_2 was observed to flow when previously there had been no $scCO_2$ flow.	There is no supercritical flow across the East Brae Kimmeridge clay natural fracture at both 40°C and 60°C at all confining pressures, even with a differential pressure across the fracture of 51MPa. There is a slight overall increase in the differential pressure across the Clashach reservoir sandstone sample as the fluid pressure increases Awaiting results from the experiment on Clashach at 60°C to compare flow properties with those at 40°C The Stuben reservoir sandstone did show increase in permeability with increasing confining pressure and minor core sample disintegration on exposure to increasing confining pressures. Awaiting XRD results to clarify if this is a result of mineralogy / dehydration effects. Awaiting XRD results for Evaporite caprock at 30 °C & 50 °C at ambient and 20MPa pressures.	SEM results on the Miller Kimmeridge Clay caprock sample show minimal changes in the matrix mineralogy. Awaiting XRD results for Miller Kimmeridge Clay caprock caprock at 40°C & 55°C. SEM results on the East Brae Kimmeridge Clay caprock sample show minimal changes in the matrix mineralogy. Awaiting XRD results for Miller Kimmeridge Clay caprock caprock at 20°C / 40°C & 60°C Awaiting XRD results for St Ninian's Shale at 30 °C & 80 °C SEM results on the Heletz caprck sample show minimal changes in the matrix mineralogy on exposure to Co_2 saturated brine. Awaiting XRD results for Heletz caprock at 55°C Awaiting XRD results for Evaporite caprock at 30 °C & 50 °C The Clashach sandstone showed no significant changes in the mineralogy in the samples exposed to all temperatures. The stuben sandstone did show minor core sample disintegration on exposure to $scCO_2$ at temperature. Awaiting XRD results for more detail.
H			There is no supercritical flow across the East Brae Kimmeridge clay natural fracture at both 40°C and 60°C at all confining pressures, even with a differential pressure across the fracture of 51MPa. When the pressure (and temperature) in the naturally fractured East Brae Kimmeridge Clay caprock was dropped to 10MPa, below the critical point, gas CO_2 was observed to flow when previously there had been no $scCO_2$ flow. When the pressure (and temperature) in the naturally fractured East Brae Kimmeridge clay caprock was dropped to 10MPa, below the critical point, gas CO_2 was observed to flow when previously there had been no $scCO_2$ flow. The Stuben reservoir sandstone did show increase in permeability with increasing confining pressure and minor core sample disintegration on exposure to increasing confining pressures at increasing temperature. Awaiting XRD results to clarify if this is a result of mineralogy / dehydration effects.	XRD, SEM and X-Ray CT results show that there is no effect on the mineralogy of the East Brae Kimmeridge Clay fracture face and microfractures exposed to gas phase CO_2 flow. The Clashach sandstone showed no significant changes in the mineralogy in the samples exposed to all flow rates. The stuben sandstone did show minor core sample disintegration on exposure to $scCO_2$ at high flow rates. Awaiting XRD results for more detail.
M				Awaiting XRD results for Evaporite caprock at 30 °C & 50 °C at ambient and 20MPa pressures. The stuben sandstone did show minor core sample disintegration on exposure to $scCO_2$ at high flow rates. Awaiting XRD results for more detail.
C				

Table 17 Summary of the key results from the full suite of THMC investigations conducted through the experimental testing on shale, claystone and evaporate caprock types and reservoir sandstones.

2.6 References

Branter, S. R. F. 2003. The East Brae Field, Blocks 16/03a, 16/03b, UK North Sea in Gluyas, J. G. & Hichens, H. M. (eds). United Kingdom Oil and Gas Fields Commemorative Millennium Volume. Geological Society. London. Memoir 20, 191-197.

Jiemin Lu Ph.D. University of Edinburgh. 2008. CO2 interaction with aquifer and seal on geological timescales: the Miller oilfield, UK North Sea.

MUSTANG Deliverable D023 report, 2011

Okiongbo, K.S. 2011. Bulk volume reduction of the Kimmeridge Clay Formation, North Sea (UK) due to compaction, petroleum generation and expulsion, Research Journal of Applied Sciences, Engineering and Technology 3(2): 132-139.

Ran Calvo & Zohar Gvirtzman: Preliminary assessment of CO2 storage opportunities in Israel. Geological Survey of Israel; 30 Malkhei Israel St., Jerusalem, Israel 95501 - http://www.co2geonet.com/UserFiles/file/ESF/3-R-Calvo_Preliminary-assessment-of-CO2-storage-opportunities-in%20Israel.pdf

Satrinsky A. 1974. Relationship between Ca-chloride brines and sedimentary rocks in Israel. PhD dissertation, Hebrew University. Jerusalem.

3 Natural Analogues

3.1 Objectives

As part of Project MUSTANG, the University of Edinburgh group (aka: "UEDIN") undertook to investigate two complementary natural analogue sites for those caprock types perceived to be highly typical for CO2 storage reservoirs with reservoir-seal combination characteristics similar to typical saline aquifer targets for large volume CCS. The investigation of the sites included both field analysis, experimental design, investigation, modelling and analysis of results.

The departure point here was an initial, partly hitherto established UEDIN focus on oil/gas reservoirs, aquifers and other hyrogeological systems that were naturally CO2 rich, e.g. Miller and Fizzy hydrocarbon fields in the North Sea (*Lu et al. 2008*) as well as surface analogue CO2 sites including oxidized sandstone settings in the Crystal Geyser, Colorado, Western US and carbonate terrains in Italy (*Roberts et al., 2011*). Analogues where CO2-brines are in contact with rock material, similar to the reservoirs and seals prepared for engineered storage, provide powerful methodS to address these concerns. By analysing analogue systems, one can improve the understanding of CO2 behaviour in geological formations. Within the MUSTANG integrated THMC coupled processes approach for caprock integrity, an objective rapidly emerged to comprehensively characterise two large scale analogues that could provide the greatest practical range of insight into thermal, mechanical, hydraulic and chemical coupled phenomena.

Selected analogues were targeted for (1) samples for laboratory investigation and (2) macro-, outcrop- and field-scale surveying data. As will be seen, (1) and (2) were not possible for all analogues objectives.

3.2 Initial Efforts

We conducted a comprehensive literature review of most suitable areas for caprock analogues. Selection criteria were (1) a similarity to, or equivalent of, caprocks noted in EU capacity assessments, and (2) accessible with reasonable use of project resources and benefit of presence of established academic network (e.g. W. Europe, NE. American continent). "Similarity" denotes: - lithologically similar in terms of (1) bulk rock type, i.e. proportions of mud, shale, etc., and (2) density and frequency of facies integrated over a required depth interval or surficial area - burial history is similar; time/depth gradients in maturation, dewatering, compaction, primary (e.g. flocculation) and diagenetic clay fabric development inclusive of chemistry and structure such as (re-)mineralisation, and has no or minimal overprint from re-emergence effects all of which must be discriminable from burial effects (e.g. deformation, fracture suites, chemical & mineralogical changes, etc.). This led to the identification of two to three main analogue targets.

3.3 Motivation for the main analogue targets

A key and obvious caprock target for UEDIN due to our proximity to the proven hydrocarbon traps (natural "storage" sites) of the North Sea was one of the numerous caprock suites therein. The widespread nature of the Kimmeridge Clay Formation and, in particular, its manifestation in and around the Viking Graben, coupled with UEDIN in-house expertise on the Kimmeridge Clay in general and, in particular, its architecture around the Miller Field (Viking Graben) led to early identification of the Kimmeridge Clay Formation as a main analogue target.

A second target that emerged was a portion of the widespread Devonian black shales in NE USA. Reports of what appeared to be "natural Hydraulic Fractures" suggested a clear opportunity for insight into the mechanical realm of THMC in caprock-like facies that was also regionally widespread and, at least locally, quite well documented

Finally, additional caprock analogue possibilities considered were the following onshore UK outcrops:

- Staithes, a seaside village and well-exposed at low tide platform in North Yorkshire, England.

- Pease Bay in the Scottish Borders area of Scotland, close to the border with East Lothian
- St Ninian's Quarry in Fife, Scotland.

These ultimately were not adopted. They are discussed below.

Much literature for these rocks exists describing the conditions that engendered a range of fracture suites thereby providing key data to WP4 UEDIN's modelling of caprock integrity. An exciting WP4 result is a fracture suite that reflects "near instantaneous" hydraulic overpressuring (these theoretically should be common but are very rare in nature)

Selected analogues were / are being used for samples for laboratory ("micro") investigation and macro-, outcrop- and field-scale surveying data. Sampling and obtaining measurements and observations across a range of scales is pivotal for our thermo-hydro-mechanical-chemical (THMC) coupled processes modelling work. The ultimate ability of a CO2 storage reservoir to allow suitable relative permeability and flow and ability of a caprock to remain intact is a product of the interplay of (THMC) coupled processes from the micro- up to the reservoir-scale. Although establishing a reservoir-scale facies architecture can be attempted solely via borehole data (well logs, recovered core), scale-dependence of fracture patterns and their characteristics (e.g. spacing, persistence, density) requires analogues with sufficient outcrop. The black Devonian "shales" in northeeastern USA satisfy this requirement.

3.3.1 Black Devonian "shales" in NE USA

The black Devonian "shales" in NE USA satisfy the UEDIN Mustang objectives' requirement of scale-dependence of fracture patterns and their characteristics (e.g. spacing, persistence, density). These rocks were thereby adopted as the main case-study analogue. Moreover, much literature for these rocks exists describing the conditions that engendered a range of fracture suites thereby providing key data to WP4 UEDIN's modelling of caprock integrity. An exciting WP4 result is a fracture suite that reflects "near instantaneous" hydraulic overpressuring (these theoretically should be common but are very rare in nature). This is detailed below.

For the western New York Devonian Catskill Delta case study analogues considered, the presence of non-core-able shale (friable, heavily-weathered mudrocks) precluded useful sample recovery of sufficient quality, scope and consistency for UEDIN's lab objectives. From the Marcellus proper, the Beaver Meadows No.1 borehole core was offered (see below) but ultimately not used, and so the main target for sample provision fell to the Kimmeridge Clay Formation.

3.3.2 Kimmeridge Clay Formation

The Kimmeridge Clay Formation (KCF) has also been selected as a preferred caprock analogue due to its comprehensively documented role as a seal in numerous hydrocarbon (oil, gas condensate) reservoirs, including over-pressured traps. Decades of industry and academic research exist for the KCF. Moreover, it s highly likely that as Northern European CCS deployment progresses over the next decade, the KCF will be the actual caprock in question for a range of North Sea geological storage targets (albeit excluding Brae, Miller and other Viking Graben fields, due to profound depths; 2500-4100 m).

3.3.3 Rationale

A central thesis to the (THMC) coupled processes work is that of Geomechanical facies (McDermott et al. 2006). On the outcrop and smaller scales, we expect a threshold quantity (for a given scale and position) of key material that, where present above this amount, must govern the suitability of a given reservoir or seal (caprock) lithology; e.g. quantity of clay & mud to silt ratio or clay & mud total density integrated over a required depth interval or surficial area below which the uncertainty (and thereby risk) associated with the suitability of

the reservoir or seal target is too large. To allow our modelling to define end members of this stratified character, we are identifying the alternating/stratified character of the caprock from the field and boreholes to construct a geomechanical facies architecture and measure representative parts of this in the lab. The Brae Field wells will give good insight on (proxy) mechano-stratigraphy. Meanwhile, the black Upper Devonian "shales" at Dunkirk, NY provide insight into hydro-mechano-stratigraphy by way of the presence versus absence of hydraulic fractures that are arresting in the caprock.

3.3.4 Analogue targets deselected or rejected

A reserve list of onshore KCF equivalents (i.e. non-KCF rocks potentially suitable for sampling and surveying) were ranked as follows:

Pease Bay, Scottish boarders, East Scotland (below photo) .

The Pease Bay Upper Devonian - Lower Carboniferous sedimentary basin sequence is roughly equivalent to the Knox Pulpit Fmn. in Fife. It is a well fractured caprock type of facies. Key differences to the KCF are that although there are mudrocks within the sequence, the Pease Bay Unit is both Porous and Permeable (the Knox Pulpit Fmn. is porous but not very permeable). Advantages are the close proximity to Edinburgh. Fundamentally, however, this is not a thick persistent anoxic mudstone like the KCF. Again, burial depths are poorly known.

Figure 51 Pease Bay Location

St. Ninian's open cast coal quarry North of Dunfermline, Fife, in Central Scotland
St. Ninian's open cast coal quarry North of Dunfermline, Fife, in Central Scotland contains the Carboniferous age Limestone Coal Fmn. Partly repeated layers of grey, locally black mudstone in the overall Scottish Carboniferous Limestone Coals were buried to "bitumen" depths (equivalent to oil-gas transition depth interval). We used this rock predominantly as a source of nearby, large extent (for plenty of choice), freshly exposed mudstone to conduct primary field sampling trials of suitable sized sampling equipment for the scCO2 experimental apparatus and for sample measurements calibration. However, although this rock was/is a possible backup, this is not a good caprock analogue for CO2 storage reservoirs due to inappropriate facies (coal swamp settings), depth of burial and proximity to subsequent widespread regional volcanism (whose heat input significantly has altered the geochemical and geophysical properties of the St. Ninian's mudrocks).

Staithes, North Yorkshire (below photo).

In Staithes on the coast of North Yorkshire, England, at the Hinderwell & Port Mulgrave section, the Jet Rock Formation outcrops. This is a laminated, anoxic Toarician, locally aluminium-rich shale similar to Hanover Shale from western New York Devonian Catskill Delta USA discussed above. Further along there is a shale with "Staithes mudstone" section. This contains grey coarsening up mudrock. The section includes good systematic alternation and

variation of physical features. Access is limited and only via low tide but then out onto a wide foreshore.

Figure 52 Straiths

A key factor in rejecting the Staithes coast are that this localities is a National Heritage type of sites; one cannot "legally"/justifiably walk off with several large blocks for a comprehensive sampling, experimental measurements programme. This was/is also true for the KCF locations of Kimmeridge Village, Skye, Helmsdale

3.4 W. New York Devonian Black Shales

Our analogue selection for a case study with ample field scale outcrops that preserve a range of fractures and all portions of the stratigraphic section is the Upper Devonian Dunkirk and Rhinestreet black shales sequence of western New York (Fig. 1). This is complemented by data and samples from boreholes and smaller outcrops of the Middle Devonian Marcellus black shale sequences in central New York. These Devonian sedimentary rocks were deposited in marine basins in the hinterland of the collided Taconic and colliding Acadian orogens. Erosion of these massifs shed sediment into these basins, the distal portions of the 100's km broad Catskill delta. A combination of eustatic changes and flexure of the Laurentian lithospheric margin due to the increasing load of the progressively advancing overthrusting Acadian block that caused (1) growth and step-wise migration of displacement on "escalator" faults that bounded basins, and (2) progressive migration of the flexural lithospheric forebulge through the basin areas all resulted in the repeated alternation of anoxic with semi-anoxic chemistry in the basins. This engenders the presence of cyclical facies of basal black shale overlain by grey shale (Lash and Blood 2004, and authors cited therein). Such architecture is crucial to the mechano-stratigraphy during the subsequent geologic history, and moreover highly analogous to reservoir-seal architecture in Europe's primary CO2 storage targets in the North Sea.

Local USA geological nomenclature uses "shale" for much of the NY Devonian case study analogue rocks. This term seeks to integrate a realm of grain size (fine silt to mud) and structure (laminated). Comparison using standard geology criteria (e.g. petrography via low-powered transmitted light microscopy) confirms that "black shale" is largely synonymous with the UK term "mudrock", whether laminated or non-laminated. The shale classification of Lundegard and Samuels (1980) is based on silt abundance and fabric and the NY Devonian laminated shales would be termed mudshales and the non-laminated fine-grained deposits termed mudstones. However, in order to remain consistent with the local terminology as used in literature, the term shale is kept for the NY Devonian rocks.

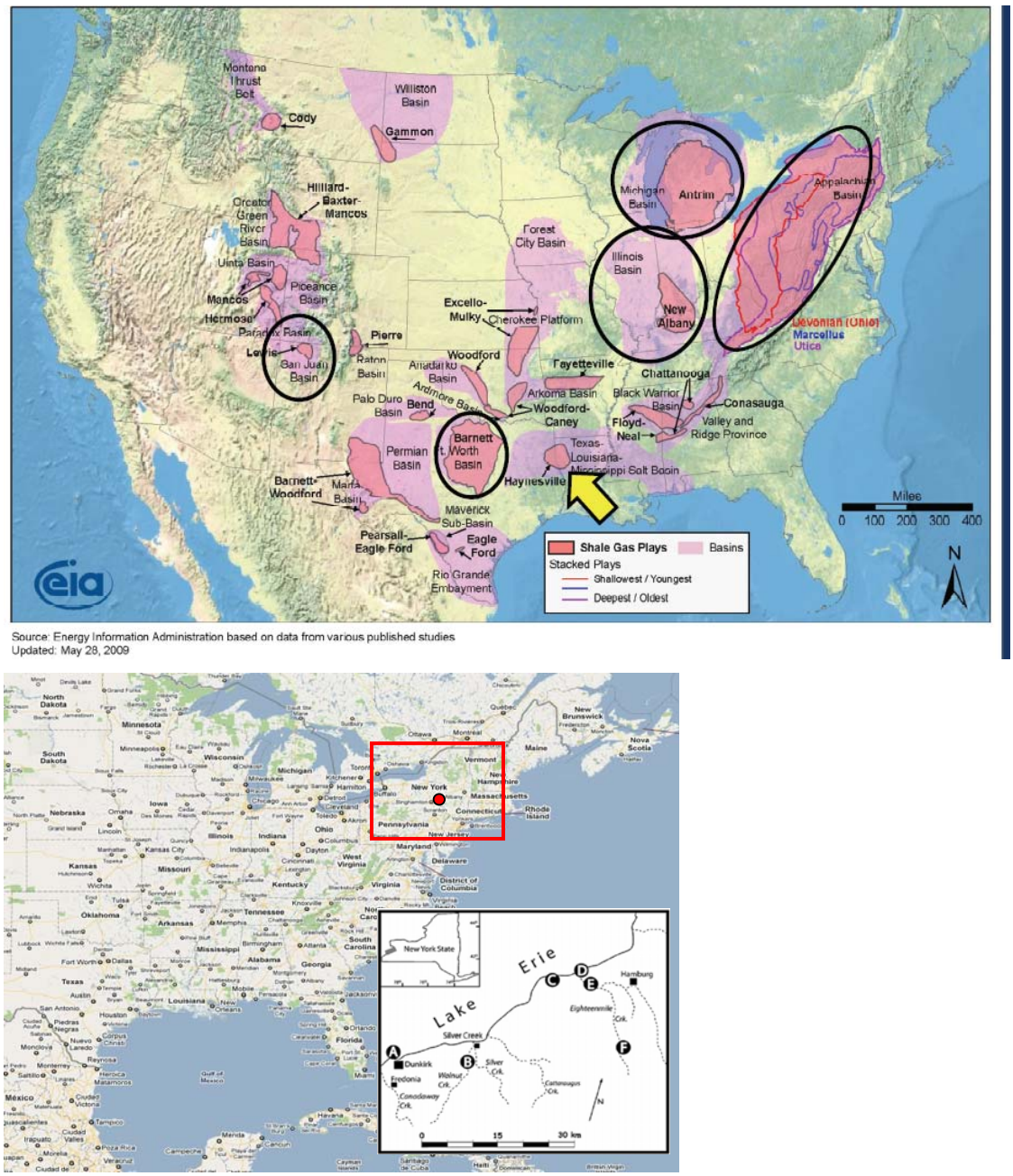

Source: Energy Information Administration based on data from various published studies
Updated: May 28, 2009

Figure 53 Location maps of outcrop region for analogue case-study in western New York (NY). Red square is location of inset-in-inset showing New York State. Red dot in main fig shows approximate realm of central New York outcrop and borehole areas for Marcellus. Area labelled A on Lake Erie inset is Point Gratiot shoreline outcrop sequence of Dunkirk Black Shale. (External sources: Google Maps; Lash & Blood 2004)

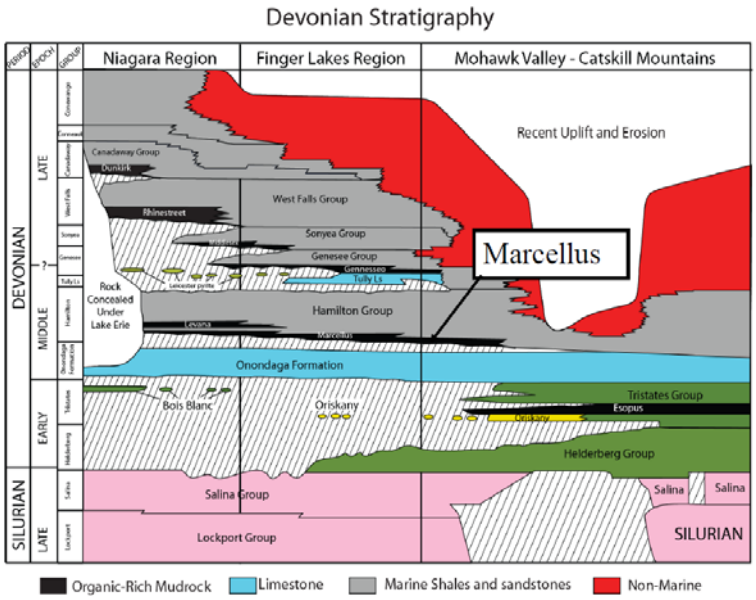

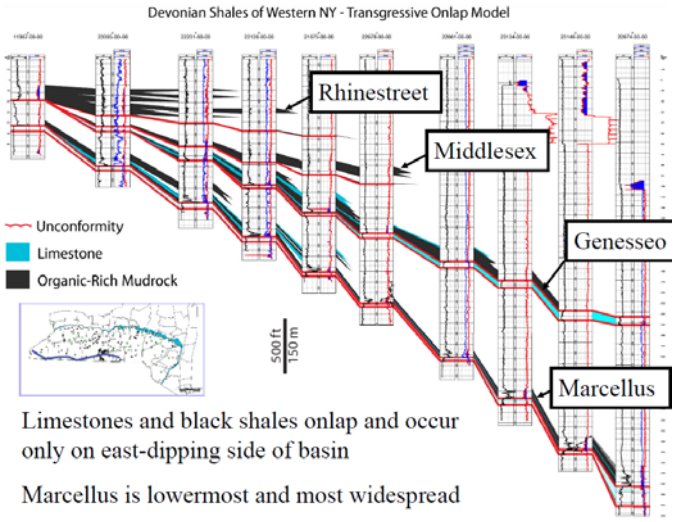

Figure 54 Overview of NYS Devonian Catskill Delta (both images after Smith et al. date - AAPG, etc)

3.4.1 Natural hydraulic fractures arrested by Dunkirk Black Shale

The Dunkirk Black Shale overlies the Hanover Grey Shale. Across much of western New York, most strikingly where these rocks outcrop along the Lake Erie shoreline of Chautauqua County, New York, USA, is a suite of N- to NNW-oriented (hereafter: J0) fractures in the Hanover Grey Shale that are markedly arrested as they enter the base of the Dunkirk Black Shale.

These are joints (i.e. fractures with no significant displacement) that are thought to have formed very early in the rock history, before complete dewatering and full diagenesis of the Hanover Grey Shale. The Dunkirk shale is thought to have acted as a seal to fluids migrating upward through the immediately underlying more permeable and porous (Fig. 5 intensely bioturbated, rarity of primary structures) Hanover Grey Shale during the early phases of the Alleghanian orogeny. This is due to the black shale's very low permeability of the, high-total-organic content (TOC), strongly aniso-tropic, bedding-parallel micro layering structured by tightly-packed, fine-grained clay platelets. The J0 fractures are thereby thought to be natural hydraulic fractures related to local over-pressuring in the Hanover Grey Shale due to differential compaction upon rapid burial that was subsequently triggered to fracture (Lash et al 2004). In this scenario, the local stress difference (of the deviatoric stress) is at one point slightly enhanced so that the magnitude of local minimum stress momentarily is lower than the

ambient pore pressure resulting in hydraulic fracturing. This model is consistent with the observations that the J0 fracture suite are very long (100's m) relative to height (3-10 m) and spacing and restricted to the upper 30% of the Hanover Gray Shales. Such hydraulic fractures theoretically should be common but are indeed very rare in nature. This highly fortuitous outcrop sequence is therefore being used by us as a case study analogue.

Crucial to THMC coupled processes modelling is the observation that J0 fractures are arrested (i.e. stopped) by the black shales; "plastic accommodation" as a strain recovery mechanism takes over in the black shales' strongly anisotropic clay fabric instead of elastic fracture response in the underlying grey shales. This mechano-stratigraphic isolation of hydraulic fracturing to the benefit of the reservoir rock (increase in permeability) whilst not to the detriment of the seal would of advantage in the storage of CO2.

J1, as opposed to J0 is part of a later (and cross-cutting) regional joint suite that is well-established as generated in the main phase of the Alleghanian orogenesis. This is ubiquitous throughout the rock sequence. Although there is some mechano-stratigraphic influence on the expression of J1 this is expected and moreover, is commensurate with >1000 km orogen-wide Alleghanian joint development and is commensurate with established joint development theory as a whole.

3.5 Initial Steps for the Evaluation of the Marcellus Fractures

A series of New York State Geological Survey maps were obtained. Topographic maps were used and digitised for key-georeference points as a basis for satellite imagery interpretation of remotely visible joint sets below the lake shore line. Satellite imagery attempted procurement (see appendix) indicated no commercial material available at higher resolution than GoogleMaps from Google Corp.

3.5.1 Marcellus potential

As part of an initial collaboration with New York State Geological Survey's Taury Smith and Jim Leone, the Beaver Meadows No.1 borehole core was offered but not used in the end. Although there was seen to be potential value in sampling "at depth' black shale with presumably characteristic vertical variation assemblages (and ultimately something equivalent to the discriminable microfacies patterns for the East Brae KCF, see below), the borehole would have single data point in a regional model with otherwise limited surface constraints (shore line and a couple of river creeks).

The Middle Devonian Marcellus Black Shale is extensively studied throughout New York and neighbouring states due to its potential contribution for longer term US national energy security through gas extraction. It is established as cap rock-like material that is locally very organic-rich. We sampled in several outcrop locations in central NY State and secured access to the Beaver Meadows No.1 borehole recovered core as well as a comprehensive suite of well-logs and down hole and lab data. Ultimately, the inaccessibility of the Marcellus, the limits of available borehole data turned attention to Lake Erie shore outcrops of the Hanover and Dunkirk Shales.

Figure 55 Tracing of Gratiot Pt Fractures on Corel georeferenced base map

Figure 56 Marcellus at NY rt20 road

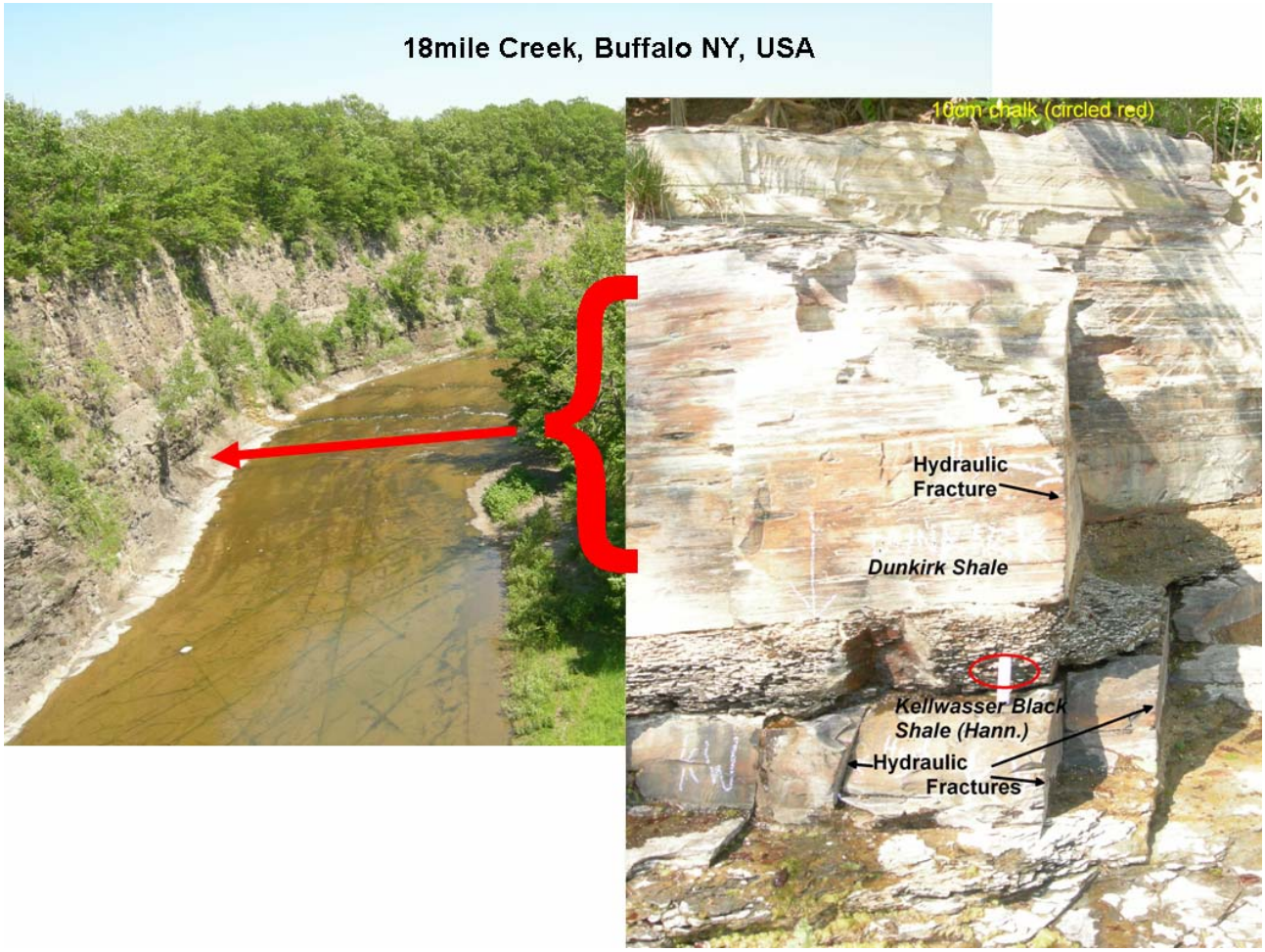

Figure 57 Marcellus Western NYS

3.6 Analysis of the fractures in shales of the lake Ontario shore near Dunkirk, NY

3.6.1 Method

The fractures were mapped are a set of lines using Google Earth. The result was saved as a .kml file. Subsequently, the .kml file was converted into a shapefile format recognized by the ArcGIS software. The conversion was carried out using the Geospatial Data Abstraction Library (http://www.gdal.org/) and the command kml2shp.
Also, for ArcGIS I have obtained:

- Geological map of the New York state from the USGS website (http://mrdata.usgs.gov/geology/state/state.php?state=NY);
- Satellite imagery of the mapped area from Google Maps.

Figure 58 Satellite image of analogue fractures

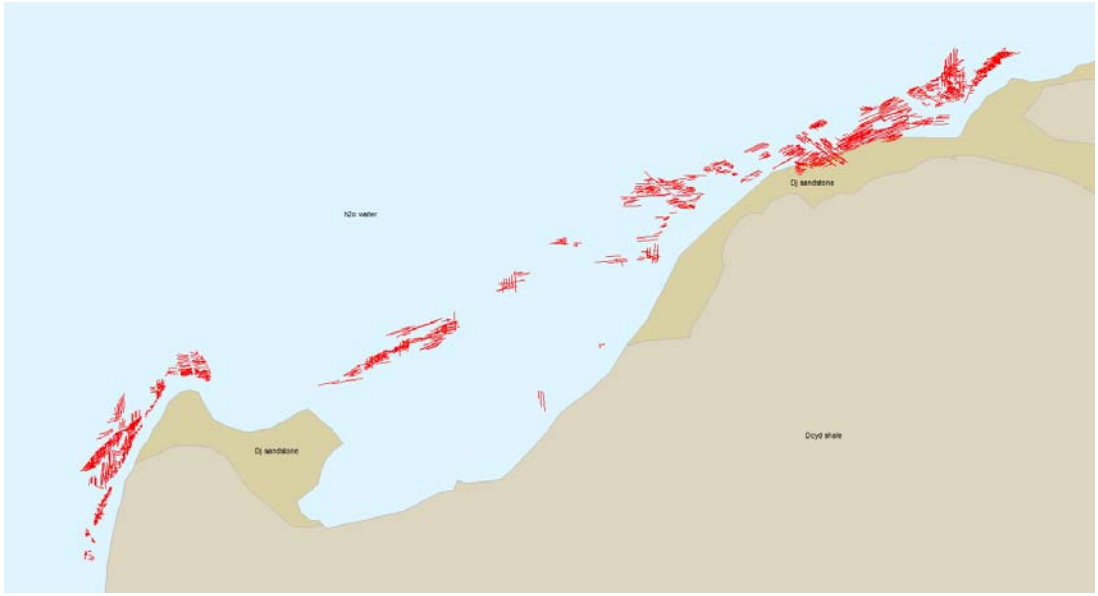

Figure 59 Fractures picked for analysis

Figure 60 Division of area into sections

Analysis done using ArcGIS

Projections and georeferencing

The geological map was uploaded with the geographic coordinate system North American Datum of 1927. The polyline shapefile converted from the .kml file was automatically plotted on the projection of the map. The original shapefile was using WGS 1984 projection and had to be projected to the NAD 1927 UTM Zone 18N to make the analysis possible (Arc Toolbox -> Data Management Tools -> Projections and Transformations -> Feature -> Project). The Google satellite imagery was georeferenced with the use of the fractures already in place. As a result the match of the fractures and the satellite imagery is very good. The mismatch of the geologic map and the fractures results from the low resolution of the geologic map at the resolution of our fracture mapping.

3.6.2 Calculations

The analysis performed using ArcGIS software included:

- Lengths of the fractures;
- Orientations of the fractures;
- Intersections between the fractures.

Calculating the lengths of the fracture lines was performed with an internal function of ArcGIS that requires that the data are using projected datum.

- Attribute Table of the polyline shapefile -> Add Field (length)
- for the new field -> Calculate Geometry -> Length, set Units to meters

Calculating the orientations of the fractures:

- Attribute Table -> Add Field (X_start)
- for the new filed -> Calculate Geometry -> X Coordinate of Line Start, set Units to meters
- repeat the above 2 points for: X Coordinate of Line End, Y Coordinate of Line Start and Y Coordinate of Line End
- Attribute Table -> Add field (azimuth)
- For the new field -> Field Calculator -> enter the formula to calculate the azimuth from the start and end point coordinates

Calculating the intersections between the fracture lines: this was done using the Spatial Analyst:

- In the projected polyline file -> Add Field (line_id)
- For this new field -> Field Calculator -> line_id = FID
- copy the polyline shapefile and add the copy to the map
- Arc Toolbox -> Analysis Tools -> Overlay -> Spatial Join
- In Spatial Join window set the projected polyline shapefile as the Target Features, set the copy of the projected polyline shapefile as the Join Features, select JOIN_ONE_TO_MAY in the Join Operation, set Match Option to INTERSECT and set Search Radius to 1 m
- Each row of the output file of this operation represents one intersection of the fracture lines, and there are 2 columns with the line_id entries for the intersecting lines
- Export the data to Excel for further analysis, Attribute Table -> Options -> Export -> All records

Since there was a considerable variation in the prevailing orientations of the fractures along the shore, further analysis was made on sections of the shallow lake area along the coast. Shale outcrop were divided in 5 segments and all analyses were conducted for the segments.

Concerns

There might be a bias in the analysis towards shorter fractures. Sometimes the topology was probably obstructing the fracture and it was not drawn continuously over the obstacle. In these cases one long fracture was represented in the analysis by 2 shorter fracture lines.

3.6.3 Dunkirk shale fractures – spacing analysis

For each of the fractures in one of the 10 azimuth groups (2 groups per each section) the distance to the nearest non-intersecting fracture was calculated in meters and for each of the 10 groups statistics were derived.

ArcGIS recipe

The projected fracture shapefile was spatially joined with the sections polygon shapefile so as to get one shapefile with all fractures including the information to which section they belong:
Right click on the fractures shapefile -> Joins and Relates -> Join
In the window select "Join data from another layer based on spatial distribution"
Choose the sections polygon shapefile as the layer to join
Select the second button and choose to give the sections attributes to fractures on the basis of them lying WITHIN the sections.
Divide the resulting output shapefile based on the different sections and azimuths (10 shapefiles resulting). For each of this files perform the following workflow:
ArcToolbox -> Analysis Tools -> Proximity -> Generate Near Table
Input Features -> select one of the files
Near Features -> select the same file (correlating with itself)
unselect Find Only Closest Feature and set the Maximum number of closest matches to 2
The table will the created in the .dbf format which is readable by excel.
On each of the resulting tables that include the distance of a given fracture to the 2 nearest fractures calculate the average, median and standard deviation for the non-zero distances (this eliminated the distances between the fracture and itself as well as intersecting fractures).
The result of the statistics is presented in Table 18.

Table 18 Fracture statistics

	Number Of fractures	Mean spacing in meters	median	stdev
section 3, azimuths range 60 to -60	241	3.316849	2.587067	2.448558
section 3, azimuths range -60 to -10	74	5.461316	4.789756	3.042735
section 2, azimuths range -20 to 30	77	9.951296	5.170016	11.39079
section 2, azimuths range 50 to -60	242	3.59189	2.823221	2.870277
section 1, azimuths range -10 to 20	195	3.853296	2.916319	4.719795
section 1, azimuths range 40 to -50	396	2.872489	2.133341	4.115423
section 0, azimuths range 60 to 90	117	2.52916	1.95078	1.887813
section 0, azimuths range -70 to -40	46	3.593456	3.692238	1.640183
section 4, azimuths range 0 to 40	35	5.863998	4.683412	4.797966
section 4, azimuths range 70 to -30	258	2.365909	1.88785	1.940143

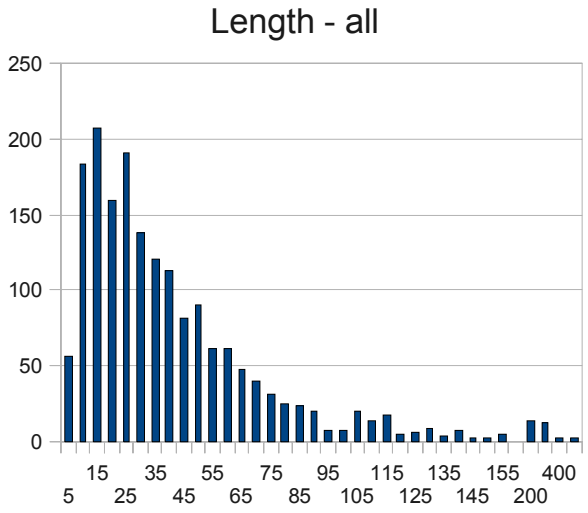

Figure 61 Length distribution of all fractures measured

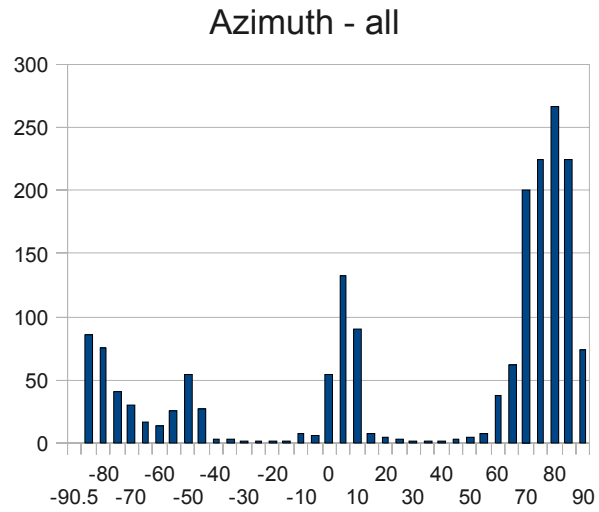

Figure 62 Azimuth of all fractures measured

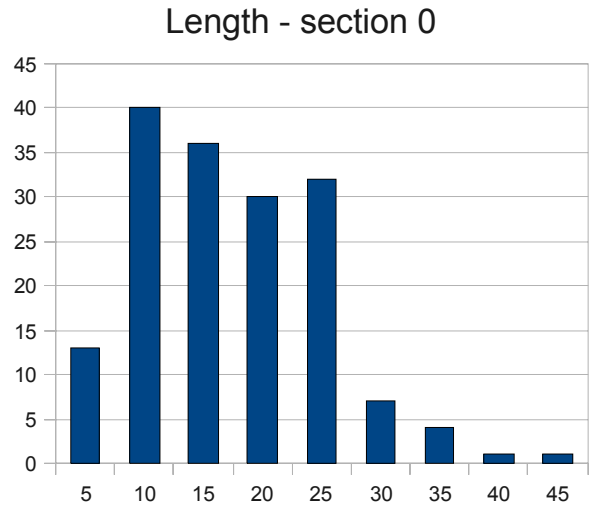

Figure 63 Length of fractures in section 0

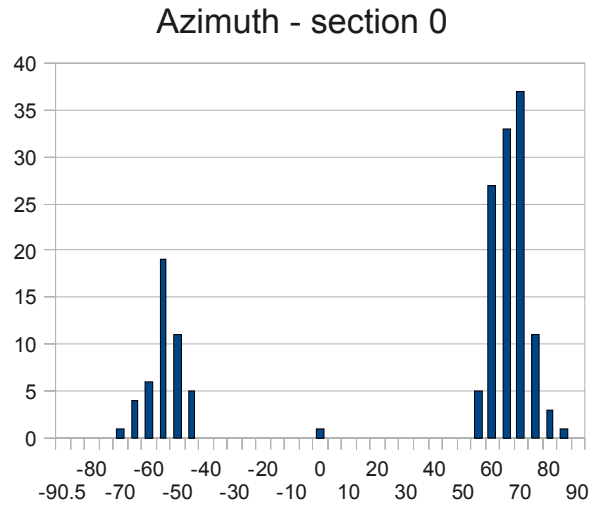

Figure 64 Azimuth of all fractures in section 0

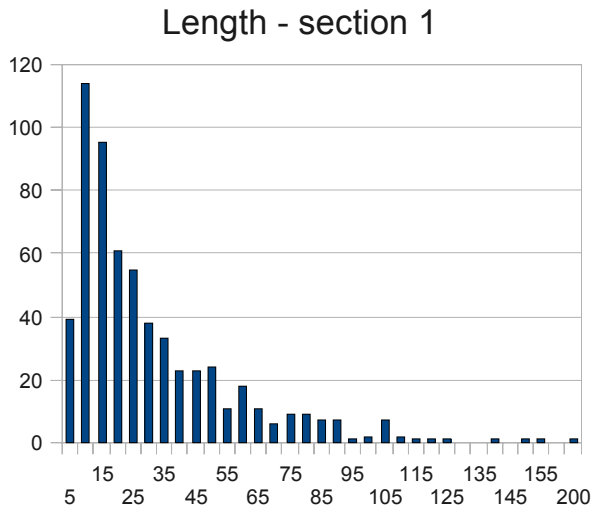

Figure 65 Length of all fractures in section 1

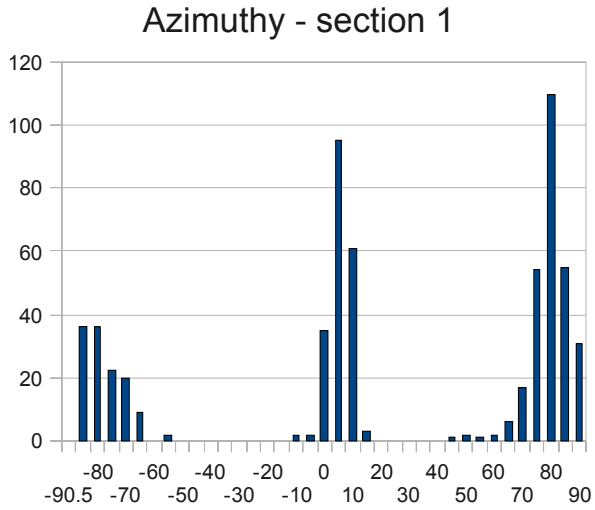

Figure 66 Azimuth of all fractures in section 1

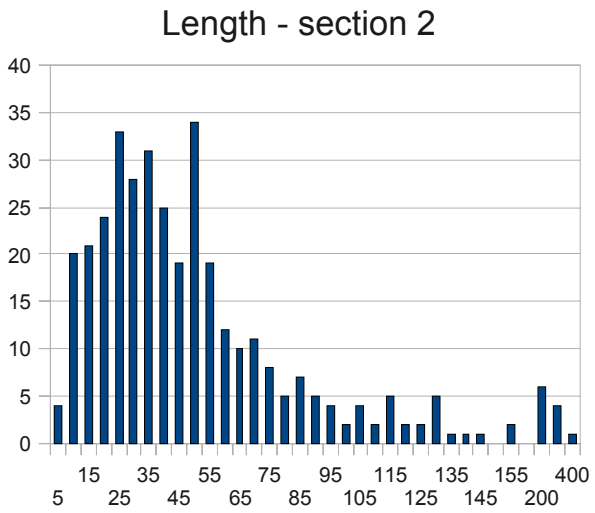

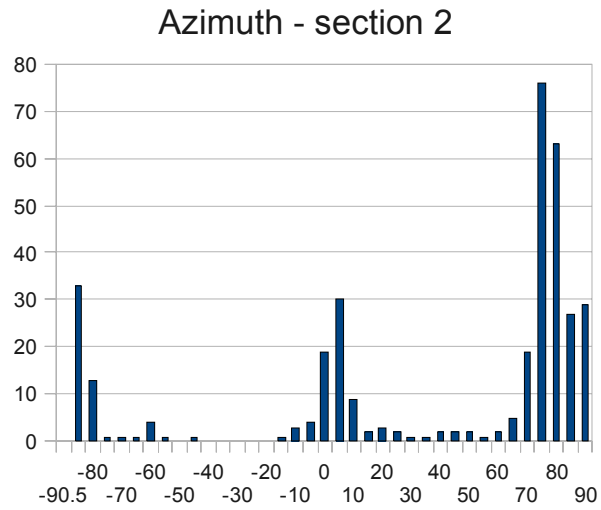

Figure 67 Azimuth of all fractures in section 2

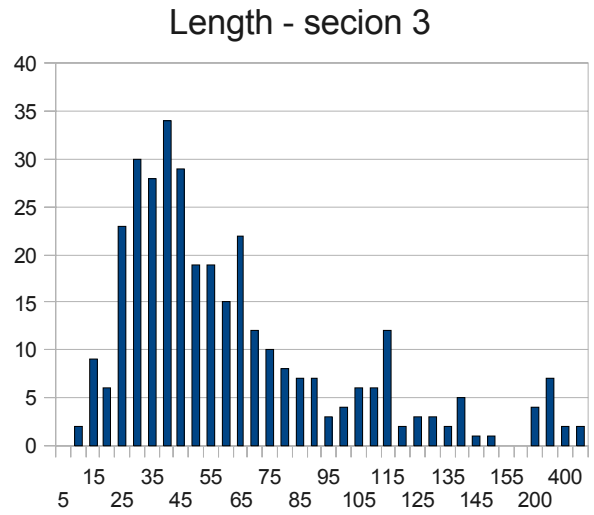

Figure 68 Length of all fractures in section 3

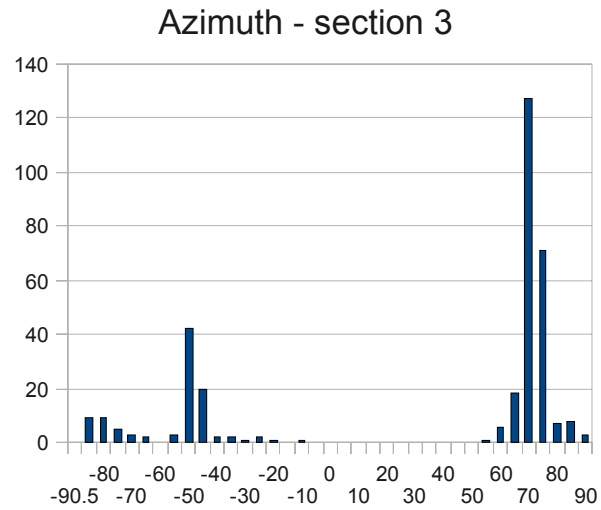

Figure 69 Azimuth of all fractures in section 3

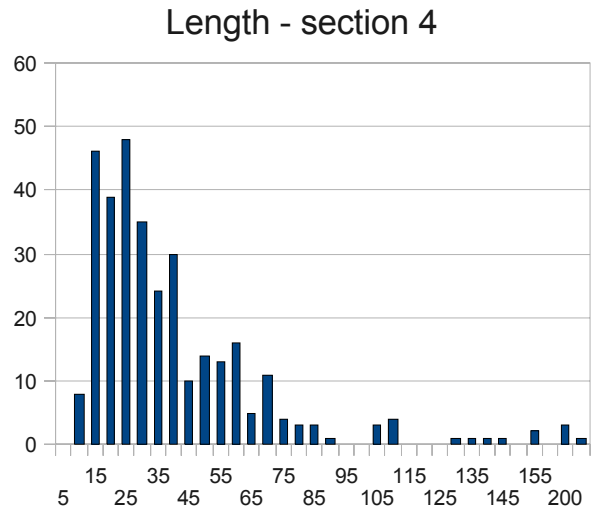

Figure 70 Length of all fractures in section 4

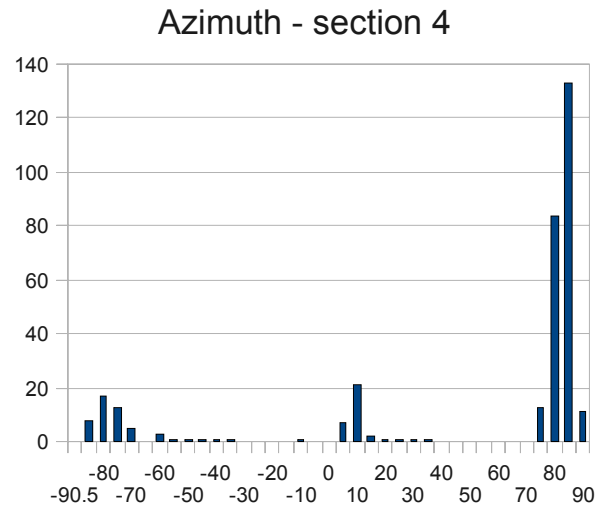

Figure 71 Azimuth of all fractures in section 4

3.7 Kimmeridge Clay Formation

The KCF is present in the North, Central and South Brae fields. These are located ca. 200 km offshore from the UK in the area of the Viking Graben in the North Sea (Fig 6). Reservoir rocks commonly comprise sedimentary fan sequences shed off higher ground to the West; the up thrown blocks of the western half graben suites of the Viking Graben system (Fig. 7). Widespread deposition of mudstone facies provides an effective seal in the form of the overlying Kimmeridge Clay Formation and, ostensibly, in fault zone rocks due to clay-reworking and/or clay-alteration (Abbotts 1991).

Age: rather than Kimmeridge Clay age, the local Kimmeridge Clay Formation is late Oxfordian to late Volgian or even locally Rhyzian in age (wellside geologists' core log notes as refs).

3.7.1 Motivation

Initially motivation was lead by the need for supercritical CO2 experiments with ancillary characterisation of North Sea field to underpin experimental programme. KCF in the UK on- and offshore is widespread.

3.7.2 Initial onshore screening for suitable KCF

For the Kimmeridge, onshore outcrops were considered:

Kimmeridge Bay in Dorset

Kimmeridge Bay in Dorset on the English South Coast (below photo) is the type locality for the Kimmeridge Clay Formation. Many descriptions of fracture suites from this locality exist. Distance from Edinburgh is large and transport of samples potentially high. Most crucially, sample availability is severely hampered due to the fact that this is a UK National Heritage type of sites where one cannot "legally"/justifiably walk off with several large blocks.

Figure 72 Kimmeridge Bay, Dorset

North Skye

The Kimmeridge Clay Formation outcrops on North Skye (below photo). Distance from Edinburgh is 4-6 hours and transport of samples straightforward. Outcrop quality is of reasonable size but poor (limited continuity of outcrop, rocks are quite weathered). Again, National Heritage type of site.

Figure 73 North Skye

Helmsdale, Sutherland

The Kimmeridge Clay Formation is locally present near Helmsdale on the east coast of Sutherland, in the NE of Scotland. Distance from Edinburgh is 3-5 hours and transport of samples straightforward. Outcrop quality is very limited and rocks are quite weathered. Again, National Heritage type of site.

Figure 74 Helmsdale, Sutherland

In all three above cases, burial depth is assumed to be significantly less than the 3-4 km of the Viking Graben, North Sea.

Initial offshore screening for suitable KCF

Suitable offshore opportunities for KCF are primarily in the North Sea major graben and their basins.

The South Viking Graben is the northern arm of the North Sea triple rift system. It is a half-graben that is fault-bounded to the west against the basement of the Fladen Ground Spur (Figure 75). The graben floor rises gently eastward to. The eastern margin is defined by smaller northwest-southeast trending faults. Mid-Upper Jurassic crustal extension across the graben (3-5%) led to further basin growth, as well as propagation and linkage of planar normal faults through the rift interval. In the Late Jurassic, extension rate reached a maximum and uplift of the footwalls of the extensional faults led to pronounced erosion, providing the source for the Brae Fmn (see below) via Upper Jurassic submarine fan systems were concentrated at the western graben margin and controlled by the very rapid syn-depositional

subsidence. The KCK is thickest and most continuous where the fans become thinner and finer-grained away from the western margin faults.

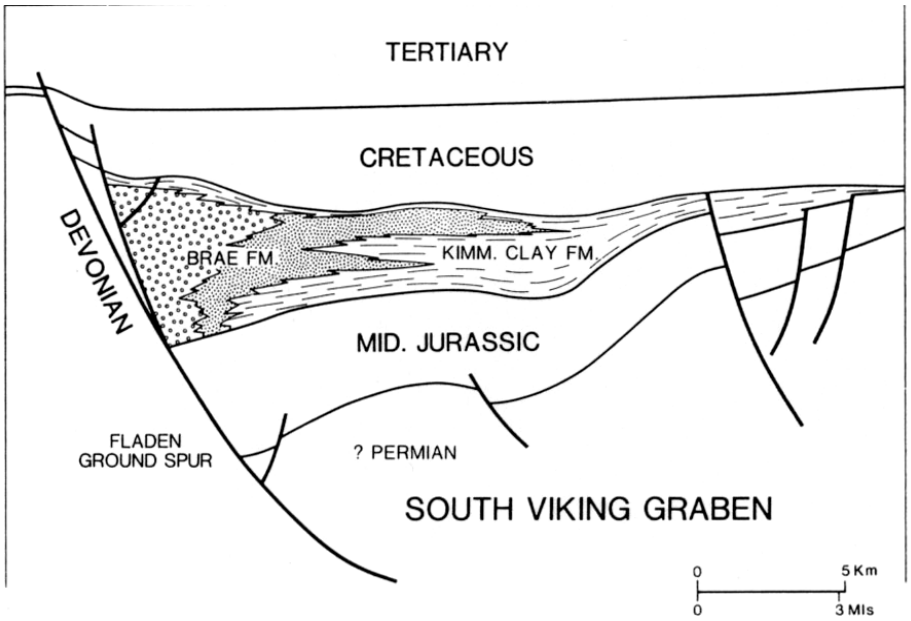

Figure 75 Conceptual cross section of South Viking Graben

The Kimmeridge Clay Formation acts as both source rock and seal for the hydrocarbon accumulations in the South Viking Graben. It usually overlies and underlies, and interfingers with, Brae Formation reservoir sandstones (Figure 75). KCF was deposited as "background" sedimentation in deep water anoxic environments during regional rifting and subsidence in the latest Jurassic. This lead to the deposition of organic-rich mudrocks. The characteristic 'black' shales interbedded with thin sand/silt beds in the most of the graben areas of the North Sea. The Miller and the Brae North Sea Hydrocarbon Fields were the main KCF alternatives here for UEDIN.

This complex of oil and gas condensate reservoirs in the Upper Jurassic Brae Formation sandstones was discovered in the western margin of the fault-bounded South Viking Graben in the early 1970s. The North Brae, South Brae and Central Brae Fields are located along the graben margin in UK block 16/7a. The East Brae Field sits further north in block 16/3a and 16/3b. The Miller Field is situated more basin-ward in the adjacent blocks 16/7b and 16/8b.

Partly hitherto established UEDIN work exists in the UK sector of the Viking Graben, primarily for the Miller Field. Unpublished, unprocessed data from SCCS work has been obtained from here for the reservoir rocks. However, for Miller Field no agreement existed with field operators (mainly BP) within the framework of Mustang.

Within UK sector drilled and cored oils and gas wells, one third (ca. 3 cm width - the so called "slab-backs" backs of the 10 cm wide original core) of all core obtained by operators is passed to UK authorities for archiving and stewardship. This stewardship role is currently undertaken by the British Geological Survey. Up until 2010, most core contained in the national UK archives was housed 1 km away from UEDIN's own labs (Gilmerton, Edinburgh). We initially considered the possibility of just using British Geological Survey core store (3cm slab-backs) for all North Sea KCF instead of going to Marathon (or other operators such as BP, etc.). We ultimately rejected this idea due to the strong nature of the Marathon offer (see below) that would meet the project objective of as large as possible coreplugs (38 mm sub cores, cored from the main 10 cm deep drilled core). In particular, the need to obtain natural fracture-bearing, intact 38 mm cores was a driver in this decision.

The decision was then made to further consider Brae Field operator Marathon.

3.7.3 The Brae Hydrocarbon Field, North Sea, UK sector

North Sea operator Marathon Oil UK was approached as part of the Mustang project and a successful agreement established. The Brae Field has been extensively developed by Marathon Oil UK Ltd. Marathon. Key fields here for which Marathon in principle hold data and borehole cores include South, Central, North, West and East Brae and Beinn. Adjacent to Brae (and nearby Miller) are also Kingfisher and Balfour.

3.7.4 Initial requests to Marathon UK

Part of our target data use (for THMC modelling) from Brae KCF is physical samples for the experimental investigations from precisely-quantified intervals in mud-silt successions to obtain a sample of representative portions across the spectrum of KCF compositions. Marathon Oil UK, as a Mustang partner, generously agreed to provide data records (maps, well logs) and physical samples (cuttings, recovered core) of the Kimmeridge Clay Formation for the various Brae fields. Typically more core, or core whose depth interval encompasses significant height of rock above the target reservoir (i.e. caprock), is obtained from appraisal and engineering wells than later production and any injection wells. This is due to the position that, early in the development stages of a hydrocarbon field, there is less confidence in the location of the operator's target formations. Coring is expensive and operators have no interest in obtaining caprock core; Kimmeridge Clay Formation is THE caprock to all the reservoir rocks of the Brae and Miller system.

By researching & data processing proprietary digital logs databases (typically data from Marathon or the CDA database, see below), we identified archived cores of existing registered (logged with UK authorities) boreholes appropriable via Marathon that met our initial screening filter-criteria for KCF-intercepting depth interval portions of sufficient magnitude and sufficient mud:silt ratio. The UK national core archives (British Geological Survey) also enabled us to identify exact core depths:

Initially scoped Kimmeridge Clay – Core Possibilities – From Marathon Brae well logs UK North Sea block 16/07a (South Brae)

16/07a-8:	Core 4	12250 – 12350	(shale within sandstone)
16/07a-8:	Core 6	12400 – 12446	(shale within sandstone)
16/07a-14:	Core 1	11906 –	11964
16/07a-11:	Core 1	12622 –	12645
16/07a-10:	Core 2	12660 –	12731
16/07a-7:	Core 1	12172 – 12249	(upper shale member not directly Kimmeridge Clay)

Marathon senior geologist Colin Turner and Roger Connel (now retired) provided information that core for East Brae field was in Aberdeen while, being the youngest (late eighties - early nineties, albeit still mature with respect to production) the quality of log records was likely to be superior to the late seventies - early eighties logging and recording technology in service for much of the other Brae fields.

We thus made the decision to focus on obtaining sample and data from East Brae. This ultimately led to our 3D caprock model.

3.7.5 East Brae geological background

East Brae is part of the Brae group. East Brae is an Upper Jurassic (Brae Fmn) gas condensate field in the South Viking Graben. The overall structure is that of a faulted anticline developed due to regional tectonics. Sediments were deposited from the south and west, through a 5-10 km long submarine canyon largely bought in as high density turbidity currents. The East brae sub basin structure was formed by basin inversion from back rotation of the main N-S governing normal faults (e.g. master fault to Fladen Ground Spur). This caused a back dip of sediments above the erosional scarp, thus a hanging wall anticline was formed. Further inversions caused truncations, onlaps and growth sequences. Uplift in the late Jurassic caused thinning of the Upper Brae Sandstones and KCF across the crest. The result is a structural trap with four-way dip closure. The (much thicker) reservoir sandstones were "inserted" into the "background|" deposition of the Kimmeridge Clay Formation by rare but volumetrically dominating turbidity currents

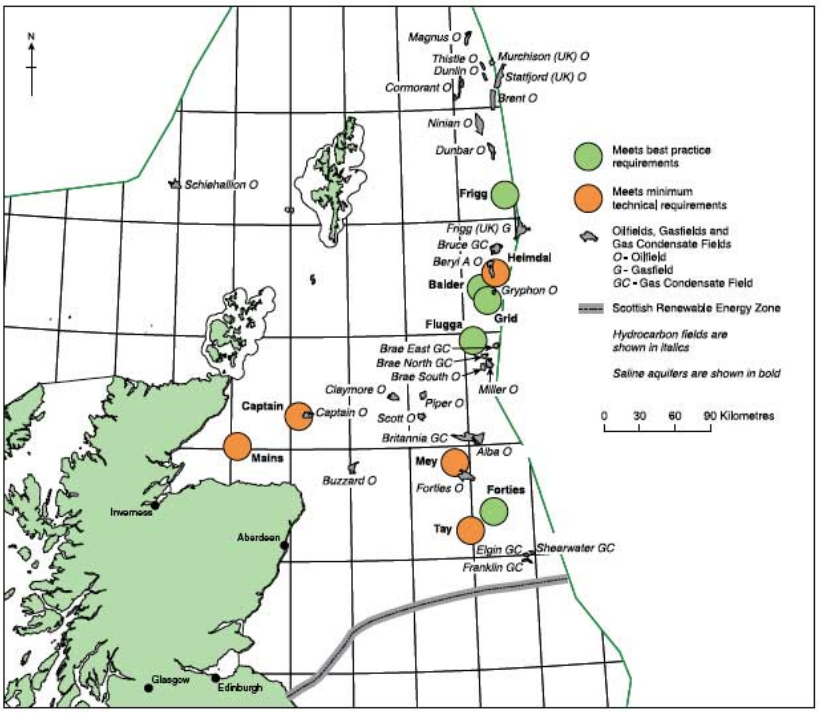

.

Figure 76 Location of selected North Sea hydrocarbon fields highlighting Marathon's operations, Source:

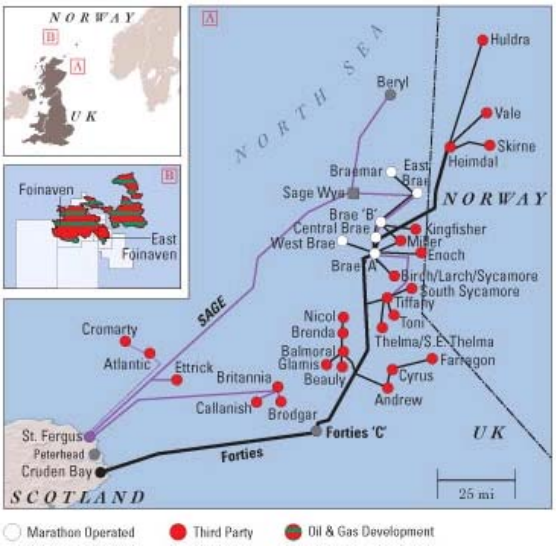

www.marathon.com/content/inline-images/marathon_com/maps/brae_2010.jpg

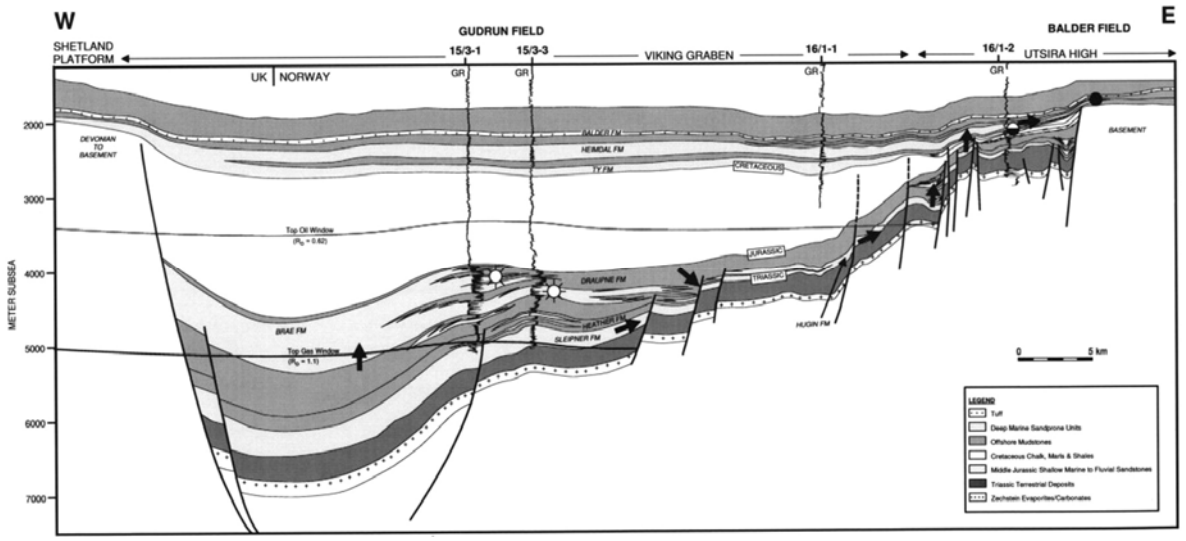

Figure 77 Geologic cross section across Viking Graben north of Brae. Source: www.marathon.com

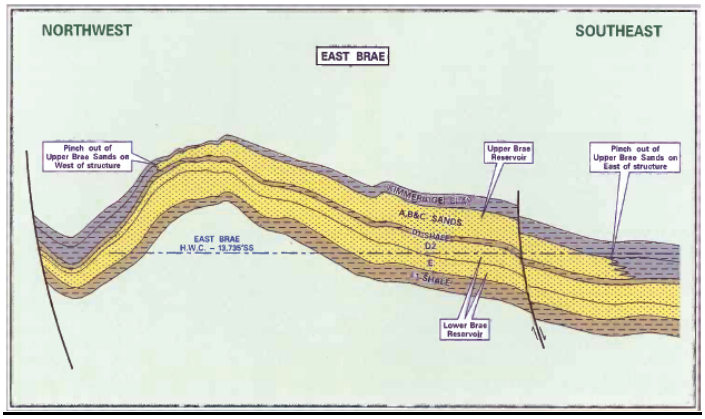

Figure 78 Geologic cross section across East Brae. Source: www.marathon.com

3.8 Development of a caprock model

3.8.1 Model build

A 3D caprock model for the E. Brae (North Sea hydrocarbon) field was developed. The model is underpinned by three reservoir-wide genetic units that use discriminable, repeating patterns wireline log signals. These genetic units were interpreted in well data throughout Brae field and interpolated to build a km-scale caprock architecture. In-situ cored samples provide material for laboratory based experimental investigation into THMC properties.

3.8.2 Geological Setting

The geological setting for the East Brae caprock model is that the lowermost seal consists of mudstones of the Kimmeridge Clay Formation (KCF). The model is underpinned by three reservoir-wide genetic units that use discriminable, repeating patterns - namely Genetic Units (GU) 1 – 3, within one main KCF sequence. Each GU shows a coarsening upwards trend that is observed within each of these facies marking the horizon surface. The thickness of the GU facies varies throughout the study area from <10 m at the domal tip to >50 m at the distal margins. It is noteworthy that both GU 1 & GU 3 pinch out at several points across the area. The Valhall Formation (VF) overburden mainly consists of marls, with some irregular layering of mudstones evident in three wells. The thickness of the VF marls ranges from 41-150 m, but averages around 110m (Johnson & Lott, 1993).

STRUCTURE: The structure of the caprock is a faulted anticline developed during the latest Jurassic and early Cretaceous in response to regional compression (Branter, 2003). Branter

(2003) suggests that the domal structure can be considered a hanging wall anticline produced above the eastern edge of the erosional scarp. Coward (1996) also notes that the inversion anticline is observed as an irregularly shaped anticline in 2D, with 'the western side of the dome' being 'relatively smooth and grading to a NE-SW trending syncline' (Branter, 2003, p 193).
FAULTS: The field is divided into three panels, resulting from two faults N1 & N3 (Branter, 2003). However, the model incorporated another major fault (N2), to give three faults that trend ESE - WNW.

3.8.3 Data distribution

A total of 38 wells were considered for this study in order to give a more complete understanding of the caprock structure. In addition, a secondary seal (VF) overlying the KCF was interpreted for 18 wells and included in the model.

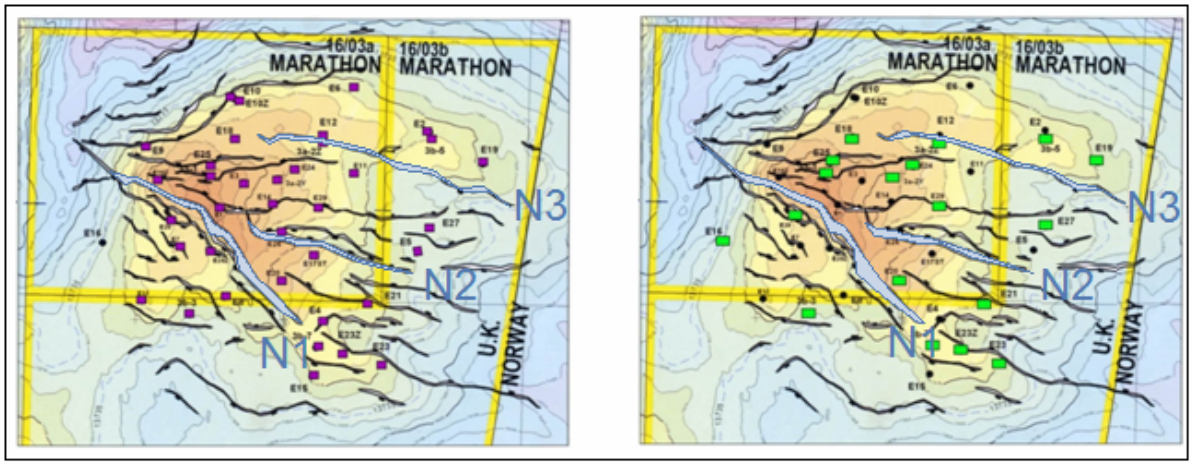

Figure 79 Map of the East Brae Field, UKCNS. (left) shows the number of wells (purple) used to discriminate the genetic units (GU's) within the KCF, (right) shows the well locations (green) used to map the secondary seal, Major Faults N1 – N3 are labelled in grey. (courtesy of Marathon Oil).

3.8.4 Core characterisation and sampling methods

Core availability was established for 16/3a-E1, 16/3a-E3 and 16/3a-E10. In the early project months, the sampling strategy as part of a comprehensive caprock model was as yet un-established. Initial visits to Marathon were mainly for those samples containing natural fractures for scCO2 and pilot lab analyses.

Drill core of the KCF caprock that was retrieved by Marathon (and its operators) from 30-40m of two of wells 16/3a-E1, 16/3a-E3 at 4-5 km depth. This core provides a sampling platform for lab analyses as part of our THMC characterisation. Forty samples (typically 2-5 kg, 5-15cm high) from the ca. 30 m available length of drill core were selected at regular intervals (30-60 cm spacing) locally adjusted to capture statistically representative heterogeneities (e.g. coarse-grained caprock seen as white bands). Samples taken are shown in the red boxes in the figures below. Core widths are 10 cm.

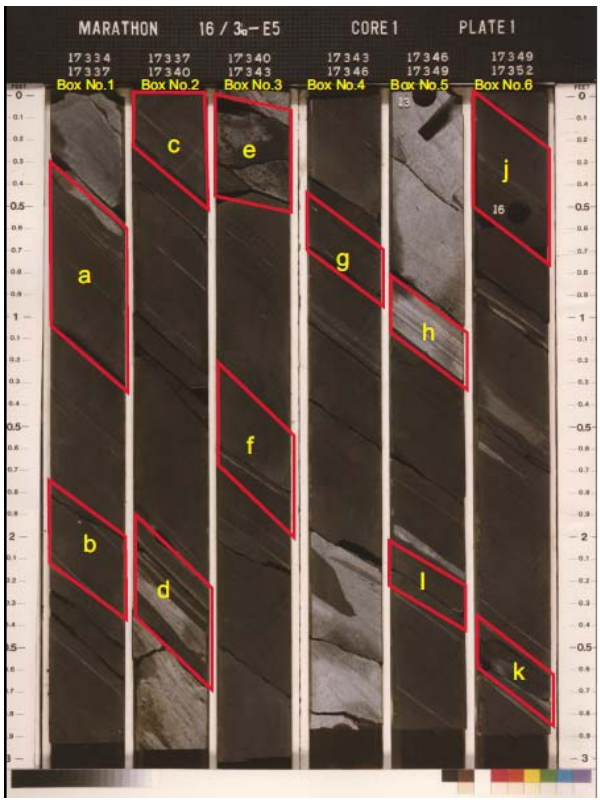
MARATHON 16 / 3α–E5 CORE 1 PLATE 1
17334 17337 Box No.1
17337 17340 Box No.2
17340 17343 Box No.3
17343 17346 Box No.4
17346 17349 Box No.5
17349 17352 Box No.6
a
b
c
d
e
f
g
h
j
k
l

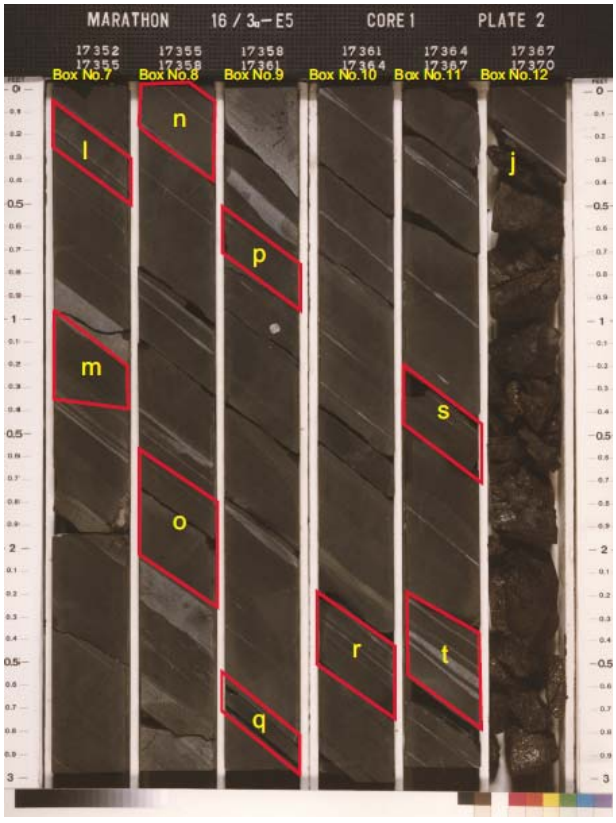
MARATHON 16 / 3α–E5 CORE 1 PLATE 2
17352 17355 Box No.7
17355 17358 Box No.8
17358 17361 Box No.9
17361 17364 Box No.10
17364 17367 Box No.11
17367 17370 Box No.12
l
m
n
o
p
q
r
s
t
j

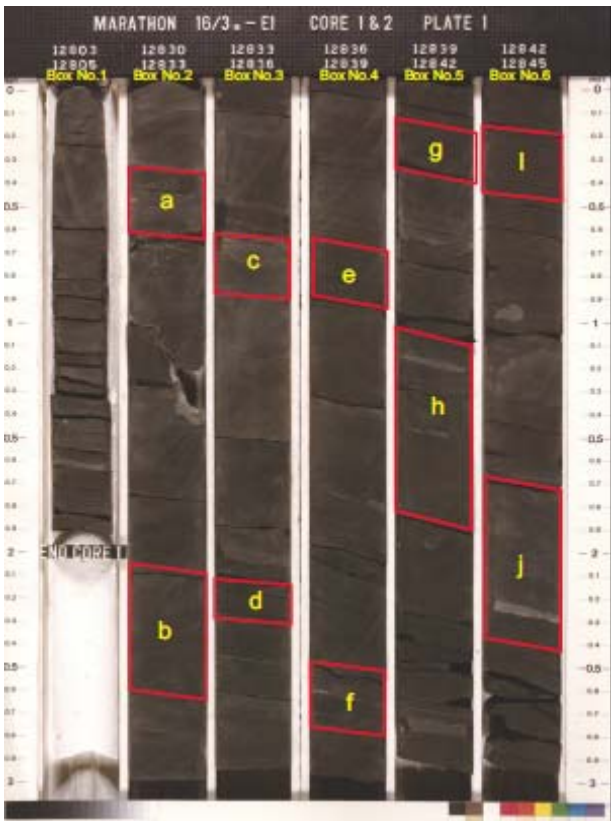

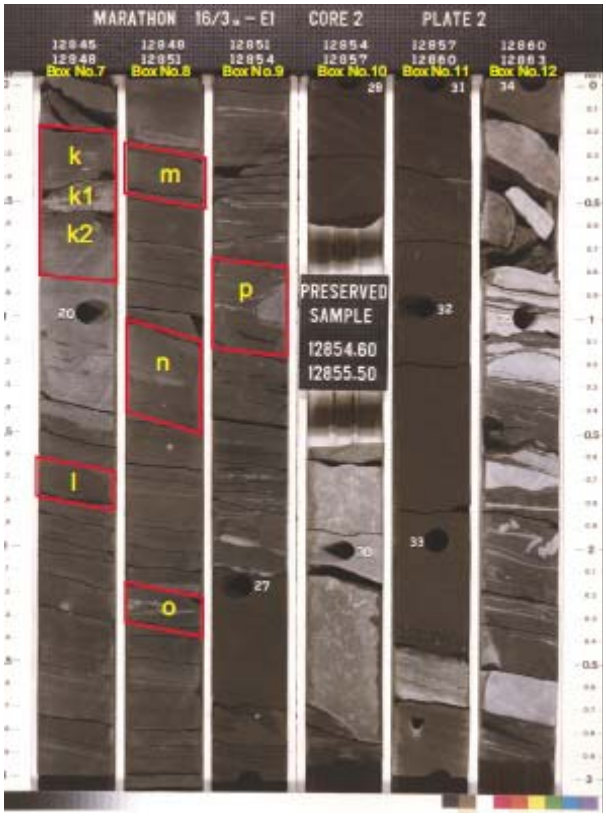

3.8.5 Microfacies

From the forty core sample blocks shown above for 16/3a-E1 and 16/3a-E3, five classes of visually discriminable banding ("microfacies") were established as the basis for THMC analyses to build a core sample architecture (see below figure)

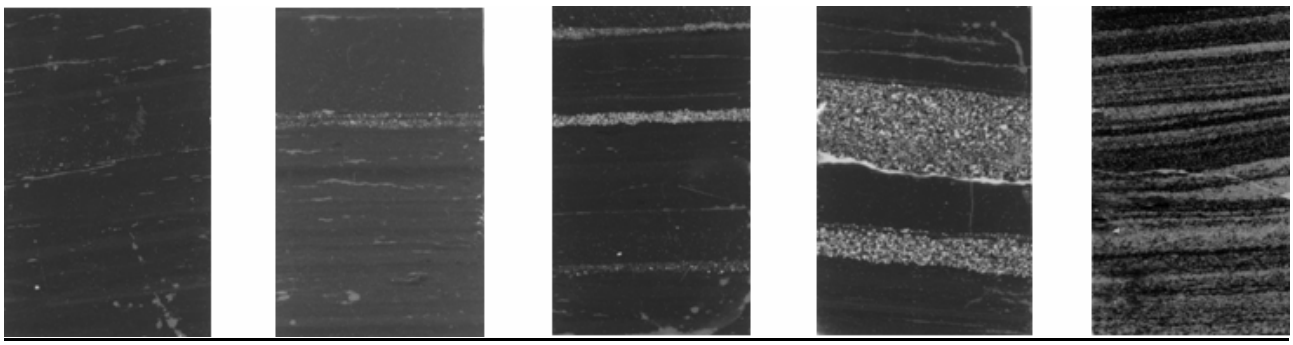

Figure 80 Each thin section is 20 mm wide. Microfacies classes shown are 1 to 5 left to right. Note banding frequency and distribution.

The robustness of this (initially) visual discrimination was substantially reinforced by subsequent lab analyses. These fives microfacies classes provide the basis for THMC analyses over six scaled steps from micron- to cm-scale. These THMC analyses include chemical: XRD, XRF, SEM-XD; mechanical: Image-J automated image measurement of [anisotropy of] porosity, desiccation crack restoration, SEM gather of plastic:brittle constitutive component ratios; integrated THMC: supercritical CO2 flux experiments at in-situ pressures), and others standard mineralogy.

These five classes of THMC-characterised microfacies were then used in a binning type approach (bins of 1 through 5 using a cm-scale linear graticule / 1D matrix) to classify the entire available length of core as the first step in upscaling to the reservoir architecture model build. This was then upscaled to the reservoir-wide genetic units grid (see above).

3.8.6 Laboratory analyses for caprock model

The principal laboratory techniques employed as part of analyses to populate caprock model with measured properties include: microscopy (SEM, energy dispersive X-ray), XRD, X-ray Tomography, and caprock integrity multiphase flow measurement via physical experiments.

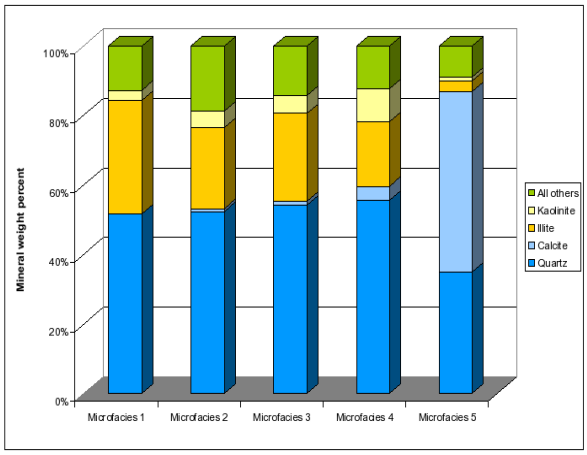

Figure 81 XRD results for different micro-facies within the East Brea Caprock

Repeat XRD analyses for suites of samples for the five classes of microfacies show key ratio variations between clay, calcite and quartz content. As part of the caprock model objective of characterisation and modelling of caprock integrity, strength is a key issue. In emerging shale gas literature the ratio variations between clay, calcite and quartz content are seen to be of considerable importance in caprock mechanical behaviour. Further supercritical CO2 multiphase flow measurements are presented in the experimental sections of this report.

3.8.7 Well Correlation Methodology

Our interpretation and correlation work used primarily scans of composite logs ranging from good (Figure 82) to moderate quality (Figure 73). Additional depth information was obtained

from geological and drilling reports. Once the targeted area (KCF) was selected from the logs, the next step was to look for wireline log signals that showed repeating discriminable patterns and to place them into groupings. These were subsequently classed into reservoir-wide architectural elements (GU 1-3), which were assumed to be conformable facies.

After the GU units were correlated, a database was constructed (see appendix 1) to record the True Vertical Depth (TVD) in ft of each GU as well as the top and bottom depth of the entire KCF unit. In this field, oil operators have drilled numerous wells off platform, resulting in major deviations. Therefore it was necessary to interpolate the GU depths. The interpolation technique used the gradient from the recorded depth at the top and bottom of the entire KCF unit for each well, to further reduce uncertainty in the results. Once the GU depths were recorded, these were converted into meters (m) to be consistent with Petrel modelling software.

3.8.8 Discriminating the genetic units

Three genetic units (GU 1-3) were interpreted within the KCF based on the petrophysical patterns from the gamma ray and resistivity logs. In several wells, neutron-density curves were available, and were used to discriminate GU 2 and GU 3. Table 19 describes GU 1-3 with their assigned log pattern and colour code.

Table 19 Three reservoir-wide genetic units were interpreted by analysing discriminable, repeating patterns in the wireline log signals.

	GU 1	Signal pattern found in most wells across E. Brae field. Shows a consistent coarsening upward trend towards the top of the KCF unit based in the gamma ray log and shows a low to moderate resistivity signal.
	GU 2	Distinguished by a slight resistivity increase; shows no coarsening upward trend, less oscillatory and separated pattern in the shallow to deep resistivity curves.
	GU 3	Defined by a higher resistivity signal compared to GU 2, and a less separated response from the resistivity curves; also displaying a similar pattern in the neutron-density logs where available. The gamma ray log was not used to distinguish between GU 2 and GU 3 as they show a similar pattern in most wells.

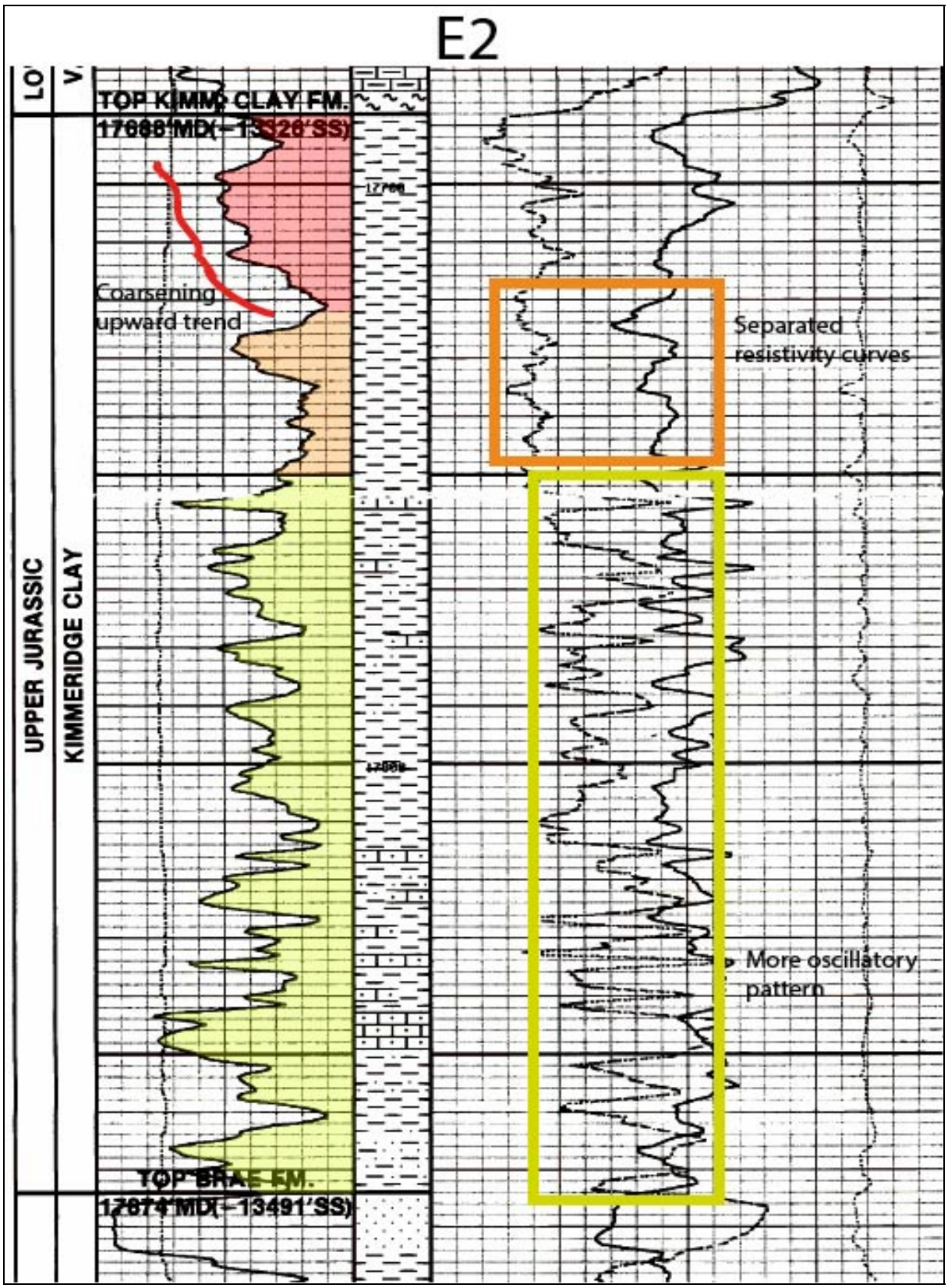

Figure 82 Well 16/03a-E2. Shows good quality wireline log displaying the 3 GU units; GU 1(red), GU 2 (orange), and GU 3 (yellow) based on the gamma ray and resistivity response. Note the difference in resistivity between GU 2 and GU 3.

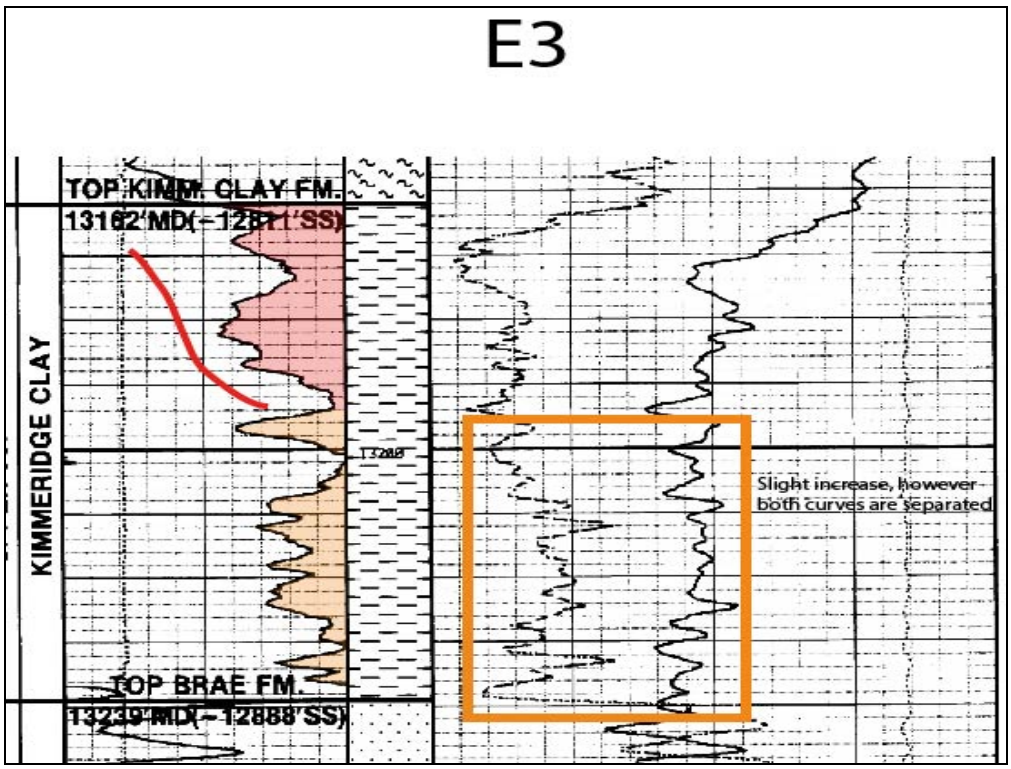

Figure 83 Well 16/03a-E3 shows GU 3 is missing; hence the section has been interpreted as two genetic units only. The separation between the resistivity curves marks the difference between interpreting the lower section as GU 2.

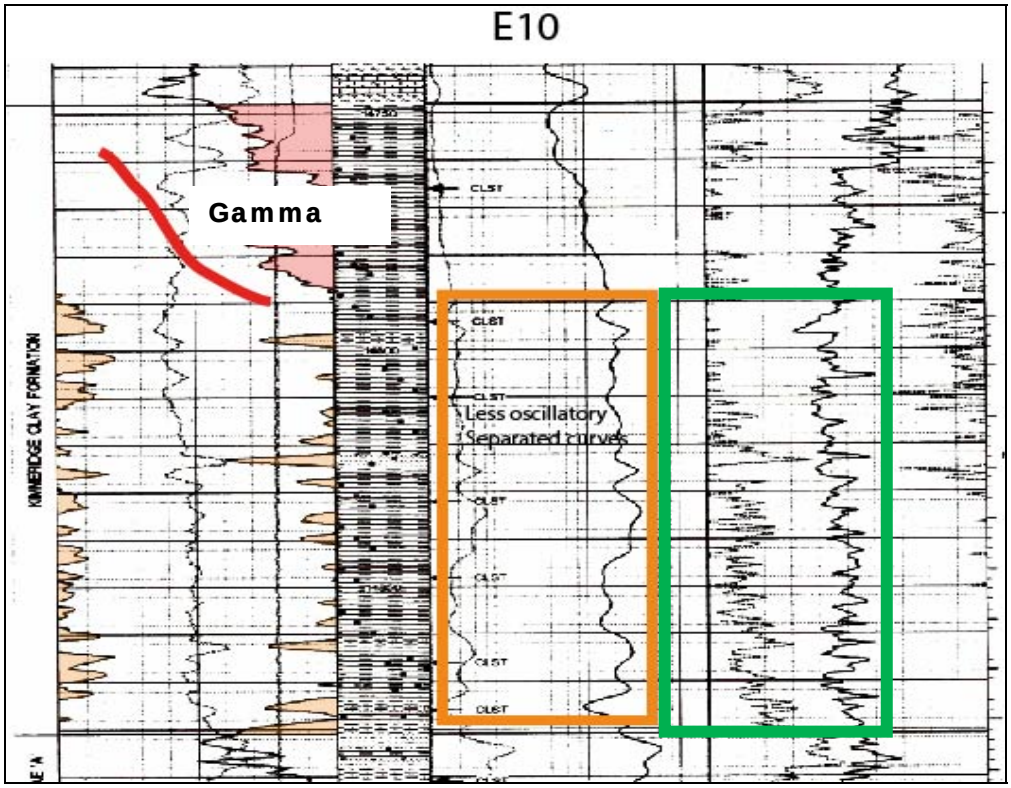

Figure 84 Well 16/03a-E10. Where available in composite logs, neutron-density curves (green) were used to discriminate GU 2 (orange). In this well, the gamma ray log shows the contrast between the coarsening upward trend on GU 1 (red) and a more serrated pattern observed in GU 2.

3.8.9 Initial correlations

Once the caprock and genetic units were interpreted, three correlation transects (Figure 85 & Figure 86) preceding the 3D model were built in Ed-Excel, illustrating the dome geometry of the KCF Caprock and the genetic units as conformable layers. From the 38 wells analysed, only the marginal well 16/03a-E16 was not conformable having repeating cycles of GU 1 and GU 2, thus there is no correlation with nearby wells that display a conformable trend. The thickness of the KCF varies significantly through the field, from 6m closer to the domal tip, to 80m at the far margins.

The correlations found a few thickness changes and little disappearance of GU 3 in several wells close to the ESE - WNW trending faults. The disappearance of GU 3 from several wells can be interpreted as a pinch out towards the dome, as part of an overall KCF thinning, associated with the early stages of uplifting during the Late Jurassic (Branter, 2003).

Figure 86 Map view illustrating three correlation transects: A-A' (green), B-B' (purple), C-C' (blue) across the Brae Formation. Note the presence of the ESE - WNW trending faults, major faults N1 – N3 (grey) are also shown.

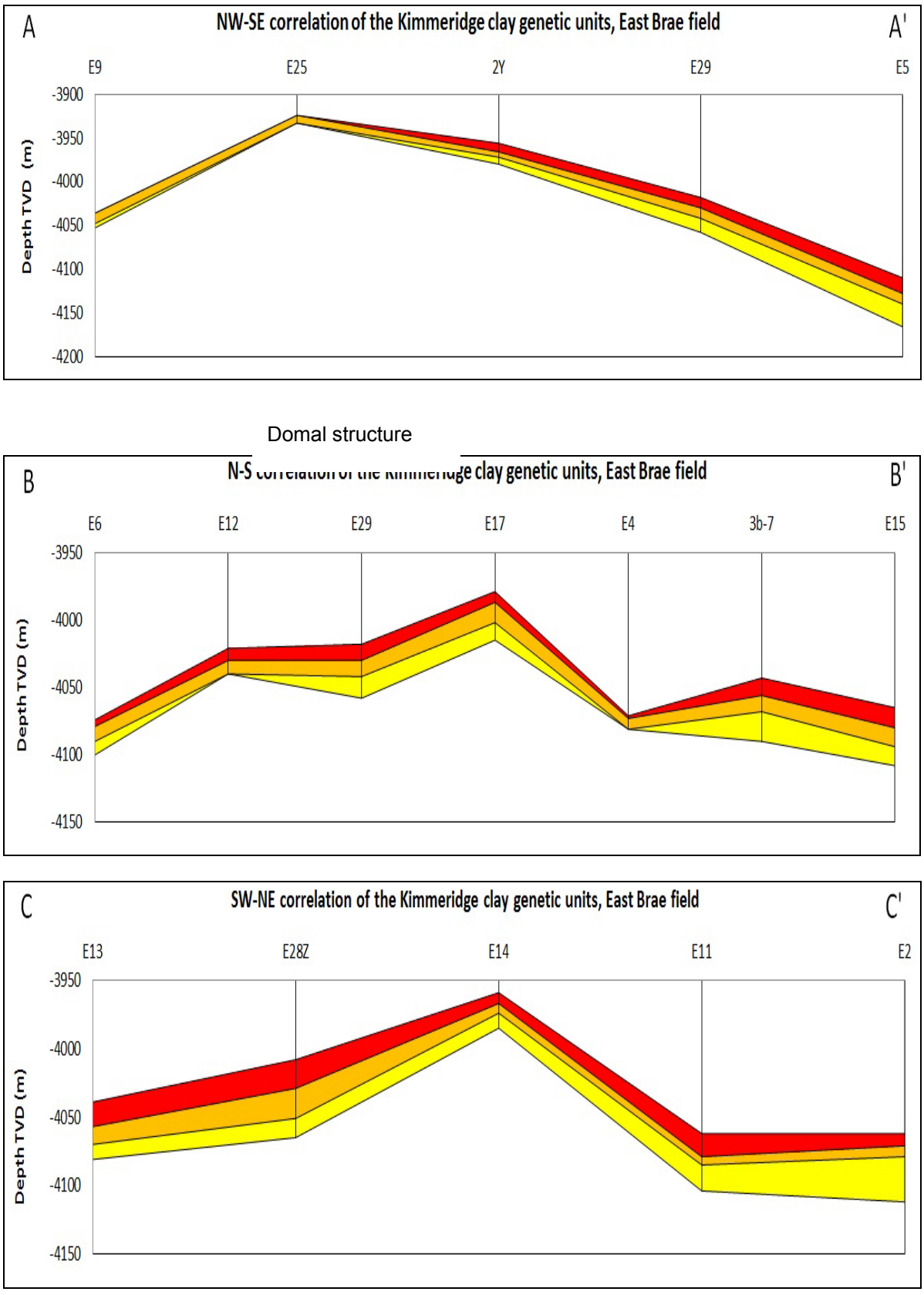

Figure 87 Series of correlations were created in excel to give a first impression of the overall caprock geometry. Transects A-A' (top) and C-C' (bottom) illustrate the anticlinal structure. In A-A' Well E25 does not have GU 3, interpreted as a pinch out towards the domal tip. Transect B-B' crosses the E. Brae field N-S showing GU 3 (yellow) is missing in wells E12 and E14, interpreted as nearby fault related events.

3.8.10 Secondary Seal Discrimination

The Valhall Formation (VF) comprises of a series of calcareous mudstones overlying the KCF for most of the UK Central North Sea (Johnson, 1993 p 36), serving as the secondary seal for our targeted area. Following a similar methodology to that employed when interpreting the KCF genetic units, the complete VF was only found in 18 wells, that was selected. From the selected wells, only 3 showed an irregular high gamma ray pattern, interpreted as interbedded mudstones. The 20 remaining wells did not contain the VF and were interpolated to create average thicknesses based on the thickness data from neighbouring wells.

The base of the VF marks where the units of lower cretaceous age begin, is characterized by a decrease in the gamma ray log, clearly contrasting the wireline pattern from the KCF. In addition, the VF is defined by a series of argillaceous limestone/marl units occasionally interbedded with claystones (Johnson, 1993 p 37). The Valhall's thickness ranges from 60 m – 150 m across the E. Brae area.

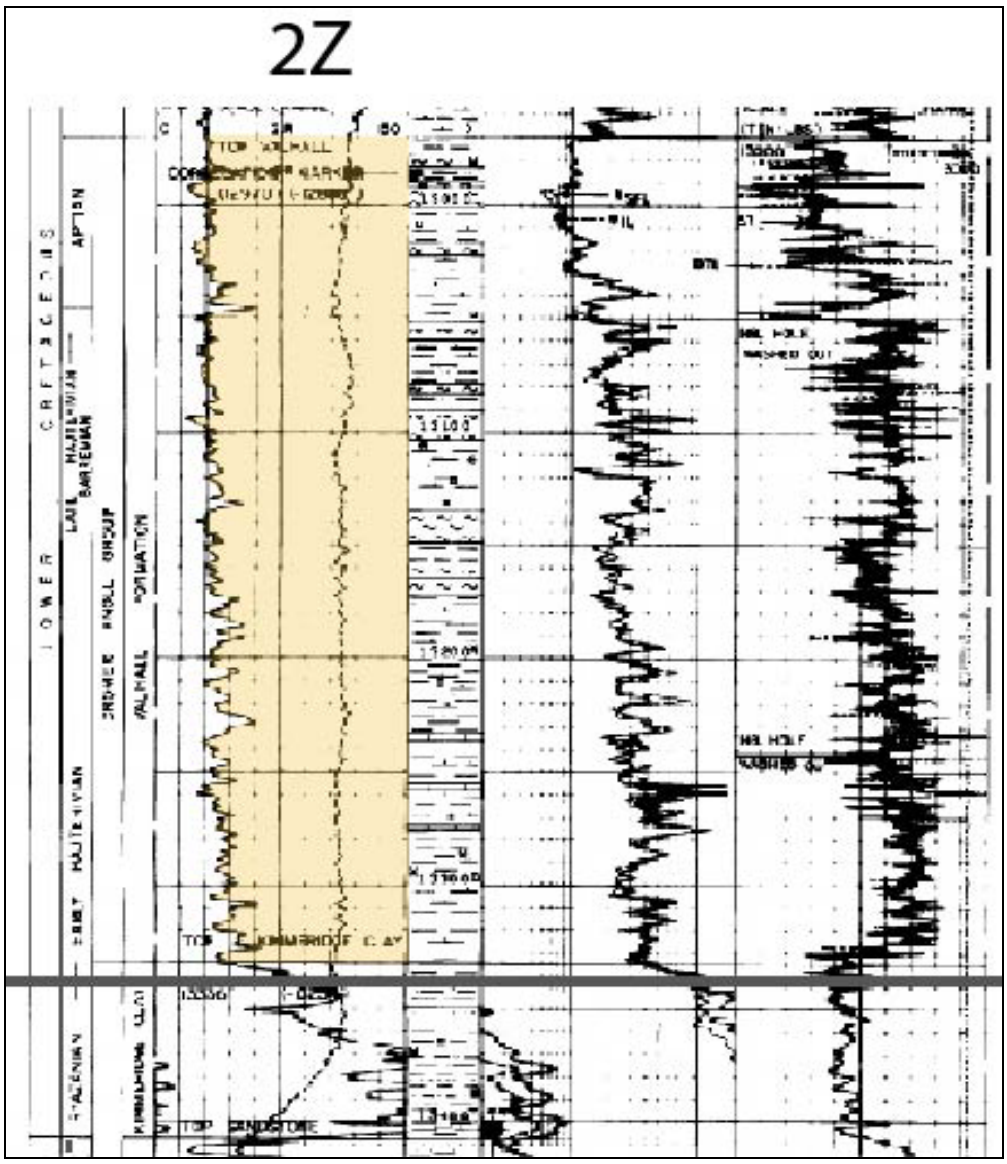

Figure 88 Well 16/03a-2Z. Composite log depicting the secondary seal overlying the KCF caprock. The Valhall was interpreted as a marl unit for most of the 18 wells across the E. Brae field based on a consistent low, blocky gamma ray pattern.

3.8.11 Model Conceptualisation

The study was carried out in order to develop and demonstrate a workflow that other CCS projects may utilise and improve upon to populate 3D caprock models and try to relate this to data sensitivity. The concept behind the work was to construct a 3D 'structure' model of the primary seal (KMF) based on a reservoir-wide network of 38 wells and also image the VF

overburden. Because there is currently a paucity of poroperm information (only present for GU1), efforts to populate the model grid with property information based on fabricated well log data were made redundant. It is possible, however, to achieve this at a later stage if property information becomes available.
It is noteworthy that the intended outcomes of the caprock model were:

1) To illustrate the 3D structural geometry of Kimmeridge Clay Formation.

2) To correlate and image the three genetic units (GU1 – GU3) and indicate where these units are likely to pinch out.

3) To produce isochore maps of the KCF seal, associated Genetic Units and VF overburden.

4) To highlight the three major faults (N1 – N3) in the study area and deduce the geological units that could act as a secondly seal in the immediate overburden overlying the primary KCF.

3.8.12 Petrel Software

Petrel is a Schlumberger owned Seismic–To-Simulation software package intended for reservoir modelling (www.slb.com/petrel). The workflow and resulting model described were developed using Petrel Version 10.2. It is expected that our approach to creating the model will remain applicable to future versions. The dynamic gridding process functionality of the software makes Petrel a powerful tool for structural modelling of the seal. It is noteworthy that the grid itself is affected by the resolution and quality of input data (Slb, 2010).

3.8.13 Stages 1 & 2 modelling, data density impact

Stage 1 modelling of the caprock assumed a non-connectivity between the genetic units. This was based on a sample size of 23 wells, where 4 wells (well 16/3a-E5; 16/3a-E15; 16/3b-3Z & 16/3a – E16) were interpreted to show a non-chronological order (Figure 89 & Figure 90). It is noteworthy that this model's interpretation was made with a considerable amount of data missing from the central portions of the study area (red dots). The dataset was therefore extended (blue dots) to 38 wells, Stage 2 modelling, to attain a more complete understanding of the subsurface geology to be incorporated.

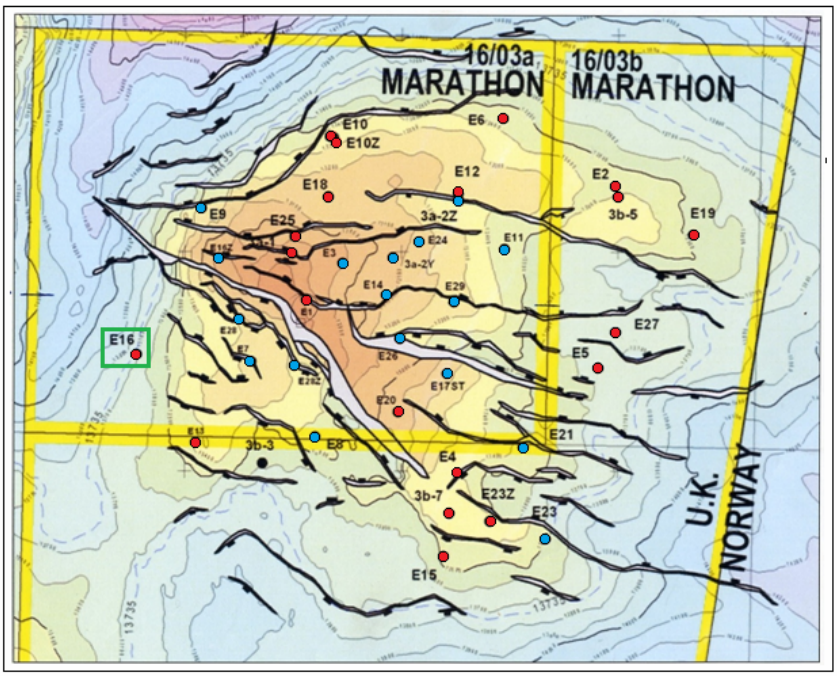

Figure 89 shows the lateral distribution of the 38 wells throughout the study area. The complete data set comprises of the original wells (red) and new downloaded wells from CDA (blue). The position of Well 16/03-E16 that shows non-chronological GU interpretation is outlined (green box). (Compliments of Marathon Oil)

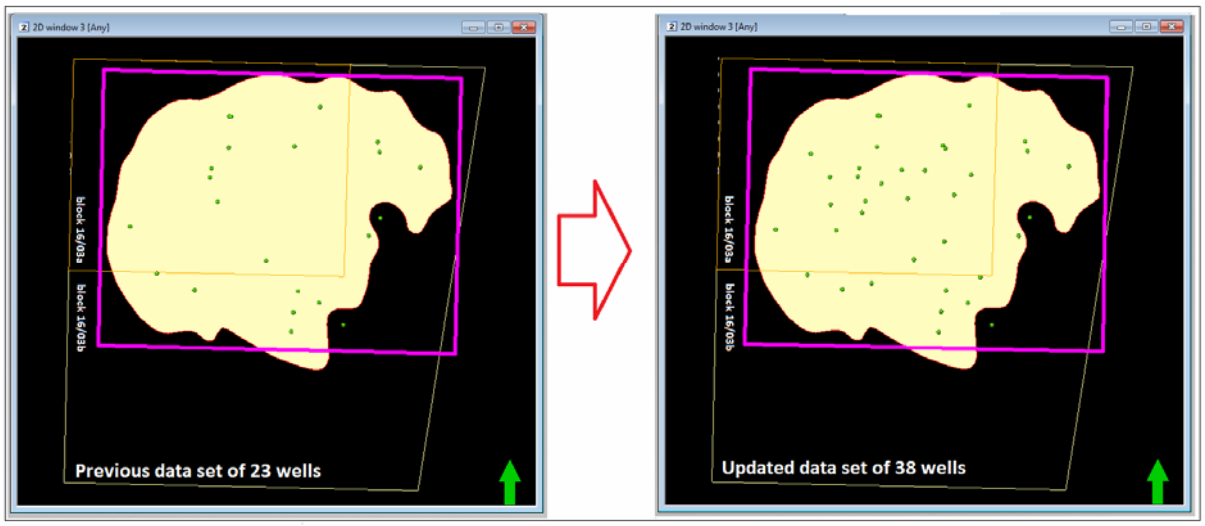

Figure 90 shows a 2D map view in Petrel contrasting the stage 1 "previous" data set (left) and the stage 2 "updated" data set (right). It shows the geographic position of the Brae Field (Cream with red boarder), Study Area (Purple box), spatial distribution of the wells (green dots) within UK North Sea block 16/03a – b. (compliments of DECC Open Government Licence V.1.0.)

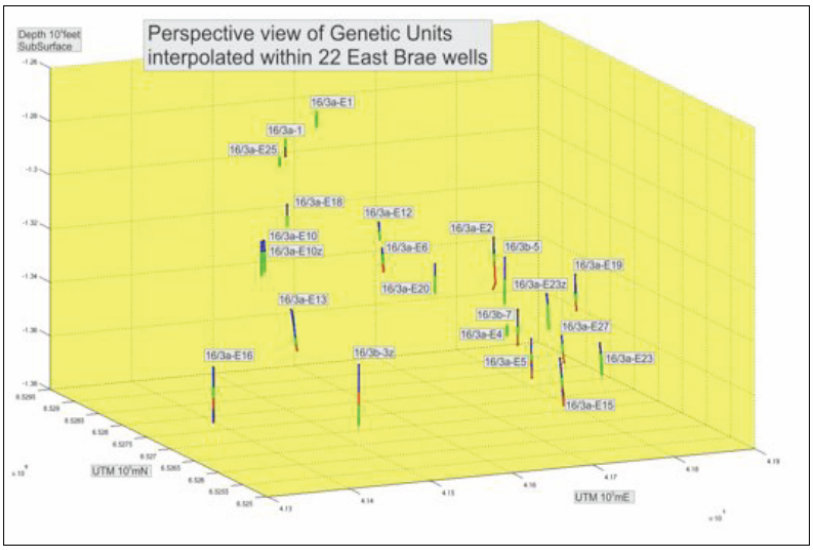

Figure 91 shows the vertical distribution of the caprock using Matlab software. This approach, however, did not image the 3D architecture of the GU's and their lateral distribution. (Stage 1 3D Visual)

Our correlation work, however, could only verify non-connectivity within one well 16/3a-E16 (green box –Figure 89). The weight of evidence in 37 wells verified that a chronological order of the GU's (1-3) is present and justified a model that was built upon a correlation of one sequence (KCF) comprised of three facies or zonal divisions (GU 1-3) across an irregularly spaced network of wells.

3.8.14 Data Loading

Well data is loaded into the input pane in Petrel. A large proportion of sample wells had deviations that exceeded 30° from horizontal. All the exploration wells are assumed to be those drilled off the central platform and are identified via extension '16/03a-'E'. Figure 92 shows a 3D perspective of the vertical wells (right) and deviated wells (left). Well tops were positioned using the top hole UTM co-ordinates given on composite well logs. Deviation files were available for deviated wells on CDA; these were downloaded and modified to be compatible with Petrel before being imported as well files in, ASCII (*asc) text formats.

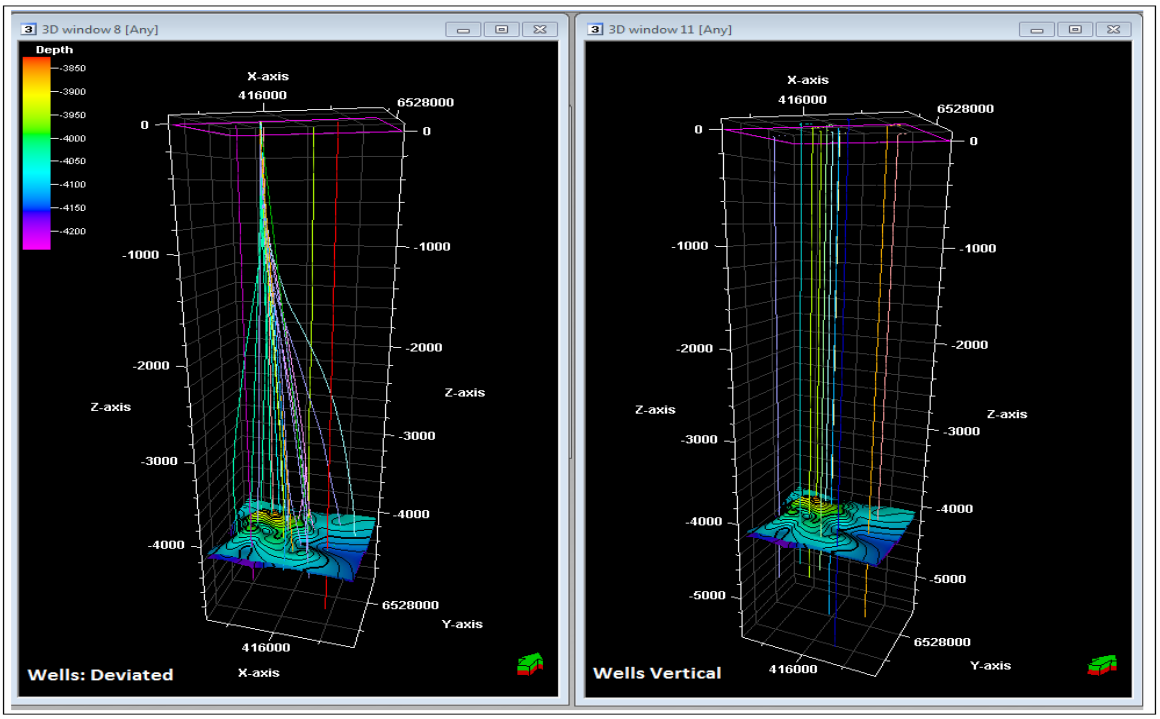

Figure 92 shows a 3D perspective of both (left) deviated and (right) Vertical well paths (multi-coloured lines) intersecting the top KCF surface.

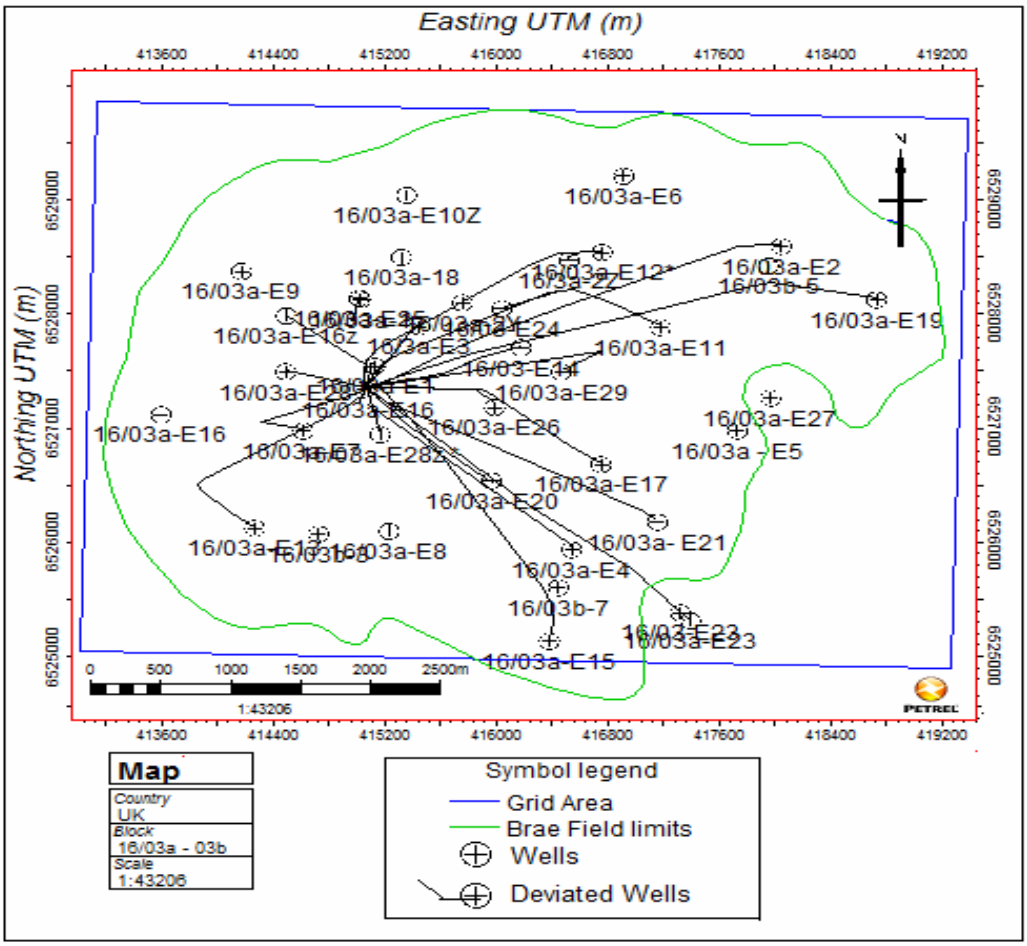

Figure 93 Shows the extent of the deviated well paths in 2D Map view.

3.8.15 Data Preparation

Petrel allows well tops to be picked for each individual well using an interactive spreadsheet. In this case, all well tops (including VF top, KCF top, GU 1, GU 2 & GU 3 horizons) could be used to create surfaces and then build the structural framework of the model. However, this method is time intensive and an alternative approach was chosen because of time constraints.

This second approach focussed on managing the data outside Petrel Software, then importing data into Petrel upon which the structural framework of the model can be built. Initially, a database was constructed in Ed-Excel based on the interpretation of the 38 correlated wells (see Appendix 2). Because Two Way Time information was not accessible for the majority of the wells, the model was assigned in terms of True Vertical Depth (TVD). The database included key parameters about the individual well and horizon: Bottom Hole (BH) depth, Measured Depth (MD) and TVD values for each facie, X, Y, Z co-ordinates UTM and thicknesses of the unit (m).

It is noteworthy that wells were only assumed to be vertical if their associated deviation files were not present on CDA. Hence, the X, Y, Z co-ordinates UTM for each data point were taken from the well head and TVD was assumed analogous to MD. However, this method was not applicable to deviated wells. In this case, the X, Y, Z co-ordinates UTM for each data point was generated through linear extrapolation using relative interval values from the deviation files. In this way well tops were imported into Petrel as data point *.txt files, modified from the Ed-Excel database.
In the VF case, only 18 wells could be used to identify the full formation thickness. It was decided to keep to keep the data points consistent with the number of wells and generated thickness values (red numbers – Appendix 2) by averaging the VF thicknesses of the three closest wells.

3.8.16 Generating surfaces and boundary polygons

In order to successfully model the geometry of the KCF, several preparatory steps need to be undertaken to create data for structural modelling. These include creating geological surfaces for the top and base mudstone and isochore surfaces (Williams & Hannis, 2010, p9). Because well tops for GU 1 and GU 3 were not continuous across the whole study area (Figure 94), boundary polygons for each of these GU's were required for accurate isochore mapping that allowed accurate mapping of pinch-out. It is noteworthy that these were manually created based on the correlation interpretation (Williams & Hannis, 2010).

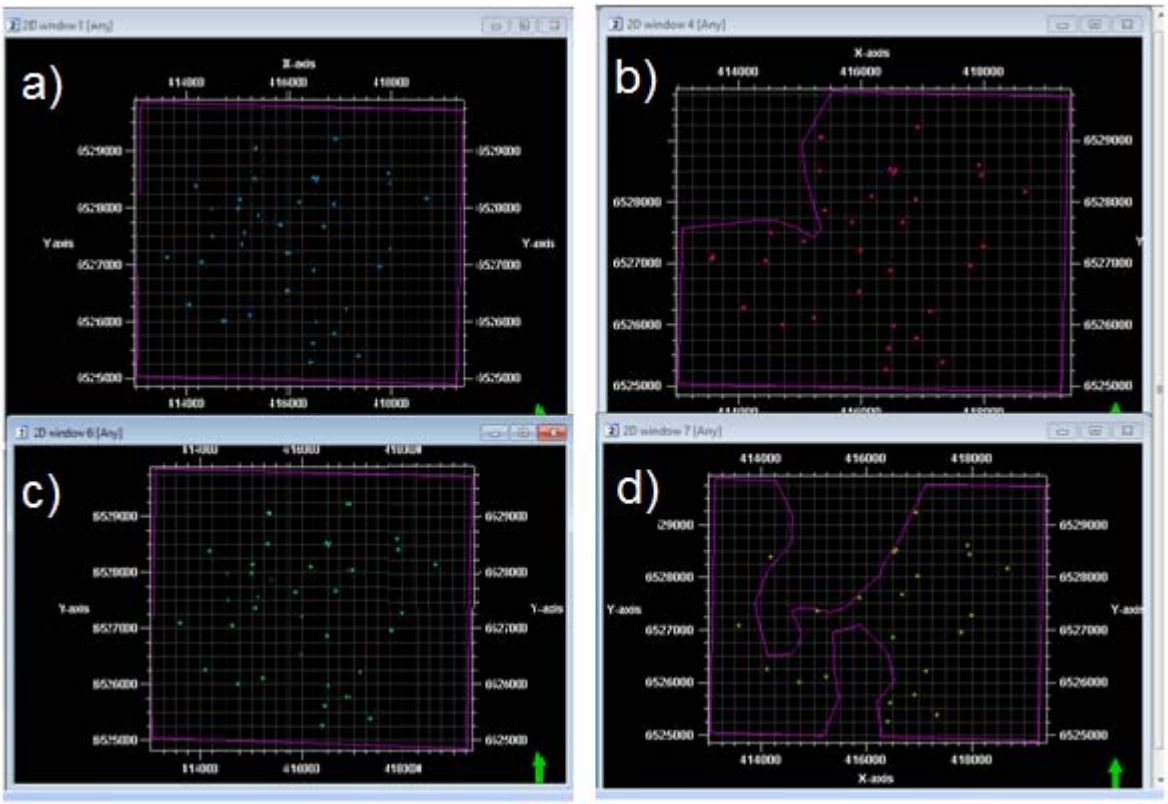

Figure 94 Petrels 2D map view of the presence of well top markers for (a) KCF top, (b) GU 1, (c) GU 2, (d) GU 3. GU 1 & 3 polygons (Purple) have been created based on their associated well top availability.

3.8.17 Generating isochore surfaces for GU 1 – 3 and smoothing 2D surfaces

As composite well logs record the top and base KCF, it was assumed that well heads at the top / base KCF were accurate and could be picked as a reference surface for the model. In our case, the KCF top data points were used to create a simple surface within Petrel and this was set as a reference surface for the model. The KCF bottom surface was then created by combing the thickness values for GU 1 – 3 and subtracting these from the reference surface. VF top was done in a similar way, but by adding VF isochors to the reference surface. A series of isochore surfaces progressing from the base to the top KCF were created for GU 1 -3, total KCF thickness, as well as VF thickness (Figure 95 & Figure 96(left)). These represent the vertical thickness between two horizons. It is noteworthy that all isochore surfaces contained roughness related to noisy data that needed to be smoothed before the surface could be used (Williams & Hannis, 2010).

This happened in two stages: initially, interactive smoothing was applied to localised points in the 2D grid where anomalous points were evident. Secondly, operation smoothing was applied (Figure 95 & Figure 96 (right)). Because large filter widths can be very aggressive in the amount of smoothing they do a filter width of 3 was the maximum value applied to the surfaces, with 4 iterons.

The grid, zones, faults and horizons used to generate the final model must all be considered in the 3D grid before the structural framework of the model is built. Figure 97 identifies the flowchart detailing the workflow for a faulted caprock.

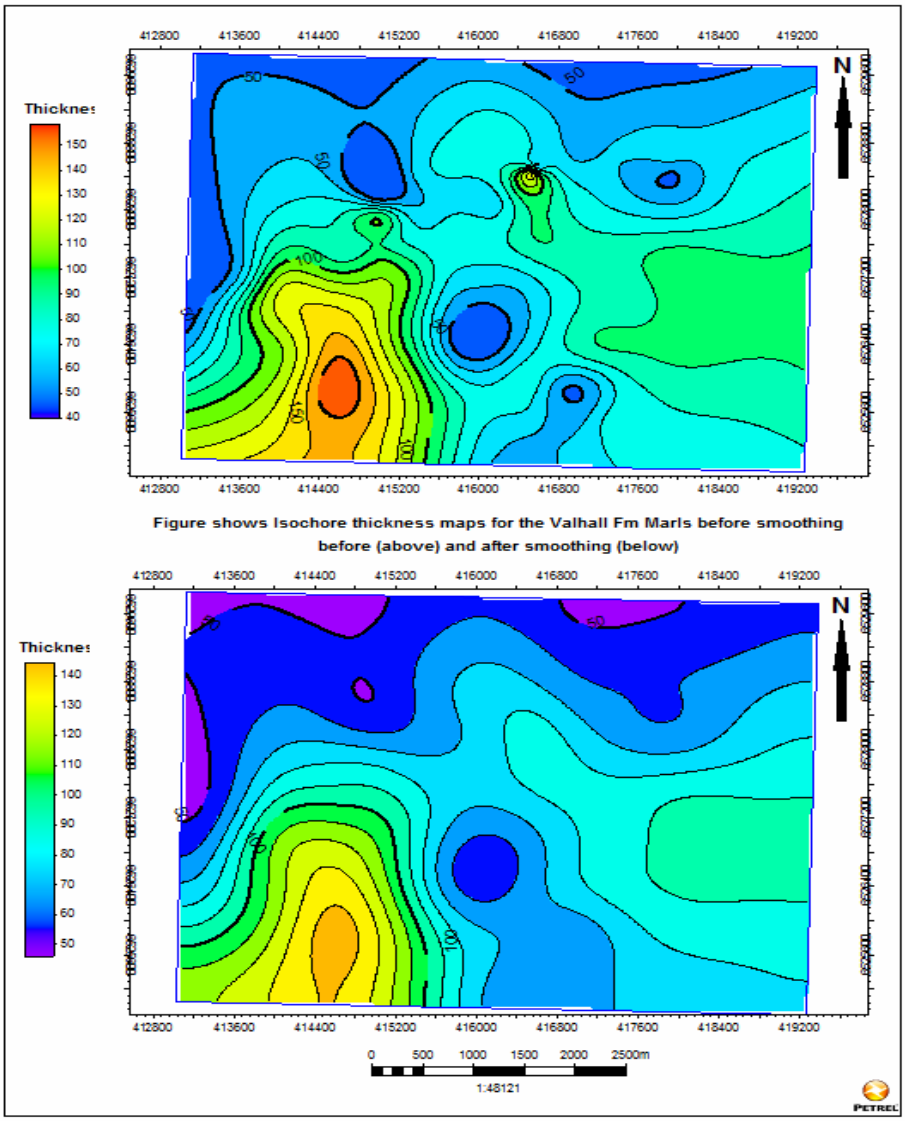

Figure 95 **shows thickness maps for VF, before (above) and after (below) Petrels smoothing operation**

Figure 96 a & b

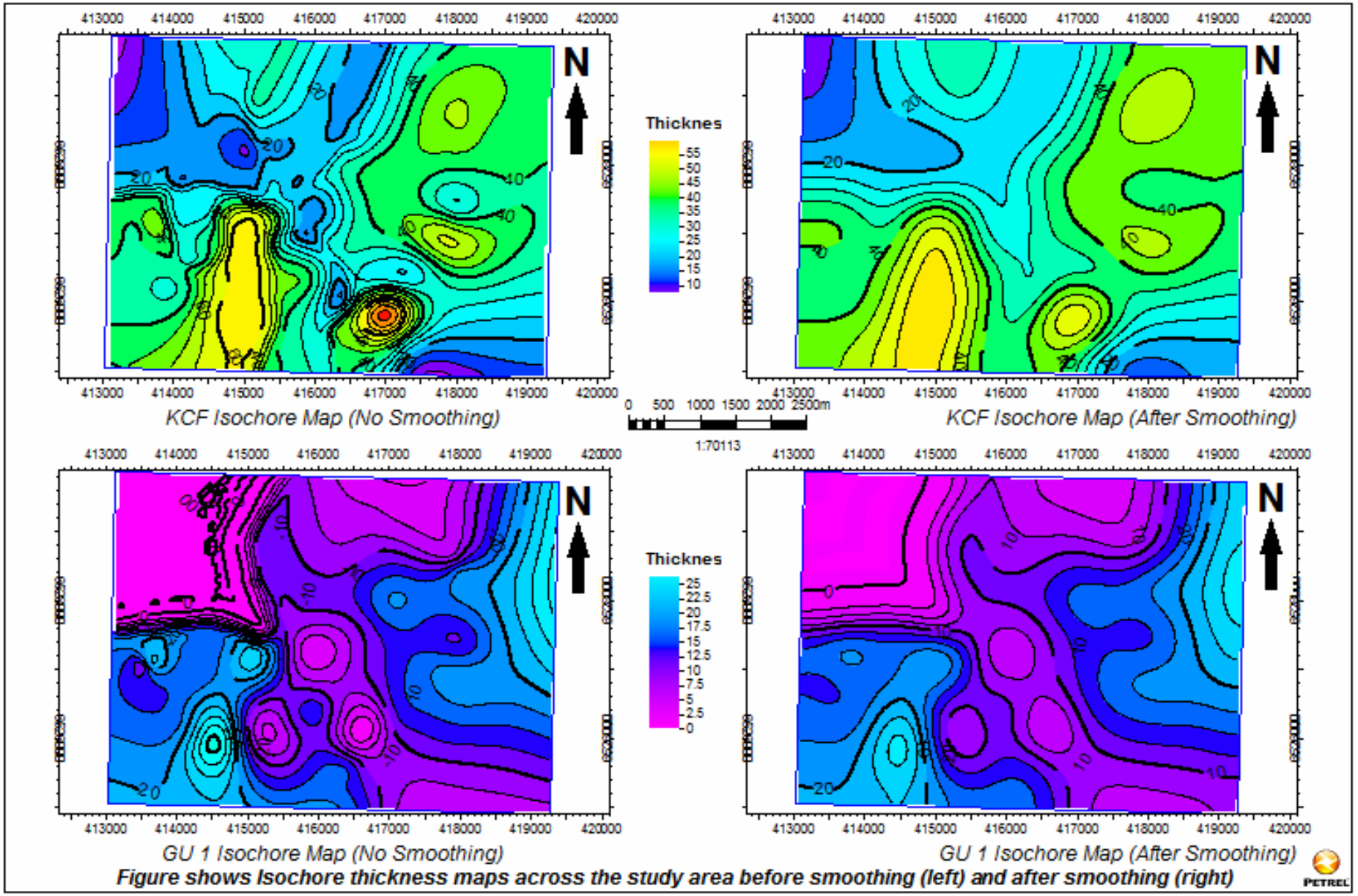

Figure shows Isochore thickness maps across the study area before smoothing (left) and after smoothing (right)

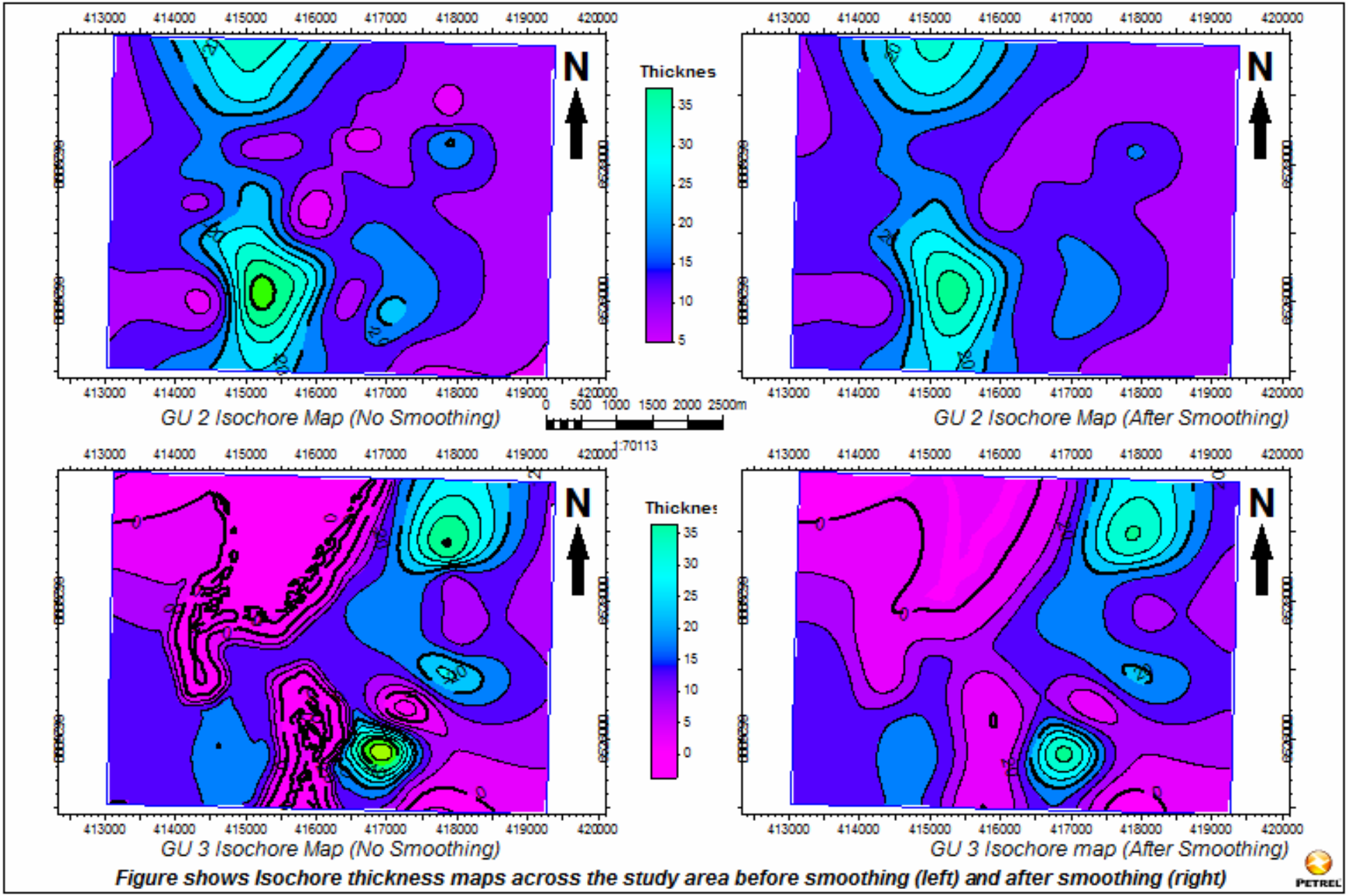

Figure shows Isochore thickness maps across the study area before smoothing (left) and after smoothing (right)

3.8.18 Structural Modelling

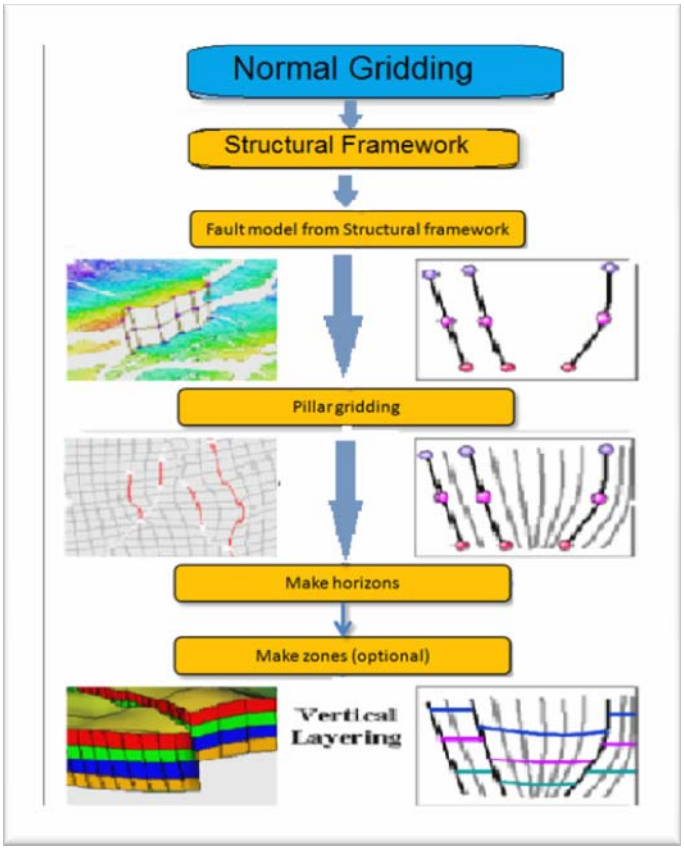

Figure 97 showing a Flowchart detailing Petrel workflow for a faulted Caprock, starting with a fault model and finishing with the vertical layering within the model. (Modified from: Slb, 2010)

3.8.19 Fault Modelling

As the model was built solely on well data, there was great difficulty in confining the exact position, geometry, 3D architecture and vertical extent of faults. Large faults (N1 – N3) were identified using Marathon Oils hinge interpretations at the top of the Brae Field. Defining the faults in the geological model forms the basis for generating the 3D grid.

3D fault-polygons were created for each individual fault using the released hinge interpretations. These were then converted into faults with gridded pillars in Petrel, then projected on to the top and base KCF surfaces. Because KCF is relatively thin (<35 m) at these fault positions, all faults were assumed to extend through the primary seal. However, faults were assumed to die within the secondary seal, given the presence of buoyant hydrocarbons in the East Brae Field. As Branter (2003) argues faults to be syn depositional, faults N1 – N3 have been modelled as growth faults. Figure 98 shows the transition from (1) the un-faulted model to (3) the faulted KCF top and bottom by incorporating faults N1 – N3.

3.8.20 Pillar Gridding

Once the faults were defined, a 3D grid was then generated from the fault model using a boundary polygon to define the areal extent of the grid while the top (VF) and base (KCF bottom) surfaces were used to constrain the grid vertically.

3.8.21 Vertical Layering

The final step was to build vertical layering into the model. Vertical layering was separated into two phases: (1) Horizon creation and (2) Zones creation.

(1) **Horizon creation** (Figure 98 (5) generates independent geological horizons from X,Y,Z input data. It is noteworthy that only the top KCF horizon was added to the model. KCF top was assumed to be an erosional surface given 'thinning across the crest of the East Brae structure was attributed to early uplift' in the Late Jurassic (Branter, 2003, p193)

(2) **Zones creation** (Figure 98 (6) adds more detail in vertical grid resolution (Slb, 2012). The GU unit surfaces were added using the relative distance to existing horizons (e.g. isochores) between the bottom KCF and top KCF.

Once the structural model had been built, the 3D cells were then populated with properties (Williams & Hannis, 2010). However, as previously mentioned efforts to populate the model grid ultimately failed because of a lack of GU information and are dependent on data availability.

3.8.22 Structural modelling Workflow

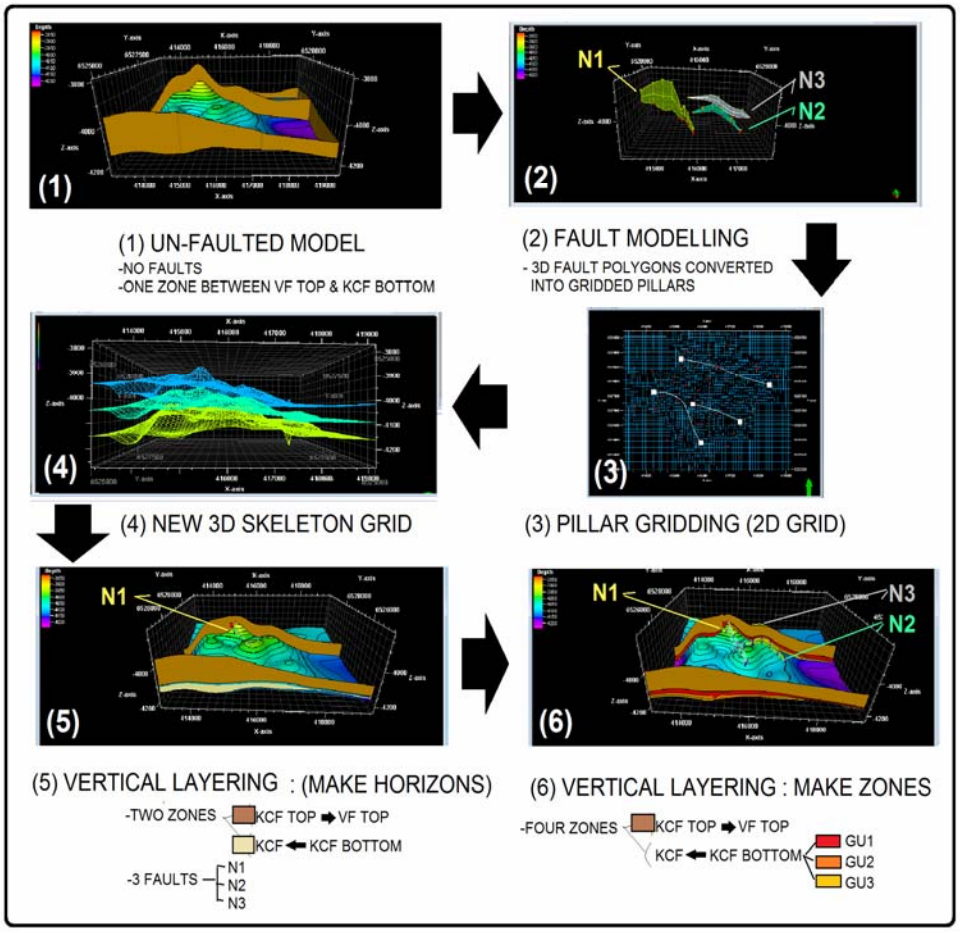

Figure 98 Flowchart detailing Petrel workflow for Structural Modelling of the faulted KCF Caprock in stages from (1) Un-faulted model, (2) Fault modelling, (3) Pillar Gridding, (4) New 3D Skeleton Grid creation, (5) Vertical Layering make horizons to (6) the final model to include zones.

3.8.23 Results: Final 38 well Model

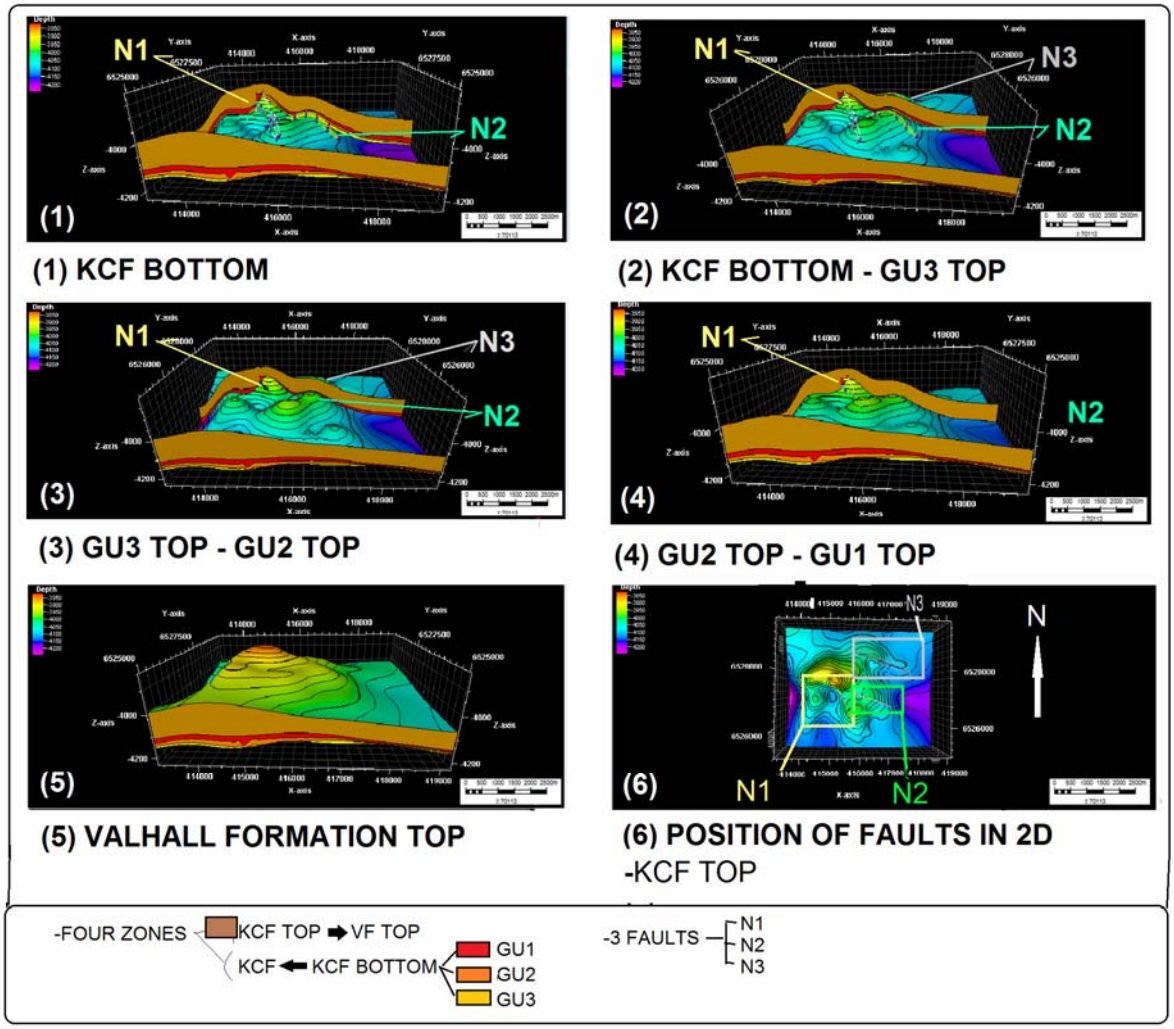

Figure 99 shows a progressive build up of the structural KCF caprock model in stratigraphic sequence (1) KCF bottom; (2) GU3 top; (3) GU2 top; (4) GU1 top; (5) Valhall Formation top; and, the distribution of major faults in the study area.

General intersection planes were then used to give a 2D representation of the structure of both the primary (KCF- separated into GU 1 - 3) and secondary (VF) seals, across the study area (Appendix 3a –d). The irregular distribution of the wells results in study area locations being poorly constrained by the model. The model interpretation at these points is purely based on Petrel's interpolating nature, hence, interpretations are considered to be Low Confidence (LC) zones that may not reflect the true nature of the subsurface geology. It is noteworthy that there are two localised points within the study area where the model is unlikely to be representative of true subsurface geology. We interpret all locations >500 m away from a well data point to be a LC zones, these zones are represented in transparent (light green) in the Appendix 3. On the other hand, regions <500 m from well data points are considered to be High Confidence (HC) zones and are shown in Figure 100 to Figure 102 (light red). Figure 100 shows a 2D map view of the 2D geometrical intersection locations. These are in two orientations, N – S (red) and E – W (purple) in relation to the three major faults N1 – N3.

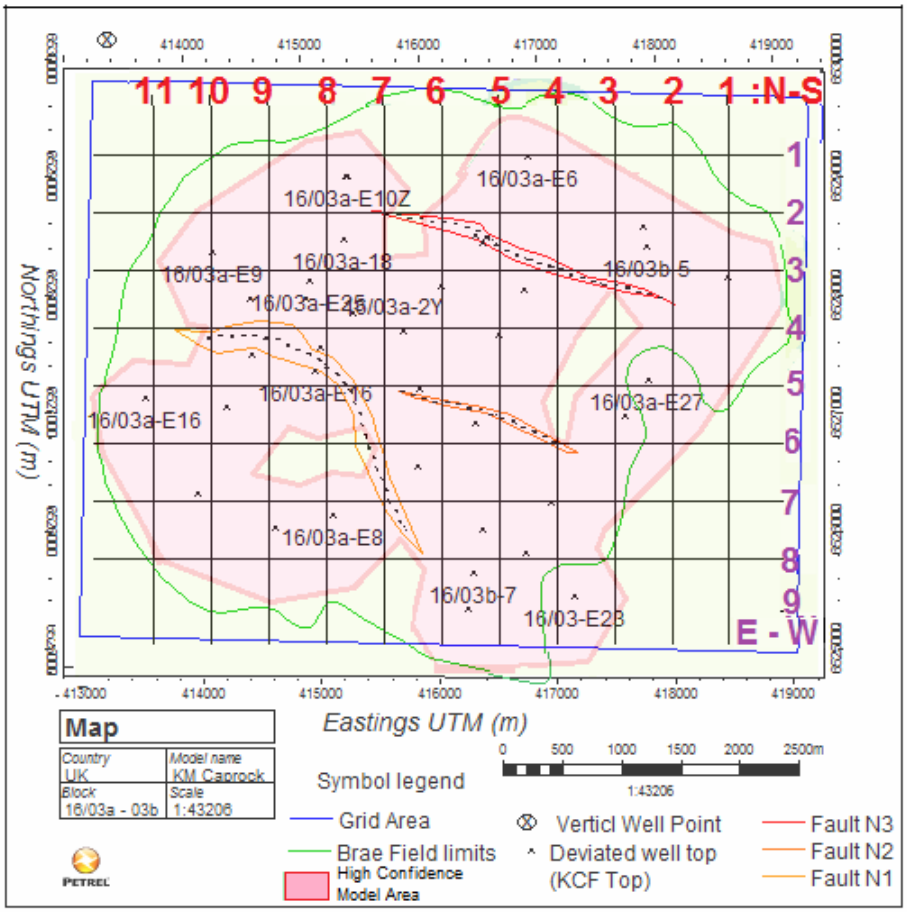

Figure 100 shows the regular grid intersections across the study area displayed relating to the 2Dviews in Appendix a – d. Both N-S and E-W intersections are spaced at 0.5km. Additionally, the high confidence zone < 650m is highlighted in light green and generally follows the Brae Field Limits.

3.8.24 Data Sensitivity of the model

The East Brae Field is considered a 'data rich area' consisting of both extensive seismic and well data. However, potential CO_2 storage sites may have much less spatial coverage of well data within the area. It is therefore important to validate the application of this methodology in data moderate (21 > no. of wells >7) or data poor (6 ≥no. Of wells>1) areas, in order to, investigate the data sensitivity of the geological model. Figure 101 and Figure 102 outlines HC regions (pale red) within data moderate and data poor areas. Because of time constraints only four transects (purple) were chosen to contrast the geological models.

Two further models were constructed using the method previously outlined. To avoid sample bias well data was selected sequentially in chronological order based on realistic scenarios. The data moderate case (Figure 101) assumes that production and development of the field was optimally managed by a combination of 6 exploration wells and 14 further development wells, whereas, the data poor scenario (Figure 102) assumed that all exploration wells were 'dry holes'.

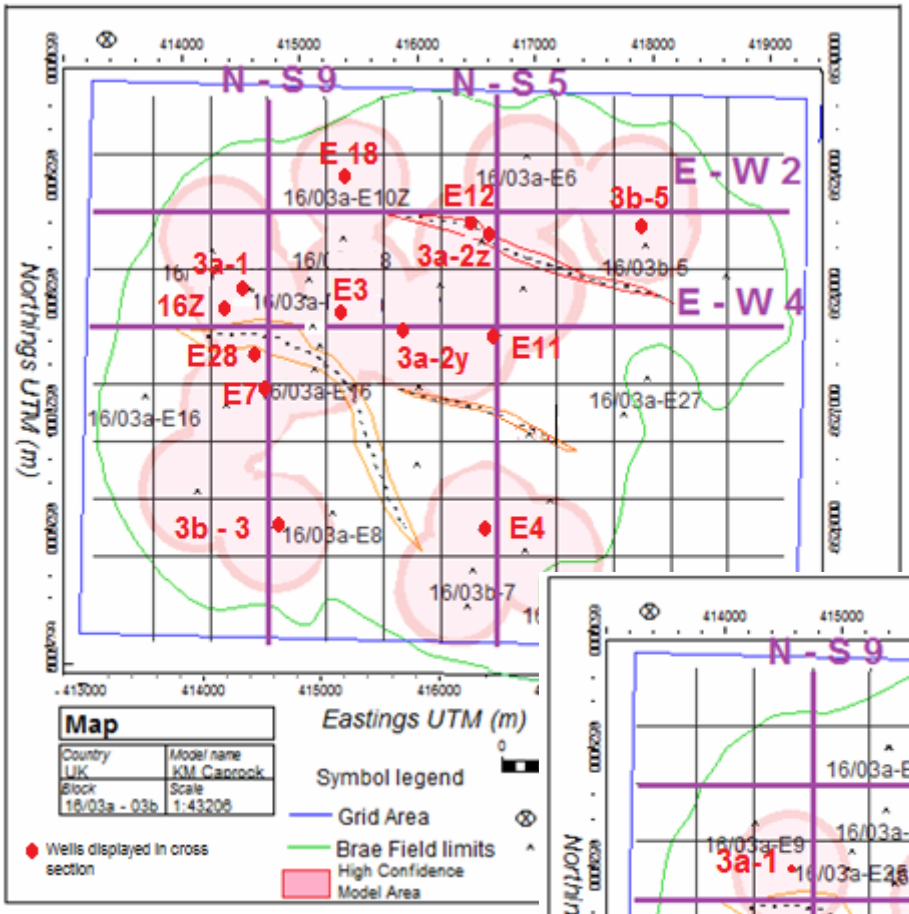

Figure 101 shows the HC locations (light red) within a moderate data area (20 wells). Well positions displayed in 20 well caprock cross sections (Figure 39 -40)

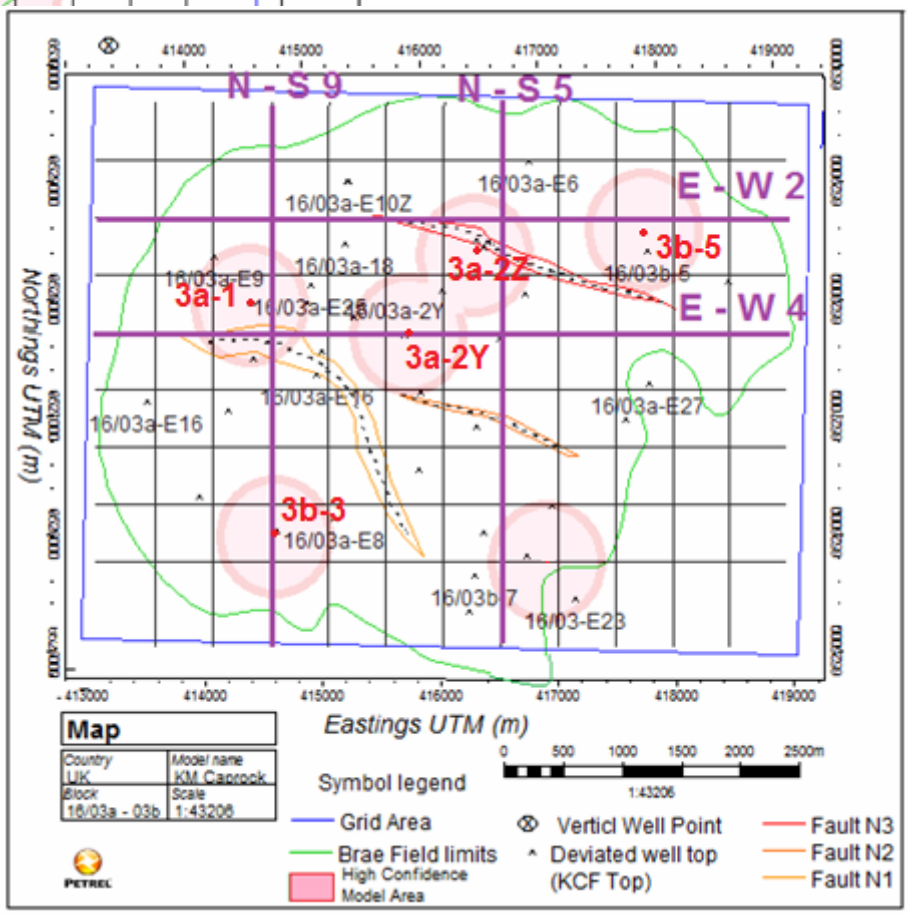

Figure 102 shows the HC locations (light red) within a data poor area based on 6 wells. Well positions displayed in 6 well caprock cross sections (Figure 39 -40)

The figures suggest a non–linear positive relationship between HC regions and well number. That is HC regions increase as wells increase. However, the most dramatic proportionate increase in HC area occurs within the range of low to moderate scenarios.

Given that smoothed isopach data provides the geological framework for model construction (Williams & Hannis, 2010), Figure 103 a & b have been created to contrast the resulting thickness' generated from the 'moderate' and 'poor' data scenarios. It is noteworthy, that the moderate 20 well case yielded similar overall results to the 38 well case. However, when considering the total KCF both models (Figure 103 a1 & a2) shows thickening up to 60 m in the far East contrasted to 45 – 50 m (38 well model), and up to 70 m in the far South-Westerly corner of the study area contrasted to 50m (38 well model). This results from the way Petrel interpolates its surfaces in the absence of data. Additionally, it is evident that this interpolating nature makes effort to always create idealised isopach contours even when this

creates unrealistic localised points of extreme thickness (shallow or deep) which have a steep gradient relative to the surrounding thicknesses. Despite smoothing operations being applied, remnants artefacts can still be observed which again may not be representative of the true subsurface geology.

Finally, the isopachs for the data poor area show oversimplified isopachs suggesting limitations of the data and its application to real geological structure. This highlights a key inference that in the absence of additional datasets such as 2D/3D seismic, any model constructed in a data poor area will not yield accurate thickness isopochs. Hence, the geological model structure is ultimately unreliable.

Figure 103 a & b

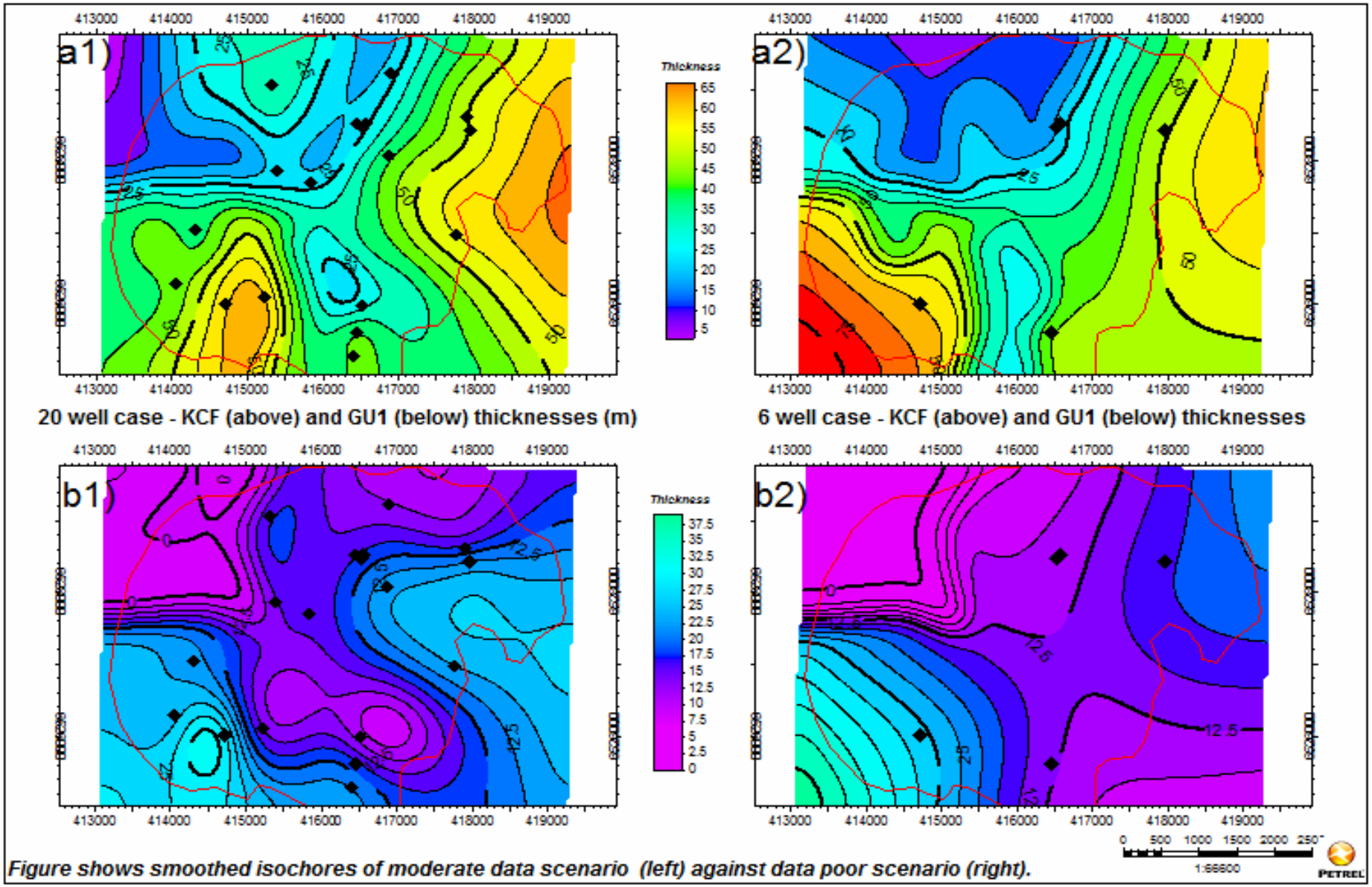

Figure shows smoothed isochores of moderate data scenario (left) against data poor scenario (right).

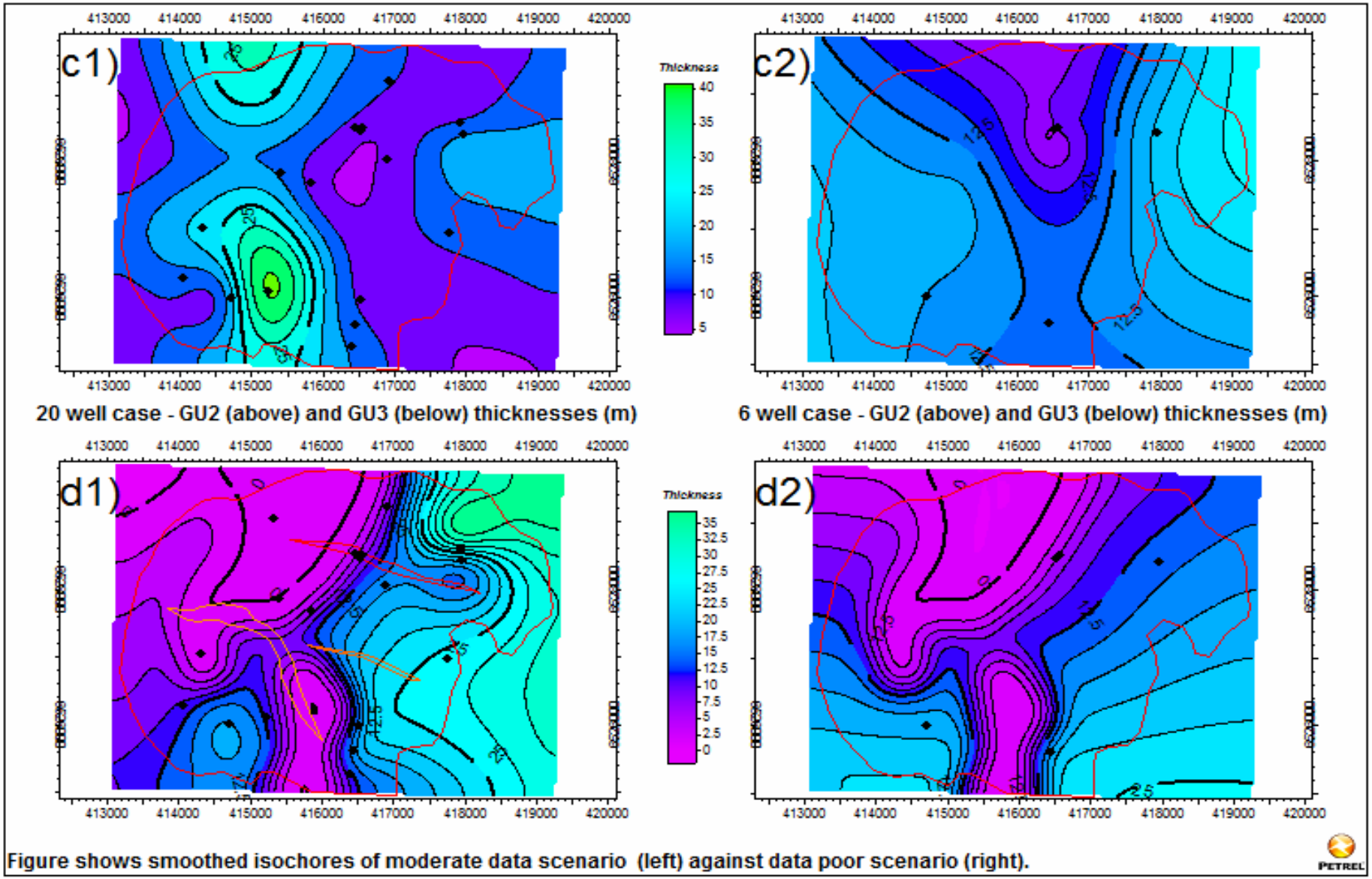

Figure shows smoothed isochores of moderate data scenario (left) against data poor scenario (right).

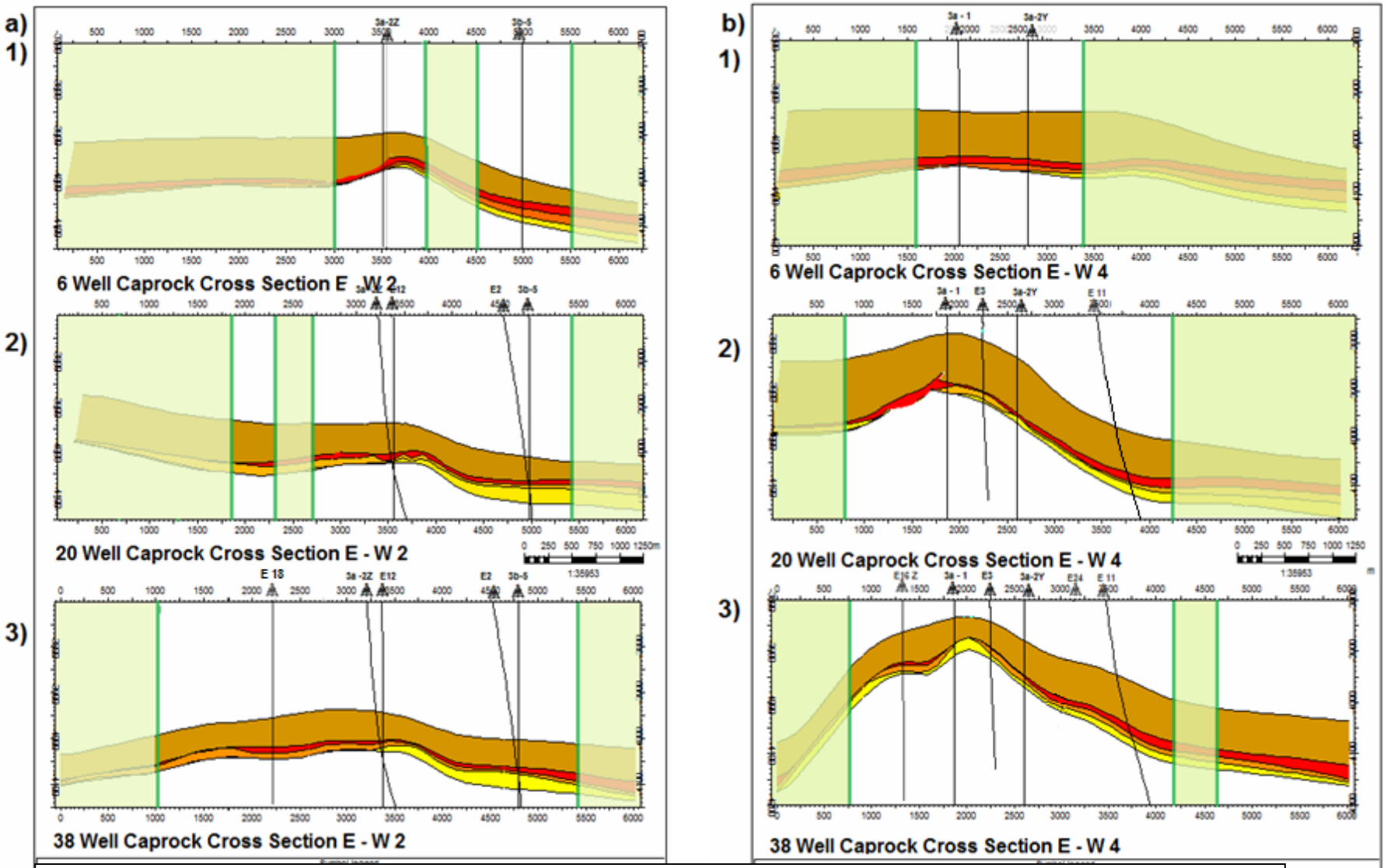

Figure 104 : shows the caprock cross sections generated from the model for transects E – W 2 (left) and E – W 4 (right), for (1) data rich model – 38 wells; (2) data moderate model – 20 wells; and, (3) data poor model- 6 wells.

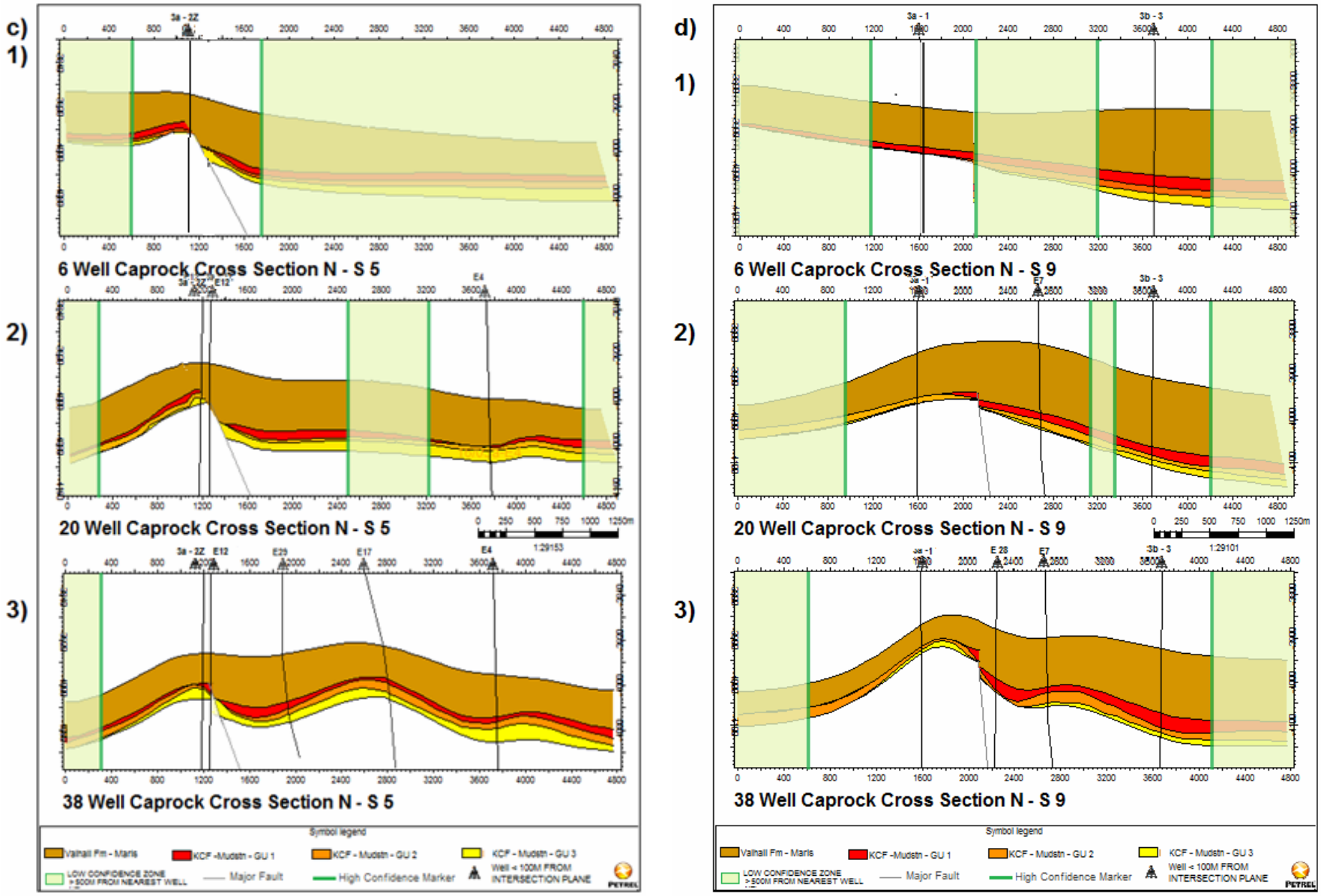

Figure 105 shows the caprock cross sections generated from the model for transects N – S 5 (left) and N – S 9 (right), for (1) data rich model – 38 wells; (2) data moderate model – 20 wells; and, (3) data poor model - 6 wells.

3.9 Model Analysis

Figure 104 & Figure 105 a – d presents four 2D Petrel-produced cross-sections of the primary KCF caprock and overlying VF secondary seal selected over the study area (Figure 102 & Figure 103 purple lines). The cross sections verify that the data poor geological model eliminates large scale resolution structures (approx 1000 m) even within the HC zone (>500 m from nearest well). A prime example is the crestal high identified by transects (1) N – S 9 (Figure 105 1-3) and (2) E – W 4 (Figure 104 (1 -3). Figures d3 and b3 suggest the domal high is characterised by GU 1 - 3, whereas, the data poor scenario shows an absence of the crustal high with only GU 1 being present.

Furthermore, the cross-sections outline the effects of increasing the well coverage on the structural model. Figure 104 b shows a model progressing from (1) no observable domal structure characterised by GU 1; (2) a domal structure that is characterised by GU 1- 2 to (3) a refined structure with GU 1-2 pinching out crest wards, to leave GU 3 at the crest. It is noteworthy that the inclusion of well E16z changes the model interpretation from representing GU 1 completely in the 20 well case to approximately 10 m GU 1, 46 m GU 2 and 5 m GU 3. This is similar to the real data that outlines a GU2 thickness of 61 m. Interestingly, all cross sections highlight a thick VF secondary seal supporting literature suggesting that the VF 'onlaps onto the crest of the East Brae Field' (Branter, 2003).

Table 20 shows a summary contrasting the real well data for the modelled data for the three models (6 wells, 20 wells and 38 wells). The figures for each GU are representative of the ratios shown in the cross section. If a well is selected within the first 250 m of a LC zone, the model figures have been recorded. However, where data is modelled within LC zones the modelled data is assumed not to be representative of structural geometry, hence, 'not available' (n/a) is input into the table. Red (n/a) inputs represent layering not properly imaged within the model because of the presence major faults.

Table 20 provides a visual representation of the overall modelled data trends contrasted to the real well data. Notably, table 2 shows that even in the data rich case (38 wells) inconsistencies with real data (red) still exist. The table suggests that overall the 38 well case best matches the real geological data comprising mainly green boxes. Whereas, the 20 well model shows poorer overall match consisting mainly of orange boxes, and least well matching 6 well case.

Table 20 suggests that in the 38 well case, the model does not match real data at a minority of points along the cross section (3b – 5, E12, E4 and E28). Inconsistencies are largely accounted for by the increasing distance from the transect line. Despite all wells lying within 100 m of the displayed cross section, some well positions lie more distant from the cross-section and, hence, do not match the model so well. Prime examples are well E12 (N – S 5) which shows a poor match with the data and wells 3a – 1 and E28 (N – S 9) which only match real data moderately well, however, they are situated approximately 70 – 90 m away from displayed cross section. This is further emphasised by the fact that the same well (E12) displays a poor fit with the N – S 5 cross-section, but has a very good fit to the E – W 2 cross section that it lies much closer to.

Table 20 shows a summary of real thickness values against modelled data for models based on a) 6 wells, b) 20 wells and c) 38 wells. The model match good (green), medium (orange) and bad (red) is outlined.

		Real Data Thickness (m)			Modelled Data Thickness (m)								
					6 Well Model			20 Well Model			38 Well Model		
Cap rock Cross section	Well no	GU 1	GU 2	GU 3	GU 1	GU 2	GU 3	GU 1	GU 2	GU 3	GU 1	GU 2	GU 3
E –W 2	3a-2z	**36**	**10**	**26**	72	0	0	65	5	2	20	26	26
	E12	**30**	**33**	**0**	n/a	n/a	n/a	65	5	2	20	26	26
	E2	**30**	**25**	**110**	n/a	n/a	n/a	40	20	105	33	12	120
	3b - 5	**55**	**60**	**45**	55	65	40	40	20	105	35	10	120
	E18	**38**	**40**	**0**	n/a	n/a	n/a	34	44	0	38	40	0
E -W 4	E16Z	**0**	**61**	**0**	n/a	n/a	n/a	61	0	0	10	46	5
	E3	**32**	**45**	**0**	39	39	0	5	67	5	10	52	10
	3a-2y	**35**	**19**	**27**	40	40	1	15	5	60	20	30	30
	E24	**37**	**34**	**0**	35	10	30	33	6	32	24	18	26
	E11	**55**	**21**	**60**	70	20	46	63	10	63	50	18	68
N -S 5	3a-2z	**36**	**10**	**26**	**n/a**	**n/a**	**n/a**	24	24	23	27	5	40
	E12	**30**	**33**	**0**	n/a	n/a	n/a	**n/a**	**n/a**	**n/a**	50	0	13
	E29	**38**	**39**	**55**	n/a	n/a	n/a	61	10	61	45	32	55
	E17	**28**	**49**	**41**	n/a	n/a	n/a	48	10	60	30	56	32
	E4	**7**	**25**	**0**	n/a	n/a	n/a	5	15	90	30	30	70
N -S 9	3a -1	**0**	**46**	**0**	46	0	0	0	46	0	16	30	0
	E28	**52**	**36**	**0**	n/a	n/a	n/a	50	38	0	88	0	0
	E7	**53**	**74**	**0**	n/a	n/a	n/a	62	63	5	55	65	7
	3B-3	**86**	**50**	**63**	86	50	63	80	25	55	90	62	47

Additionally, inconsistencies within the modelled horizon boundaries of the GU facies at Wells 3b – 5, E4 and E28 result from Petrel's interpolating nature with the model exhibiting a bias towards the thicknesses of the majority of the surrounding wells. !f surrounding wells have a consistently different GU thickness interpretation then the smoothing operations on the isopachs will eliminate localised point with different GU thicknesses and model displays an average thickness. Well E4 (N – S 5) is a good example of this interpolation artefact. Thicknesses from the 38 well model (Table 2) suggests the presence of GU 1-3 where as, well E4 only has GU 1–2. In this case the model incorporates data from proximal wells 3b–7 (GU 1-44 m; GU 2- 40 m; GU 3- 72 m) and E23z (GU 1- 40 m; GU 2- 66 m; GU 3- 158 m) that are interpreted to have GU 1-3 presence. It is noteworthy that the model would more closely match an average of these thicknesses.

Inconsistencies within the geological structures are also highlighted within the LC regions of the cross sections. Figure 103a – 2 (E - W 2) shows that layering that trends upwards in the eastwards direction away from the dome in the 20 well model.

3.9.1 Limitations

The model can be viewed as a good means to visually understand the 3D geology of the caprock, given limited data availability. Historically, seal analysis and associated structural models have been applied with a combination of 3D/2D seismic data, alongside well data (Cartwright et al 2007). Two dimensional (2D) seismic data has been used to 'map 2D shapes and the spatial distribution of leakage-related anomalies' (Loseth et al, 2009, p1306). This is particularly relevant for accurate horizon and fault mapping and to confirm the vertical extents of the faults (Robbins, 2011). It is noteworthy that several seismic datasets exist over the study area including 2D data acquired between 1980-1985 and a 3D seismic survey (Branter, 2003). Despite the 3D survey being shot with primary objective to allow more 'detailed and accurate structural and stratigraphic interpretation' (Branter, 2003 p195), seismic data was not available for the purpose of the study. Consequently, the model suffers from three main uncertainties: (1) the quality of original interpretation; (2) fault geometry; and (3) accuracy of the 3D geometry of the model.

3.9.2 Quality of stage 1 interpretation

As the Petrel grid is dependent on the resolution and quality of input data (Slb, 2010), variations within the original correlations would lead to inconsistencies within the modelled data. Interpretive uncertainty is suggested by wells 3b – 5, E4 and E28. It is noteworthy that digitized log data (ASCII Standard (LAS) files) was not available for this study. Consequently, the correlation work was interpreted using scanned, non-digitized images. Because readability was low in some places, there is still some uncertainty as to the exact GU thicknesses in these places. Several insights can be drawn from this:

I. Non uniqueness in the well correlation work: The well correlation exercise could be subject to a multitude of different interpretations.

II. This could change the boundary polygons selected for GU extents over the study area.

3.9.3 Fault geometry

Because of the unknown nature, 3D architecture and vertical extents of the faults, major faults were assumed to be syn depositional faults (Branter, 2003) dying out at the top of the KCF. Consequently the GU facies are modelled to thicken towards the faults outlined by N – S 5. However, cross section N – S 9 reveals that this features has not been modelled consistently. Consequently, GU facies horizons modelled close to the fault present a large uncertainty and interpreted horizons may not always be representative of the real geology at these points.

3.9.4 Accuracy of the 3D geometry of the model

The three models provide a basis to analyse the subsurface geometry of the model. It is apparent that the 38 well data rich model provides the most refined representation of the KCF caprock seal. However, without well tying using seismic data to construct the 3D geometry of the model, the model is more representative of Petrels ability to interpolate an accurate reference horizon (top KCF). This leads to spatial aliasing effects in between wells and subsurface inconsistencies arising from a lack of constraint in the second/third dimension and ultimately generating a less refined interpretation. Consequently, the predicted juxtapositions of foot-wall and hanging-wall rocks at faults N1 - 3, will in most cases be slightly different from the architecture actually present.

3.10 Future work

The limitations previously outlined indicate the uncertainty still remaining around the detailed modelling of the KCF caprock. Though expanded seismic datasets would help refine the resultant thickness maps, GU horizon trends would be relatively consistent with those observed. It is noteworthy that maximal model refinement would be to effectively model GU horizons close to faults and image the vertical extents of these faults and outline where they die out within a stratigraphic framework (Robbins, 2011).

Faults are assumed to be sealing because they act as baffles to flow, hence, compartmentalizing the East Brae Field, (Branter, 2003). However, recently published literature (SCCS, 2011) documents the presence of natural shallow gas chimneys and

pockmarks above sealing faults in the Captain aquifer (Robbins, 2011). This suggests faults have reactivated or leaked in the past and have allowed fluid expulsion. These features represent direct evidence for major fluid migration episodes, which may provide clues to plausible migration pathways (Heggland, 1998; Cole et al, 2000).

We would advocate for the interpretation and analysis of 'Boomer' and 'Sparker' shallow seismic data In any case, the shallow seismic data could help constrain the relationship between expressions of fluid expulsion (observed in 'Sparker' and 'Boomer') with the fault locations of deeper structures (interpreted from Marathon Oil).

Assuming faults extend into the secondary VF seal (comprised of marls), future consideration must be given to how hydro-fracturing might affect the seal integrity (Ingram et al, 1997). This phenomenon occurs when high pressure subsurface CO_2 injection exceeds the prevailing formation pressure, potentially leading to the reactivation of pre-existing faults and the creation of new ones (Gibson-Poole et al, 2004). Future work should also aim to examine containment issues such as fault stability in relation to maximum sustainable pore fluid pressure (Gibson-Poole et al, 2004; Streit et al, 2004). It is noteworthy that this could only be done if 2D/3D seismic data are acquired. Interpreted orientation of faults in 2D can provide relevant information for intricate geo-mechanical modelling focusing on the tendency of a fault to slip at a given point (Streit et al, 2004). Streit and Hillis's paper (2004, p1445), argues that incorporating geo-mechanical modelling of fault stability into the assessment of the seal will help 'evaluate the stability of faults' and allow the estimation of 'estimate fluid pressures that are sustainable in CO_2 storage sites'. Future work will, therefore, predict the effects of CO_2 injection on seal integrity and identify those faults that are most likely to slip by assigning an empirical value.

3.11 Concluding Remarks to Caprock Model

- This study demonstrates a workflow that other CCS projects may utilise to populate 3D caprock models when only well data is present. Models built within Petrel can be viewed as a good means to visually understand the structural geometry of the KCF caprock, outline the genetic unit facies within the primary seal and show where they are likely to pinch out, as well as, situating this in the context of an overlying secondary seal.

- The caprock is divided into three main genetic units which can be found throughout the whole of the East Brea field.

- Some uncertainties still exist within (1) the quality of the stage 1 model interpretation based on a limted number of wells; (2) fault geometry; and (3) accuracy of the 3D geometry of the model. Despite this our stage 2 model incorporating 38 wells appears to closely match real data.

- In the case of faults N1-N3 cross sections highlight a thick VF secondary seal supporting existing literature (Branter, 2003).

- It is noteworthy that the thickness maps are most reflective of the generalised thickness trends. However, these do not incorporate faults N1 – N3 and so are not reflective of localised points with large thickness variation.

- The study highlights data sensitivity issues suggesting that in the absence of seismic data, sites require moderate well coverage (20 wells) to yield a model that is reasonably representative of the true geological structure. In data poor areas as would be typical of most fields, the resultant model smoothes out even large scale features, due to spatial aliasing effects, and yields a model that poorly reflects the true structural geometry and GU horizons.

3.12 Discussion on proxies for mechanical behaviour

In Jarvie et al. 2007 Unconventional shale-gas systems: The Mississippian Barnett Shale of north-central Texas as one model for thermogenic shale-gas assessment.- AAPG Bulletin 91(4), the term "Brittleness of caprock" is employed. H-M Schultz (presentation to UEDIN - EAGE 2012) uses the following ternary plot of sandstone, calcite, clay:

For the Barnett Shale (from Jarvie et al. 2007)

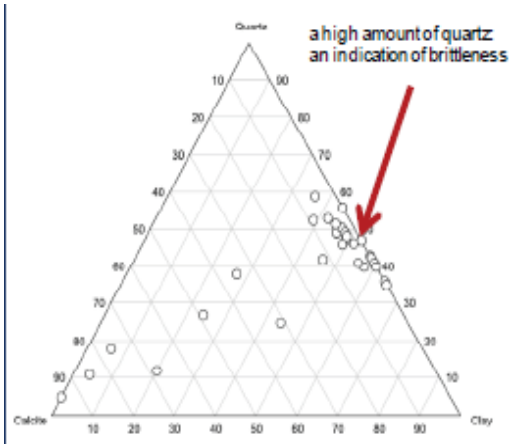

and

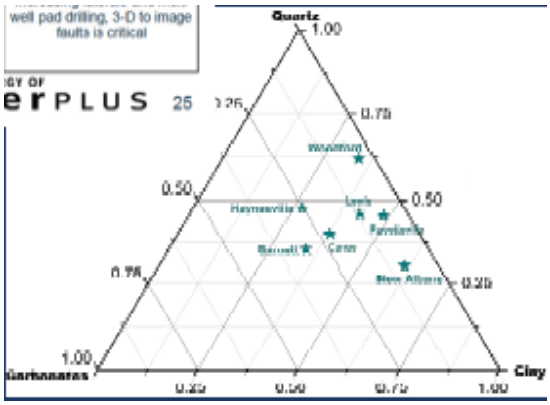

An alternative approach is classical Young's Modulus / Poisson's ratio relationships.

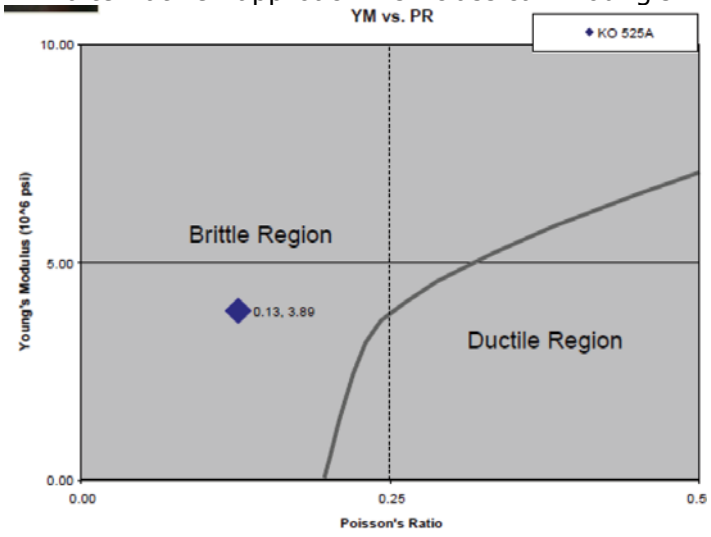

Again from Schultz to UEDIN 2012 via Rockenbauch courtesy Rohoeluntersuchung A.G.

A key issue that has thus far not been resolved is lab measurement (e.g. Poisson's ratio and Young's Modulus) variations between depth (c. 4000m) and surface and post-coring changes to clay moisture, oil-impregnation, etc. Hitherto, UEDIN have used a more classical shear strength definition for materials:

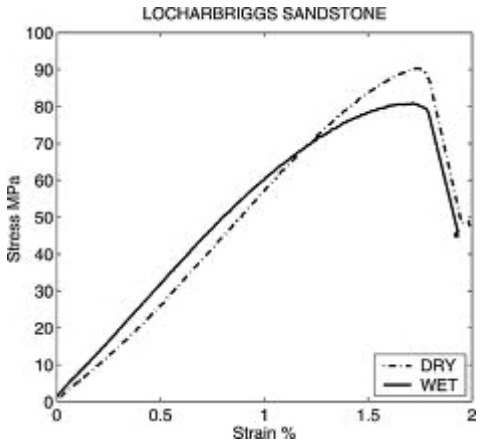

(from Ojala et al 2004 - http://www.era.lib.ed.ac.uk/bitstream/1842/501/1/irathesis.pdf)

The issue of tensile and not shear strength at depth is also little addressed. It is not clear whether meaningful Young's Modulus values and, moreover, clay shear and tensile strength values can be obtained &/or reliably used. Leak off test values LOT do provide some insight on the issue of tensile and not shear strength. LOT's are, however, rarely conducted in caprock (to our knowledge, unknown for the KCF). "Caprock" LOT's certainly exist for the shale gas plays but these data are presently commercially restricted.

Finally, it is unclear how specific a role there might be for the "calcite" microfacies (i.e. how mechanically independent)

3.13 Acknowledgements

This portion of the work was assisted by many. Data gathering; North Sea: Marathon Oil UK's Roger Connel and Colin Turner; USA: Gary Lash at SUNY Fredonia, NY, Jim Leone NY State Geological Survey and WSF Kidd SUNY Albany, NY; Data Processing: Arash JafarGandomi; Specific data or methodologies decsriptions were sourced from J.M.Lu, J.M.M.Flood, N.Odling, and M.Wilkinson. All SCCS and MUSTANG members are thanked for free and open discussion of results and ideas.

3.14 Appendices to Analogue Section

3.14.1 Appendix 1 Common Data Access

COMMON DATA ACCESS LIMITED (CDA) TECHNICAL NOTES

Overview
Common Data Access Limited (CDA) is a not-for-profit subsidiary of Oil & Gas UK. Their CDA "Well DataStore" holds various types of digital well information for >10,000 UKCS wells. Data is browsed and downloaded via a web portal. Access for University of Edinburgh researchers at the time of writing is free, on the condition of fair academic use. This data is not otherwise available to the public.

Common Data Access Limited "Well DataStore" Well Data Types

Available

The well data types available in the CDA "Well DataStore" are:

1) Raw Digital Well Logs: stored in the original format recorded by the logging contractor such as LIS, DLIS or BIT. They are the definitive raw archive set of this data and may contain many individual curves.

2) Well Reports and Well Logs: scanned images or native digital files held as well report images and well log images.

3) Digital Well Deviation Data: stored as digital, machine readable files with geodetic and calibration information in the file header. The recommended format for this data type is P7/2000.

4) Digital Data Files: digital well core analysis data (SCAL and CCA), digital seismic data (checkshots) and digital well test data (e.g. DST results).

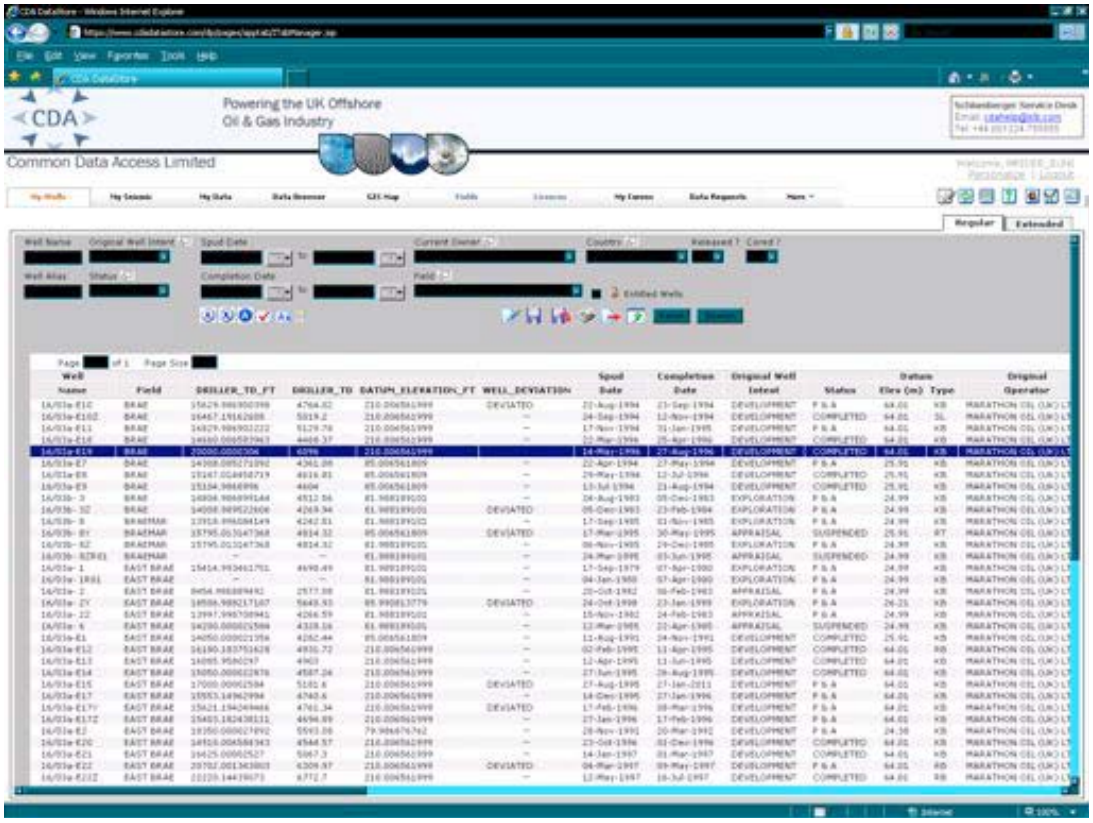

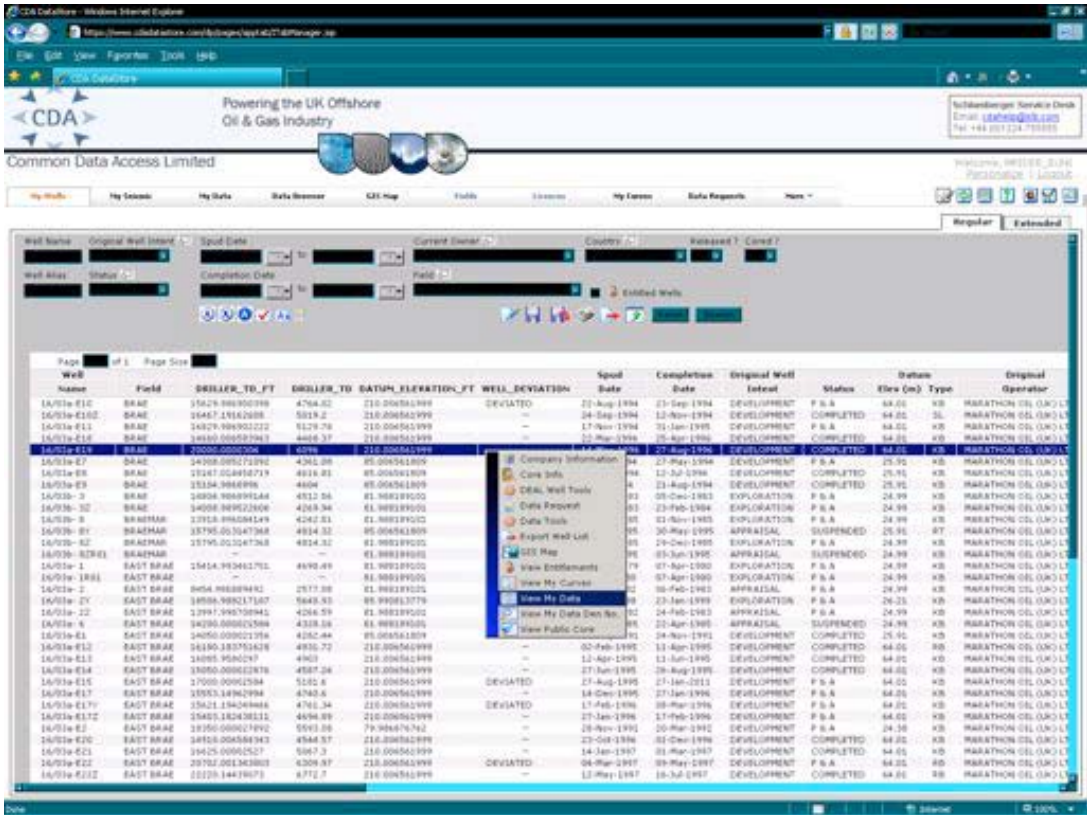

Common Data Access Limited "Well DataStore". This website contains various types of digital well information for more than 10,000 UKCS wells. Data can be browsed and downloaded via this web portal. Well data types include raw digital well logs, geological reports, core analysis data, and well deviation reports.

3.14.2 Appendix 2: Database from interpreted Kimmeridge Clay Formation Genetic Units and Secondary Seal.

Well	Z (MD, ft)	Z (TVDss, ft)	Z (TVDss, m)	Y UTM (m)	X UTM (m)	KB	GU Thickness (ft)	GU Thickness (m)	GU type	Total Depths (Driller - MD (ft)	Total Depths (TVD) (ft)
16/03a- 1	12528	-12503	-3811	6527988	414983	82	289	88	Top Valhall		
16/03a- 1	12874	-12792	-3899	6527988	414991	82	46	14	2	15415	
16/03a- 1	12920	-12838	-3913	6527988	414993	82					
16/03a-E1		-12365	-3769	6527564	415126	85	285	87	Top Valhall		
16/03a-E1	12793	-12650	-3856	6527564	415126	85	73	22	2	14050	-13906
16/03a-E1	12866	-12723	-3878	6527563	415126	85					
16/03a-E2		-13124	-4000	6528607	417922	85	202	62	Top Valhall		
16/03a-E2	17688	-13326	-4062	6528607	417922	85	30	9	1	18350	-13916
16/03a-E2	17722	-13356	-4071	6528607	417921	85					
16/03a-E2	17750	-13381	-4079	6528607	417921	85	25	8	2		
16/03a-E2	17874	-13491	-4112	6528607	417915	85	110	34	3		
16/03a-2Y	13361	-12758	-3889	6528518	416564	86	220	67	Top Valhall		
16/03a-2Y	13593	-12978	-3956	6528518	416564	86	35	11	1	18507	
16/03a-2Y	13630	-13013	-3966	6528518	416564	86					
16/03a-2Y	13650	-13032	-3972	6528518	416564	86	19	6	2		
16/03a-2Y	13678	-13059	-3980	6528518	416564	86	27	8	3		
16/03a-2Z	12970	-12888	-3928	6528478	416524	82	366	112	Top Valhall		
16/03a-2Z	13336	-13254	-4040	6528478	416524	82	36	11	1	13998	
16/03a-2Z	13372	-13290	-4051	6528478	416524	82					
16/03a-2Z	13382	-13300	-4054	6528479	416524	82	10	3	2		

16/03a-2Z	13408	-13326	-4062	6528479	416524	82	26	8	3		
16/03a-E3		**-12590**	-3837	**6527866**	**415403**	82	221	67	Top Valhall		
16/03a-E3	13162	-12811	-3905	6527866	415403	82	32	10	1	13910	-13559
16/03a-E3	13194	-12843	-3915	6527866	415403	82					
16/03a-E3	13239	-12888	-3928	6527866	415403	82	45	14	2		
16/03a-E4		**-13109**	-3996	**6525985**	**416525**	85	247	75	Top Valhall		
16/03a-E4	15330	-13356	-4071	6525983	416527	85	7	2	1	15868	13875
16/03a-E4	15337	-13363	-4073	6525982	416528	85					
16/03a-E4	15364	-13388	-4081	6525981	416528	85	25	8	2		
16/03a-E5		**-13191**	-4021	**6526984**	**417744**	85	293	89	Top Valhall		
16/03a-E5	17222	-13484	-4110	6526969	417766	85	60	18	1	17700	-13853
16/03a-E5	17300	-13544	-4128	6526963	417777	85					
16/03a-E5	17350	-13583	-4140	6526959	417784	85	39	12	2		
16/03a-E5	17458	-13667	-4166	6526950	417800	85	84	26	3		
16/03a-E6		**-13183**	-4018	**6529215**	**416876**	85	**182**	55	Top Valhall		
16/03a-E6	16556	-13365	-4074	6529220	416916	85	17	5	1	17200	-13846
16/03a-E6	16580	-13382	-4079	6529223	416921	85					
16/03a-E6	16630	-13419	-4090	6529226	416927	85	37	11	2		
16/03a-E6	16677	-13453	-4100	6529229	416939	85	34	10	3		
16/03a-E7		**-12677**	-3864	**6527050**	**414000**	210	**393**	120	Top Valhall		
16/03a-E7	13497	-13070	-3984	6527050	414313	210	53	16	1	14308	-13880
16/03a-E7	13550	-13123	-4000	6527050	414439	210					
16/03a-E7	13624	-13197	-4022	6527050	414616	210	74	23	2		
16/03a-E8		**-12864**	-3921	**6526111**	**415232**	210	**368**	112	Top Valhall		
16/03a-E8	14047	-13232	-4033	6526111	415232	210	15	5	1	15147	-13830
16/03a-E8	14072	-13247	-4038	6526111	415232	210					

16/03a-E8	14320	-13394	-4082	6526111	415232	210	147	45	2		
16/03a-E8	14395	-13439	-4096	6526111	415232	210	45	14	3		
16/03a-E9		-13029	-3971	6528385	414175	210	211	64	Top Valhall		
16/03a-E9	14416	-13240	-4036	6528385	414175	210	42	13	2	15105	-13922
16/03a-E9	14458	-13282	-4048	6528385	414175	210					
16/03a-E9	14473	-13297	-4053	6528385	414175	210	15	5	3		
16/03a-E10		-13088	-3989	6529052	415333	210	190	58	Top Valhall		
16/03a-E10	14748	-13278	-4047	6529056	415335	210	39	12	1	15630	-14115
16/03a-E10	14790	-13317	-4059	6529058	415336	210					
16/03a-E10	14881	-13403	-4085	6529062	415339	210	86	26	2		
16/03a-E10Z		-13078	-3986	6529052	415364	210	196	60	Top Valhall		
16/03a-E10Z	14772	-13274	-4046	6529052	415359	210	35	11	1	16467	-13648
16/03a-E10Z	14815	-13309	-4057	6529052	415355	210					
16/03a-E10Z	14911	-13388	-4081	6529052	415371	210	79	24	2		
16/03a-E11		-13063	-3982	6528067	416890	210	264	80	Top Valhall		
16/03a-E11	15552	-13327	-4062	6528067	416890	210	55	17	1	16830	-13905
16/03a-E11	15666	-13382	-4079	6528048	416889	210					
16/03a-E11	15710	-13403	-4085	6528041	416978	210	21	6	2		
16/03a-E11	15835	-13463	-4104	6528020	416968	210	60	18	3		
16/03a-E12		-12918	-3937	6528529	416450	210	274	84	Top Valhall		
16/03a-E12	15124	-13192	-4021	6528529	416463	210	30	9	1	16180	-13817
16/03a-E12	15166	-13222	-4030	6528530	416471	210					

16/03a-E12	15212	-13255	-4040	6528530	416478	210	33	10	2		
16/03a-E13		-12888	-3928	6526300	414050	210	364	111	Top Valhall		
16/03a-E13	15016	-13252	-4039	6526293	414060	210	58	18	1	16087	-13929
16/03a-E13	15100	-13310	-4057	6526277	414081	210					
16/03a-E13	15160	-13352	-4070	65262566	414096	210	42	13	2		
16/03a-E13	15213	-13389	-4081	6526256	414109	210	37	11	3		
16/03a-E14		-12729	-3880	6527725	415835	210	259	79	Top Valhall		
16/03a-E14	13564	-12988	-3959	6527698	415841	210	27	8	1	15050	-13872
16/03a-E14	13600	-13015	-3967	6527669	415848	210					
16/03a-E14	13630	-13038	-3974	6527644	415854	210	23	7	2		
16/03a-E14	13677	-13074	-3985	6527606	415862	210	36	11	3		
16/03a-E15		-13140	-4005	6525284	416409	210	197	60	Top Valhall		
16/03a-E15	16319	-13337	-4065	6525276	416407	210	49	15	1	17000	-13936
16/03a-E15	16374	-13386	-4080	6525269	416405	210					
16/03a-E15	16426	-13432	-4094	6525262	416403	210	46	14	2		
16/03a-E15	16477	-13478	-4108	6525256	416402	210	46	14	3		
16/03a-E16	15114	-13300	-4054	6527165	413634	210	224	68	Top Valhall		
16/03a-E16	15489	-13524	-4122	6527130	413598	210	69	21	1	16379	-14113
16/03a-E16	15600	-13593	-4143	6527109	413585	210					
16/03a-E16	15670	-13636	-4156	6527096	413577	210	43	13	2		
16/03a-	15740	-13679	-4169	6527084	413569	210	43	13	3		

E16											
16/03a-E16	15810	-13723	-4183	6527070	413561	210	44	13	1		
16/03a-E16	15854	-13750	-4191	6527062	413556	210	23	7	2		
16/03a-E16Z		**-12518**	-3815	**6527978**	**414505**	210	**250**	76	Top Valhall		
16/03a-E16Z	14515	-12768	-3892	6527978	414505	210	61	19	2	15472	-12575
16/03a-E16Z	14553	-12829	-3910	6527978	414505	210					
16/03a-E17		**-12859**	-3919	**6526930**	**416450**	210	194	59	Top Valhall		
16/03a-E17	14555	-13053	-3979	6526901	416469	210	28	9	1	15500	-13790
16/03a-E17	14590	-13081	-3987	6526888	416479	210					
16/03a-E17	14650	-13130	-4002	6526864	416490	210	49	15	2		
16/03a-E17	14700	-13171	-4015	6526857	416501	210	41	12	3		
16/03a-E18	13873	**-12892**	-3929	**6528508**	**415321**	**210**	**198**	60	Top Valhall		
16/03a-E18	14072	-13090	-3990	6528508	415322	210	38	12	1	14660	-13677
16/03a-E18	14110	-13128	-4001	6528508	415323	210					
16/03a-E18	14150	-13168	-4014	6528508	415324	210	40	12	2		
16/03a-E19	19143	-13176	-4016	6528167	418643	210	243	74	Top Valhall		
16/03a-E19	19396	-13419	-4090	6528166	418664	210	71	22	1	20000	-14000
16/03a-E19	19470	-13490	-4112	6528166	418671	210					
16/03a-E19	19500	-13519	-4121	6528165	418673	210	29	9	2		
16/03a-E19	19537	-13555	-4132	6528165	418677	210	36	11	3		
16/03a-E20	13854	-12843	-3915	6526534	415972	210	126	38	Top Valhall		

16/03a-E20	13981	-12969	-3953	6526536	415972	210	41	12	1	14910	-13897
16/03a-E20	14022	-13010	-3965	6526537	415972	210					
16/03a-E20	14100	-13088	-3989	6526538	415972	210	78	24	2		
16-03a-E21	15678	-13053	-3979	6526226	417118	210	262	80	Top Valhall		
16-03a-E21	15950	-13315	-4058	6526221	417122	210	39	12	1	16625	-13971
16-03a-E21	15990	-13354	-4070	6526219	417124	210					
16-03a-E21	16050	-13413	-4088	6526216	417129	210	59	18	2		
16-03a-E21	16076	-13437	-4096	6526215	417130	210	24	7	3		
16/03a-E23	17051	-13157	-4010	6525411	417319	210	241	73	Top Valhall		
16/03a-E23	17330	-13398	-4084	6525392	417325	210	25	8	1	18005	-13974
16/03a-E23	17360	-13423	-4091	6525389	417329	210					
16/03a-E23	17400	-13457	-4102	6525385	417333	210	34	10	2		
16/03a-E23	17438	-13489	-4111	6525382	417336	210	32	10	3		
16/03a-E23Z	16778	-13063	-3982	6525791	416890	210	162	49	Top Valhall		
16/03a-E23Z	16991	-13225	-4031	6525782	416898	210	40	12	1	17784	-14016
16/03a-E23Z	17030	-13265	-4043	6525779	416902	210					
16/03a-E23Z	17100	-13331	-4063	6525772	416909	210	66	20	2		
16/03a-E23Z	17141	-13489	-4111	6525765	416913	210	158	48	3		
16/03a-E24	14688	-12853	-3918	6528104	416188	210	221	67	Top Valhall		
16/03a-E24	15006	-13074	-3985	6528101	416177	210	37	11	1	15918	-14074
16/03a-E24	15050	-13111	-3996	6528099	416168	210					

16/03a-E24	15090	-13145	-4007	6528097	416162	210	34	10	2		
16/03a-E25	14002	-12741	-3883	6528153	415020	210	134	41	Top Valhall		
16/03a-E25	14163	-12875	-3924	6528149	415018	210	29	9	2	14970	-13710
16/03a-E25	14198	-12904	-3933	6528143	415016	210					
16/03a-E26		-12985	-3958	6527205	415988	210	212	65	Top Valhall		
16/03a-E26	13878	-13197	-4022	6527205	415988	210	11	3	1	14474	-14001
16/03a-E26	13890	-13208	-4026	6527204	415988	210					
16/03a-E26	13898	-13216	-4028	6527204	415988	210	8	2	2		
16/03a-E27	17237	-13212	-4027	6527276	417949	210	323	98	Top Valhall		
16/03a-E27	17622	-13535	-4125	6527276	417969	210	45	14	1	18144	-13889
16/03a-E27	17700	-13580	-4139	6527276	417980	210					
16/03a-E27	17750	-13609	-4148	6527276	417987	210	29	9	2		
16/03a-E27	17823	-13652	-4161	6527276	417997	210	43	13	3		
16/03a-E28	13530	-12848	-3916	6527499	414529	210	281	86	Top Valhall		
16/03a-E28	13874	-13129	-4002	6527499	414525	210	52	16	1	14700	-13813
16/03a-E28	13940	-13181	-4018	6527500	414522	210					
16/03a-E28	13986	-13217	-4029	6527500	414520	210	36	11	2		
16/03a-E28Z		-12811	-3905	6527360	415067	210	337	103	Top Valhall		
16/03a-E28Z	13933	-13148	-4008	6527360	415067	210	70	21	1	14980	-13938
16/03a-E28Z	14030	-13218	-4029	6527360	415067	210					
16/03a-E28Z	14130	-13290	-4051	6527360	415067	210	72	22	2		
16/03a-	14193	-13335	-4065	6527360	415067	210	40	12	3		

E28Z											
16/03a-E29	15782	-12886	-3928	6527670	416676	210	297	91	Top Valhall		
16/03a-E29	16091	-13183	-4018	6527670	416676	210	38	12	1	16782	-13856
16/03a-E29	16130	-13221	-4030	6527670	416676	210					
16/03a-E29	16170	-13260	-4042	6527670	416676	210	39	12	2		
16/03a-E29	16227	-13315	-4058	6527670	416676	210	55	17	3		
16/03b-3Z	12960	-12878	-3925	6526004	414722	82	504	154	Top Valhall		
16/03b-3Z	13464	-13382	-4079	6526004	414722	82	86	26	1	14805	
16/03b-3Z	13550	-13468	-4105	6526004	414722	82					
16/03b-3Z	13600	-13518	-4120	6526004	414722	82	50	15	2		
16/03b-3Z	13663	-13581	-4139	6526004	414722	82	63	19	3		
16/03b- 5	13204	-13122	-4000	6528433	417955	82	161	49	Top Valhall		
16/03b- 5	13365	-13283	-4049	6528433	417955	82	55	17	1	14208	
16/03b- 5	13420	-13338	-4065	6528433	417955	82					
16/03b- 5	13480	-13398	-4084	6528433	417955	82	60	18	2		
16/03b- 5	13525	-13443	-4097	6528433	417955	82	45	14	3		
16/03b- 7	13115	13033	3972	6525615	416448	82	231	70	Top Valhall		
16/03b- 7	13346	-13264	-4043	6525615	416448	82	44	13	1	14525	
16/03b- 7	13390	-13308	-4056	6525616	416448	82					
16/03b- 7	13430	-13348	-4068	6525616	416448	82	40	12	2		
16/03b- 7	13502	-13420	-4090	6525616	416448	82	72	22	3		

3.14.3 Appendix 3: Caprock Cross Sections

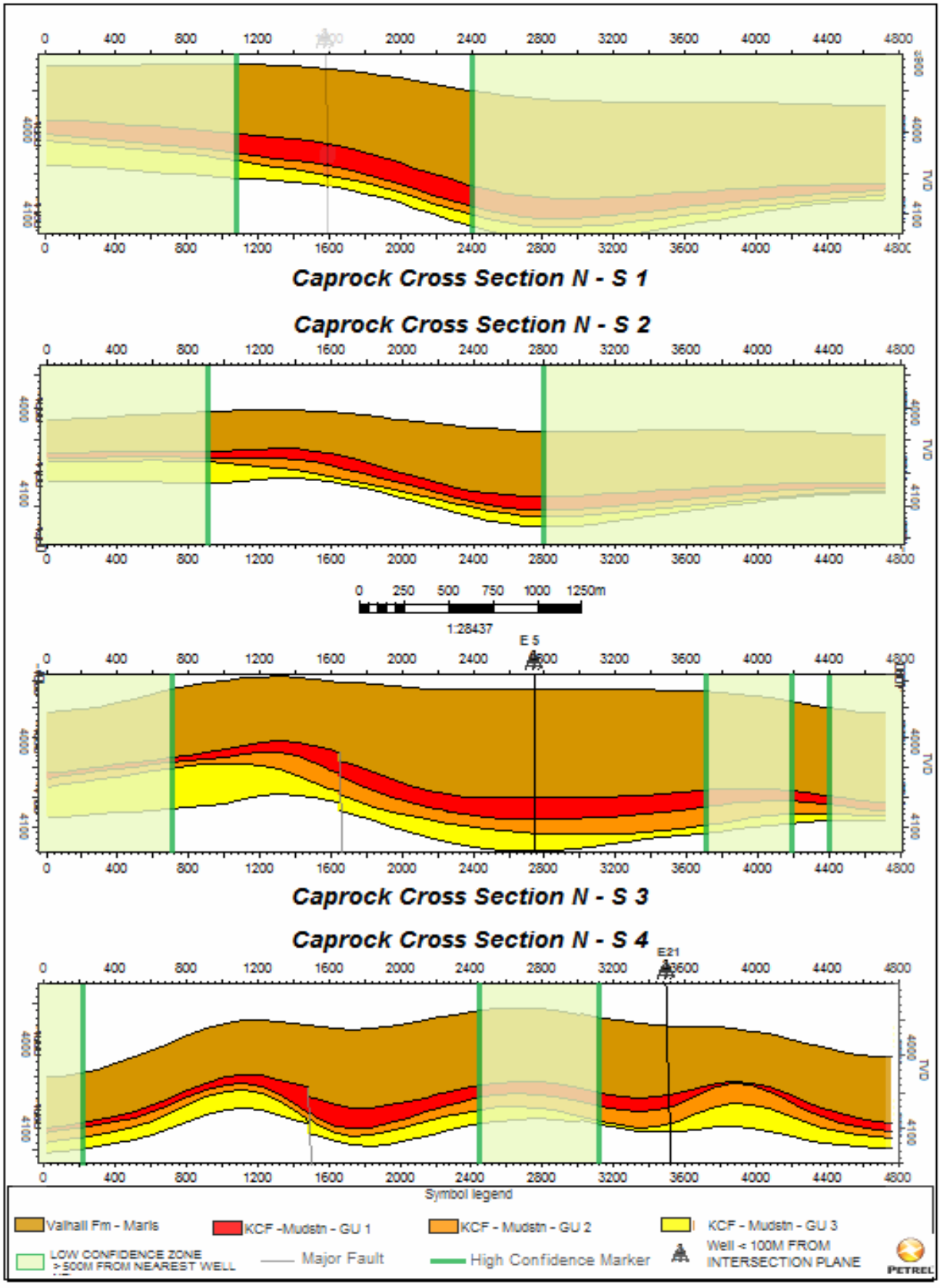

APPENDIX 3B

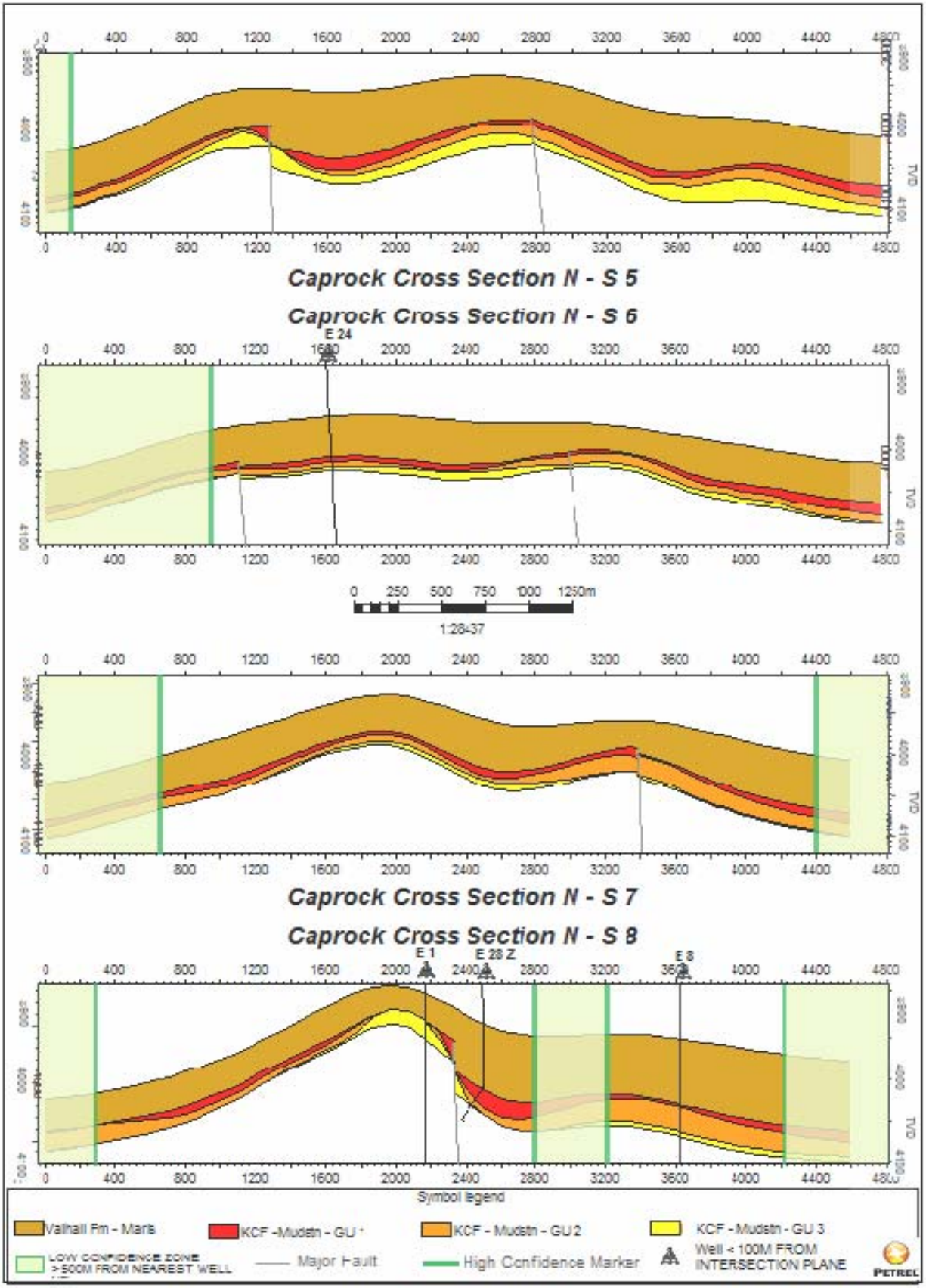
Caprock Cross Section N - S 5
Caprock Cross Section N - S 6
E 24
0 250 500 750 1000 1250m
1:28437
Caprock Cross Section N - S 7
Caprock Cross Section N - S 8
E 1
E 28 Z
E 8
TVD
Symbol legend
Valhall Fm - Marls
KCF -Mudstn - GU 1
KCF - Mudstn - GU 2
KCF - Mudstn - GU 3
LOW CONFIDENCE ZONE >500M FROM NEAREST WELL
Major Fault
High Confidence Marker
Well < 100M FROM INTERSECTION PLANE
PETREL

APPENDIX 3C

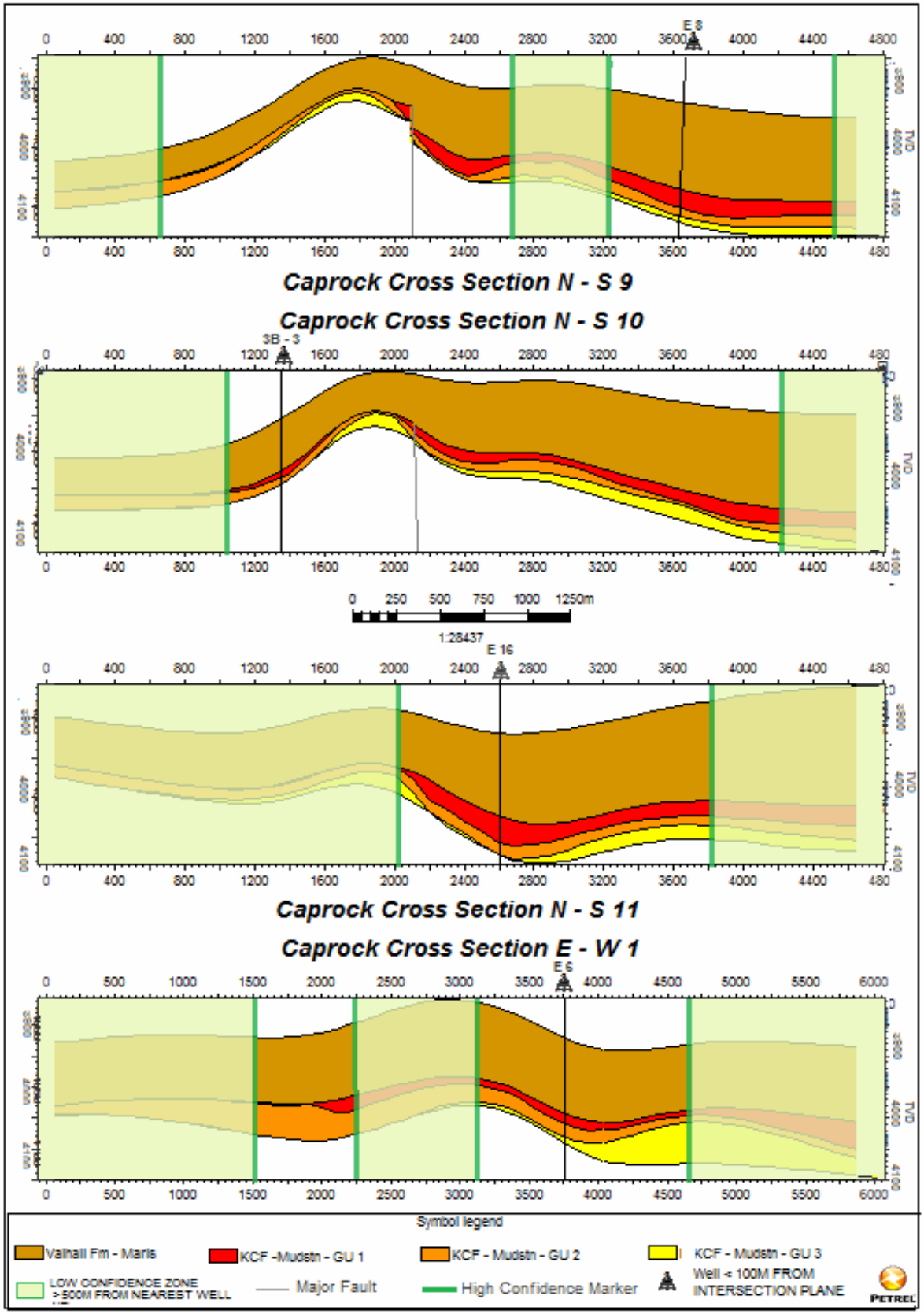
E 8
Caprock Cross Section N - S 9
Caprock Cross Section N - S 10
3B - 3
0 250 500 750 1000 1250m
1:28437
E 16
Caprock Cross Section N - S 11
Caprock Cross Section E - W 1
E 6
Symbol legend
Valhall Fm - Maris
KCF -Mudstn - GU 1
KCF - Mudstn - GU 2
KCF - Mudstn - GU 3
LOW CONFIDENCE ZONE >500M FROM NEAREST WELL
Major Fault
High Confidence Marker
Well < 100M FROM INTERSECTION PLANE
PETREL

APENDIX 3D

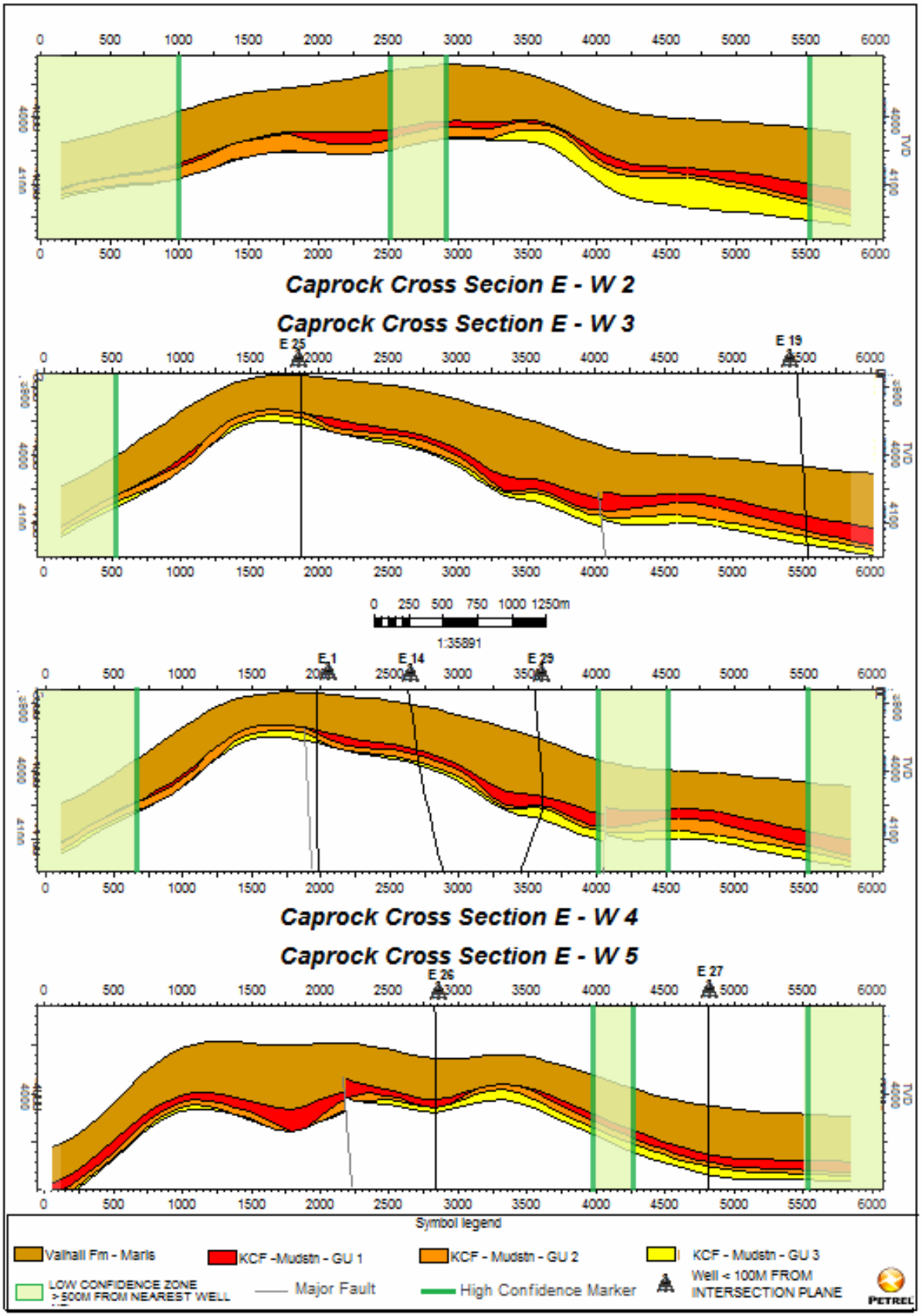
Caprock Cross Secion E - W 2
Caprock Cross Section E - W 3
E 25
E 19
0 250 500 750 1000 1250m
1:35891
E 1
E 14
E 29
Caprock Cross Section E - W 4
Caprock Cross Section E - W 5
E 26
E 27
Symbol legend
Valhall Fm - Marls
KCF -Mudstn - GU 1
KCF - Mudstn - GU 2
KCF - Mudstn - GU 3
LOW CONFIDENCE ZONE >500M FROM NEAREST WELL
Major Fault
High Confidence Marker
Well < 100M FROM INTERSECTION PLANE
PETREL

APPENDIX 3E

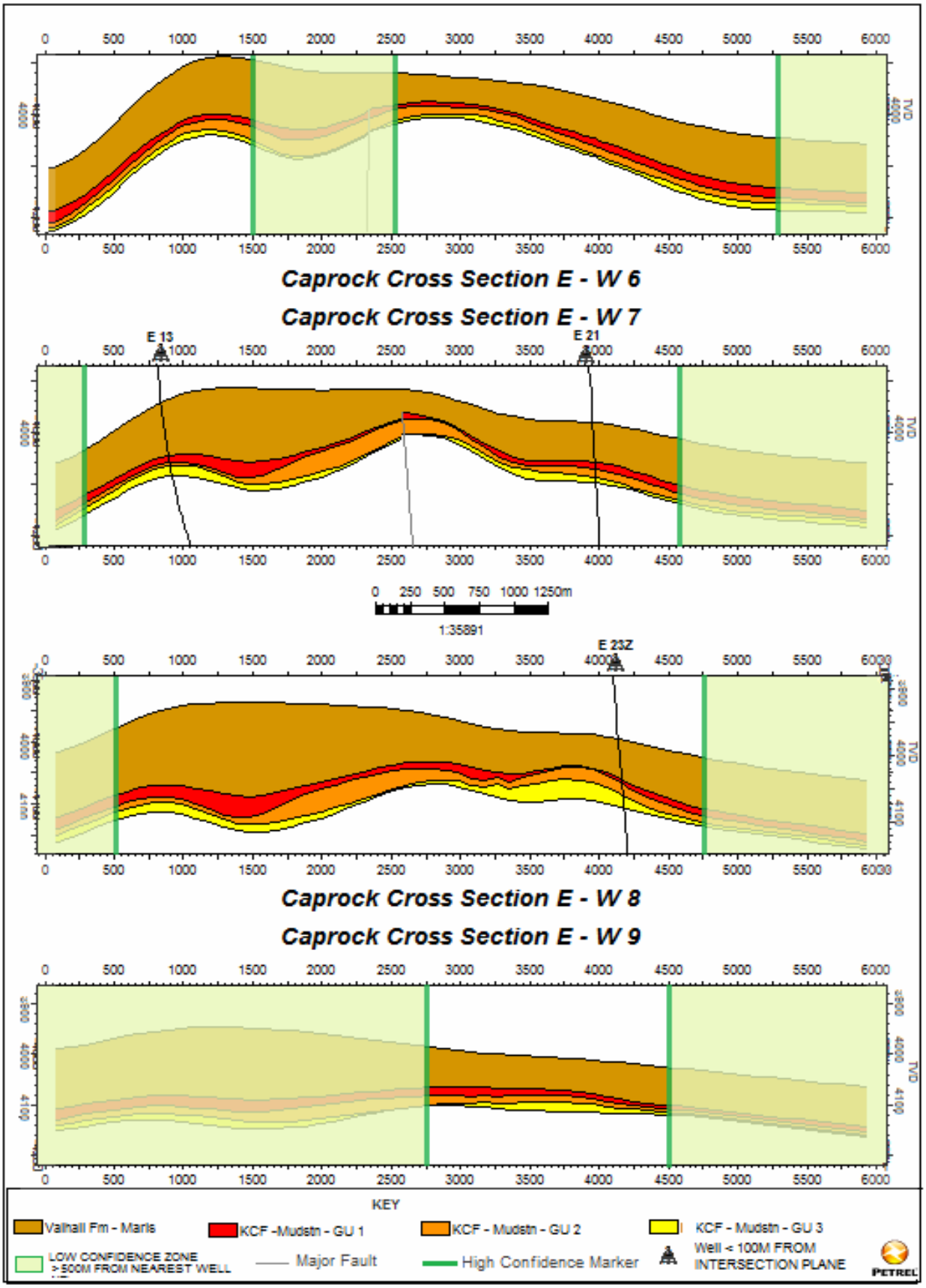
Caprock Cross Section E - W 6
Caprock Cross Section E - W 7
E 13
E 21
0 250 500 750 1000 1250m
1:35891
E 23Z
Caprock Cross Section E - W 8
Caprock Cross Section E - W 9
KEY
Valhall Fm - Marls
KCF -Mudstn - GU 1
KCF - Mudstn - GU 2
KCF - Mudstn - GU 3
LOW CONFIDENCE ZONE >500M FROM NEAREST WELL
Major Fault
High Confidence Marker
Well < 100M FROM INTERSECTION PLANE
PETREL

3.14.4 Kimmeridge Clay Formation Core Samples

E Brae availability of Kimmeridge Clay Formation

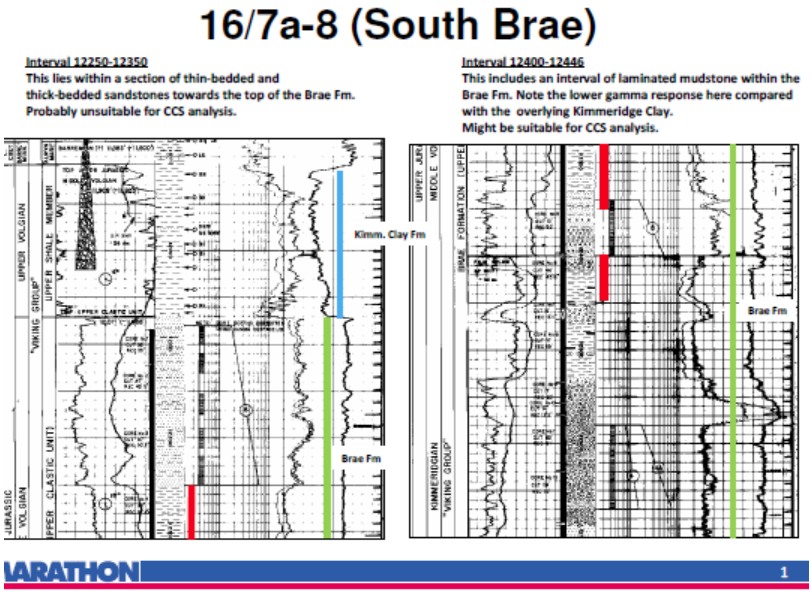

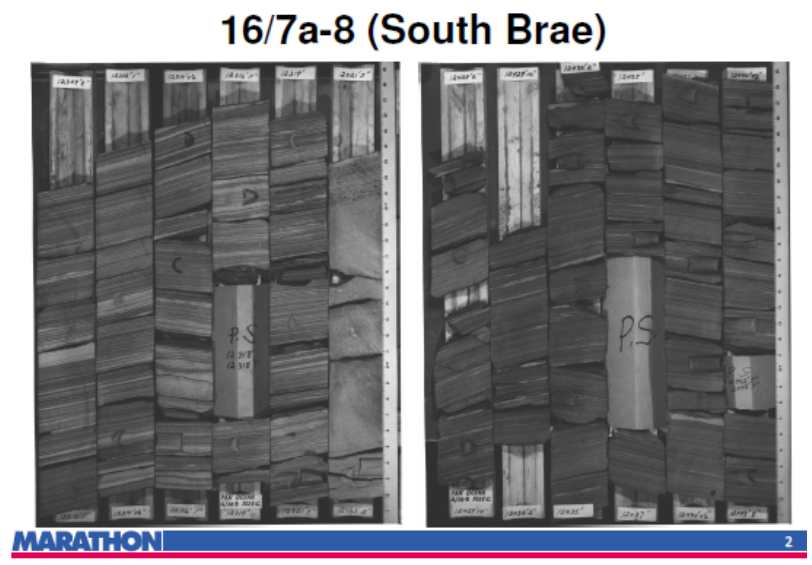

16/7a-10 (South Brae)

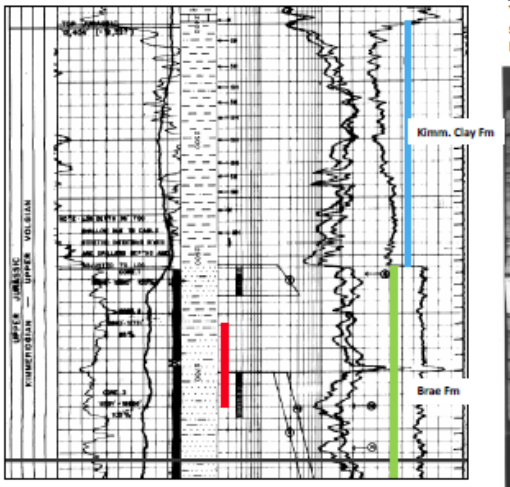

Interval 12660-12731
This lies within a section of thin-bedded sandstones towards the top of the Brae Fm.
Probably unsuitable for CCS analysis.

MARATHON

16/7a-14 (North Brae)

Interval 11906-11964
This lies within the lowest part of the Kimm. Clay and comprises massive and laminated mudstone.
Should be suitable for CCS analysis.

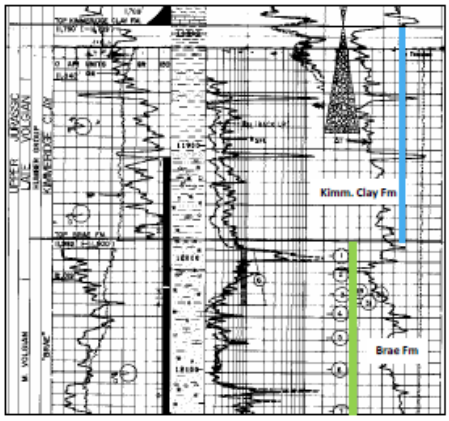

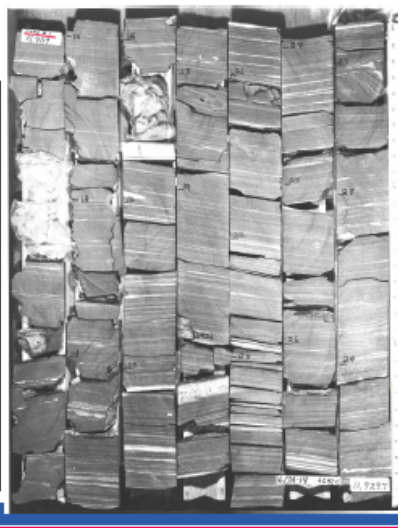

MARATHON

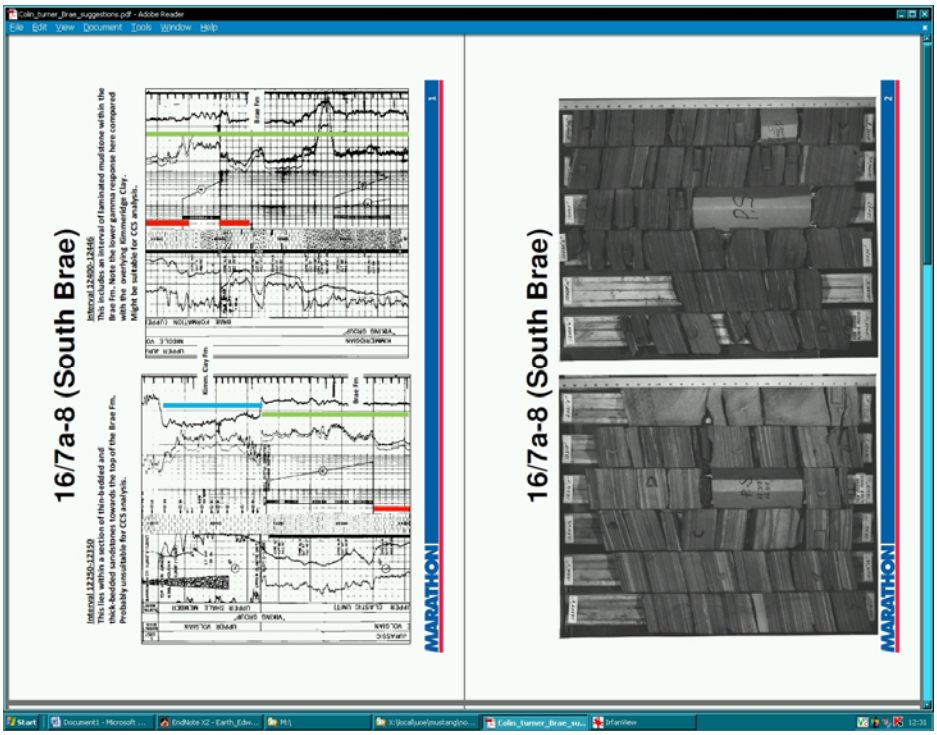

3.14.5 List of websites or sources checked for W. New York sate satellite imagery

***Notes**: M. A. Edwards*
***Date**: Monday, 15 November 2010*

Key Target; Gratiot Point

http://www.landmap.ac.uk
seem to only be UK ???

Using geohack, basically only two sat. data sources available as per, Bing versus Google

http://www.wikimapia.org/#lat=42.4942967&lon=-79.3540147&z=19&l=0&m=b
is also google

http://www.terraserver.com/view.asp?cx=-79.333889&cy=42.440833&proj=4326&mpp=2.5&pic=img
is also poor

http://maps.google.com/maps?ll=42.493889,-79.353889&spn=0.01,0.01&t=m&q=42.493889,-79.353889

http://browse.digitalglobe.com/imagefinder/main.jsp
Offers inspection strips, Interactive map tool found and used, requested inspection image, selected "max available
Res." from the dropdown; no sufficiently high resolution samples offered for area of interest, otherwise high cost commercial (screen shot below) ……

But….. ImageFinder Order Inquiry…….A representative from DigitalGlobe will be in contact with you shortly !
Price enquiry made.

http://resmap.com/imagery.aspx
too slow to know if good resolution

Quickbird or Ikonos, as part of...
http://www.satimagingcorp.com/
not free.....

USGS offer LIDAR of excellent quality but NOT OFFSHORE !! (see screenshot below)

http://www.nysgis.state.ny.us/
NYS GIS Digital Clearinghouse - Free Orthoimagery:
Orthoimagery is 1 "foot" per pixel good downloading options... Interactive map tool found and used, downloaded from 2 packages of State Plane grids for zoomed into Gratiot Point:
Chautauqua County (2008) data, New York State Plane , Western Zone , NAD 83, US Survey Feet, Orthoimagery Type: 12 - inch Resolution 4 band Digital. JP2 (used IrfanView in Windows, for first look)

.....and is identical to Google Satellite ! (see screenshot below)

RESULT: use Google

see also:
http://landsat.usgs.gov/panchromatic_image_sharpening.php

digitalglobe.com….

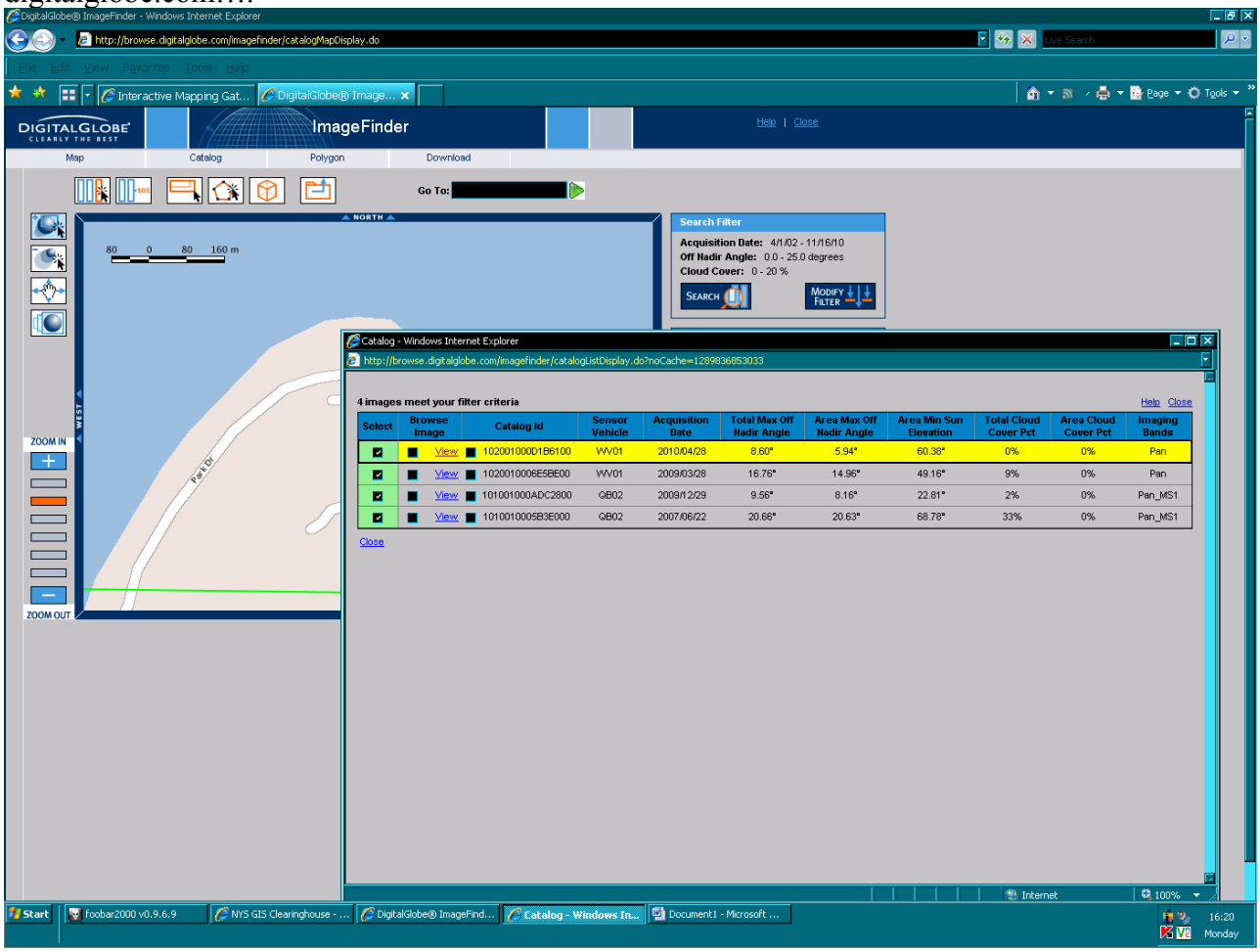

www.nysgis.state.ny.us.....

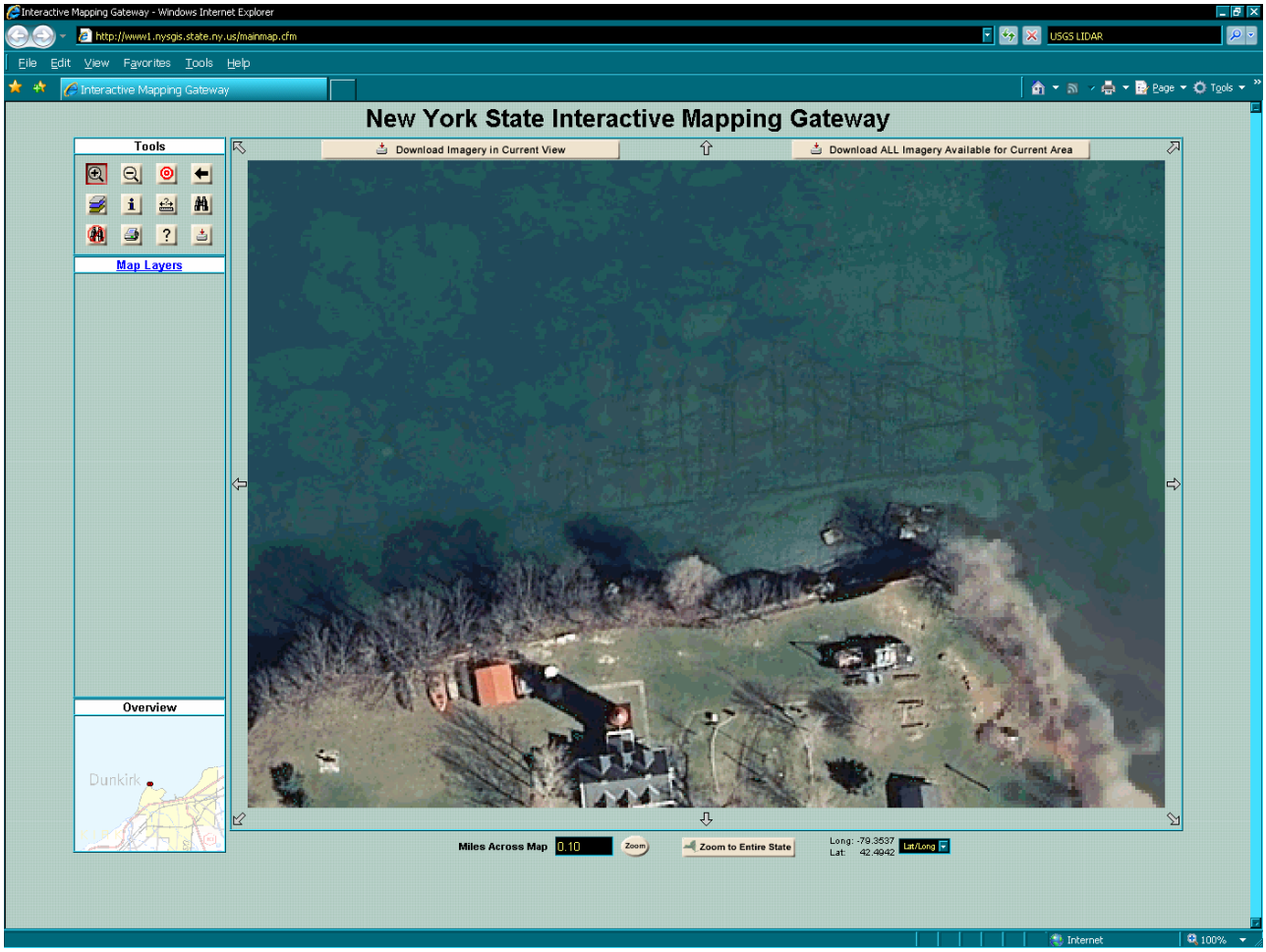

...is also that which appears for GoogleMaps.

3.14.6 Mustang caprock sampling strategies notes

Although Marathon posses km's of Brae core, core reports are minimal (both for the CDA-archives AND Marathon's own) and notably, Marathon's KCF archive does not have:

- glossy folder
- photos of resined slabs
- fracture map
- (poro-perm from plugs - restricted to sand intervals)
- luminsence scan
- rel permeability test data off plugs
- petrophysics test data off plugs

3.14.7 Contact Addresses and Locations of selected collaborators outwith main Mustang group

Roger Connell....

Marathon House
Rubislaw Hill
Anderson Dive
Aberdeen AB15 6FZ
Tel +44 1224 80 3000
Fax: +44 1224 80 3190

also for Colin Turner & Mark Stephenson

Graham J Tulloch

Scottish Collections Administrator
British Geological Survey
NGDC Gilmerton Core Store
376 Gilmerton Road
Edinburgh
EH17 7QS

4 Numerical Investigation of Experimental and Analogue Results

4.1 Overview

Two papers and a third manuscript in preparation are presented demonstrating the linkage between the analogue, experimental and numerical modelling work. The numerical work focuses on the development of an existing open source code to reflect THMC observation and behaviour of CO2 injected in the storage reservoir.

Paper 1 *Christopher I. McDermott, Alex Bond, Wenqing Wang and Olaf Kolditz, Front Tracking using a Hybrid Analytical Finite Element Approach for Two Phase Flow applied to Supercritical CO2 Replacing Brine in a Heterogeneous Reservoir and Caprock, Transport in Porous Media: Volume 90, Issue 2 (2011), Page 545-573, DOI 10.1007/S11242-011-9799-5, Appendix.*

Paper 2: *C.I. McDermott, K. Edlmann, M. Edwards, R.S. Haszeldine, Draft of Paper Currently in Review, Predicting hydraulic tensile-fracture spacing in strata-bound systems, Journal of Structural Geology, Appendix.*

Paper 3: *C.I. McDermott, K. Edlmann, O. Kolditz, R.S. Haszeldine, In preparation, Predicting hydraulic fracturing in multilayered sequences using a hybrid numerical analytical approach, to be submitted to the Journal of Petroleum Geoscience, with a further submission regarding the numerical methods employed possibly to computational geoscience, Appendix.*

4.2 Discussion

Numerical modelling has shown the importance and impact of heterogeneities on the distribution of CO2 both in the reservoir and the development of preferential flow paths due to two phase flow and the impact of self reinforcing relative permeabilities both within the reservoir and within the retaining media and overburden. Consideration of the impact of coupled processes requires that the front location of the CO2 brine interface is understood stochastically to enable the prediction of the impact of coupled processes such as seismic release due to discontinuity reaction under changing mechanical regime due to the increase of fluid pressure and the change in the properties of the fluids migrating through the porous/fractured materials.

Predicting fluid replacement by two phase flow in heterogeneous porous media is of importance for issues such as supercritical CO2 sequestration, the integrity of caprocks and the operation of oil water/brine systems. Modelling two phase flow using grid based techniques presents a problem as the fluid-fluid interface location is approximated within the scale of the discretisation used. Adaptive grid methods allow the discretisation to follow the interface through the model, but are computationally expensive and make coupling to other processes (Thermal, Mechanical, Chemical) complicated due to the constant alteration in grid size. Interface tracking methods have been developed that apply sophisticated reconstruction algorithms based on either the ratio of volumes of a fluid in an element (Volume of Fluid Methods) or the advective velocity of the interface throughout the modelling regime (Level Set Method). In this paper we present an "Analytical Front Tracking" method where a generic analytical solution for two

phase flow is used to "add information" to a finite element model and predict the location of the front within individual geometrical elements. This removes the necessity for grid adaptation, and reduces the need for assumptions as to the shape of the interface. The method is verified against a standard benchmark solution and then applied to the case of supercritical CO2 pooling and forcing its way into a heterogeneous caprock, replacing hot brine and eventually breaking through. The hybrid analytical numerical method presented proves to be computationally efficient, and able to solve two phase flow in heterogeneous fields.

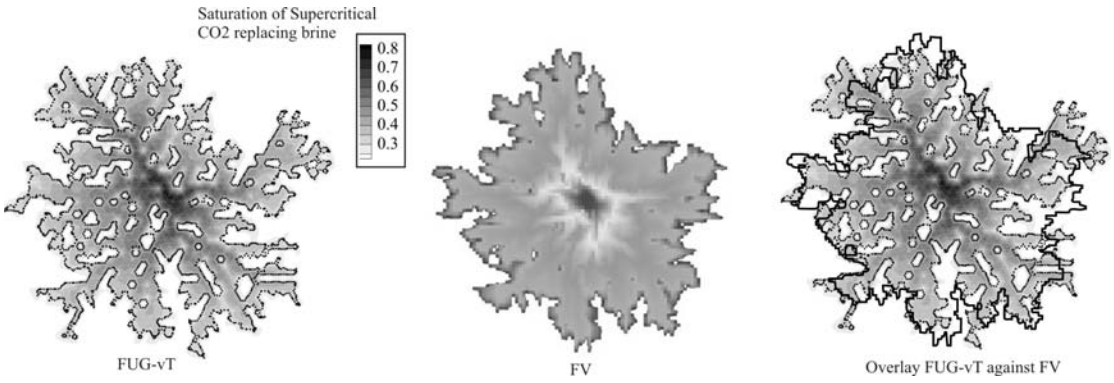

Figure 106 Comparison of finite element with front tracking and a finite volume approach for CO2 spreading in a heterogeneous reservoir.

During fluid injection into a reservoir the pore pressure of the reservoir increases as one fluid displaces another. This fluid pressure will be most easily relaxed by vertical migration in a system where horizontal stresses outweigh vertical stresses. The impact is vertical movement of fluids, uplift of retaining caprocks and the development of overpressure in sealed systems. Strat bound fracturing is considered to be both a combination of extensional uplift in sedimentary systems and fluid pressure fracturing.

A model is presented which predicts the spacing of tensile-fractures due to fluid pressure increase in a multilayered sedimentary sequence comprising different typical sedimentary deposits such as mudstones, siltstones, sandstones. This model is both applicable for engineered applications such as the injection of fluid into a reservoir thereby causing an increase of fluid pressure beneath a caprock, and for sedimentary sequences during normal digenetic processes of burial and fault activation. The model predicts many of the field observations made about strata bound fracture systems. A standard normalised relationship is provided for most sedimentary systems predicting the spacing of discontinuities based on the variability of the tensile strengths of the layers of a sedimentary sequence and the thickness of the beds. The model provides a tool for assessing the historic fluid pressures in beds based on fracture spacing observations, and will aid in the prediction of the behaviour of such strata and the development of discontinuities during engineered fluid injection

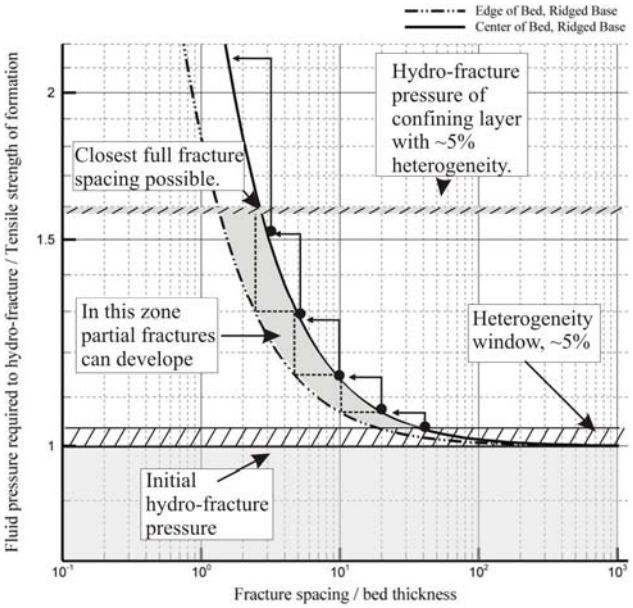

Figure 107 Model predicting tensile fracturing of layered sedimentary sequences during fluid injection

To be of use to industry this approach has been developed to allow the natural heterogeneities in a system to be expressed numerically within the confines of a finite model grid approach. We present a hybrid numerical analytical model describing the development of strata bound tensile fracturing in multilayered sedimentary systems. The model uses the open source code OpenGeoSys as a development platform for the integration of functions describing rock behaviour as the fluid pressure is increased due to injection. The solver is used to evaluate iteratively fluid pressure in the layer sequences during injection coupled with material behaviour models to represent the development of fractures under critical tensile failure pressure conditions. The model and numerical approach is shown to reproduce typical hydrofrac pressure flow profiles, and is then expanded to describe the development of strat bound fracturing in multilayered systems. An analytical model based on elastic stress solutions is integrated to express the mechanical interaction of fractures and predict the location of the formation of the fractures. The model allows for the heterogeneity of the mechanical parameters in a sequence to be described, as well as key factors such as tensile strength, permeability, bed thickness and injection rates to be investigated. The results of the modelling agree with general field observations and suggest that this tool may be a useful approach to evaluating the impact of fluid pressure increase in stacked sedimentary (but also igneous) systems.

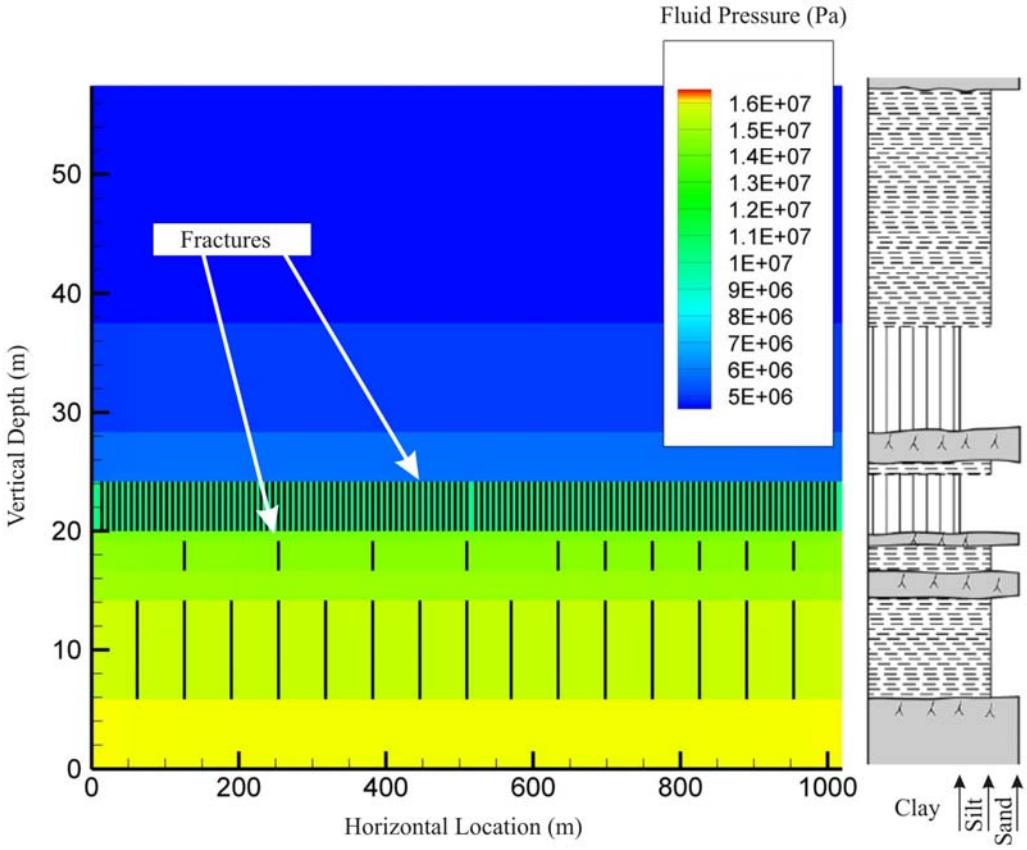

Figure 108 Illustration of a caprock fracturing during fluid pressure increase, sedimentary section of cyclical sequence after Kassi et al. 2004, from the lower Carboniferous of Scotland.

Further work is continuing on coupling fluid pressure increases, mechanical uplift with extensional regimes due to strata uplift.

4.3 Paper: Front Tracking using a Hybrid Analytical Finite Element Approach for Two Phase Flow Applied to Supercritical CO2 Replacing Brine in a Heterogeneous Reservoir and Caprock.

Christopher I McDermott

Edinburgh Collaborative of Subsurface Science and Engineering (ECOSSE), School of Geoscience, University of Edinburgh, West Mains Road, Edinburgh, EH9 3JW, Scotland

Email cmcdermo@staffmail.ed.ac.uk

Alexander E Bond

Quintessa Ltd., Chadwick House, Birchwood Park, Warrington, Cheshire, UK, WA3 6AE

Email alexbond@quintessa.org

Wenqing Wang

Helmholtz Center for Environmental Research, Leipzig, Germany

Technische Universität Dresden, Applied Environmental System Analysis, Germany

Email wenqing.wang@ufz.de

Olaf Kolditz

Helmholtz Center for Environmental Research, Leipzig, Germany

Technische Universität Dresden, Applied Environmental System Analysis, Germany

Email olaf.kolditz@ufz.de

Abstract

Predicting fluid replacement by two phase flow in heterogeneous porous media is of importance for issues such as supercritical CO_2 sequestration, the integrity of caprocks and the operation of oil water/brine systems. When considering coupled process modelling, the location of the interface is of importance as most of the significant interaction between processes will be happening there. Modelling two phase flow using grid based techniques presents a problem as the fluid-fluid interface location is approximated across the scale of the discretisation. Adaptive grid methods allow the discretisation to follow the interface through the model, but are computationally expensive and make coupling to other processes (Thermal, Mechanical, Chemical) complicated due to the constant alteration in grid size and effects thereof. Interface tracking methods have been developed that apply sophisticated reconstruction algorithms based on either the ratio of volumes of a fluid in an element (Volume of Fluid Methods) or the advective velocity of the interface throughout the modelling regime (Level Set Method). In this paper we present an "Analytical Front Tracking" method where a generic analytical solution for two phase flow is used to "add information" to a finite element model. The location of the front within individual geometrical elements is predicted using the saturation values in the elements and the velocity field of the element. This removes the necessity for grid adaptation, and reduces the need for assumptions as to the shape of the interface as this is predicted by the analytical solution. The method is verified against a standard benchmark solution and then applied to the case of CO_2 pooling and forcing its way into a heterogeneous caprock, replacing hot brine and eventually breaking through.

Key words

Two phase flow; Hybrid analytical numerical; CO_2 sequestration; Caprock integrity; Front tracking.

Notation

A	Area of element normal to the fluid flux (m^2)
$A_{2D}^{'}$	2D local coordinate system
A_{3D}^{g}	3D global coordinate system
A_{ne}	Area of influence assigned to a node in the element (m^2)
C_{ij}^{e}	Element storage matrix
C_{ij}	Global storage matrix
D_{t_n}	Distance from an origin at time step n (m)
D_{front}	Distance of a node normal to the saturation front (m)
D_{node}	Distance of a node to the saturation front (m)
$D1_{front}$	Distance of node with S_{max} normal to the saturation front (m)
$D2_{front}$	Distance of node with S_{mid} normal to the saturation front (m)
f_1	Flow rate of phase 1 into or out of a volume (m^3/s)
f_{1i}	Flow rate of phase 1 into or out of a volume discretised to node i (m^3/s)
$f_{\alpha i}^{e}$	Element contribution to flow rate of phase α discretised node i (m^3/s)
g	Acceleration due to gravity (m/s^2)
i, j, k	Iteration integers
$k_{r\alpha}$	Relative permeability of phase α (-)
$\mathbf{k}$	Intrinsic permeability tensor (m^2)
md	Maximum distance predicted by analytical solution from origin (m)
$MN\beta$	Shape function for the node, β=1 for node S_{max} to β=3 for node S_{min}
n_β	Node number β
ne	Number of elements
nn	Number of nodes
P_{Smax}	Global point coordinates for node with maximum saturation in element
p_α	Fluid pressure of phase α (Pa)
p_1, p_2	Fluid pressure of phases 1 and 2 (Pa)
p_c	Capillary pressure (Pa)
p_w	Fluid pressure of phase of wetting phase (Pa)
Q_{total}	Total flow rate of all phases (m^3/s)
Q_1	Flux of phase 1 (m/s)

q_{total}	Total Darcy flow velocity of all phases (m/s)
$\mathbf{q}_\alpha$	Fluid velocity vector (m/s)
$\mathbf{q}'$	Fluid velocity vector in local coordinates (m/s)
S_1	Saturation of fluid phase 1 (-)
S_2	Saturation of fluid phase 2 (-)
S_α	Saturation of fluid phase α ($\alpha = 1 \text{ or } 2$)(-)
SF	Scaling factor (-)
$SF(t_e)$	Scaling factor dependent on t_e (-)
S_{front}	Saturation of phase 2 at the top of the saturation front (-)
S_{max}	Maximum saturation of phase 2 of the element nodes (-)
S_{min}	Minimum saturation of phase 2 of the element nodes (-)
S_{mid}	Middle saturation of phase 2 of the element nodes (-)
S_{res}	Residual saturation (-)
S_{tn}	Saturation at time step n (-)
S_{1r}, S_{2r}	Residual saturation of fluid phase 1 and 2 (-)
sv_β	Side vectors of the element in local coordinates
T	Thickness of an element (m)
${}_{2D}T_{3D}$	Transformation matrix from 3D global coordinates to 2D local coordinates
t	Time (s)
t_1, t_0	Indicates time step, 0 precedes 1
t_e	Time since the front entered an element (s)
Δt	Time step length (s)
V	Integration volume (m^3)
V^e	Element volume (m^3)
V^n	Mesh volume mapped to a node (m^3)
v_α	Advective velocity of fluid α (m/s)
x	Distance (m)
x_n	Normalised distance from origin (-)
x_{real}	Actual distance from origin (m)
x', y'	Local coordinate system
x_g, y_g, z_g	Global coordinate system
$\mathbf{u}$	Displacement tensor (m)
z	Height above datum (m)

α	Fluid phase (-), 1 or 2
β	Number from 1 to 3 unless otherwise stated
ϕ	Porosity (-)
μ	Dynamic viscosity (N/m²s)
ρ_α	Density of phase α (kg/m³)
ϖ_i	Weighting function of Galerkin Finite Element Scheme (-) for node i
ω_j	Weighting function of Galerkin Finite Element Scheme (-) for node j

$a_x, b_x, c_x, d_x, e_x, f_x, g_x$	Polynomial coefficients for a function $y = f(x)$
$a_s, b_s, c_s, d_s, e_s, f_s, g_s$	Polynomial coefficients for a function $y = f(S)$

1. Introduction

In this paper a hybrid analytical numerical approach for the modelling of two phase flow is presented. The application addressed is the forced replacement of hot brine in a caprock by supercritical CO_2 under reservoir conditions of temperature and pressure to be found at a depth of 1300 m. Modelling two phase flow using standard grid based numerical techniques presents a problem due to the sharpness of the front developed by the replacement of one fluid with another, balanced against the need to discretise the model into grid points and elements. One of the issues is that changes due to coupling to other processes, such as mechanical faulting and pressure release of the fluid, is likely to occur as the front passes. Depending on the resolution of the fluid flow grid, this time dependent signal may be missed or smeared with other signals loosing information on the integrity of the reservoir. In finite element approaches lower order based interpolation functions often fail to represent the sharp front and this can also lead to oscillations around the true solution. Finite volume methods can avoid these oscillations, but there are issues concerning the relative computational expense of these formulations and difficulties in representing smoothly varying heterogeneity fields while minimising discretisation overheads. Mixed finite element solutions whereby both the velocity field and the pressure solution are considered primary variables are finding some acceptance, however they are computationally more complicated to implement, especially with respect to solver capabilities, *Younes et al.* [2010].

Three main approaches have been adopted to address this problem. The most widely adopted approach is that of grid refinement, or adaptive mesh refinement in the vicinity of the front. The geometry of the grid is locally adapted to better represent the numerical processes operating at a local scale and represent steep gradients within the model. Recent examples for highly heterogeneous fields include *Chen, et al.*, [2003] and *Durlofsky, et al.*, [2007]. Such adaptive grid methods allow the discretisation scale to follow the front through the model, however the front location will always be approximated within the scale of the discretisation used. Such methods are extremely useful but can be computationally expensive and make coupling to other processes such as Thermal, Mechanical, reactive Chemical (TMC) more complicated due to the constant alteration in grid size and location.

Interface tracking methods have been developed that apply sophisticated reconstruction algorithms based on either the ratio of volumes of a fluid in an element (Volume of Fluid Methods) or the advective velocity of the interface throughout the modelling regime (Level Set Method). *Meakin and Tartakovsky*, [2009], with references therein, review these approaches and conclude that there has actually been very little application of these techniques to multiphase fluid flow in fractured and porous media. Recent examples of their application include *Huang and Meakin*, [2008] and *Huang, et al.*, [2005]. *Unverdi and Tryggvason* [1992] followed the interface by explicitly representing the interface as a second grid moving through a stationary grid. *Glimm, et al.* [1999] tracked the front throughout the computational domain using a grid based interface reconstruction based on information in the grid element and the information from surrounding elements.

Interface tracking methods described above address the problem of the location of the front based on the volumetric fluid fluxes into and out of an element, the understanding that there must be continuity between elements and assumptions as to the shape of the front. The "front tracking" method developed in this paper uses a generic analytical solution to "add information" to the model and predict the location and shape of the front within the elements. This removes the necessity for adaptive mesh refinement and the need for further sophisticated reconstruction of the front surface. The information on the geometry of the front surface under the conditions given in the element is being predicted by the analytical solution. The method increases the accuracy of the prediction of the

front location, but is still bound by the overall accuracy of the numerical method applied to determine the primary variables which the analytical solution depends upon. Examples of other hybrid analytical numerical methods where information is added to the model and thereby the computational load is reduced can be found in e.g. *McDermott, et al.*, [2007] and *McDermott, et al.*, [2009].
The method is developed within the object oriented, open source finite element code OpenGeoSys [www.opengeosys.net, *Wang et al.* 2009]. Although this Front Tracking method was specifically designed for the replacement of brine by supercritical CO_2 in a caprock under reservoir conditions, the generic nature of this approach is demonstrated.
The standard two phase flow equations are solved using the IMPES (implicit pressure explicit saturation) formulation (e.g. *Helming*, 1997). We formulate the saturation equation in terms of the volume of replacing fluid in the discretised elements. This volume may either be predicted using a standard first order approximation, or by using the analytical solution of the location of the front directly and integrating under this front. The latter approach works for homogenous conditions, and predicts radial flow better than the standard numerical methods using full upwinding schemes, however still requires further development for heterogeneous conditions. For clarity we will divide these approaches as follows

- FUG Full Upwinded Galerkin Finite Element Solution of the Pressure Equation
- FUG-v As 1 with a first order shape function approximation of the saturation equation (v stands for volumetric)
- FUG-a As 1 with the analytical solution used to derive the shape functions for the solution of the saturation equation (a stands for analytical)
- FUG-vT as 2 with the analytical solution and a volumetric reconstruction used to locate the front but not to evaluate the shape functions (T stands for front Tracking).

The emphasis of this paper is not the introduction of a new numerical method, but the combined use of a standard numerical techniques and analytical techniques. The analytical solution is used to introduce physical process understanding into the system, and to predict the location of the front at a sub-element scale based on both the fluid saturations present and the advective velocity field. Two key developments are shown

- The integration of an analytical solution in the finite element IMPES formulation to explicitly represent the shape and location of the saturation front
- The prediction of the location of the front in heterogeneous fields at a sub element scale.

2. Theory

Modelling of two phase flow in porous media can be described by the mass balance equations for each fluid phase and Darcy's law describing fluid flux under a pressure gradient (5).

$$S_\alpha \rho_\alpha \nabla \frac{\partial \mathbf{u}}{\partial t} + \frac{\partial \left(\phi S_\alpha \rho_\alpha\right)}{\partial t} + div\left(\rho_\alpha \mathbf{q}_\alpha\right) - \rho_\alpha Q_\alpha = 0 \qquad (5)$$

This equation includes poro-elastic deformation of the pore space, and changes in density of the fluid. The fluid velocity $\mathbf{q}_\alpha$ is a non-linear function of the pressure gradient, after Darcy's law

$$\mathbf{q}_\alpha = \phi S_\alpha \mathbf{v}_\alpha = \frac{Q_\alpha}{A} = -\frac{k_{r\alpha}\mathbf{k}}{\mu_\alpha}(\text{grad}\, p_\alpha - \rho_\alpha \mathbf{g}) \tag{6}$$

Where $k_{r\alpha} = f(S_\alpha)$ given following. Here for the wetting phase (phase 1, brine in our example)

$$p_\alpha = p_w \tag{7}$$

and for the non wetting phase (phase 2, CO_2 in our example)

$$p_\alpha = p_w + p_c \tag{8}$$

here p_c is expressed as a negative suction pressure. *Helmig and Huber* [1998], discussed the solution of these equation systems using the Galerkin-type discetization Finite Element Methods (FEM), and showed the limitations and advantages of the standard Galerkin approach, the Petrov-Galerkin method and the Fully Upwinded Galerkin (FUG) method. *Klieber and Riviere* [2006] presented work whereby several different Galerkin formulations were used creating a discontinuous Galerkin approach to model the two phase flow equations sequentially coupled with adaptive grid methods. *Hoteit and Firoozabadi* [2008], used a mixed finite element formulation and a discontinuous Galerkin approach to investigate the effects of capillarity on the flow system. They solved the saturation equation using fractional flow formulation and a total mobility approach. They showed that the permeability field as well as the effects of capillary entry pressure have a significant impact on the flow paths developed in two phase flow. From examination of equation (6) this is apparent, but it can also be seen that the effect of capillary entry pressure can be presented in the relative permeability function as a first approximation.

A full description of the finite element method may be found e.g. in [*Istok*, 1989; *Lewis and Schrefler*, 1998; *Zienkiewicz and Taylor*, 2005], and the finite volume method in *Versteeg and Malalasekera* [2007]. The hybrid analytical method presented here can be described as a multi scale approach [*Juanes and Patzek*, 2004]. The unknowns of the wetting phase pressure and the non wetting phase saturation are solved sequentially using different approaches. For the pressure formulation we apply the FUG (maximum mobility) approach, and for the solution of the saturation equation we introduce extra information in the model by including an analytical derivation of the shape function for the evaluation of the saturation front.

The advantage of using an analytical derivation for the location of the saturation front is that it removes the necessity to refine the mesh in the locality of the saturation front whilst still maintaining the sharpness of the front without numerical oscillations. The method, however, still has the requirement that the Courant time criteria apply for the advective flux of the front,[*Kolditz*, 2001], and, as is the case using a FUG scheme numerical diffusion is introduced. In addition the accuracy of the location of the front prediction is dependent on the accuracy of the numerical solution of the primary variables. It is true that mesh refinement can introduce a better representation of the field, but mesh refinement usually does not include further heterogeneity information, and therefore the accuracy of the prediction of the heterogeneity remains at the original grid scale [Thorenz et al. 2002].

To demonstrate the use of this hybrid method for the solution of (5) for two phase (liquid-liquid) flow and the prediction of the front we assume simplistic conditions. First that there is no pressure difference across the liquid-liquid phase fronts, i.e. capillary pressure effects are negligible, and that the solid-liquid-liquid contact angles have no significant impact on the flow characteristics. At a pore scale size it would be necessary to include these effects, discussed in detail by *Meakin and Tartakovsky*, [2009] and references therein. *Niessner and Hassanizadeh* [2008] examines the role of fluid-fluid interfaces and the impact they can have such as hysteresis. At the macro size, given the heterogeneity of geological medium (pore size distribution) and in this example the assumption of

generally continuous fluid phases, these simplifications have some validity. Allowing this approximation means that the term p_c in (8) is neglected in the pressure formulation.
For the demonstration of the method we assume constant density and no deformation. This allows (5) to be expressed for a unit volume as (9) i.e. a volume balance equation

$$\phi \frac{\partial S_\alpha}{\partial t} - \operatorname{div}\left(\frac{k_{r\alpha}\mathbf{k}}{\mu_\alpha} \left(\operatorname{grad} p_\alpha - \rho_\alpha \mathbf{g} \right) \right) - Q_\alpha = 0 \tag{9}$$

As $\sum_{0}^{phases-1} S_\alpha = 1$ in (10) by summing all the phases together we have

$$\begin{gathered} \sum_{1}^{phases} \left[\phi \frac{\partial S_\alpha}{\partial t} - \operatorname{div}\left(\frac{k_{r\alpha}\mathbf{k}}{\mu_\alpha} \left(\operatorname{grad} p_\alpha - \rho_\alpha \mathbf{g} \right) \right) - Q_\alpha \right] = 0 \\ \Downarrow \\ \sum_{1}^{phases} \left[\operatorname{div}\left(\frac{k_{r\alpha}\mathbf{k}}{\mu_\alpha} \left(\operatorname{grad} p_\alpha - \rho_\alpha \mathbf{g} \right) \right) + Q_\alpha \right] = 0 \end{gathered} \tag{10}$$

Consequently the governing equations for the two phases are turned into one parabolic and one Poisson equation as

$$\begin{gathered} \phi \frac{\partial S_1}{\partial t} - \operatorname{div}\left(\frac{k_{r1}\mathbf{k}}{\mu_1} \left(\operatorname{grad} p_1 - \rho_1 \mathbf{g} \right) \right) - Q_1 = 0 \\ \sum_{1}^{phases} \left[\operatorname{div}\left(\frac{k_{r1}\mathbf{k}}{\mu_1} \left(\operatorname{grad} p_1 - \rho_1 \mathbf{g} \right) \right) + Q_1 \right] = 0 \end{gathered} \tag{11}$$

Discretising the weak form of (11) into a grid with *np* grid nodes and *ne* elements, and integrating applying the Galerkin Finite Element method, we can write for the pressure field for all nodes, $i \in (0,\ldots,nodes-1)$ [*Thorenz* 2001], where the test function ϖ is the same as the shape function.

$$\begin{gathered} \int_V \left(\phi \frac{\partial S_1}{\partial t} - \operatorname{div}\left(\frac{k_{r1}\mathbf{k}}{\mu_w} \left(\operatorname{grad} p_1 - \rho_1 \mathbf{g} \right) \right) - Q_1 \right) \omega_i dV = 0 \\ \int_V \sum_{1}^{phase} \left[\operatorname{div}\left(\frac{k_{r1}\mathbf{k}}{\mu_1} \left(\operatorname{grad} p_1 - \rho_1 \mathbf{g} \right) \right) + Q_1 \right] \omega_i dV = 0 \end{gathered} \tag{12}$$

Solving this equation allows the derivation of (6) for all nodes. The saturation field for phase 2 and all nodes, $i \in (0,\ldots,nodes-1)$ is given by

$$\int_V \left(\phi \frac{\partial S_2}{\partial t} - \operatorname{div}\left(\frac{k_{r2}\mathbf{k}}{\mu_2} \left(\operatorname{grad} p_2 - \rho_2 \mathbf{g} \right) \right) - Q_2 \right) \omega_i dV = 0 \tag{13}$$

After solution of equation (10) inserting (6), (13) can be rewritten for a unit volume as

$$\int_V \varphi \frac{\partial S_2}{\partial t} \omega_i dV = -\int_S \mathbf{q}_2 \cdot \mathbf{n} \omega_i dS + \int_V Q_2 \omega_i dV = f_2^i \tag{14}$$

where the term $\int_S \mathbf{q}_2 \cdot \mathbf{n} \omega_i dS$ is a surface integral and represents the sum of the fluxes of phase 2 into and out of the element across the surface S with a volume V. Expressing this in the discretised weak formulation and applying the Galerkin approach

$$\sum_{j \in N_i} \int_V \phi \omega_i \omega_j dV \frac{\partial \hat{S}_2^j}{\partial t} = f_2^i, i = 1, 2, \ldots, np \tag{15}$$

where N_i denotes the set of nodes connected to node i, and $\hat{S}_w^j$ is the node value of the water saturation. Equation (15) forms a global system of equations where the number of equations corresponds to the number of grid points (np). This is expressed in matrix form as

$$\sum_{j\in \mathrm{N}_i} C_{ij} \frac{\partial \hat{S}_2^j}{\partial t} = f_2^i \qquad i = 1, 2, \ldots, np \tag{16}$$

where

$$C_{ij} = \int_V \phi \omega_i \omega_j dV \tag{17}$$

Decomposition of the computational domain into finite elements means that the global matrices can be expressed as

$$C_{ij} = \sum_1^{ne} C_{ij}^e \tag{18}$$

$$f_{2i} = \sum_1^{ne} f_{2i}^e \tag{19}$$

This forms what we will refer to as the standard FUG-FE approach.

However, to be able to include analytical solutions predicting the geometry of the saturation front we use the solution of (14) derived from the pressure equation to calculate the flux into or out of an element, and integrate with respect to time to explicitly include the actual volume of CO_2 (phase 2) change in an element. The total amount of phase 2 present can then be expressed in volumetric terms using *t* to represent the time step of evaluation as

$$V_2^{n(t_1)} = V_2^{n(t_0)} + f_2\left(t_1 - t_0\right) \tag{20}$$

were V^n represents the finite volume of the modelling area represented by a node surrounded by *ne* elements, each attached element with *nn* nodes, where V^e represents the volumes of the elements surrounding the node.

$$V^n = \frac{\sum_{e=1}^{ne} V^e / nn}{ne} \tag{21}$$

To relate (20) to the saturation of a phase we use

$$V_2 = S_2 V^n \tag{22}$$

which leads to (20) being expressed at an element level as

$$\phi V^n \int_{S_2^{(t0)}}^{S_2^{(t_1)}} \partial S_2 = f_2 \int_{t_0}^{t_1} \partial t \tag{23}$$

Using a finite difference formulation (23) can be solved explicitly for $S_\alpha^{(t_1)}$ as

$$S_2^{(t_1)} = \frac{\left(\phi V^n S_2^{(t_0)} + f_2 \Delta t\right)}{\phi V^n} \tag{24}$$

Again the above equation (24) forms a global system of equations where the number of equations corresponds to the number of nodes, or grid points.

The evaluation of $\mathbf{q}_2$ (6), and therefore f_2 explicitly by the finite element method has the advantage of including the off-diagonal components in the evaluation of the flow vector, but the disadvantage that local mass conservation is not always adhered to, both in contrast to the standard box finite volume approach. Prior to introducing a more rigorous method of calculating fluxes at the nodes, we include a term to remove the effects of local mass imbalances. This term can be seen as an enhanced numerical dispersion term, but has the advantage in coupled

process modelling that the solution is stable without oscillations. To correct for this missing local mass balance information, after solution of the saturation equation, the saturation at all the nodes is checked to ensure all are equal to or above the residual saturation value within a defined tolerance level. Where nodes are found where saturation is below the residual value, then mass from the surrounding, now "donating" nodes, weighted by these donating nodes saturation above the residual saturation, is taken and added to the "offending" node to reach residual saturation. By this means the overall mass balance is not impaired and a satisfactory saturation solution is obtained.

Inclusion of the analytical solution (FUG-v, FUG-a and FUG-vT approaches)

The term $V^n \phi S_2^{(t_0)}$ represents the volume of the replacing fluid at the previous time step. Using a linear interpolation (FUG-v approach) this can be represented as the sum by the number of nodes (nn) of the product of the saturations multiplied by the volume represented by that node in the element. Here *T* is the thickness of the element and A_{ne} is the planar area represented by the node in an element.

$$V^n \phi S_2^{(t_0)} = T\phi \sum_1^{ne} S_2 A_{ne} \tag{25}$$

The analytical solution for the presence of the front within the element provides the location of the front both according to the saturations at the nodes in the element and the advective flow velocity and direction. In the FUG-a approach (25) is replaced as

$$V^n \phi S_2^{(t_0)} = \phi \sum_1^{ne} \int_\Omega \Phi d\Omega \tag{26}$$

Where $\int_\Omega \Phi d\Omega$ represents the integration of the predicted saturation surface of the analytical solution Φ where $\Phi = f(v_x, v_y, v_z, S_{2\,n=1..nn})$ in the volume Ω being that space in an element occupied by part of the saturation surface.

The analytical solution can be used to both evaluate the location of the saturation front and to calculate the volume of the replacing fluid around a particular node. What we call the FUG-vT approach is where we use (25) for the solution of two phase flow with the analytical solution $\Phi = f(v_x, v_y, v_z, S_{2\,n=1..nn})$ to predict the actual location of the front within elements. We note here, discussed later, that there are some locations where there is not a unique solution for the analytical approach. Und under these conditions we use a volumetric reconstruction method.

2. Front Tracking

2.1 Choice of analytical solution

To be able to evaluate the volume of the replacing fluid, the volume underneath the saturation surface needs to be calculated. Triangular elements offer the possibility of representing a global three dimensional flow field (q_x, q_y, q_z) in two dimensions in the local coordinate system of the elements [Kolditz 1995]. This method has been used several times for instance for fracture network simulations, e.g. *McDermott, et al.* [2006] as well as standard 2D cross sections. In addition it is often standard practice to represent large scale aquifers as 2D bodies with a certain thickness. Unique to triangular elements is the possibility to further reduce this two dimensional flow field uniquely to one dimensional flow representative of the entire element using a standard three point approach. In this manner the flow in the element is reduced to a one dimensional flow field,

within the coordinate system *x,y,z*. Different analytical solutions can be considered for determining the location of the two phase flow front, in this work for the demonstration of the method we apply the original 1D solution derived by *Buckley and Leverett* [1941] for the replacement of one fluid with another in two phase flow. This solution is developed for equilateral triangular elements as these are geometrically simplest for the integration of the volumes of the elements.
The *Buckley and Leverett* solution is one of the simplest for two phase flow where capillary pressures are not considered to be causing any resistance to flow. We discussed earlier our reasoning behind this as a first approximation leaving out the capillary pressure term in our evaluation of the pressure field. The capillary pressures is, however, included indirectly in terms of allowing residual trapping by the consideration of a residual saturation for the calculation of the relative permeability functions below. There are several publications where the capillary pressure term is included, and it would be possible also to include a more sophisticated solution for front tracking e.g. *Chen* [1988], *Fucik, et al.*, [2008], *McWhorter and Sunada* [1990] *van Duijn and de Neef* [1998]. *Buckley and Leverett* [1941] used relative permeabilities described by the functions given below (27) derived from their laboratory work. Presentation of more complex constitutive relationships can be found e.g. in [*Brooks and Corey*, 1964; *Helmig*, 1997; *Helmig, et al.*, 2002; *Ippisch, et al.*, 2006; *van Genuchten*, 1980].

$$k_{r1} = \frac{\left(S_1 - S_{1r}\right)^2}{\left(1 - S_{1r} - S_{1r}\right)^2} \quad \text{and} \quad k_{r2} = \frac{\left(1 - S_1 - S_{2r}\right)^2}{\left(1 - S_{1r} - S_{2r}\right)^2} \tag{27}$$

The *Buckley and Leverett* analytical solution of the saturation equation considering fractional flow functions is presented by *Thorenz* et al. [2002] as being

$$\Delta x = -\frac{q_{total}}{\phi} \frac{\partial\left(\dfrac{1}{1 + \dfrac{k_{r2}\mu_1}{\mu_2 k_{r1}}}\right)}{\partial S} \Delta t \tag{28}$$

From this equation it is possible to derive the saturation curve presented in Figure 109. Helmig (1997) presents two methods of solving this equation. The equation (28) has two possible saturations for one location. Using the equal area solution the actual location of the saturation front is determined by constructing a shock front whereby "Area 1" is equal to "Area 2".

2.2 Locating the saturation front

In Figure 109, the solution of the *Buckley and Leverett* equation has been normalised against the maximum distance md from the origin for the extension of the saturation front. Examining (28) it can be seen that the term $\frac{q_{total}}{\phi}\Delta t$ is a scaling term, and for the solution presented in Figure 109 we set this to 1.

This means that it is possible for any combination of flow rates, porosity and time to be compared with the normalised analytical solution via a scaling factor. This fact is central to the application of this analytical solution.

The shape of the analytical solution from the origin to the saturation front can be approximated by a polynomial (29) fitted to match the normalised analytical response (Figure 110). Therefore a standard response for the solution assuming constant material permeabilities and viscosities within an element may be evaluated by solving (28)

$$x_n = a_s S_2^{\,6} + b_s S_2^{\,5} + c_s S_2^{\,4} + d_s S_2^{\,3} + e_s S_2^{\,2} + f_s S_2 + g_s \quad \text{i.e. } x_n = f(S_2) \tag{29}$$

The coefficients $a_x \ldots g_x$ are the fitted polynomial coefficients for the normalised distance approximation. To calculate profile under operating conditions we can now apply

$$x_n = \frac{x_{real}}{\left(\frac{q_{total}}{\phi} \Delta t \bullet md \right)} \tag{30}$$

For simplicity we define a scaling factor term so that

$$SF = \frac{q_{total}}{n} \Delta t \bullet md \tag{31}$$

Therefore the location of the saturation front from an origin given the flow, porosity and time conditions in the scaling factor is given as

$$x_{real} = x_n \bullet SF \tag{32}$$

Likewise we define the inverse polynomial function so that

$$S_2 = a_x x_n^{\ 6} + b_x x_n^{\ 5} + c_x x_n^{\ 4} + d_x x_n^{\ 3} + e_x x_n^{\ 2} + f_x x_n + g_x \quad \text{i.e. } S_2 = f(x_n) \tag{33}$$

with $a_s \ldots g_s$ being the polynomial coefficients for the saturation approximation.

These approximations allow for the calculation of either the distance to the front from a known saturation (29) or the saturation at a known distance (33).

2.3 Implementing the analytical solution information

To demonstrate the ease of the implementation of this approach for the user, as an example the required input code for OpenGeoSys to trigger the HAN approach is presented in Figure 111. Four extra lines of text are required in the numerical description. The lines marked ";" being commented out and for description. The lines marked with "$" acting as triggers for the reading of the code, the numerical values referring to values and coefficients required in the analytical solution. The polynomial coefficients, equations (29) and (33), the scaling factor (31) and the front saturation are derived by fitting of the analytical solution using an external program, in this case Excel. The values of residual saturation and maximum saturation are defined by the constitutive relationships used for the calculation of relative permeability.

2.4 The front in triangular elements

At any particular time during the solution of (13) the value of saturation of the three nodes in the triangular element is known. These nodal values for phase 2 are defined as S_{max}, S_{mid} and S_{min} being the maximum, middle and minimum values respectively. S_{front} is the saturation front calculated from the analytical solution and S_{res} is the residual saturation of the phase 2. Depending on the saturation values of the nodes, the saturation front may be

- Present within the element
- Have passed through the element
- Not have reached the element.

Each of these cases are now studied consecutively in detail. In each case we determine a volume (m^3) in the element to be filled by the incoming saturating fluid phase 2. For all cases the volume available to the incoming fluid is calculated for an element of unit height. To include non-unit element height, e.g. fracture aperture, the element storage matrix can be scaled with the given element height.

2.4.1 The front is present within the element

Figure 112 and Figure 113 illustrate the two cases when the front has entered the triangle element. In one or two nodes the saturation values are above S_{front}. The location of the saturation front in an element is determined as a distance from a fixed point, and the surface integrated within the local element coordinates to give the volume available for the incoming saturating fluid to occupy.

The element global coordinate $\left(x_g, y_g, z_g\right)$ system is transferred into a local coordinate system $\left(x', y'\right)$ whereby the node with S_{max} is located at the origin (0,0).

$$\left[A_{2D}^{'}\right] = \left[A_{3D}^{g} - P_{S\max}\right]\left[{}_{2D}T_{3D}\right] \tag{34}$$

$$\left[{}_{2D}T_{3D}\right] = \begin{bmatrix} \cos(x', x_g) & \cos(y', x_g) \\ \cos(x', y_g) & \cos(y', y_g) \\ \cos(x', z_g) & \cos(y', z_g) \end{bmatrix} \tag{35}$$

Locating S_{max} with the origin in the local coordinate system provides a fixed point from which to calculate the location of the front. The velocity vector is also transformed such that

$$\mathbf{q}' = \sum_{1}^{phases} \mathbf{q}_{\alpha}\left[{}_{2D}T_{3D}\right] \tag{36}$$

The scaling factor SF (31) of the element is now calculated from the porosity, the flow velocity, and the time passed since the front entered the element t_e. Allowing D_{node} and D_{front} to be the distance of the front to the origin of the two phase flow difference $D = D_{front} - D_{node}$ represents the downstream distance of the front from the node in the element. In the case where two nodes have a higher concentration than the saturation front then two distances are calculated.

D_{front} is the normal distance from the node to the front. It can be shown that for a length of time t_e since the front has entered the element that the distance between the saturation front and the node with a saturation S_{max} $\left(D1_{front}\right)$, and in the case where Smid > Sfront, (also for this node with saturation S_{mid} $\left(D2_{front}\right)$) is :-

$$\begin{aligned} D1_{front} &= SF\left(t_e\right)\bullet\left(f(S_{front}) - f(S_{max})\right) \\ D2_{front} &= SF\left(t_e\right)\bullet\left(f(S_{front}) - f(S_{mid})\right) \end{aligned} \tag{37}$$

The time t_e is the difference between the current time step and the time when the front is recorded at having first entered the element, marked by the saturation concentration of the node first exceeding the front saturation $S_{front} / 2.0$.

Now that the distance of the saturation front to the nodes is known, the volume under the saturation surface is evaluated and allotted to the nodes in the triangular element to define the element matrix C_{ij}^{e}, such that

$$C_{ij}^{e} = \phi\begin{bmatrix} MN1 & 0 & 0 \\ 0 & MN2 & 0 \\ 0 & 0 & MN3 \end{bmatrix} \tag{38}$$

Where the individual sum for each node is then

$$V_i^n \phi S_2^{(t_0)} = \sum_{1}^{ne} C_{jk} \text{ where i=j=k } C_{jk} = MN, \text{ else } C_{jk} = 0 \tag{39}$$

MN represents the volume of replacing fluid in the element. In (38) we have assumed that the nodes in the triangular element are ordered S_{max}, S_{mid} and S_{min}, naturally this may be different. For ease we have defined MN1 as the volume to be attributed to the node with the maximum saturation, down to MN3 with the lowest saturation.

For the case that volume of replacing fluid within an element is to be calculated using the analytical solution, the location of the front within the element is located as described above, and the polynomial expression describing the shape of the front integrated to provide the volume. Local geometrical considerations need to be taken into account. The implementation can be time consuming.

2.4.2 The front has passed through the element

In this section we consider the case where the saturation front has passed the element completely. This means that the saturation of all the nodes is higher than the front saturation. For this scenario we use for a first order linear approximation of the volume of replacing fluid. Here

$$C_{ij}^{e} = \frac{\phi A}{nn}\begin{bmatrix} MN1 & 0 & 0 \\ 0 & MN2 & 0 \\ 0 & 0 & MN3 \end{bmatrix} \tag{40}$$

Where

$$\begin{aligned} MN1 &= Smax \\ MN2 &= Smid \\ MN3 &= Smin \end{aligned} \tag{41}$$

Only where the saturation front is strongly curved is it of conceivable advantage to include a function integrating under the surface to determine more the volume more accurately. The implementation is time consuming and from experience the extra accuracy brings little advantage.

2.4.3 The front has not yet reached the element

The last case is if the replacing fluid has not yet entered the element, i.e. $S_{front} > S_{max}$ and S_{mid} and S_{min}. For this case we apply (40) and (41) as above.

2.4.4 Boundary conditions

For the solution of (10) for the pressure throughout the system, a pressure boundary condition and initial condition are necessary. Examining the saturation equation (13) it can be seen that all the entries in this equation system are flux entries. The boundary integrals need to represent the flux into or out of the model area. Where the boundary integrals are directly entered in the modelling as source terms or pressure dependent source terms in the input commands this is accounted for. However where there is no specification, to ensure a stable solution of the equation the boundary integrals need to be included in the evaluation of the equation. In practice an "Open boundary" is identified, and when the saturation front arrives at this boundary, the flux entering the boundary element, i.e. an element with a node on the boundary, is used to specify a source term on the open boundary. If the total flux entering the boundary element equals the sum of the source terms removing the flux from the element representing the open boundary then the saturation front never reaches the boundary, being always removed before it gets there. In the present work we use a gradient approach based on the saturation of the nodes. The average saturation of the nodes in an element on the boundary $S_{\alpha b}$ or on the inner side of the model, S_{wi} is given by

$$S_{2b} = \frac{\sum_{0}^{nb} S_2}{nb}\ ,\quad S_{2i} = \frac{\sum_{0}^{ni} S_2}{ni} \tag{42}$$

Where nb and ni represent the number of nodes on the boundary or inside the model respectively of the element in question. The saturation is linearly interpreted and added to the boundary saturations to interpret the next time steps saturation such that

$$S_{2b\,t_1} = \frac{S_{2i\,t_0} - S_{2b\,t_0}}{2} + S_{2b\,t_0} \tag{43}$$

where t_1, t_0 represent time steps

These values of saturation are substituted in to the current solution for saturation, and the boundary integrals (fluxes) for the next time step are evaluated

$$f_{2i} = C_{ij} S_{2i} \tag{44}$$

2.4.5 Adaptive time step control

For the front to be effectively tracked through the elements, it is necessary to ensure that no time step is so large as to cause the front to pass right across the area represented by a node in an element in one time step. As the saturation of the elements in the model area increases, so the relative permeability increases, and so the fluid velocity increases. We have not observed a control on the lower end of the time step, i.e. it can be small without causing numerical problems. However for a time efficient solution, the time step needs to be as large as possible without compromising the model accuracy. The velocity of the saturating phase can be calculated throughout the model area after each time step, and the time step adjusted to ensure that the Courant stability criterion for ½ of the element length is not exceeded.

2.4.6 Discussion of the method and application

The grid based FUG finite element solution provides nodal values of flux. The method includes numerical dispersion induced by fully upwinding which prevents oscillation around the sharp front, (Helmig 1997). This can be seen as a tendency for the front to diffuse downstream from its actual location, the mass thereof being taken from upstream of the front. Without going into more complicated methods of reconstructing the front this seems to be a necessary penalty for using the FUG method. The values of flux and saturation in the grid based approach represent the best approximation for a smooth solution of the balance equations. The saturation equation is, however, not continuous, and therefore the value for the saturation in the vicinity of the front is averaged out. This is best understood by considering a front passing through a node. Only when the front has passed through the node and completely filled the volume assigned to that node will the saturation of that node be calculated as of at least the front value. Whilst the front is still within the refines of the node, the average saturation of the node will be less than the front. This created a problem for a method which relies on the knowledge of the saturation of the node as a pin point value, and leads to a numerical smearing of the approach by the length of one element. For the case where we use the analytical solution to find the location of the front (FUG-vT) the search criteria can be attuned to this issue by taking into account this smearing, enabling the analytical solution to identify the correct location of the front. However, so far in the case that we want to use the analytical solution to determine the volume of CO_2 present exactly at the front where this smearing occurs, we have only achieved partial success (FUG-a) .

A further problem arises due to the combination of the analytical solution and the FUG approach. When a front is passing through an element the FUG approach assigns flux to the downstream nodes, even although the front has not yet reached that node. Within the analytical solution there is no information for saturations between the front saturation and residual saturation. According to the analytical solution they do not exist. Using only the analytical solution as the basis function to define the volume of replacing fluid will lead to incorrect assumptions about the fluxes at the element boundaries. For the homogeneous case this can be corrected by considering the flow direction, and the amount of missing mass and scaling accordingly. However in the heterogeneous case it has

not been possible yet to get a stable satisfactory solution. The FUG-v approach does not have this problem.
We demonstrate the use of the analytical solution alone (FUG-a) for homogeneous cases, and then the FUG-vT for the determination of the location of the front in heterogeneous systems. Where no solution from the analytical approach exists for the location of the front, we apply a volume correction method to predict its location. That is the mass is redistributed within the element so that a front with the appropriate saturation can be constructed whist still adhering to the volume predicted by the saturations at the nodes.

3. Model Validation and Application

The main aim of this modelling development is to aid in the understanding of coupled processes operating during the injection of supercritical CO_2 beneath a caprock and the breakthrough of this CO_2. In addition we want to identify the location of the front at a scale smaller than the element discetisation we are using and be able to apply this information computationally efficiently coupled to other processes. To demonstrate the modelling approach, the fluid properties of the supercritical CO_2 and brine were selected to represent conditions at a depth of approximately 1300 m below the ground surface. A pressure of 130 bar was chosen and a temperature of 40 °C. Five models are presented with increasing degrees of complexity.

1) Initially a comparison is made between the simplified 1D analytical solution for two phase flow by *Buckley and Leverett* [1941], the FUG-a and FUG-v scheme and show the prediction of the location of the front using the FUG-vT approach.
2) Secondly a model of the caprock is considered with supercritical CO_2 injection and heterogeneity in the permeability field.
3) The radial injection of CO_2 into a homogeneous field is considered
4) Injection to the base of a caprock is considered with a randomly distributed heterogeneous permeability field.
5) Finally the method is compared to a standard finite volume simulation of a heterogeneous field using a finite volume rendition of the triangular finite element grid.

3.1 Model 1: Analytical, numerical and hybrid model comparison

Comparison of the purely analytical, purely numerical FUG-a, FUG-v and FUG-vT approaches is based on the caprock application, illustrated in Figure 116. At the base of the caprock supercritical CO_2 pooling is represented by source terms providing circa 1.67 litre/day. The results presented in Figure 116 are for the distribution of the CO_2 after 42.6 days of injection. There is a pressure control on the upper boundary, ensuring that when the supercritical CO_2 breaks through the upper boundary it is free to escape, and no pressure control on the lower boundary, meaning with increased rate of injection there is an increase in pressure on the lower boundary. The upper boundary is defined as an open boundary for the saturation equation. As the injection of supercritical CO_2 is source term driven rather than pressure driven, until the CO_2 finds a pathway

through the caprock, pressure at the injection boundary increases. Once a pathway starts to develop towards the upper boundary so the significant flows of CO_2 can occur as the fluid is no longer required to displace large volumes of brine, hence the pressure reduces. A capillary entry pressure term would increase the amount of pressure required to be built up in the system prior to the CO_2 creating its escape path.
The fluid and material properties for this model are presented in Table 21 & Table 22 respectively. The relative permeability functions assumed are those from *Buckley and Leverett* [1941], and illustrated in Figure 117.
A comparison in profile with the *Buckley and Leverett* analytical solution is provided in Figure 118. Here FUG method for the solution of the pressure equation is presented coupled with the three different approximations of the solution of the saturation equation (FUG-v, FUG-a, FUG-vT). First the standard linear interpolation, secondly using the volume predicted by the analytical function, and thirdly again using the volume predicted by the analytical function, but redistributing mass to upstream nodes to allow for the mass correction, i.e. accounting for the saturations between the front saturation and residual saturation which the analytical solution suggests does not exist and is a product of the FUG scheme. All three schemes can be seen to approximate the purely analytical solution. It is interesting to note that all three approaches produce similar results.
When identifying the location of the front (FUG-vT), what is striking is that the combination of the FUG-v scheme using the standard linear interpolation coupled with the analytical method for the prediction of the location of the saturation front yields a result which is almost exactly the pure analytical result, illustrated as "Location of front tracking estimate". This result suggests that the FUG-vT combination can be relied upon to produce accurate predictions of where the front is likely to be provided a solution to the analytical formulation exists.

3.2 Model 2: Well injection in a homogeneous media

By definition upwinding schemes propagate downstream information in elements instantaneously upstream to the front. This prevents information downstream (infront of) of a propagating front from impacting the movement of fluid which is controlled only by upstream (behind the front) information. The disadvantage of this useful approach is that as soon as fluid enters an element, the entire element gets the upstream flow characteristics, and therefore the numerical dispersion caused by this approach propagates in the shape of the elements through the grid. The evaluation of the saturations in this case is based only on the flux at each node. As the evaluation of the saturation surface in the FUG-a case is based upon the predicted saturations and the flow field, some shape correction due to the flow field contribution can be expected. This correction can be to the degree that the propagation from a point source becomes circular, as demonstrated in Figure 119, the parameters being the same as model 1.

3.3 Model 3: Single band of low permeability material in higher permeable field.

In this model we repeat the scenario described in model 1, except we introduce a low permeability band just above the injection area (see Table 22 for parameters). Fluid flow is forced around this band, the performance of the purely numerical FUG-FE scheme and the hybrid FUG-vT models are compared in Figure 120. The numerical model is no longer able to cope with the heterogeneity in permeabilities. It can no longer satisfactorily represent the saturation front, and the linear averaging technique in the volumetric averaging leads to oscillation in the solution below the residual saturation (20%) and above the maximum saturation (80%). The FUG-vT hybrid model copes well with the heterogeneity, the reduction in the minimum saturation to 19.5% is within the tolerance written into the model code. The solution time for the FUG-vT approach is approximately

½ that of the standard FUG finite element numerical approach. In addition we note that the front prediction is reasonable. The disjointed nature of the front comes from the fact that information from the flow field and the saturations is used to form the front location prediction and where the analytical solution can not predict the location of the front, a volume interpretation approach is used. In addition the graphic program used to shade the regions utilises a linear approximation for shading, which is not always appropriate.

3.4 Model 4: Application to a heterogeneous cap rock

Here we again repeat the scenario described in model 1, except we now introduce three orders of magnitude of random heterogeneity (Table 23). In this model we introduce the time step control discussed above.

The FUG numerical model without grid adaptation can no longer come to a reasonable solution of the model. After a model total time of circa 50 days had been reached, the solution showed a maximum saturation of 102% and a minimum saturation of -40%. In comparison the FUG-vT approach after 1000 time steps had reached a model time of circa 75 days, required less real time to reach this solution and showed no oscillation on the saturation solution, i.e. a maximum saturation of 80% and a minimum of 20%.

Figure 121 presents the results of the FUG-vT method for the injection into the caprock represented by a heterogeneous field of permeabilities. The solution is stable between 20% saturation and 80% saturation. In addition the front location is also demonstrated to be reasonable.

3.5 Model 5: Well injection in a heterogeneous media

The FUG-vT approach is now used to simulate injection of supercritical CO_2 into a layer which can be taken as underlying a caprock. The CO_2 spreads out laterally from the injection point, and forms channels as a result of the heterogeneity (see Table 23). This is demonstrated in Figure 122, here again the front tracking can be seen to be providing sub element scale information the location of the saturation front. As the most significant changes in coupled processes will occur at the location of the front this information is important. Although exact heterogeneity of the subsurface is unlikely to be known, the general distribution of heterogeneity will be known. Therefore is it important to be able to predict the density and general distribution of the channels in the subsurface to be able to relate them to other processes, such as seismic signals due to mechanical coupling. In Figure 123 we compare a larger area subject to well injection, and again the models are scalable, so what is of relevance is the density of the mesh elements and the heterogeneity they represent.

In Figure 15 we also compare the results of a finite volume approach utilising an identical physical model and the FUG-vT method presented here. In this figure the front tracking location is presented, then removed for comparison to the finite volume (FV) approach. The FV calculation was implemented in the Quintessa Ltd multi-physics code QPAC (www.quintessa.org/qpac), adopting the same element structure for the finite volume grid. The two codes had previously been successfully cross-compared using Models 1 and 3 discussed above. We note that the overall shape of the predicted radial flow patterns is similar, and many features can be cross referenced. The FUG-vT method predicts the formation of more discrete and higher saturated channels, the FV scheme predicts more distribution in the saturating phase. This is due in part to the differences in the numerical schemes, specifically concerning the tendency for the finite element approach to 'blur' permeability contrasts across elements as the fluxes are assigned to the nodes by integrating across the elements. This creates the possibility for channelled pathways that the finite volume approach would not include. Previous experience has indicated that grid convergence exercises simply sub-dividing the existing triangular elements (and hence keeping the heterogeneity pattern identical) would yield further convergence of results.

Particularly the FUG-vT prediction would suggest that should micro seismics occur as a result of the injection of CO_2 that the signals would be more localised to the channel locations, and that they would also not be confined to a radial distribution at the outer edges of the injection plume. However we also note that given the uncertainty in the prediction of the subsurface heterogeneity that both methods provide a valid approach to identifying the general spread of CO_2.
Strictly speaking the FUG-vT model does not allow capillary trapping to occur, although the pattern of flow predicted by the results would suggest this. The flow in the system is driven by the source term representing the well and pressure field developed by the well. Preferential flow as a consequence of the heterogeneous permeability field leads to the partial isolation of low permeability blocks within the flow system. This is exaggerated by the positive feedback caused by the relative permeability functions, i.e. the higher the saturation, the higher the permeability. Should capillary pressure also be included in the calculation, these low permeability areas would be even more sealed from the preferential flow channels.

3.6 Application & scaling of model results

In the scenarios selected, the rate of flow through the heterogeneous media is controlled by the source term injecting the fluid. The fluid pushed into the domain must escape at the other end or side of the model. This dictates the rate of breakthrough, and to that end the pressure will build up until the breakthrough occurs. The pressure solution is a reflection of (slave to) the rate of fluid entry into the system and the permeability of the system.
To illustrate this more clearly, one could write the standard Darcy equation where the term *Q* represents the flow rate through the whole model (m^3/s), *A* represents the cross sectional area of the model (m^2), $\frac{k}{\mu}$ the ease at which fluid flows through the whole model system ($m^2 / Pa\ s$), sometimes called mobility, and i the pressure gradient across the model (Pa / m) see (45).

$$Q = A\frac{k}{\mu}i, \tag{45}$$

Keeping *A* and $\frac{k}{\mu}$ constant means that $Q \propto i$. Likewise if Q is kept constant, and only k is altered, as perhaps would be the case in fitting the permeability to different caprock values, then the pressure gradient i would change. An example would be a situation where the predicted entry of supercritical CO_2 into the caprock is $1/10^{th}$ of the rate modeled, and the permeability of the caprock two orders of magnitude less than used here. The time required for breakthrough would then be 10 times longer than given here, and the pressure build up two orders of magnitude greater.
Applying this concept to reality for a system with a heterogeneous permeability from 1 mD to 0.001 mD (i.e. $1\times10^{-15} m^2$ to $1\times10^{-18} m^2$) the pressure build up would be of the order of 0.6 MPa. The entry pressure of the CO_2 into the caprock would also impact the pressure build up, but the effect would be that of reducing the permeability until the capillary pressure had been overcome. Increasing the thickness of the caprock linearly decreases the pressure gradient, but as the pressure gradient does not control the flow in this system, rather the amount of CO_2 entering the base of the caprock, this will only have a significant impact where the pressure gradient falls below the capillary entry pressure. For a system described above where the capillary entry pressure is not considered, doubling the thickness of the caprock will double the time required for breakthrough to occur.
The scenario presented in 3.5 clearly suggests that in a heterogeneous system that the spread of CO_2 is dominated by channel flow. This is logical, as the

saturation relative permeability relationship provides a positive feed back mechanism, i.e. the more saturation, the higher the permeability and vice-versa until full saturation is reached. The consequences of channelling in the reservoir will be to localise the impact of the injected CO_2.

4. Conclusions

In this paper we have presented a new hybrid analytical numerical method for modelling two phase flow through heterogeneous porous media and locating the saturation front. This method uses a generic analytical solution of two phase flow though porous media to add extra information into a standard Galerkin Finite Element numerical procedure for solving two phase flow. The advantage this technique brings is that it removes the necessity of adaptive mesh refinement in the vicinity of the shock front generated by two phase flow replacement, to capture the location of the front. The front location is tracked as it passes through the triangular elements, this information can be passed onto other coupled processes. The fluid pressure in the area to be modelled is solved using a Fully Upwinded Galerkin (FUG) approach. The saturation equation is reformulated so that the shape functions represent the volume under the two phase flow surface available to the incoming saturating fluid. The volume in elements where the front is present is given both by applying the analytical solution under the flow conditions found in the element being considered and using a linear averaging approach.

Under homogeneous conditions the calculation of the distribution of the saturating fluid in the elements using the analytical function can be used to satisfactorily solve the saturation equation, provided that the area where the analytical solution provides no values of saturation for (at the shock front) is taken into account. As the analytical function combines information on both the element saturations and on the flow field in an element, it is able to represent radial injection in a homogeneous system better than a fully upwinded system. For more complex heterogeneous flow fields further development would be required to develop better flux transfer functions across the elements. However the information within the element can still be used satisfactory to predict the location of the front at a sub element scale, information which is important when considering heterogeneous flow fields and the scale of modelling.

The modelling work was developed to consider the replacement of brine by supercritical CO_2 in a both virtual caprock under conditions of pressure and temperature equivalent to a burial depth of 1300m, and a reservoir rock under the same conditions of temperature and pressure. The development was carried out in the open source code Open GeoSys.

For verification the methods are compared against a standard analytical solution for two phase flow, the standard FUG-Finite Element (FUG-FE) numerical scheme with volume averaging for the saturation equation and a Finite Volume model for heterogeneous permeability distribution. The standard FUG-FE scheme was not able to cope sufficiently with the heterogeneities without grid refinement, and quickly started to predict saturations below the residual saturation of above the maximum saturations of the fluid in the system. However the FUG-vT approach could deal with the heterogeneities without grid refinement, the saturation profiles it predicted were smooth and within the residual and maximum saturations for the fluid in the system. In all cases the FUG-vT approach required significantly less time than the standard FUG FE approach to come to a stable solution.

In the modelling comparison it was shown that the results are scalable depending on pressure, permeability and the volume applied by the source term. This model as it stands can be used to make an initial assessment of caprock integrity during CO_2 injection and the potential pattern of lateral migration of CO_2 in a reservoir.

Removing the requirement for grid refinement and providing a stable solution to the flow equations creates a stable basis for the further consideration of coupled

processes, such as heat transport, reactive mass transport and mechanics on the same grid scale.
Beyond the current application, the Front Tracking FUG-vT method whereby an analytical solution is integrated into the numerical formulation to add physical information to the model provides a new approach to modelling other two phase flow systems, for instance hydrocarbon systems. The approach is not confined purely to the reservoir conditions chosen, it is a simple matter to apply different fluid and material properties derived from other constitutional relationships reflecting different temperatures, pressures, fluids and models of relative permeability.
Introduction of different analytical solutions in the model to predict the volumes of the fluids is possible adding extra information, thereby reflecting conditions and processes to be investigated more accurately, for instance further work in this area includes the addition of the analytical solution for two phase flow under the influence of capillary entry pressure. Further work could also include coupling the scheme to higher order estimates of the pressure and velocity field in heterogeneous conditions ensuring that the local as well as global mass balance is better adhered to.
Finally we note that the injection of supercritical CO_2 into a reservoir rock will be strongly influenced by the heterogeneities present and the development of viscous fingering. It seems that it is over simplistic to assume a radial spread of CO_2 from the well centre. Monitoring for the front of a radial plume may loose a lot of the important details in the mechanics of the spread and distribution of the real CO_2 plume. A front tracking method may help to better identify the coupled processes operating and methods of managing CO_2 migration.

Acknowledgements

The research leading to these results has received funding from the European Community's Seventh framework Programme FP7/2007-2013 under the grant agreement No. 227286 as part of the MUSTANG project and from the Scottish Funding Council for the Joint Research Institute with the Heriot-Watt University which is part of the Edinburgh Research Partnership in Engineering and mathematics (ERPem).

References

Brooks, R. H., and A. T. Corey, Hydraulic Properties of Porous Media., *Hydrol. Pap.*, *3*, Band 3, Colorado State University, Fort Collins, (1964).

Buckley, S. E., and M. C. Leverett, Mechanism of Fluid Displacements in Sands, *Transactions of the American Institute of Mining and Metallugical Engineers (TAIME)*, *146*, 107-116, (1941).

Chen, Y., L. J. Durlofsky, M. Gerritsen, and X. H. Wen, A coupled local-global upscaling approach for simulating flow in highly heterogeneous formations., *Advances in Water Resources*, *26*, 1041-1060, (2003).

Chen Z, X. Some invariant solutions to two-phase fluid displacement problems including capillary effect, Soc. Pet. Eng. Reservoir, Eng., 3(2), 691-700, (1988).

Durlofsky, L. J., Y. Efendiev, and V. Ginting, An adaptive local-global multiscale finite volume element method for two-phase flow simulations, *Advances in Water Resources*, *30*, 576-588, (2007).

Fucik, R., M. J., B. M., and I. T. H., Semianalytical solution for two-phase flow in porous media with a discontinuity, *Vadose Zone*, *7*, 1001-1007, (2008).

Glimm, J., J. W. Grove, X. L. Li, and N. Zhao, Simple front tracking *Contemporary Mathematics*, *238*, edited by G.-Q. Chen and E. DiBenedetto, pp133-149, Am. Math. Soc., Providence, R.I. (1999).

Helmig, R., *Multiphase flow and transport processes in the subsurface; a contribution to the modeling of hydrosystems*, Environmental Engineering., Springer, Berlin, ISBN 3-540-62703-0, pp367, (1997).

Helmig, R., C. Braun, and S. Manthey, Upscaling of two-phase flow processes in heterogeneous porous media: Determination of constitutive relationships, *IAHS AISH Publication*, *277*, 28-36, (2002).

Helmig, R., and R. Huber, Comparison of Galerkin-type discretization techniques for two-phase flow in heterogeneous porous media, *Advances in Water Resources*, *21*, 697-711, (1998).

Hoteit, H., and A. Firoozabadi, Numerical modeling of two-phase flow in heterogeneous permeable media with different capillarity pressures, *Advances in Water Resources, 31*, 56-73, (2008).

Huang, H., and P. Meakin, Three dimensional simulation of liquid drop dynamics within unsaturated vertical Hel-Shaw cells, *Water Resources Research*, *44*, 10pp, (2008).

Huang, H., P. Meakin, and L. Moubin, Computer simulation of two phase-immiscible fluid motion in unsaturated complex fractures using a volume of fluid method., *Water Resources Research*, *41*, 12pp, (2005).

Ippisch, O., H. J. Vogel, and P. Bastian, Validity limits for the van Genuchten-Mualem model and implications for parameter estimation and numerical simulation, *Advances in Water Resources*, *29*, 1780-1789, (2006).

Istok, J., *Groundwater Modeling by the Finite Element Method*, American Geophysical Union, 2000 Florida Avenue, NW, Washington, DC 20009, (1989).

Juanes, R., and Patzek, T.P., Multiscale-stabilized finite element methods for miscible and immiscible flow in porous media, *Journal of Hydraulic Research,* Vol 42, Extra Issue, 131-140, (2004).

Klieber, W., and B. Riviere, Adaptive simulations of two phase flow by discontinous Galerkin methods, *Computer Methods in Applied Mechanics and Engineering*, *196*, 404-419, (2006).

Kolditz, O. Modelling of flow and heat transfer in fractured rock: Conceptual model of a 3-D deterministic fracture network. Geothermics, 24 (3): 451-470, (1995).

Kolditz, O., Non-linear flow in fractured rock, *International Journal of Numerical Methods for Heat & Fluid Flow*, *11*, 547-575, (2001).
Lewis, R. W., and B. A. Schrefler, *The Finite Element Method in the Static and Dynamic Deformation and Consolidation of Porous Media*, 2 ed., 492 pp., John Wiley & Sons, Chichester, England, (1998).
McDermott, C. I., M. Lodemann, I. Ghergut, H. Tenzer, M. Sauter, and O. Kolditz, Investigation of coupled hydraulic-geomechanical processes at the KTB site: pressure-dependent characteristics of a long-term pump test and elastic interpretation using a geomechanical facies model, *Geofluids*, *6*, 67-81, (2006).
McDermott, C. I., S. A. Tarafder, and C. Schüth, Vacuum assisted removal of volatile to semi volatile organic contaminants from water using hollow fiber membrane contactors II: A hybrid numerical-analytical modeling approach., *J. Membrane Science*, *292*, 17-28, (2007).
McDermott, C. I., R. Walsh, R. Mettier, G. Kosakowski, and O. Kolditz, Hybrid analytical and finite element numerical modeling of mass and heat transport in fractured rocks with matrix diffusion, , *Computational Geosciences, DOI: 10.1007/s10596-008-9123-9,* (2009).
McWhorter, D.B., and D. K. Sunada. Exact integral solutions for two-phase flow. *Water Resources Research*, 26:399–413, (1990).
Meakin, P., and A. M. Tartakovsky, Modeling and simulation of pore-scale multiphase fluid flow and reactive transport in fractured and porous media., *Rev. Geophys.*, *47*, 47pp, (2009).
Niessner, J., and S. M. Hassanizadeh, A model for two-phase flow in porous media including fluid-fluid interfacial area, *Water Resources Research,* 44, W08439, (2008) doi:10.1029/2007WR006721.
Thorenz, C., Model adaptive simulation of multiphase and density driven flow in fractured and porous media. PhD thesis, Universitaet Hannover, 2001, ISSN 0177-9028, pp179, (2001).
Thorenz C, Kosakowski G, Kolditz O and Berkowitz B, An experimental and numerical investigation of saltwater movement in partially saturated systems. *Water Resources Research*, vol. 38(6), (2002), 10.1029/2001WR000364.
Unverdi, S. O., and G. Tryggvason, A Front-Tracking Method for Viscous, Incompressible, Multi-Fluid Flows, *J. Computational Physics.*, *100*, 25-37, (1992).
van Duijn, C.J., and M. J. de Neef, Similarity solution for capillary redistribution of two phases in a porous medium with a single discontinuity. *Advances in Water Resources.*, 21:451–461, (1998).
van Genuchten, M. T., A closed form equation for predicting the hydraulic conductivity of unsaturated soils., *Soil Science Society of America Journal*, *44*, 892-898, (1980).
Versteeg, H. K., and W. Malalasekera, *An Introduction to Computational Fluid Dynamics, The Finite Volume Method,* Second Edition ed., 503 pp., Pearson Prentice Hall, (2007).
Wang, W., and O. Kolditz, Object-oriented finite element analysis of thermo-hydro-mechanical (THM) problems in porous media, *International Journal of Numerical Methods in Engineering*, vol. 69 (1): 162-201, (2007).
Wang WQ, Kosakowski G and Kolditz O, A parallel finite element scheme for thermo-hydro-mechanical (THM) coupled problems in porous media. Computers & Geosciences, vol 35(8): 1631-1641, (2009).

Younes, A., Ackerer, P. and Delay, F. Mixed finite elements for solving 2-D diffusion type equations, Reviews of Geophysics, 48, RG1004/2010 pp 26, (2010).
Zienkiewicz, O. C., and R. L. Taylor, *The Finite Element Method*, 6 ed., 752 pp., Butterworth Heinemann, (2005).

Table 21 Fluid properties, models 1,2 & 3

Parameter	Brine	Supercritical CO_2
Density	1050Kg/m^3	740Kg/m^3
Viscosity	0.65×10^{-3}	0.0598×10^{-3}

Table 22 Material parameters, model 1&3

Parameter	Model 1&2	Model 3
Permeability	$1\times10^{-14}m^2$	$1\times10^{-14}m^2$, $1\times10^{-16}m^2$
Porosity	0.20	0.20

Table 23 Material parameters model 4 & 5.

Permeability	Model 4	Model 5
$1\times10^{-12}m^2$	12%	8%
$1\times10^{-13}m^2$	18%	17%
$5\times10^{-14}m^2$	18%	16%
$1\times10^{-14}m^2$	20%	16%
$5\times10^{-15}m^2$	11%	17%
$1\times10^{-15}m^2$	21%	17%
$1\times10^{-16}m^2$	-	8%
Porosity	0.2	0.2

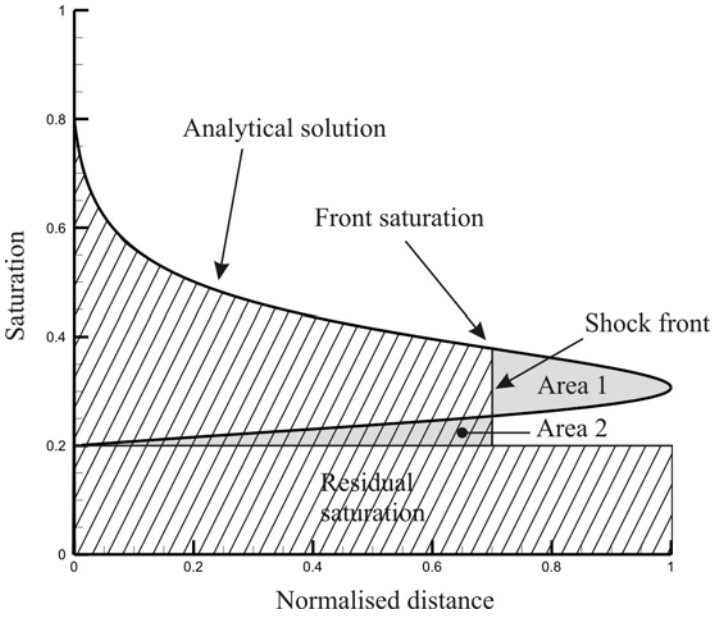

Figure 109 Analytical solution for two phase flow.

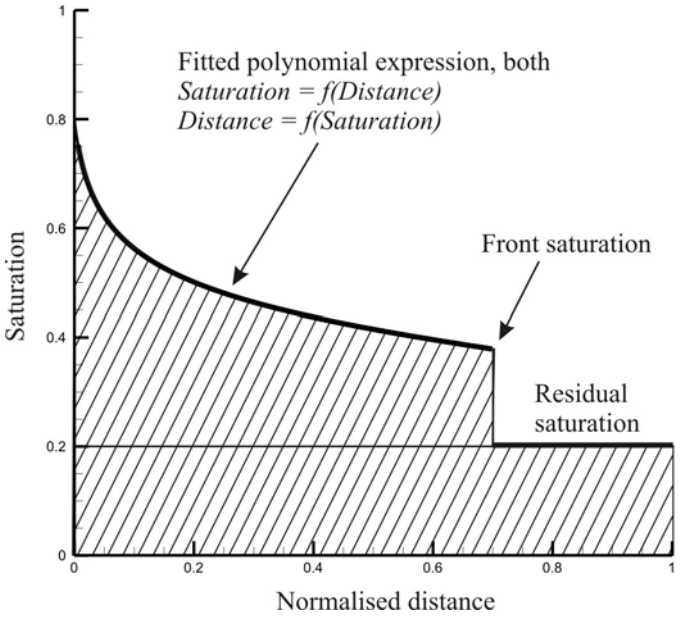

Figure 110 Two phase flow surface is approximated by a polynomial expression.

```
$TPF_ANALYTICAL_CURVEDSURFACE
;Front saturation, Residual saturation, Maximum saturation , Scaling factor,   Polynomial coef. 7 values x^6 x^5 x^4 x^3 x^2 x c
    0.378                0.2                0.8                5.1          -275.33  971.28  1375  976.29  -346.05  47.182  0.974
$TPF_ANALYTICAL_INVERSE
; Polynomial coefficients 7 values x^6 x^5 x^4 x^3 x^2 x c
516.45  -973.06  714.0  -258.89  49.222  -5.1998  0.7835
```

Figure 111 Extra input code to trigger and describe the HAN method in OpenGeoSys .

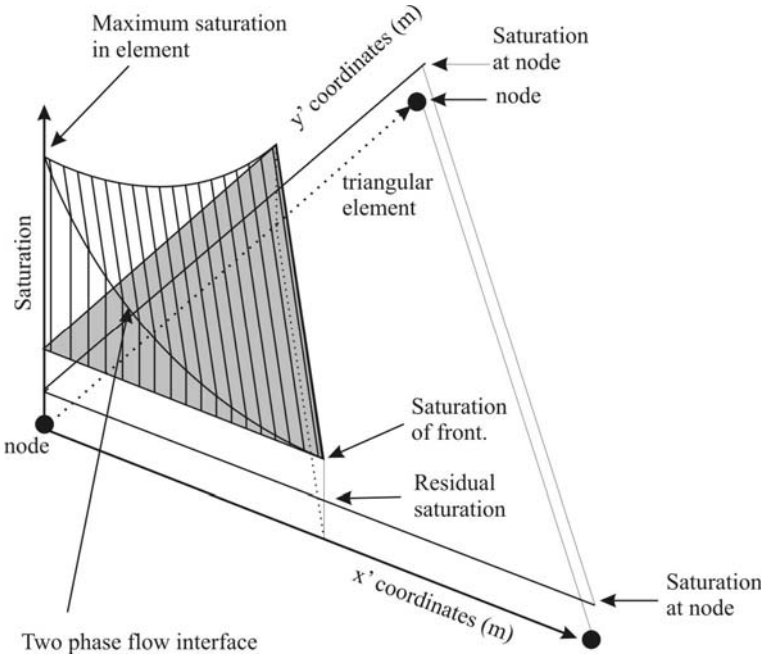

Figure 112 The front has passed one node in the element.

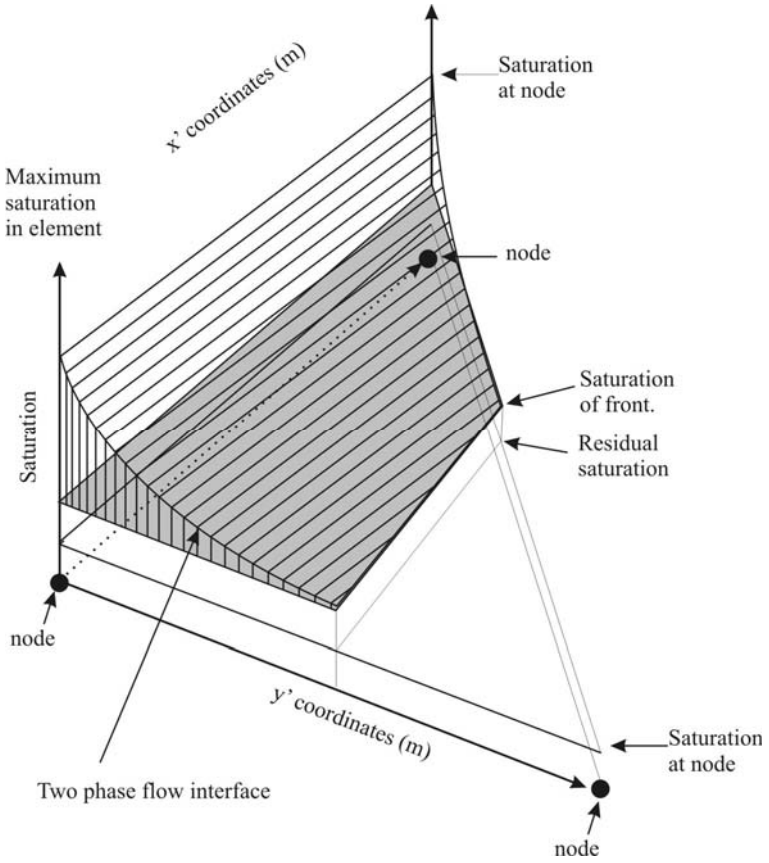

Figure 113 The front has passed two nodes in an element.

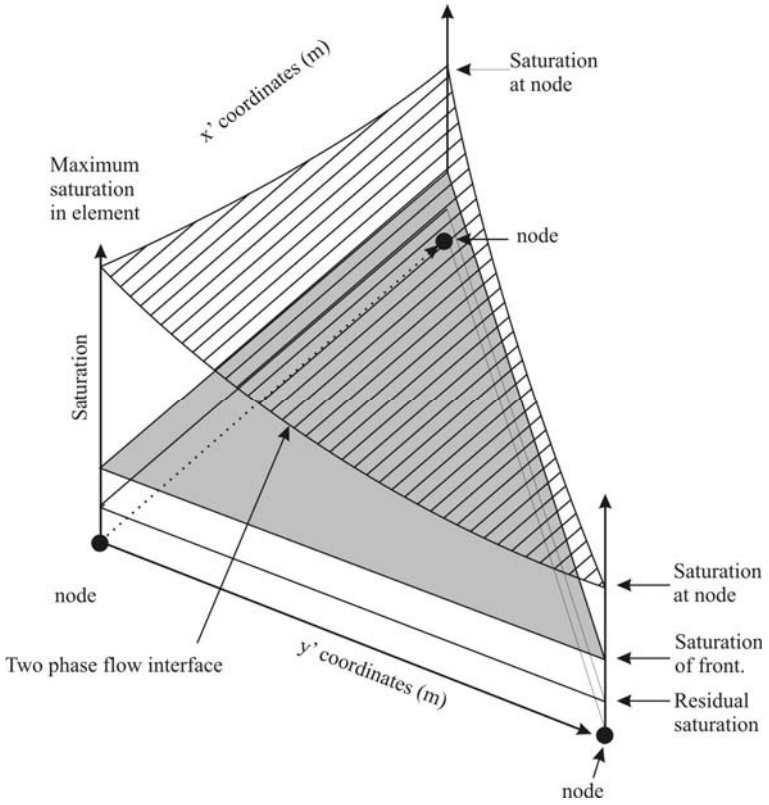

Figure 114 Two phase flow front has passed an element

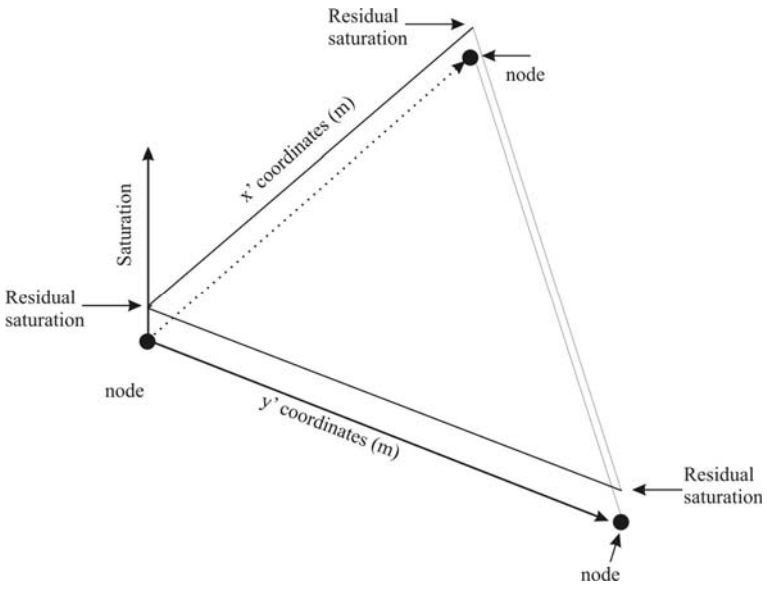

Figure 115 Two phase flow front has not yet reached the element

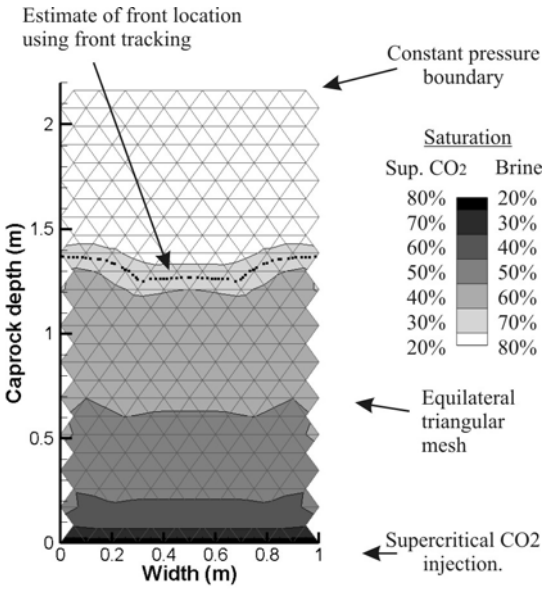

Figure 116 Model for injection of supercritical CO_2 at the base of homogeneous caprock, application of front tracking method.

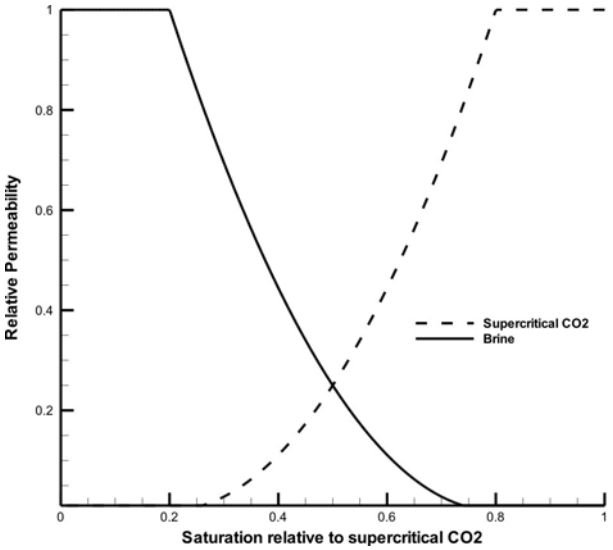

Figure 117 Relative permeabilities functions from *Buckley and Leverett* [1941]

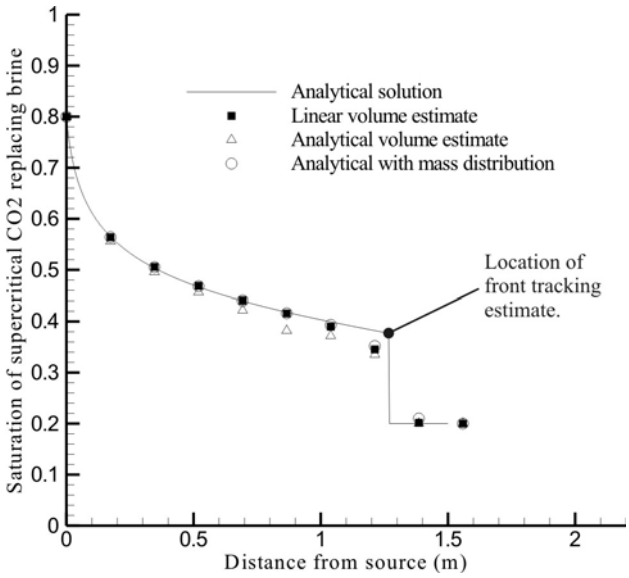

Figure 118 Comparison of the analytical solution to volumetric method, the analytical method with and without mass distribution and the estimation of the front tracking method.

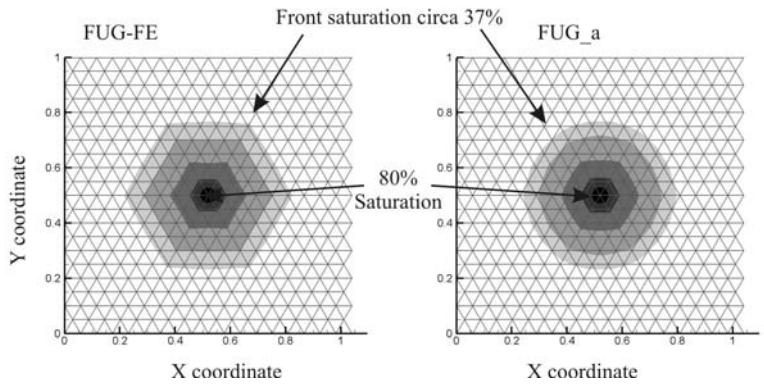

Figure 119 Comparison of radial solutions using the FUG-FE and the FUG-a approaches.

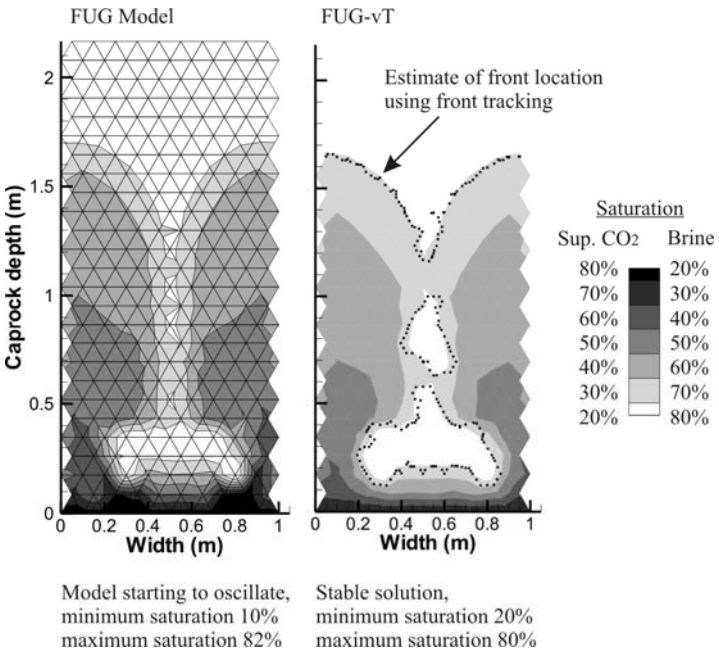

Figure 120 Low permeability layer just above the injection front, comparison of FUG and FUG-vT model performance, 40.5 days after start of forced injection.

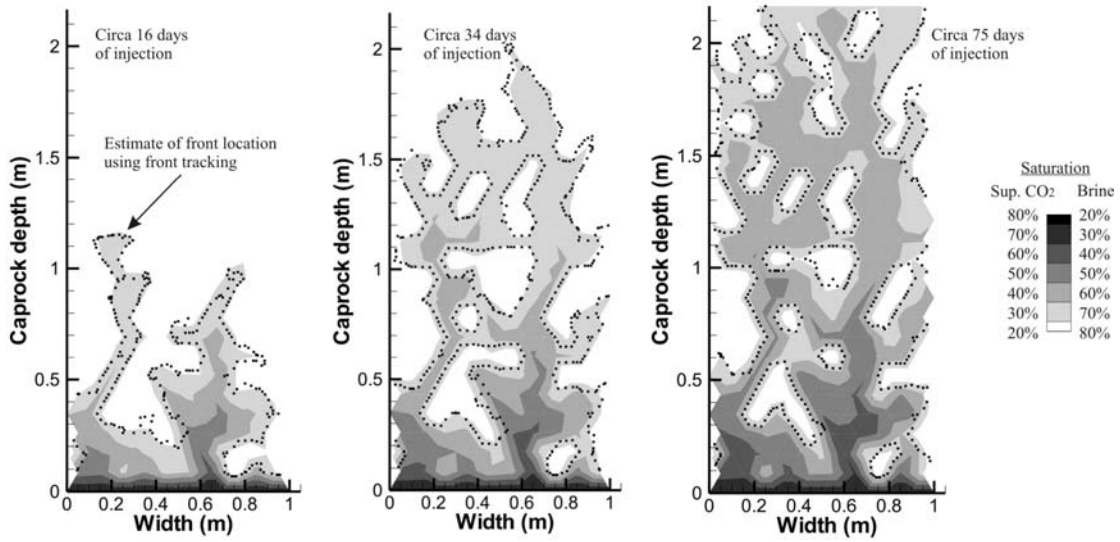

Figure 121 Injection into a heterogeneous field

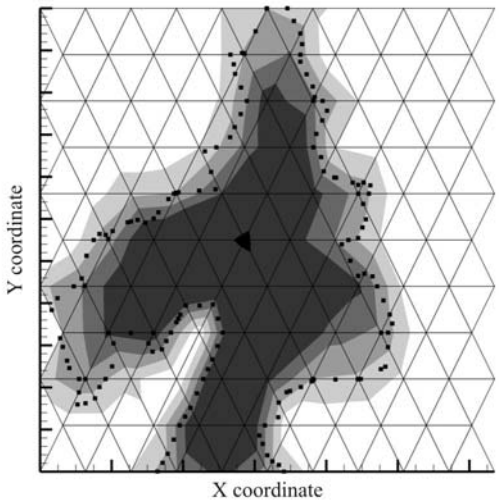

Figure 122 Front tracking provides sub element scale information on the location of the saturation front in a heterogeneous field.

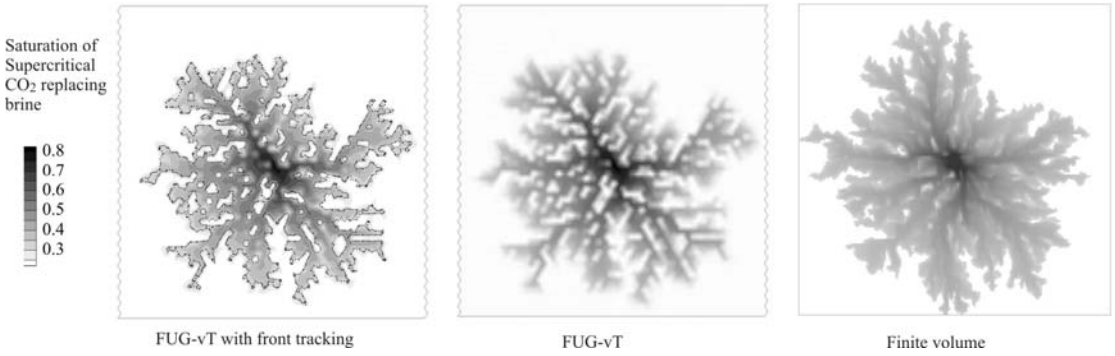

Figure 123 Comparison of well injection of supercritical CO_2 in a heterogeneous reservoir rock with front tracking, then without front tracking and continuous colouring for FUG-vT and a Finite volume solution.

4.4 Paper: Predicting hydraulic tensile-fracture spacing in strata-bound systems.

[1]C.I. McDermott, K. Edlmann, M. Edwards, R.S. Haszeldine

Edinburgh Collaborative of Subsurface Science and Engineering (ECOSSE), School of Geoscience, University of Edinburgh, West Mains Road, Edinburgh, EH9 3JW, Scotland

[1]Corresponding author
cmcdermo@starffmail.ed.ac.uk
Fax: +44 (0)131 650 5738

Abstract
A model is presented which predicts the spacing of tensile-fractures due to fluid pressure increase in a multilayered sedimentary sequence comprising different typical sedimentary deposits such as mudstones, siltstones, sandstones. This model is both applicable for engineered applications such as the injection of fluid into a reservoir thereby causing an increase of fluid pressure beneath a caprock, and for sedimentary sequences during normal digenetic processes of burial and fault activation. The model predicts many of the field observations made about strata bound fracture systems. A standard normalised relationship is provided for most sedimentary systems predicting the spacing of discontinuities based on the variability of the tensile strengths of the layers of a sedimentary sequence and the thickness of the beds. The model provides a tool for assessing the historic fluid pressures in beds based on fracture spacing observations, and will aid in the prediction of the behaviour of such strata and the development of discontinuities during engineered fluid injection

Key words: Hydro-fracking, discontinuity spacing, CO_2 analogue, caprock, fluid injection.

1. Introduction
In the evaluation of caprock and analogue seals the discontinuity spacing is of vital importance. In proposed CO_2 storage sites it is not the intact matrix of the caprock that causes concern for the retention of the injected CO_2 rich fluids, or pure dense phase CO_2. Rather it is the presence of discontinuities at a series of scales which need to be quantified and analysed in terms of their flow and transport properties. During the investigation into a reservoir, the fluid pressure history and digenetic analysis of the caprock plays an important role in understanding how it will react to the presence of increased aggressive fluid pressure loading beneath it. Here we present a model looking particularly at the impact of increased fluid pressure in multilayered sedimentary systems, the physical requirements for fluid driven fracturing of the strata in these layered systems and the characteristics the systems are likely to show. The model particularly emphasises the importance of the development of local stress distributions on the development of fractures. It can also be used to predict the likely fracture patterns of fluid driven (hydro-fracturing) in strata bound systems and may be used to influence the affectivity of fracking procedures.

Several authors discuss joint formation mechanisms. Here we concentrate on opening mode fractures. Key work of Price (1966) discusses joint / discontinuity development wherever the effective tensile stress exceeds the tensile strength of the rock. Possible causes being a result of fluid

overpressure, expansion of the rock mass under uplift and erosion, pull apart due to tension induced by a regional extension, salt diapirism and folding.

There are obviously several mechanisms which will lead to the formation of discontinuities. Which mechanism is dominant at any particular time and the characteristics of deposit (the packet of sediment and hard rock, including any existing fracturing) will influence the nature of the response of the deposit to the mechanism.

Bonnet et al. (2001) review several methods of scaling fracture systems, including the lognormal distributions, exponential distributions and gamma law distributions, and indicated a recent preference for the fractal approach. They point out that recent studies indicate lithological layering from the scale of a single bed to the whole crust is reflected in fractures system properties and influence the scale range over which individual scaling laws are valid. The above named distributions are mathematical fits of probability distributions, and to understand the cause of fracturing it is necessary to reference the mechanical constraints and drivers. In certain cases one model, with certain limiting factors fits better than another, but there is no ubiquitous law to match the whole population of fractures.

In a typical discontinuity measurement set, several types of fractures will be present, to understand the spacing of the fractures it is important to understand the mechanisms which have lead to the development of the fracturing. The observation that lithological layering is reflected in the fracture systems suggests that a process operating at the scale of the lithological bed size is important in controlling the development of the fractures. Here we concentrate on strata bound fractures and suggest that the stress field developed during dynamic fracturing significantly influences the location of the development of further fractures.

Identifying the key processes behind fracturing as creating "separate fracture packets" or end members will help in the analysis of the fracture spacing and the nature of the process leading to the fracturing. Also in prediction of the behaviour of a fractured system understanding the driving mechanisms will also aid in determining the location and physical influence of the fractures in the rock formation.

Bai and Pollard (2000) summarised work from many authors to make the observation that "the fracture spacing in layered sedimentary rocks is roughly proportional to the thickness of the fractured layer, with a ratio of thickness's from less than 0.1 to greater than 10." They developed a finite element model describing fracture spacing as a result of a pull a part model, and a transition of stress from higher strength beds into a fracturing bed. From the results of this they subdivided the fracture spacing to bed thickness ratios into four categories, whereby they could explain two categories with their extensional model and the further two categories where the joint spacing was too tight to have been caused by the extensional mechanism explained. They concluded that the other sets of joint spacing ratios required flaws and fluid pressure to produce the spacing. They note that between two fractures as the tensile stress increases eventually a fracture will be initiated either as a result of a local heterogeneity, such as a pre-existing zone of weakness, or due to the increase in fluid pressure overcoming compressive strength. Bai et al. (2000) note that experimental and field results indicate fracture spacing decreases approximately as the inverse of the applied strain in the direction perpendicular to fractures, by fractures forming between earlier formed fractures. Gross, (1993) used the term "sequential infilling" to describe this process. Bai and Pollard, (2000) developed the concept of a maximum

fracture saturation distance, being related to the stress distribution caused by the presence of a fracture leading to an area of "stress shielding" and thereby setting a lower limit as to possible fracture spacing. The stress shielding is caused by the compressive stress caused by vertical shortening of the fractures and the horizontal constraint in the central area between two fractures.

Odling et al. (1999) examined several high quality data sets of fracture systems from four reservoirs and identified two end member types of fracturing, named as "strata bound" and "non strata bound". They suggest that in strata bound systems there is little mechanical coupling between the layers. The individual joints are confined to single layers, and there is a clear relationship between bed thickness and joint spacing. Such sequences are found in systems with strongly developed interbedded weak and strong layers, e.g. interbedded sandstones, limestones, mudstones and shales. They describe the system as having weak adhesion between the layers. Odling et al. (1999) describe strata bound fracture systems as confined to single layers, the sizes are scale restricted and the spacing is regular. We note also from observation of typical caprock analogues that fracturing may at times go slightly beyond the limits of the bed and that half fractures, i.e. fractures extending only a partial distance in the fractured bed are also present.

The focus of this paper is on strata bound systems and the role of fluid overpressure, and we suggest that it plays a more significant role than previously acknowledged in the formation of strata bound systems. Here we suggest that the extensional model provided by Bai and Pollard, (2000) presents one end member of possible mechanisms leading to bed thickness related fractures, and that a fluid pressure driven model can also provide another end member for these opening mode fractures with similar characteristics. Indeed the results of Rutqvist and Tsang (2002) illustrate that hydraulic fracturing can be expected in the lower layers of a caprock after a relatively short period of time of fluid injection. The model we present predicts not only the main characteristics of strata bound fractures, but also under the right loading conditions the formation of orthogonal fracture system. This makes the model suggested here distinct from a pull apart model. It is reasonable to assume that during the normal digenetic development of a sediment, flexing and burial, both models will be applicable, and reinforcing one another. During engineered hydro-fracking the fluid pressure driven model presented here will be prevalent.

2. Hydro-fracking in strata bound systems

Fluid pressure build up will occur naturally during the development of a multilayered sedimentary deposit as a result of burial and compression, a fluid charge from a deeper source or sudden settlement events such as on going tectonic activity. For burial to cause a sustained fluid overpressure, fluid migration in the layers needs to be restrained due to lower permeability layers. A stack of sediments will typically comprise sandstones, mudstones and siltstones. The model we present shows that the difference in the tensile strength and the difference in the permeability of the beds is a cause behind the development of the strata bound fracture systems, the parameters thereof influencing the density of the fractures.

We start by postulating a simplified sedimentary sequence as a cut out from a typical multi-layered sequence (Figure 124). The sequence is saturated, and from base to top, there a relatively permeable sandstone or carbonate rock (maybe a reservoir rock), above this are two less permeable layers, whereby the tensile strength of the lower bed is less than the tensile strength of the upper bed, for instance the lower bed may be a mudstone, the upper bed a

siltstone. The lower tensile stress bed has fractured normal to the minimum principal stress direction, σ_h . Possible mechanism for this are discussed below, but for now what is important is consideration of the impact a fracture in this layer will have on the development of the local stress field in response to further hydrostatic pressure increase.

#Figure 124 Stack of sedimentary deposits

If higher pressure fluid is injected into the fractures, the geometry of the fractures will cause them to exert the hydrostatic pressure within them normal to the fracture walls. The key behind the stress influence of the fractures on each other is the ability of the fracture wall to act as a load bearing surface in relation to the influx of extra fluid and increase in pressure within the fracture. The lower the permeability of the fracture walls (being in a low permeability deposit) the higher the load will be that is sustained and applied throughout the matrix, and the more localised the impact of the higher fluid pressure. In contrast in a higher permeability matrix the extra fluid pressure in the fracture will quickly be transferred to the matrix and be seen as a pore pressure increase.

The increase in fluid pressure in the fracture exerts a directional compressive stress on the bed normal to the fracture wall. This causes the development of a stress field represented by the Bousinesq bulbs of pressure sketched in Figure 124. As the fluid pressure continues to rise eventually a new fracture will propagate in the area of least horizontal stress development and depending on heterogeneities present, the most likely location being half way between the existing fractures.

At the location where a new fracture will be formed the pore pressure is being driven from the shortest drainage path, either from the bed itself due to compaction or from the fluid source coming through the layer either above or below it. For the existing (vertical) fracture, the increase in fluid pressure is working against the fracture walls to increase the amount of horizontal stress in the bed. The extra compression due to the fracture loading works against the increased expansive force of the fluid pressure at the location where the new fracture is to be formed (and all other locations in the bed). The two forces are not equal however, due to the distribution of stress from the fracture wall, eventually the expansive force at the location of the new fracture overrides the minimum horizontal tectonic stress, the compressive force of the existing fractures and the tensile strength of the bed. This causes the formation of a new fracture normal to the minimum horizontal stress.

2.1 Conditions causing hydro-fracturing

The tensile breaking point σ_f of the individual layers of tensile strength σ_t in a confining stress field of σ_h can be given as a first approximation as

$$\sigma_f = \sigma_t + \sigma_h \tag{46}$$

that is to cause a tensile fracture to develop both the confining stress and the tensile strength of the rock need to be overcome. If the fluid pressure exceeds this value then a tensile fracture must develop, literally the rock is being blown apart from within. The effective stress is given by

$$\sigma_e = \sigma - u \tag{47}$$

In a draining medium the amount of effective stress is a measure of the amount of drainage occurred. In the case where u is increasing the effective stress becomes tensile, and failure occurs where it exceeds the absolute

value $\left|\sigma_f\right|$. The permeability of a bed influences the rate of the change in effective stress proportional to the drainage path length. Basically the fluid is either trying to get out of the bed (drain) or make space for itself.

Following Terzaghi (1943), if the fluid pressure is caused by compaction of the fracturing bed then the higher fluid pressures are likely to be developed in the centre of the layer, as this has the longest drainage path to the higher permeability zones. Should the fluid be a charge, assumed from underneath then we envisage the highest fluid pressure at the start of the fracturing at the contact of the fracturing rock with the reservoir rock. We note that during compaction the fracturing layer could be above or below the reservoir layer.

Once the fracturing is initiated, it propagates normal to the least principal stress, σ_h. Fluid migrates into the fracture developing in the caprock until the fracture reaches the overlying layer of higher tensile strength. At this point the fluid in the fracture is at a higher pressure than the fluid in the surrounding matrix of the fracturing layer and at a higher pressure than the fluid in the confining layer. Drainage of this pressure occurs both through the overlying layer and into the fracturing layer depending on the relative permeabilities of these layers to each other, and the rate of recharge of the fracture fluid. Should there be a rapid rate of recharge then a higher pressure in the fracture can be expected and vice versa.

#Figure 125 Generic sedimentary sequence

For the model, what is important is that the confining layer (Caprock facies II) retains a higher pressure than is required to fracture the fracturing layer (Caprock facies I). The confining layer does not fail until even more fluid pressure is applied.

Once a fracture has been developed in the fracturing layer, this fracture exerts the fluid pressure normal to the least principal stress. For the case where there is a fluid charge from beneath, vertically there is no differential stress seen in the fracturing layer as we assume the plan view extent to the layer is significantly more than the thickness of the layer. If the sequence is mechanically restrained vertically then the increase in the horizontal stress as a result of the increase in the vertical pressure is given by

$$\sigma_{h\Delta u} = \frac{\upsilon\left(1+\upsilon\right)}{1-\upsilon^2}\Delta u \tag{48}$$

where υ is Poissons ratio, with Δu being the increase in the fluid pressure in the reservoir layer which we assume pushes the fracturing layer, but does not enter the fracturing layers matrix, i.e. the layer is squashed together a bit. If the strata is not mechanically restrained vertically then some uplift will occur without a significant increase in the vertical stress.

At this point we have higher fluid pressure in the fracture than in the fracturing layer. This will equilibrate with time, the rate being dependent on the permeability of the bed, and if we allow some mechanical pore deformation then it is also inversely proportional to the storage of the bed, the combined effect being the pressure diffusivity, e.g. Kessels et al. (2004). At the edges of the area if there is little constraint on the layer, plastic and elastic strain accommodation of stress will occur (either the material squashes out a bit, or squashes up against a harder material). Outside of the boundary region this release is not available, therefore there is an increase in the least principal stress experienced by the fracturing rock. How this stress is

distributed can be predicted using analytical elastic solutions for the distribution of stress under loading (bulbs in Figure 124).

2.2 The effect of vertical discontinuities on the horizontal stress distribution

Integrating the Boussinesq (1878) equation for a point load, e.g. Davies and Selvadurai (1996), it is possible to obtain a number of elastic solutions for different geometrical conditions. Referring to Figure 125, we approximate the fracture which has been developed in the fracturing layer as an infinite strip foundation with a width of 2B (Figure 126) exerting pressure normal to the strip, in the fracture case normal to the fracture wall. The standard solution and geometrical arrangement for the elastic solution of this stress field development for a semi-infinite layer is presented in Figure 126, (Poulos and Davis, 1974).

#Figure 126 Standard elastic strip solution on a semi–infinite layer

Interestingly applying the Bousinesq approach, the elastic modulus is taken as not having a significant impact on the stress distribution. In the extensional model suggested by Bai and Pollard (2000), they show that contrasting moduli introduce minor quantitative differences in fracture spacing. In applying this strip solution we are interested only in the stress distribution, and assume some degree of mechanical contact between the individual layers. Also we assume that there is a smooth frictionless contact between the fluid pressure in the fracture and the matrix, and that the side of the walls of the fracture are detached from one another.

The semi-infinite layer assumption suggests that the stress seen at the fracture will be seen in some way throughout the whole of the fracturing layer. As a first assumption this method is useful in understanding the distribution of stress in the fracturing layer, and the principle of stress superposition can be applied for subsequent fractures. However to take into account that fractures in the fracturing layer will be developing parallel to each other and significantly influencing each other the closer they are together, it is necessary to select an analytical solution which encompasses this.

The increase in horizontal pressure as a result of the increase in vertical stress via Poisson's ratio is considered ubiquitous as the plan area of the bed is considered significantly more than the thickness of the bed. Therefore this stress increase will not be dissipated. However to calculate the dissipation of the increase in horizontal stress caused by the loading at the fracture walls we apply a solution developed by Poulos (1967) for a foundation underlain by an adhesive rigid base.

#Figure 127 Elastic solutions for a rough strip foundation underlayen by a rigid base.

The solution provided is for the stress increase with depth (z) under the corner of a strip foundation upon a finite layer of thickness (h) underlain by a rigid base. The rigid base can be taken as the point of meeting of the influence of two fractures on each other, acting as a rigid base (see Figure 125), that is any stress applied to the base is reflected equally by the same stress being applied from the opposing fracture. There is no movement of any particle along this line as a result of the fluid pressure in the fractures. We approximate the influence factor I_{st} shown in Figure 127 as a polynomial function of B/h, whereby substituting B/h with x

$$I_{st} = 0.0568x^6 - 0.524x^5 + 1.6629x^4 - 1.9318x^3 - 0.4443x^2 + 2.6624x + 0.0004 \quad \text{for } 0 \le x \le 2 \tag{49}$$

The increase in stress as a result of the additional fluid pressure loading (Δu) on the fracture is then

$$\sigma_{\Delta u_f} = I_{st} \frac{\Delta u}{\pi} \tag{50}$$

The ration B/h is crucial, and is used to evaluate the size of the influence factor, which in turn is used to evaluate the stress at the rigid base. Looking at Figure 125, it can be seen that the stress at the edges of the layer can now be approximated using this approach directly by inputting the appropriate values of B and h (Figure 127). The stress at any location along the rigid base is calculated using the principle of stress superposition, in that two strip foundations running alongside each other are assumed with different values of B and h, the influence factors evaluated and the stresses calculated. The resulting compressive stress across the layers is given by the superposition of these stresses, i.e. they are added together.

For a point in the centre of the layer the stress increase is

$$\frac{\sigma_{\Delta u_f}}{2} = I_{st} \frac{u}{\pi} \text{ where B = 0.5 bed thickness} \tag{51}$$

For a point at the edge of the layer the stress increase is

$$\sigma_{\Delta u_f} = I_{st} \frac{u}{\pi} \text{ where B = bed thickness} \tag{52}$$

At first glance it would appear that (51) and (52) should give the same value. This is not the case as I_{st} is non linear, as illustrated by the comparison to the linear line presented in Figure 127. If a linear function was applied then the stress change the edges of the bed would be predicted to be the same as the stress change at the centre of the bed. However the nonlinearity of this function predicts that the stress increase at the edge of the bed will be slightly less than the stress increase in the centre of the bed, an important fact we will come back to later.

Applying this model we find that the most likely position for another fracture to develop will be halfway between two existing fractures. The influence these fractures have upon the compressive strength between these two layers can be calculated, and therefore the fluid pressure required to cause hydro-fracturing in at this location can be evaluated.

As long as the stress is distributed geometrically in the layer and surrounding layers there will be a difference between the fluid pressure in the fractures and the pressure required to fracture the rock.

2.3 Dynamic system

As fluid pressure is building up at the base of the layer being fractured, so also the fluid pressure is increasing in the fractures. This leads to a dynamic system.

To follow this through in example now, let us assume that we require an overpressure of 1MPa (100m water column height, 50m sediment loading) to cause the first tensile fracturing uninfluenced by surrounding fractures. This pressure we call u_{fs}, (where s (set) = 1 being the first set of fractures to form), is the fluid pressure required to cause the first set of fractures,

initiated due to the heterogeneities in the rock at random weak locations. Should the pressure now remain at 1MPa, we can predict the extra pressure now required to cause the next set of fracturing $u_{f(s+1)}$, say from evaluation this is 1.1MPa. Should the pressure now increase to 1.1MPa, we need to take account of the fact that the 0.1 MPa increase in pressure in the fractures will also have a further compressive effect across the new fracture location (note the numerical modelling work of Rutqvist and Tsang (2002) indicated after 10 years of fluid injection that a minimal pressure increase of 0.1MPa could cause further hydraulic fracturing). This can also be evaluated as (51) and (52) above, however we note that we now have a dynamic system, where the compression across the new fracture location is increasing with the fluid pressure increase in the existing fractures. The pressure required for a new fracture $f(s+1)$ to form can be expressed as a power series

$$u_{f(s+1)} = u_{fs} + u_{fs}\frac{I_{st}}{\pi} + u_{fs}\left(\frac{I_{st}}{\pi}\right)^2 .... + u_{fs}\left(\frac{I_{st}}{\pi}\right)^{\infty} \tag{53}$$

Which is a convergent series as long as $\frac{I_{st}}{\pi} \le 1$ expressed as

$$u_{f(s+1)} = \sum_{n=0}^{n=\infty} u_{fs}\left(\frac{I_{st}}{\pi}\right)^n \tag{54}$$

The impact of a term $\left(\frac{I_{st}}{\pi}\right)^n$ can be seen as a multiple of the value u_t, we solve (54) for an accuracy of convergence of c% (55). The number of terms need to be evaluated to cover this being given by

$$n = \frac{\ln\frac{c}{100}}{\ln\left(\frac{I_{st}}{\pi}\right)} \tag{55}$$

Once the pressure has been reached for the next set of fractures to infill, $u_{f(s+1)}$ the pressure for the following set of infilling fractures can be evaluated as s = 2.

To include the effect of the vertical stress developed if the strata sequence is mechanically restrained vertically, the horizontally induced component of the vertical stress is calculated as in (48). We set the first tensile stress fracture of the layer at a defined value as per (46), and assume that σ_h in the layer at this moment contains all the resolved stress components. Further increases in the fluid pressure in the underlying rock now act also to uplift and further compress the fracturing rock, leading to an increase in the horizontal compression. This is included in (53) as follows.

$$u_{f(s+1)} = u_t + \sum_{n=1}^{n=\infty}(1+\frac{\upsilon(1+\upsilon)}{1-\upsilon^2})u_{fs}\left(\frac{I_{st}}{\pi}\right)^n \tag{56}$$

3. Results and discussion

The evaluation of the impact of bed thickness and fracture spacing can be normalised against initial tensile strength of the bed and the ratio of bed thickness to distance to the next fracture to provide a standard relationship. This is given in Figure 128 for the case where σ_h in (46) is zero. To calculate

the actual fluid pressure required to cause fracturing the initial value of σ_h needs to be added.

#Figure 128 Standard relationship for tensile fracturing conditions

As an example, let us say we want to evaluate the fluid pressure required to create strata bound fractures at a spacing of 20m in a bed with a thickness of 2m. Let us postulate that the tensile strength of the bed is 5MPa, and that there is an overlying bed with a higher tensile strength, and low enough permeability to cause the necessary pressure build up in the bed we are looking at.

From Figure 124, the bed thickness to fracture spacing ratio is 10, therefore the fluid pressure to tensile strength ratio is circa 1.2. This means that the fluid pressure required is then the tensile strength of the bed 5MPa multiplied by 1.2 giving 6MPa plus the horizontal stress.

It is interesting to note that the elastic modulus is not included in the development of the stress field due to loading (Boussinesq, 1878; Poulos, 1967). The impact of Poisson's ratio on the stress fields is estimated as described above and presented in Figure 129. This is also negligible. This means that the relationship described is a fairly ubiquitous relationship for beds during hydraulic fracturing, and the processes it illustrated can be applied to understand a number of phenomena.

#Figure 129 Natural hydraulic fracturing conditions, impact of Poisson's ratio (u in figure)

The difference between the fluid pressure required to fracture the center of the bed and that required to fracture the edge of the bed is minimal until a spacing of about four times the bed thickness has been achieved. This suggests that fractures which do not fully transect the bed will develop in the later stages of fracturing at higher pressures.

As fluid pressure increases, we note that should the horizontal stresses be of a similar size, as may be expected during early burial, that it is possible to fracture the systems orthogonally. Differences in σ_h and σ_H would be reflected in the spacing of the fracture sets.

Figure 130 Development of five fracture sets

Figure 130 demonstrates the development of fracturing with a fracture spacing to bed ratio of down to circa 1.5. If we postulate the tensile strength of the bed fracturing is 1MPa, then the layer causing the pressure build up in this case has a tensile strength of circa 4.7MPa. As the fluid pressure increases the degree of heterogeneity in the fracturing layer will determine initially the location of the first sets of fractures (moving on Figure 130 from right to left along the bottom). However, as soon as the difference caused by the heterogeneity is less than the stress superposition of the fracture systems, the general heterogeneity will play less of a determining role in the location of the fractures. Obviously the presence of already existing fractures and other significant plains of weakness may dominate the location of all the fracturing. From Figure 128 it can be seen that the influence of stress interference becomes more significant under a strata bound fracture spacing of circa 100 bed thicknesses.

Following again Figure 130, as the pressure increases so the next four sets of sequential infilling fractures arise until the fluid pressure for the next smallest set of fractures exceeds the tensile strength of the confining layer.

The spacing and therefore the number of fractures within a bed will be a function of the relative tensile strength of the bed in comparison to the other beds within the stratagraphic sequence. As soon as the fluid pressure has been able to rupture the confining layer, hydraulic fracturing in that bed will stop until a higher pressure can be retained.

This means for more general observations there will be no hard and fast rule for the spacing of fractures as a function of the tensile strength, rather in a sequence the lower tensile strength deposits will be more densely fractured, and in sequences with high amounts of tensile strength variability this will be reflected in the increased variability of the strata bound fracture spacing.

As discussed previously the key behind the stress influence of the fractures on each other is the ability of the fracture wall to act as a load bearing surface in relation to the influx of extra fluid into the fracture and the matrix when fluid is present within it to act under hydrostatic stress. If due to the high permeability of the bed the fracture wall is not able to act as a load bearing surface the process will be arrested, and therefore there will be less control on the location of new fractures. This suggests that there should be more variability seen in the spacing of strata bound fractures within higher permeability deposits than within lower permeability deposits once normalised against the bed thickness and the tensile strength of the rock.

Additionally the amount of fluid pressure generated in the sedimentary profile will also be a function of the rate of the source supply, the permeability of the individual beds and their thickness. Allowing normal Darcy flow, the amount of flow is a linear function of both the pressure gradient and the permeability. Therefore if a source is defining how much flow there is to be through a system, this will define the pressure gradient in the system as a function of the contrasting permeabilities of the beds to each other. The pressure gradient across a bed is a linear function of its permeability and an inverse function of its thickness. Therefore the thicker a bed and the lower its permeability the higher the pressure will be necessary to sustain a constant flow rate. In a source term driven system, the source term is forcing fluid through a sequence and if the rate of the source term increases then the pressure gradient has to increase to accommodate this. This increase in pressure could be enough to trigger the hydraulic fracturing described above.

4. Conclusions

We identify the hydro-fracturing process as one possible mechanism for tensile fracture development and present a model for investigating the characteristics of tensile fracturing driven by fluid pressure increase in multilayered sedimentary systems. The model allows the derivation of a standard normalised rule applicable to all strata bound systems. We suggest that both extension fluid pressure-fracturing can operate during a normal digenetic burial process, but suggest that the fluid pressure model presented here will better explain certain features seen such as orthogonal fracturing and also be applicable during engineered fluid injection.

The model predicts that strata bond fracture systems will follow a standard curve during hydraulic fracturing which can be used to determine the pressures of fracturing as a function of the spacing of the factures and the tensile strengths of the beds. The key feature of the model is the interaction of fractures with one another, the build up in fluid pressure and the tensile

strength of the individual layer. The stress superposition caused by the fluid pressure loading in the fractures coupled with the heterogeneities in the beds defines the development of the spacing if the fractures. The model predicts that the following factors will be related to the spacing of the strata bound fracture

1) The bed thickness: is directly related to the fracture spacing, as the thickness of the bed acts as the length of the load bearing surface which defines how far the effects of the differential stress increase at the fracture walls permeates into the bed fracturing.
2) Permeability: the higher permeability of a bed, the more varied the possible fracture spacing (as with increasing permeability the fracture walls will act less efficiently as load bearing surface, spreading the load distribution and thereby increasing possible fracture spacing). Also the variability in the contrasting degree of permeability within the system (larger span in permeability, more possibility of a low permeability layer causing fluid pressure increase)
3) Bed thickness variability: the variability in the contrasting degree of bed thicknesses within the system, particularly the lower permeability beds (thick low permeability beds will allow the build up of higher pore pressures)
4) Rate of source: the faster the rate of fluid charge, the less variability there will be in fracture spacing (as the fracture walls will be able to act more efficiently as load bearing surfaces)
5) Tensile strength: the variability in the contrasting degree of tensile strength within the system (high tensile strength of beds will reduce fracturing, a high tensile strength bed of low permeability will cause the beds under it to hydro fracture)
6) The size of the principal horizontal stresses will define whether parallel or orthogonal fracturing will occur, and their spacing.
7) There is a minimum fracture spacing, however combined with an extensional regime fracture spacing can be reduced.

This is summarised in Figure 131

#Figure 131 Sedimentary sequence and hydro-fracturing

The model also provides an explanation for fractures which extend only partially through a bed, and suggests that they are formed at later stages and higher fluid pressures. Also in agreement with other work the model suggests that the elastic moduli (Young's modulus and Poisson's ratio) have little impact on the fracture spacing.

5. Acknowledgments
The research leading to these results has received funding from the European Community's Seventh framework Programme FP7/2007-2013 under the grant agreement No. 227286 as part of the MUSTANG project and from the Scottish Funding Council for the Joint Research Institute with the Heriot-Watt University which is part of the Edinburgh Research Partnership in Engineering and mathematics (ERPem).

References

Bai, T., and Pollard, D.D., 2000, Fracture spacing in layered rocks: a new explaination based on the stress transition.: Journal of Structural Geology, v. 22, p. 43-57.

Bai, T., Pollard, D.D., and Gao, H., 2000, Explanation for fracture spacing in layered materials: Letters to nature, v. 403, p. 753.

Bonnet, E., Bour, O., Odling, N.E., Davy, P., Main, I., Cowie, P., and Berkowitz, B., 2001, Scaling of fracture systems in geological media: Reviews of Geophysics, v. 39, p. 347-383.

Boussinesq, J., 1878, Équilibre d'élasticité d'un solide isotrope sans pesanteur, supportant différents poids (Elasticity equilibrium of an isotropic solid body supporting different loads, in the absence of gravity). C. Rendus Acad. Sci. Paris, v. 86, p. 1260-1263.

Davies, R.O., and Selvadurai, A.P.S., 1996, Elasticity and Geomechanics, Cambridge University Press.

Gross, M.R., 1993, The origin and spacing of cross jionts: examples from Monterey Formation, Santa Barbara Coastline, California: Journal of Structural Geology, v. 15, p. 737-751.

Kessels, W., Kaiser, R., and Gräsle, W., 2004, Hydraulic Test Interpretation with Pressure Dependent Permeability -Results from the Continental Deep Crystalline Drilling in Germany, 2nd International Symposium on the Dynamics of Fluids in Fractured Rocks: Feb 10-12, 2004, Berkeley, CA.

Odling, N.E., Gillespie, P., Bourgine, B., Castaing, C., Chiles, J.P., Christensen, N.P., Fillion, E., Genter, A., Olsen, C., Thrane, L., Trice, R., Aarseth, E., Walsh, J.J., and Watterson, J., 1999, Variations in fracture system geometry and their implications for fluid flow in fractured hydrocarbon reservoirs: Petroleum Geoscience, v. 5, p. 373-384.

Poulos, H.G., 1967, Stresses and displacements in an elastic layer underlain by a rough rigid base: Geotechnique, v. 17, p. 378-410.

Poulos, H.G., and Davis, E.H., 1974, Elastic solutions for soil and rock mechanics, John Wiley and Sons Inc. New York, USA., 411 p.

Price, N.J., 1966, Fault and joint development in brittle and semi-brittle rock., Permagon Press, Oxford.

Rutqvist J, Tsang CF., 2002, A study of caprock hydromechanical changes associated

with CO2-injection into a brine formation. Environmental Geology, v.42, p. 296–305.
Terzaghi, K., 1943, Theoretical soil mechanics, Theoretical soil mechanics, John Wiley.

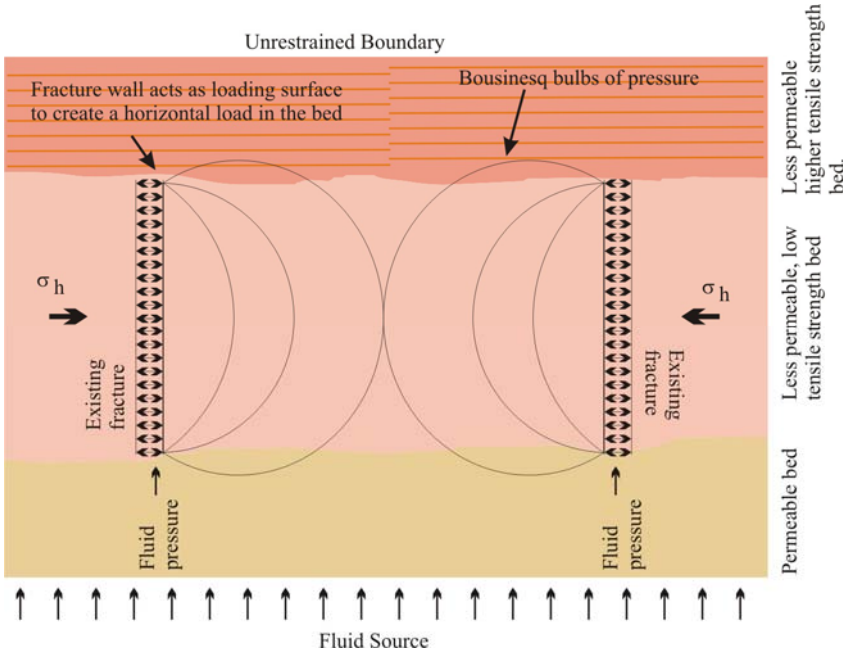

Figure 124 Stack of sedimentary deposits

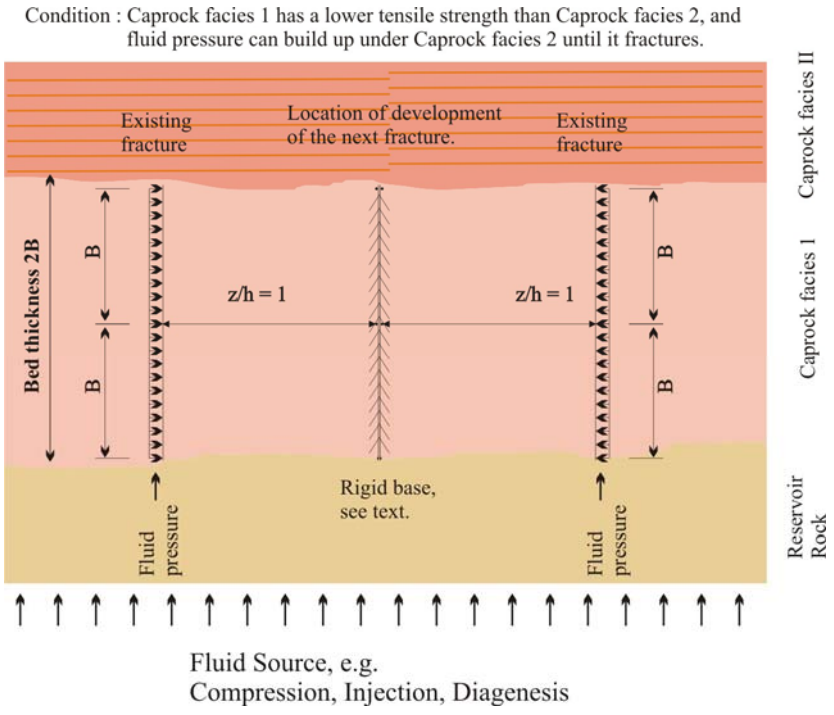

Figure 125 Generic sedimentary sequence

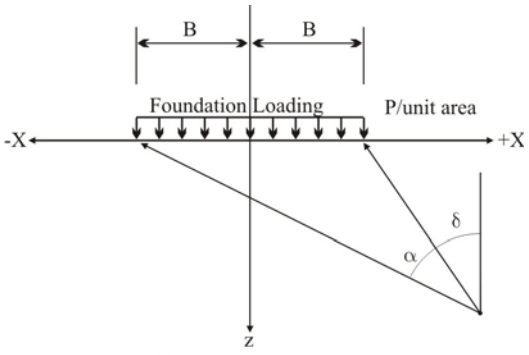

Figure 126 Standard elastic strip solution on a semi–infinite layer

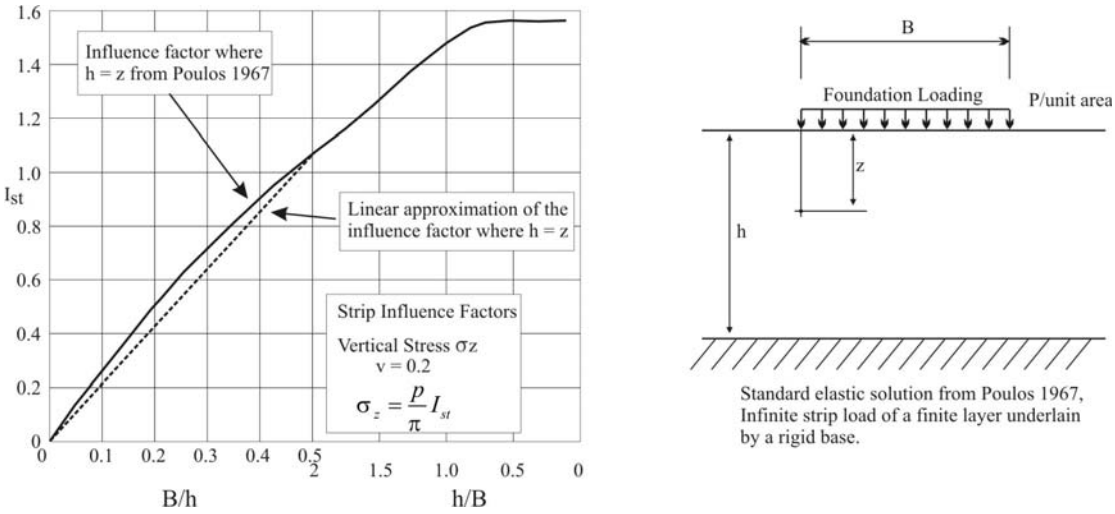

Figure 127 Elastic solutions for a rough strip foundation underlayen by a rigid base.

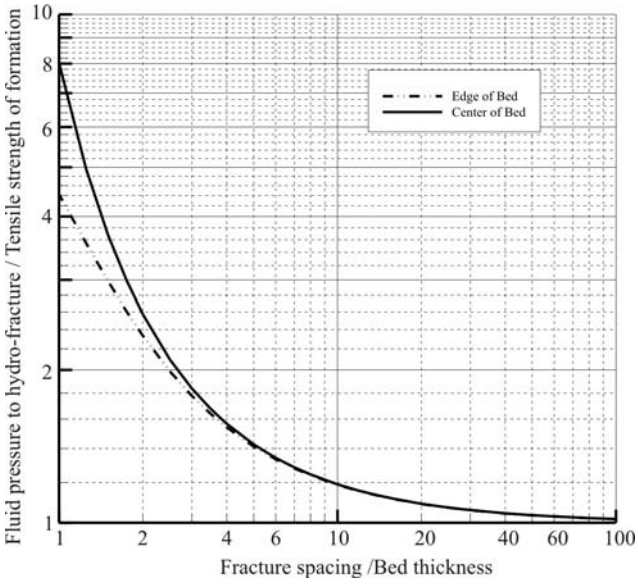

Figure 128 Standard relationship for tensile fracturing conditions

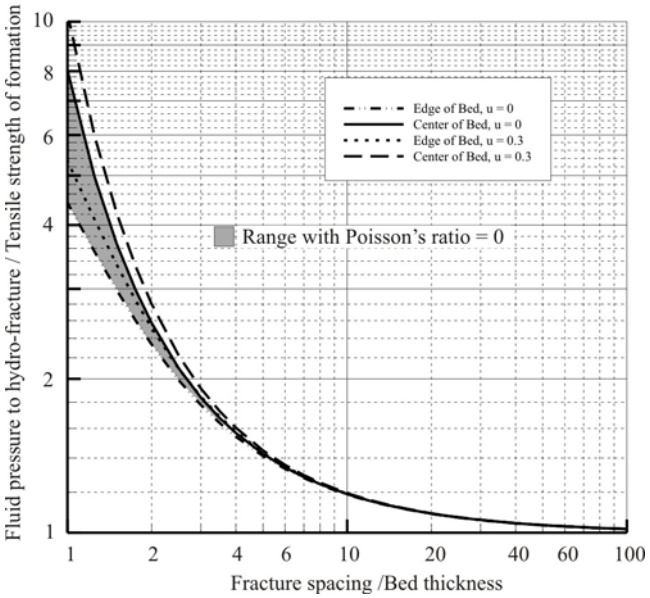

Figure 129 Natural hydraulic fracturing conditions, impact of Poisson's ratio (u in figure)

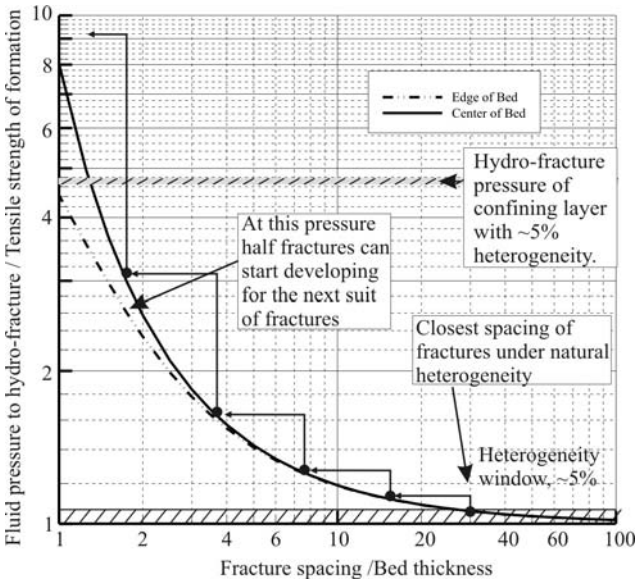

Figure 130 Development of five fracture sets

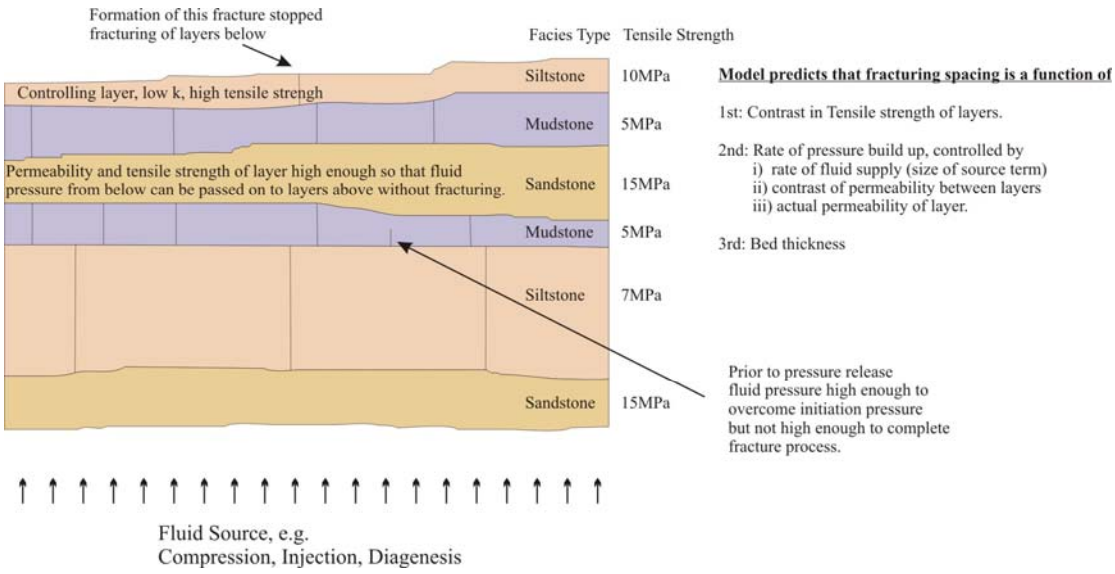

Figure 131 Sedimentary sequence and hydro-fracturing

5 Geomechancial Facies Approach

5.1 Introduction and Overview

Here we start with the premise that the subsurface is not a random package of sediment. Rather there are clear sedimentary and tectonic controls on the deposition and the stress environment in which reservoirs and caprocks are formed. Using reservoirs as a storage media requires a certain combination of mechanical parameters, that is a large storage volume represented by the reservoir a containing layer able to resist buoyant flow represented by the caprock, a depth and pressure where the reservoir is still commercially reachable for fluid exchange (circa 4km) and CO2 remains in a dense phase, or supercritical phase (> circa 800m). The suitability of these deposits to fulfil their intended engineering role is determined by the geometry of the layers and their physical characteristics. The different physical characteristics of the layers with respect to the engineered intervention (fluid injection and storage) allow us to categorise the layers into geo-mechanical facies. By classifying the different tectonic and sedimentary environments according to their likelihood to produce sedimentary sequences suitable or unsuitable to the injection of CO2 in terms of the geomechanical facies present allows an evaluation of the types of environment, the suitability to storage and key risks in terms of THMC problems which may occur. An example of the results of an initial consideration of these properties is presented in the table below taken from the manuscript following.

Table 24 Basin type and susceptibility to problems relating to CO2 storage

Basin Type	**Susceptibility to problems**						
	Storage opportunity	Preservation potential	Major rotation	Uneconomic location	risk of major orogenesis modification	Predictive geometry?	Risk of overprint or destruction
Extensional systems							
Oceanic basin	poor	poor	possible	yes	high	poor	high
Passive continental margin	good	fair	unlikely	no	mid	fair	mid
Terrestrial rift basin	fair	good	unlikely	no	low	poor	mid
Convergent systems							
Trench	poor	poor	likely	yes	high	poor	mid
Forearc basin	fair	fair	possible	sometimes	high	poor	mid
Backarc basin	fair	fair	possible	sometimes	mid	fair	mid
Foreland basin	good	good	unlikely	no	low	fair	mid
Wrench systems							
Strike slip pull apart basin	poor	poor	likely	no	mid	poor	high

5.2 Paper : Appraisal of caprock security in commercial CO2 storage; a thermo-hydro-mechanical-chemical coupled processes and geomechanical facies approach

M.A.Edwards[1 *], X.J Qiao[1 2], R.S.Haszeldine[1], K.Edlmann[1], C.I.McDermott[1]

1 SCCS, School of GeoSciences, University of Edinburgh, West Mains Road, Edinburgh EH9 3JW, Scotland
2 Institute of Geology and Geophysics, Chinese Academy of Sciences, 19 Beitucheng Western Road, 100029 Beijing, China
* corresponding author: m.edwards@ed.ac.uk; Tel: +44 (0)1316507339; Fax: +44 (0)1316683184

Words (Main text only): 10769

References 62

Tables: 3

Figures: 9

Abstract

Commercial methodologies for CO_2 storage site selection and injection design typically prescribe detailed characterisation of caprock integrity at somewhat late stages, thereby harbouring an un-quantified commercial risk through much of the appraisal process. To address this, we explore coupled process modelling of thermo-hydro-mechanical-chemical (THMC) processes on caprock integrity. We review THMC coupled phenomena for caprock properties relevant processes. Rock type physical properties strongly influence THMC coupled process modelling outcomes, and (particularly mechanical) are in turn governed by original sedimentary depositional settings, and thereafter compaction. The depositional setting defines a scope of possible model input types, magnitudes and frequencies for sedimentary strata while further model boundaries are defined by subsequent events that can be constrained through prior knowledge - frequently coupled to the regional depositional setting. Thus, we propose the notion of a geomechanical facies and use three examples to illustrate THMC coupled processes modelling together with consideration of the geochemical facies for each site can provide sufficient information to determine key site unknowns. We recommend the implementation of THMC coupled processes modelling with geomechanical facies classification as a standard tool in commercial CO_2 storage site screening and appraisal for all types of storage sites, worldwide.

KEYWORDS:

CO_2 Geological Storage; caprock integrity; THMC coupled processes; geomechanical facies; commercial risk

Introduction

Storage of CO_2 into subsurface deep saline formations or other underground geologic formations whose properties render them suitable as secure storage reservoirs has been proposed to reduce anthropogenic CO_2 emissions and thereby mitigate global climate change [1-8]. Carbon storage involves injecting CO_2 into deep (>1000 m), naturally porous geological formations where the CO_2 will remain for very long time periods (>1000 years). The scale of storage opportunities that will be required for meaningful levels of emissions reduction are being discussed, as are some of the commercial challenges for operators of static CO_2 emitters that need to be overcome or reduced [1-7, 9-11].

A major challenge remains in advancing technological understanding of these subsurface geological storage opportunities to the level of commercially well-established methods, all within an attenuated timeline. Overcoming this challenge is critical for the safe but timely worldwide implementation of CO_2 sequestration, if the required international targets and timetables to mitigate and attenuate rates of atmospheric CO_2 are to be attained [1-7, 9-11].

Much work has been done on global, national and regional scales in initial estimates of storage capacity and on generic and country- or region-specific methodologies to orient (newcomer) operators in the CO_2 sequestration sector to plan and develop commercially-achievable storage [1, 5, 7, 9-14]. In addition, a technological understanding is rapidly emerging to understand the behaviour of CO_2 during and after injection into storage formations. These techniques are frequently ported from the hydrocarbon production sector however and, in our view, caprock security is under-represented (see section 1.1, below).

The motivation behind this work therefore is the above noted risk that a practical method of incorporating caprock security in initial site appraisals and subsequent site-specific detailed characterisation is lagging behind. Although almost all methodology studies urge comprehensive modelling and characterisation of caprock integrity, this process step appears late in the (implicit or explicit) project path. A large business risk is thereby built into this plan; commercially unacceptable levels of storage site security may be masked until long after initial

and even further rounds of site screening and selection are undertaken and the comprehensive modelling and characterisation of caprock integrity is finally conducted. In this contribution, we therefore explore options for best practises in reservoir - caprock assessment at various stages in the decision path to site selection and injection strategy. We explore the benefits of using a thermo-hydro-mechanical-chemical (THMC) coupled processes modelling approach, introduce the notion of geomechanical facies and address whether there is scope for a regional or (sub) basin scale control on THMC coupled processes. Our target audience is: geologists, asset teams for CCS storage operators, and non-specialist modellers.

Storage background

Commercial target storage reservoirs typically include sedimentary rock formations associated with deep saline aquifers, (saline formations) coal beds, depleted oil or gas reservoirs, occasionally deep non-producible coal seams, and, very rarely, igneous formations like basalt or pumice [e.g., 11 and references therein]. Saline formations typically occur in highly porous sedimentary rock formation media like sandstone or fractured media like carbonate; depleted oil or gas reservoirs typically occur in sandstone, carbonate and underground salt bodies. Compared with other kinds of geological storage media, porous sandstone formations offer great advantages not only because they offer worldwide the volumetrically largest storage capacity, but also because, for many industrial countries, they have the most optimal distribution with respect to anthropogenic CO_2 source areas [e.g., 11 and references therein]. They are logistically therefore an obvious choice for study by the global CO_2 sequestration community. Furthermore, they are a good choice because of the widespread historical or contemporary presence of hydrocarbon (crude oil, natural gas and its liquid condensates) and/or potable / non-potable water supplies in sandstone reservoir formations that has led to comprehensive understanding of physical processes in these rocks founded on decades of scientific research.

Much subsurface technology thereby calls upon engineering that was established for oil and gas or groundwater management. Such engineering primarily considers only removal (extraction via well production) or, at best, replenishment (removal and some replacement) of one or more phases to/from the porous media of the reservoir rock unit. In addition, there is little need for detailed knowledge of the overlying caprock or aquitard. The injection and enduring storage of CO_2 in deep saline formations differs in that it adds (via injection) one or more phases into a reservoir. Moreover, it further differs in that there is essential need for comprehensive knowledge of the overlying caprock to the reservoir; it's short and long term integrity is central to future predictions and long term guarantee of performance as part of safe sequestration of CO_2. These differences to the oil /gas and groundwater management sectors pose specific new challenges in, for example, the understanding of potentially complex 3D distributions of pressure increase, temperature decrease, and CO_2 reactivity. We now explore these differences, considering the principal processes relevant to secure, long term CO_2 injection, storage and monitoring. We consider only clastic-type reservoirs; do not consider unconventional targets such as coal beds, shales, basalts. As noted above we explore whether clastic-type reservoirs and their caprocks can be classed into basin architectures that have predictable geomechanical facies [e.g., 15, 16].

Governing processes in CO2 sequestration

The injection and storage of CO_2 in deep subsurface porous media reservoirs is inextricably intertwined with the thermal, mechanical, chemical and fluid-associated processes that are present during and (long) after injection. There is a clear need to understand the interactions and reciprocal feedback or coupling loops that interconnect and bind the individual processes of the THMC system. Caprock architecture in typical sedimentary rock systems will comprise areally semi-continuous, heterogeneous at some scale, multiple, typically alternating layers of less-then-more impermeable media (e.g. clay-rich and silt-rich mudstone sequences) of

varying thickness. Each comprises varying mechanical "imperfections" such as density of pre-existing fractures (including total length, spacing, aperture, within-layer height, etc), potential for (elastic) fracture generation and/or propagation ("fracture strength") or re-opening, uni-, bi- or poly-modal pore size (and grain size) distribution, and wettability for a given fluid's capillary entry & breakthrough pressures (e.g. CO_2 or brine), all of which are part of an overall parameterisation of mechanical anisotropy. Grains and pores in ubiquitous clay- and silt-rich sequences are notably susceptible to THMC changes; smectite converts to illite with sufficient T, P conditions as well as appropriate chemistry, This conversion, typically associated with clay swelling, may either be mineralogical morphological replacement (grain by grain replacement) with little anticipated change in porosity and minor strength change, or may be full dissolution replacement with accompanying degrees of porosity collapse via re-crystallisation of illite in the lowest stress directions. The latter is a mass transfer strain accommodation that brings about large changes in porosity and strength. These rock properties and their associated potential for any undesirable change (from the standpoint of safe CO_2 storage) can collectively be regarded as the caprock integrity.

The thermal and hydraulic conditions are primary influenced by the injection depths (>800 m) and temperatures (300-350 K). At these conditions CO_2 sits within the temperature and pressure range to be in the supercritical phase. At supercritical conditions, CO_2 exhibits the viscosity of a gas but the density of a liquid. One reason that a supercritical state for CO_2 is desirable is that (saline) groundwater or other naturally occurring formation fluids are present in the target reservoir; injection of CO_2 requires the displacement or compression of these existing formation fluids and thus injection needs to be at pressures above that of the prevailing fluid. Noteworthy is that, close to the critical point, small changes in pressure or temperature result in large changes in density, allowing many properties of the supercritical CO_2 to be "fine-tuned". Because existing formation fluids are being displaced by, and are interacting with, supercritical CO_2, fluid flow in the aquifer is multi-phase (including liquid water, liquid or supercritical CO_2 and gaseous CO_2) instead of simple liquid water flow. Simultaneously, the increase of the formation pressure and temperature changes both the hydraulic properties of the aquifer and the caprock. The temperature / pressure realm for supercritical CO_2 imparts a strong P-T sensitivity; hydrothermal effects combined with those of phase transition between supercritical and gaseous CO_2 are expected to lead to very complex flow processes. The supercritical realm at reservoir conditions is > c.31^{o}C and > 8 Mpa (or >9 MPa for typical flavours of impure CO_2).

Secondly, injection of CO_2 produces an increased pore pressure which, at least locally, will change the effective stress, and even may change the orientation of principal stress directions, depending on any isotropy in the 3D flow network (permeability) of the reservoir or caprock. In addition, because CO_2 is more buoyant than water and because the volume over time for dissolution of CO_2 in the existing pore fluids (i.e. brine) is slow with respect to flux of buoyant CO_2, much of the injected CO_2 will rise up through the pore spaces in the reservoir rock until it reaches the caprock. This can rapidly impose further THMC processes at the reservoir caprock interface. This poses the risk of breaching the integrity of the caprock depending on its architecture. Once breaching initiates, for example via (re-)fracturing, the creation of new flow paths for CO_2 will quickly change a range of THMC conditions at the reservoir - caprock interface and is expected to further dramatically influence the caprock integrity.

Thirdly, injected CO_2 in a deep reservoir formation, as it dissolves in existing formation waters will interact chemically and react with minerals in the reservoir and caprock to precipitate and redistribute existing or grow (new, different) minerals. Although under many conditions this process is extremely slow, it is anticipated that at temperatures and pressures of CO_2 injection, reactions would be dominated by coupled THMC processes, become complex, and in cases may proceed very rapidly giving rise to local porosity and permeability changes such as the clay mineral alterations noted above.

The important observation is that the processes are complex because one process encourages the other which will in return (re-)encourage the first. In deep CO_2 sequestration, not only pressure but also temperature increases with depth; thermal effects will induce heat diffusion and thermal convection which in turn will change the hydraulic properties and cause mineral (dis)solution which will influence the geochemical process. Coupled processes linking thermo-hydro-mechanical and chemical phenomena play an important role in the storage of CO_2

because CO_2 sequestration involves many problems such as non-isothermal multi-phase flow, mechanical deformation of anisotropic rock mass, thermal effects and chemical reactions.

thermo-hydro-mechanical-chemical coupled processes

The thermo-hydro-mechanical-chemical (THMC) coupled processes approach to modelling is proposed to investigate the THMC behaviour of CO_2 sequestration in reservoir - caprock systems for all aspects concerning the initial geological depositional environment of the aquifer, properties of the caprock, fractures and the overarching structure in the system, the temperature, and the injection pressure. We extend previous studies on single caprock system and apply THMC coupled processes modelling to different geomechanical facies to different geological reservoir systems for assisting operators, regulators and insurers to securely appraise CO_2 storage sites.

The mechanisms for breaching the integrity of, and for general failure of, the caprock depend not only on the geological media feature but also on the THMC processes which are based on heat and multiphase fluid flow in geological media in which pressure increases and temperature either increases or even decreases (due to the Joule-Thomson effect) upon commencement of CO_2 injection in the reservoir. Modelling the effects of all these processes on the reservoir - caprock system must incorporate the coupling of these processes. An approach using THMC coupled processes in descriptive prediction modelling takes into consideration the effects of thermal and hydraulic and chemical processes on the mechanical behaviour as a whole system. Figure 1 shows, for a given reservoir-caprock sedimentary rock system architecture, what the spectrum of processes is between each of the four THMC nodes and how they reciprocally interact and feedback with one another. From figure 1, it is clear that the fluid properties and fracture properties in the centre part are the essential junctions affected by all the processes, which means the thermal, geochemical, hydraulic processes and mechanical response all build up the linkage and act on each other through the properties. Many of the values for the range of properties listed out in the diagram will be known or can be easily measured directly (e.g. lab rocks tests, down-borehole measurements) or by proxy (e.g. geophysical monitoring). Other values can be calculated once the manner in which they are coupled (or linked back) to the measurable values are known. The fluid properties include viscosity, density, heat capacity and heat conductivity. The hydraulic properties such as permeability, porosity, fracture apertures are all relevant to fracture properties dominated by pressure and temperature. Based on the relationship in the diagram, we analyse the links among different coupled processes and different reservoir types.

Previous research

Comprehensive (mostly reservoir-focussed) studies have hitherto paid attention mainly to the effects of just one or two processes. For example, hydromechanical effects during CO_2 injection were analysed through fault stability. In rock media, fault stability analysis including shear failure and fault-slip and migration along sub vertical faults or fracture zones have been studied by many researchers [17-25]. Hydro-mechanical processes always accompany the thermal influence that occurs with constant injection and effects the stress distribution. The mechanical processes involve thermal stress and heat transfer under high temperature [26]. The heat transfer behaviour and chemical effects has been investigated by Pruess [27] and Watson and Gibson-Poole [28].

Various numerical experimental approaches can be used to analyse the quantitative relationships of different processes. There are a number of numerical codes developed to solve the coupled problem linking thermo-hydro-mechanical and chemical effects. [29, 30] use TOUGH-FLAC to study CO_2 migration in single-caprock and multilayer systems. Hassanzadeh and co-workers [31] developed a new 2D numerical model and modelled diffusive and convective mixing in geological CO_2 storage by solving the convection-diffusion equation while

considering the CO_2-brine interface as a boundary condition. [32] investigated the possibility of using the temperature signals induced by carbon dioxide to monitor CO_2 plume propagation in the formation using a numerical multi-phase simulation program to investigate the non-isothermal effects during CO_2 injection. Pruess and colleagues [27, 33] analysed fluid flow and heat transfer behaviour through similar modelling methods. Other researchers have focused on the role of geological sedimentary depositional environment (the "facies") in coupled modelling. McDermott [34] further develop OpenGeoSys [35] to focus on following the CO2-brine interface at a sub grid scale whilst modelling two phase flow in heterogeneous caprock and reservoir rock. In this paper, we focus on the coupled processes because they resolve important factors associated with the integrity of the caprock and dominated the safety of geological storage. We also consider the geomechanical role of the original sedimentary facies.

Core architecture of THMC coupled processes

Injection pressure, fluid pressure and effective stress

The long-term performance of a caprock seal in natural CO_2 storage depends on the pressure and stress directly. As the formation pressure increases with the depth, the injection of CO_2 needs to be injected under greater pressure which causes the fluid injection changes in the pore pressure that take place in the aquifer and induces stress around the caprock. In addition both thermal stress and buoyancy provide additional stress on the rock.

Inevitably, injection of CO_2 increases the subsurface pressure, especially near the injection location. The relationship among total normal stress σ_n, effective stress $\sigma_n^{'}$ and hydraulic pressure u can be presented as follows:

$$\sigma_n^{'} = \sigma_n - u \text{ ---------- (1)}$$

and for a 3D representation of the stress system

$$\sigma_n = l^2\sigma_1 + m^2\sigma_2 + n^2\sigma_3 \text{ ---------- (2)}$$

where *l*, *m*, and *n* are directional cosines. The injection pressure can cause pore volume to be reduced and the pore pressure to increase. The total mean stress increase during injection is a common phenomenon; patterns of effective stress changes are rather complicated. The changes in effective stress in the aquifer/caprock system depend on the rock's physical property as well as the pore pressure whose changes have a relationship to the injection rate; the injection is rapid, the reduced pore volume will tend to compress pore fluids rapidly so that the fluid has no time to flow out, thereby increasing pore-fluid pressure. However, if the injection is slow, the influence is opposite.

Hydraulic properties - Fracture apertures

For both the reservoir and caprock system fractures, the effective fracture aperture dominates the hydraulic response of the system. The quantity of flow Q in the fracture depends on the fracture apertures penetrability including the width and length of the fracture. Apertures of fractures can change due to normal stress and shear stress. The change in fracture aperture occurs from two basic mechanisms: normal stress-induced closure or opening, and shear stress induced dilation. Changes in aperture and in permeability of a fracture are functions of normal and shear stresses across the fracture [36, 37]. Thermally induced stresses around the reservoir also can significantly change the hydraulic conductivity in that thermal stresses are expected to be superimposed on tectonics stresses [16, 26]. Thermal stress for geologic media is defined as

$$\sigma_t = K_r E \Delta T \text{ ---------- (3)}$$

where K_r is the coefficient of restraint, E is the elastic modulus, and ΔT is the change in temperature in the system. Figure 2 shows a conceptual model of this.

CO_2 injection will cause stress concentration around the fracture opening, which in turn changes the local fracture aperture and permeability. If the injection pressure is high, e.g. above the lithostatic pressure, hydraulic fracturing will occur, while, at lower pressure, water pressure working against mechanical stress may enlarge the fracture aperture [38].

Hydraulic properties - Porosity and Permeability

In highly consolidated materials, the changes of microstructure, and thus in volume, are less than for soils [39]. For porous sedimentary rock, the porosity is important factor dominating and reflecting the change of the system $\sigma_n^{'}$ [40]

$$\phi = \phi_r + (\phi_0 - \phi_r)\exp(a \times \sigma_n^{'}) \text{ ---------- (4)}$$

ϕ_0 is the porosity when stress is zero, ϕ_r is residual porosity at high stress and the exponential a is determined experimentally. In a fractured rock, minor changes in the fracture aperture have significant impacts on the permeability, with the intrinsic permeability related to the square of the fracture aperture

$$k = \frac{e^2}{12\mu} \text{ ---------- (5)}$$

where μ is the dynamic viscosity.

Changes in the values of matrix porosity and fracture apertures result in changes to the permeability of the reservoir and caprock. The permeability of fractured rock is stress dependent. The permeability of the aquifer/caprock tends to be sensitive to stress changes. The different responses depend on the stress. Klinginger (2006 – unpublished undergraduate project) showed that the most important property influencing the carbon dioxide propagation in the subsurface is the rock permeability.

The permeability is related to the porosity, [40] and the following function for stress dependency

$$k = k_0 \exp\left[c \times (\phi / \phi_0 - 1)\right] \text{ ---------- (6)}$$

where k_0 is the permeability at zero stress, and the exponent c can be determined. Coupling the two equations above, permeability is indirectly dependent on the effective stress. There are several empirical formulations relating porosity to permeability (e.g. the Kozeny-Carman relationship). Generally

$$k = fcd_{10}^{\ 2} \text{ ---------- (7)}$$

where c is some material constant, and d_{10} is the pore diameter of the 10% finest fraction of the sample. We remark that it is debateable to what extent the standard understanding of permeability is valid in low permeability seals such as caprock.

Thermal properties - Pressure and temperature

Variations in the heat transport properties depend on thermodynamic conditions. The temperature change is one of the important indices of thermodynamic conditions in the system. The large changes in temperature and pressure associated with reservoir exploitation will affect the porosity and permeability of the rock and the properties of the fluid flowing through the rock mass, which will, in turn, affect the flow and heat transport of the system (McDermott et al., 2006). Pruess (2008) analysed the heat transfer behaviour in the subsurface, following leakage from a geologic storage reservoir. This work and others shows that it is important for the modeller not to lose sight of the near-field versus far-field

behaviour; near-field will be subject to initially high gradient in temperature if large differences are forthcoming upon injection whereas far-field effects will be more diffuse, subject to the thermal conductivity & thermal capacity of the rock (see below).

During isenthalpic expansion, the temperature change arising in decompression without heat transfer is known as the Joule–Thomson effect. In fact, the CO_2 flow would not be entirely isenthalpic, it is impossible that CO_2 would expand to atmospheric pressure with no heat transfer as the expanding and cooling CO_2 would pick up heat from the surroundings of the pathway through which it would be migrating. However, the rate of such heat supply depends on the geologic media properties, especially the thermal conductivity. The thermal conductivity of most geological media is low and heat transfer will be limited, especially where the thermal conductivity & capacity is very low. Because of the heat transfer, thermal stresses are exerted on the reservoir and caprock (as well as the formation stress) during the injection process. The failure analysis step for the fracture system (and any faults) is more complex and is influenced by the superposition of stresses. It is clear that the thermal effects must differ between hard caprock and soft caprock due to different expandability and thermal conductivity.

In addition, changes in stress in the rock will be most reflected in in the fracture system where there is little restraint. This can transpire on both the small scale (i.e. around the immediate area of the injection (or water production) well-bore as well as over a larger scale, such as (vertically) compartmentalised reservoirs (and their caprocks) and even, for example throughout a single large horizon of a stack of multiple cycles of sealing and non-sealing rock layers at the reservoir-scale after the lowest layer in the architecture of a caprock series has been breached and CO_2 has begun migrating to a higher layer.

Solubility of CO_2

During injection of CO_2 for geological storage, the physical capillary trapping mechanism of the CO_2 flowing within the porous media that is due to surface tension with meniscus ("wetting angle") adhesion is thought to represent a major portion of the storage capacity for most sandstone type reservoirs [e.g., 11, and references therein]. CO_2 solubility is however a further key process that has implications for the properties of the formation waters and will ultimately lead to mineral precipitation.

CO_2 starts as a separate phase and dissolves into formation waters over time. Once the CO_2 is dissolved, the chemical processes in the system are enhanced and may well affect the security of the geological storage (i.e. caprock integrity). Geochemical processes involve two aspects here; one is the solubility of CO_2, and the other is the reaction between CO_2 and the surrounding minerals - which may lead to the formation of new minerals. The solubility of CO_2 is controlled by the temperature, pressure and composition of the formation water. The solution of CO_2 in water depends on both the thermodynamic conditions and the variation of the hydraulic properties. Thermal processes impact the phase changes through both the chemical reaction and the amount of carbon dioxide dissolution and the evaporation (which depends on temperature, pressure and salinity conditions). The hydraulic process as a whole influences the geochemical process through hydraulic pressure changes and density and salinity of water. Solubility decreases with increasing temperature and salinity, and increases with pressure [41]. We can conclude that the chemical process is not independent; it influences the system by linking with thermo- and hydro-processes and will affect the mechanism and the integrity of the reservoir - caprock system.

Migration path analysis under THMC

The overall deformation of the fractured (or faulted) reservoir is controlled by potential Coulomb failure of the pre-existing individual fractures (or faults) through reactivation or through original rupture of the intact rock. The natural tendency (solely for buoyancy) for the injected CO_2 to migrate upwards along the steepest gradient (with horizontal spreading) to just beneath the caprock (and accumulate near there) is very likely overcome by (1) heterogenieities and (2) self-reinforcing fronts. In most general cases, geological setting-related phenomena such as pre-existing fault stabilities can be affected by hydraulic factors,

for instance, the change of the pore pressure induced by injection stresses. The slipping-fault disturbs the integrity of the caprock and supplies new migration paths.

Fracture aperture aggravates reservoir heterogeneity which may influence the migration of CO_2. For instance, a highly heterogeneous geological sedimentary package with a high permeability fracture network can lead to significant horizontal migration of CO_2 before it reaches the caprock. Pore fluid pressure changes fault stability. In another words, higher pore fluid pressures decrease the frictional resistance to sliding. Fault stability is frequently evaluated in terms of the ratio of shear stress to effective normal stress, which is called slip tendency as illustrated by the "fault failure" curve shown in Figure 3a. For a single fault, the shear strength may be expressed by the Coulomb failure criterion.

$$\tau_r = C + \mu(\sigma_n - P_f) \text{ ---------- (8)}$$

$$\frac{\tau}{\sigma_n - P_f} \geq \mu \text{ ---------- (9)}$$

Where τ is the shear stress along the fault, σ_n is the normal total stress acting across the fault surface, P_f is the fluid pressure, μ is the coefficient of static friction, C is the cohesion. σ_n' is the effective normal stress. The equation indicates that increasing fluid pressure during injection may induce shear slip. For a cohesionless fault, if $\frac{\tau}{\sigma_n'} \geq \mu$, slip will be induced. Figure 3b shows an example of a natural fracture population distribution and co-plotted on a model for associated pore fluid pressure magnitudes contoured through all orientations with respect to σ_1 / σ_3.

Geomechanical facies

The notion of geomechanical facies [15] is particularly relevant to the properties of any geological formation for secure CO_2 storage. It is clear that geological sedimentary deposits are not randomly formed; rather that control is exerted by depositional and structural process on the in-situ properties. Facies most commonly refers to sedimentary depositional environment but can be understood on more than one scale. The overarching tectonic control on the regional basin that hosts the potential reservoir caprock system can be considered as a highest order descriptor. Settings such as a continental passive margin (the entire East coast to all of the Americas or West Coast of Africa, for example) or a foreland basin to a major collisional mountain chain (the belt of sedimentary deposition located directly north of the Alps or directly South of the Himalayas) are examples. Certain situations might be expected where a geometric control on the basin geometry and / or a predictable historical or even present-day stress field is dictated by the tectonic setting. We consider this below.

Within any tectonic setting there are a range of sedimentary depositional settings (e.g. delta, subaerial alluvial clastic fan, submarine turbiditic clastic fan). Some of these are present in more than one tectonic setting while some are not always present in a given tectonic setting (e.g. submarine fans are not found in the Himalayas or Alps foreland basin examples but would be found in the foreland basin to the Australia - Timor collisional mountain chain because it is submerged). At a lower hierarchical order, within a given sedimentary depositional setting (such as a delta), a range of factors can govern the overall sequence of sedimentary deposition at any one time, in any one area [11, e.g., 42]. Thereby an alternating sequence of sands, silts and muds with sufficiently suitable geometry to form an economical yet safe CO_2 store will almost certainly be formed at some point over a very long depositional history (e.g. the Mississippi Delta).

It can be seen, therefore, that core mechanical properties are to some extent dependent upon the geologic facies at varying levels. Because potential seal failure mechanisms depend on the geological media fundamentals such as permeability, porosity, fracture aperture, mineralogy and history of the tectonic setting, it is worthwhile exploring if THMC coupled processes models can be quantitatively shaped using geomechanical facies information. We attempt to identify if and where predictions can be made for the parameter properties of the aquifer and caprock

and even for (present and historical) stress distribution based upon fitting THMC coupled processes modelling to geochemical facies.

The concept of architectural elements within geological deposits, particularly sedimentary deposits has been proposed [e.g. 43, 44-48]. An architectural element defines a principal building block of the geological deposit being considered to which specific parameters are assigned Adapting this for a hydro-geological and geo-mechanical situation (i.e. the coupling of hydraulic, mechanical, thermal and geochemical properties as necessary in the consideration of geothermal reservoirs) allows the definition of geomechanical facies which could be deterministic of the geoprocesses of CO_2 injection and migration.

Potential of the geomechanical facies approach

A more transparent parameterisation of the rock packages that will form for a given basin and a linkage to basin (growth) deformation is an essential step in the research that aims at understanding the effects of THMC coupled processes on caprock fracture and deformation in reservoirs and thereby understanding how CO_2 storage security can be potentially enhanced. Failure in reservoirs of basins formed in convergent tectonic settings where the present day tectonic boundary conditions have not changed with respect to the historical situation (be this at the time of deposition or at any stage prior to the present) will differ from failure in reservoirs formed at extensional passive margins (again only where the present day tectonic boundary conditions have not changed with respect to the historical situation). Different reservoirs might be expected to fail in a different ways; different tectonic settings should promote different stress regimes which in turn affect (fracture) permeability. Secondly, the type of basin and its location will impact the thickness, type of deposit and so have a direct effect on the characteristics of the caprock. Identifying the various hierarchical levels of geomechanical facies that are present in a reservoir caprock system, as related to the tectonic setting, allows an architectural approach to the understanding of the reservoirs dynamics and an ordered approach to identifying which risks can occur under some kinds of scenarios. A geomechanical facies approach allows the description of separated architectural elements of the geological reservoir caprock system in terms of the physical parameters of the coupled processes of interest, e.g. with definite flow, transport, chemical and mechanical characteristics. We explore this further attempting a reservoir classification starting with tectonic settings of basin types.

Tectonic settings of basin types

We review characteristics of reservoirs in typical basins, including key strata, permeability, porosity, faulting, thickness, depth and material types and problems in attempting to categorise geomechanical facies for predictive input to holistic THMC coupled processes modelling. Several kinds of reservoirs are presented as an example. The reservoir type depends on its location and depositional environment. Figure 4 shows tectonic settings of basin types for the three plate tectonic kinematics (Fig. 4a) with a conceptual model of which media types may be present and their respective likely dominant reservoir flow characteristics (Fig. 4b). As per Figure 4a, we group the settings into extensional (7.1), convergent (7.2), and wrench (7.3). Figures 5, 6 and 7 are schematic summaries for each respective group.

Extensional systems

Oceanic basin

Ocean basins can be described as saucer-like depressions of the seabed. They vary in size from relatively minor features of the continental margin to vast structural divisions of the deep ocean. Mid-ocean ridges are typically at depths of about 2500m. The depth of the ocean basin increases away from the ridges to 4000-5000m. Spreading ridges tend to be irregular, offset by transform faults which create some areas of local topography. In the deeper parts of the ocean basins sedimentation is mainly pelagic, consisting of fine-grained biogenic detritus and clays. Nearer to the edge of the basins terrigenous clastic material may be deposited as turbidites.

Examples are:

All deep oceans (ca. 65% of area on Earth)

Problems are:

1. they are too far offshore to be of economical use

2. they have very low preservation potential over geological timescales

3. preserved portions are those that have collided and accreted onshore and are uplifted as mountain regions (total overprint with new deformation and total re-ordering of original basin architecture)

4. any reservoir opportunities will be very rare and non-predicable

Passive continental margin

A passive margin is the transition between oceanic and continental crust which is not an active plate margin. It is constructed by sedimentation above an ancient (half-)rift, now marked by transitional crust. The subsided continental crust is marked by normal faults that should dip seaward (but this may be biased by up dip growth faults accommodating salt-glide processes whose distribution and orientation is largely controlled by the distribution of salt deposits, a substantially palaeo-climate governed rock type). On the slope and rise, sedimentation is dominated by mud, silt and fine sand transported in nepheloid layer and as thermohaline contour –following currents. On present day continental margins, the thickness of sediment varies considerably. Basins of two (mutually exclusive) principal types can be present: tensional –rifted basins due to normal extension perpendicular to the continental margin, and tension-sheared basins due to oblique shear. The first type is the more typical way that passive margins form, as separated continental tracts initially must move at a high angle to the coastline. Faulting tends to be listric and normal faults may flatten with depth. Sheared margins are highly complex and tend to be rather narrow. They also differ from rifted passive margins in structural style and thermal evolution during continental breakup. As the seafloor spreading axis moves up along the margin (like a zipper unzipping), thermal uplift produces a ridge. This ridge traps sediments, thus allowing for thick sequences to accumulate.

The quality of passive margin deposits depends on (1) distance from sedimentary sources, for example the E. Red Sea reservoirs are proximal to the (Miocene uplifted) graben shoulder, and (2) the length of the deposition history, for example the Mississippi Delta is >>1000 km from the sedimentary source highland areas but continual deposition throughout much of the last 150 m.yr. history has resulted in a several km's thick basin network.

Examples are:

The entire East coast to all of the Americas, the West Coast of northern Norway, all margins of Antarctica, and the W. S. and E. coasts of Australia, India, and Africa, W. Coast of the Arabian peninsula at the Red Sea

Problems are:

1. that separated tracts may move at a low angles to the overall coastline where Euler pole angles for spreading geometries are significantly large

2. that pre-existing tectonic fabric may govern rifting geometries and so significantly deviate from spreading-perpendicular (e.g. the Variscan fabric engendered a strongly irregular margin to the opening of Tethys and now underlies the piecemeal geometry of the Alps collision)

3. continental crust normal faults may deviate significantly from seaward dipping where up dip (growth) faults accommodate salt-glide processes whereby the distribution and orientation is largely controlled by the distribution of salt deposits, a substantially palaeo-climate governed rock type

4. Obliquely sheared margins are highly complex and expected to be frequently evasive of predicable traits

Terrestrial rift basin

The terrestrial rift basin can be grouped into symmetrical rifts composed of asymmetrical segments, half graben and failed rifts.

The east Africa rift system is the most extensive intra-continental rift system. It is nearly 3000 km long and 40-50 km wide with a steep escarpment ascending some 2 km to the surrounding plateau. In the rift, clastic sediment is limited to material derived from neighbouring fault scarps and uplifted blocks within and is transported through the few river channels that do flow along the rift. The dominant sediments are those of alluvial fans and lakes, both freshwater and saline. In fact, terrestrial rift basins are commonly half-graben, with a single dominant boundary fault and highly asymmetric basin geometry. The architecture of these basins and the basin fill are strongly influenced by the displacement geometry on the bounding normal fault systems.

Examples are:

The North Sea - North Netherlands-German-Polish basin network, the Dniepr-Donets Basin [the textbook modern aulacogen e.g., 49], the Teisseyre-Tornquist Zone (although this later becomes strike slip - see section 7.3.1, below), the US mid continent and the Southern Oklahoma aulacogens

Problems are:

1. Short duration over geological timescales (quickly filled and buried) and post-formation changes (see below) are difficult to detect

2. Failed rifts are often 3-way, i.e. complex

3. Bounding normal fault systems typically use, at least in part, non-predictable (in the absence of prior information) pre-existing fabric and then resulting fault linkage and relay suites that connect these faults to "fresh" fractures of isotropic rock are equally non-predictable.

Convergent systems

Convergent systems are by definition, settings of alteration and consumption of crust, which poses major problems for predicting simple basin setting parameters that will exert a process control on the THMC coupled system.

Trench

Trenches are long, narrow, canyon-like structures, most often found adjacent to a continental margin. The sedimentation and deformation of trench deposits varies widely within and amongst trench systems. For example, some seismic profiles show little deformation of the sedimentary fill. Most trenches contain only 200-500m of sediment, mostly pelagic and hemipelagic. A few trenches such as the southern part of the Peru-Chile trench and the Eastern Aleutian trench are partly filled by up to 2500m of sediment. No trench is apparent off the Washington-Oregon coast and the east of the Lesser Antilles, but very thick sediments occur above the subduction zone.

There are four types of facies in trenches: trench fans which are relatively small with radial current patterns possibly with radial current patterns possibly disturbed by the restricted shape of the basin; axial channel sandstones passing laterally into levees and overbank fines with longitudinal currents; non-channelized sheet flow spreading over and down the trench as in basin plains with longitudinal palaeocurrents and starved trench free of coarse clastic material and in which only hemipelagic mud, fine-grained turbidites and possibly slumps. A CCS target site offshore Japan is located in the extreme inner portions of the Japan Trench (albeit this can also be considered the forearc basin - see section 7.2.2, above)

Examples are:

Globally there are >50,000 km of active (or very recently discontinued) convergent plate margins, including most of the Pacific Ocean margin, much of the SE Asia seas, Antilles, Calabrian, Hellenic, Makran.

Problems are:

1. most portions are too far offshore (or too deep) to be of economical use (but see Japan example, in section 7.2.1, above)

2. they have very low preservation potential over geological time

3. preserved portions are those that have collided and accreted onshore and are uplifted as mountain regions (total overprint with new deformation and total re-ordering of original basin architecture)

4. most reservoir opportunities will be very rare and have highly non-predicable geometry due to large (i.e. 180 degree) possible range of angles of incoming subducting oceanic crust and effectively random occurrence and distribution of incoming features like ocean rises and seamount chains which engender very local stress perturbation and unexpected skew and rotation of (inner and outer) trench fault blocks

Forearc basin

A forearc basin is a depression in the sea floor located between the main trench (see section 7.2.1, above) of a subduction zone and an associated volcanic arc. It is typically filled with sediments from the adjacent landmass and the island arc in addition to trapped oceanic crustal material.

Modern fore-arc basins are 50-100km wide and can be thousands of kilometres long. The sediments are derived from three sources: the outer arc, the magmatic arc and longitudinally from the adjacent continent. Clastic sedimentation predominates, with turbidites and other mass-flow deposits commonly passing up sediments into deltaic and fluvial sediments. Predominantly marine sediments during subduction are probably main-trained by isostatic subsidence in response to tectonic elevation of the outer arc and up building of the volcanic arc.

Examples are:

The ancient forearc basin in California, the late Mesozoic to Palaeogene Great Valley sequence was deposited in a trough about 100km wide between the outer arc of the Fransciscan Complex to the west and magmatic arc of the Sierra Nevada To the east. It overlies oceanic crust and contains up to 12km of sediment, mostly volcaniclastic turbidites, but including deltaics and shallowing towards the top.

Problems are:

1. Similar to trench in terms of preservation and non-predictability from modifications due to accretionary orogenesis (see section 7.2.1, above)

2. other alteration or destruction to persistent plate boundary (e.g. continental collision, conversion to strike slip system a la San Andreas Fault)

Backarc basin

Three types of basin can be recognized in backarc regions; Inter-arc basins are extensional basins which form in intra-oceanic arc-trench systems where the roll back of the trench results in rifting in the overriding plate. Marginal basins lie between an island arc system and a continental margin. They may also form by rifting and spreading but some are neither in extension or compression in neutral arcs systems. Retro-arc basins occur in continental margin arc-trench systems which are under compression.

Inter-arc basins which lack any terrigenous input contain volcaniclastic debris and montmorillonitic clays derived from the volcanic chain biogenic ooze, and wind-blown continent-derived dust. Near the magmatic arc a volcaniclastic an apron develops, beyond the distal end of the apron, pelagic brown clay with a high content of montmorillonite, glass and phenocrysts accumulates. Pelagic oozes with a high $CaCO_3$ content are deposited in the distal parts of the basin until it subsides below the carbonate compensation depth when brown clays or siliceous ooze accumulate.

In marginal basins, the sedimentation patterns are complex because of large and varied terrigenous input. There are pelagic sediments overlying newly-formed basin crust, several thousand metres of turbidites in abyssal plains and continental shelves. The facies of marginal basins differ from those of true oceans only in the scarcity of significant ocean bottom current deposits and the abundance of volcaniclastic sediments and ash.

In retroarc basins, fills tend to evolve from an initial phase of coarse, clastic deposition into shallow-marine environments, and then to thick, molasse-type sediments derived largely from the volcanic arc and its basement [50].

Examples are:

Numerous marginal seas and piecemeal collisional microplates in SW Pacific, islands of SE Asia (e.g. Gulf of Thailand), and Mediterranean arc like Carpathians (Pannonian Basin - stretched

not failed continental crust in the back arc where some CO_2 EOR sites operate; Ploesti Oilfields and Focsani depression in the forearc).

Problems are:

1. for interarc basins, great depths and distances render these uneconomic

2. for both interarc and marginal basins, unperturbed preservation potential is low due to proximity to active arc and likelihood of re-closure of back arc in collisional scenario (this is less likely for forearc basins as most continental crust underthrust in collisional results in major attenuation or outright cessation of convergence)

3. With the final stages of subducting residual oceanic crust pieces in SE Asia or Mediterranean type settings, major rotation is common (e.g. >180degr swings in the Carpathian arc in the last 30 m.yr.)

Foreland basin

A foreland basin is a depression that develops adjacent and parallel to a mountain belt. Foreland basins can be divided into two categories: Peripheral (Pro) foreland basins, which occur on the plate that is subducted or underthrust during plate collision (i.e. the outer arc of the orogen); Retroarc (Retro) foreland basins, which occur on the plate that overrides during plate convergence or collision (i.e. situated behind the arc that is linked with the attempted subduction of lithosphere)

Foreland basins are filled with sediments which erode from the adjacent mountain belt. The width and depth of the foreland basin is determined by the flexural rigidity of the underlying lithosphere, and the characteristics of the mountain belt. As for forearc basins, where continental crust being collisionally underthrust is mainly finished, preservation potential is good. The geometry of the exposed adjacent mountain belt should have a first order geometric fabric that can be associated with the accompanying basin.

Examples are:

Indo-Gangenic foreland basin south of the Himalaya, Po plain (Italy) South of, and Austro-Bavarian belt of sedimentary deposition North of the Alps.

Problems are:

Antecedent mountain belts (e.g. the Hercynian - Variscan that pre-date and coincide with the Alps) can dramatically overprint and alter local geometries from the prevailing geometries expected for the belt as a whole

Wrench System

Strike-slip basin

Basins formed through strike-slip action occur where a vertical fault plane curves. The shape of the basins depends on the pattern of faulting. Strike-slip faults are those whose primary motion is parallel to the fault trace. Curving faults and anastomosing faults result in wedge-shaped or elliptical basins. Side-stepping faults produce rectangular or rhomboidal pull-apart basins. The faults range in size from plate boundaries to small-scale fractures with only a few hundred metres or even just tens of centimetres of movement. Typically the margins are sites

of deposition of coarse facies (alluvial fans and fan deltas) and these pass laterally over short distance to lacustrine in continental setting or marine deposits. In the stratigraphic record, facies are varied and show lateral facies changes over short distances.

Examples are: Salton trough in San Andreas Fault transform, small pull aparts along Dead Sea Fault transform, Tibet plateau basins along Kun Lun Fault, Marmara Sea Basin along Anatolian Fault

Problems are:

1. Basins are very transient and preservation is rare due to protracted nature of active displacement (i.e. plate tectonic boundary), leading sometimes to total inversion and architectural restructuring, like in the Californian transverse ranges associated with the San Andreas Fault.

2. Even where a basin is youthful and the geometry of basin-bounding fault sets seem clear, this geometry is not predictive of fracture / fault structures through the basin due to protracted and ongoing rotation of crustal blocks in pull aparts (with diminishing amounts of total rotation up through the sedimentary sequence of the basin, as shown in most palaeomagnetic studies of active and exhumed ancient wrench fault systems)

Caveats for THMC process control by basin types

A recurring problem with all the above is post-formation changes. By this we mean the (very likely) changes in the contemporary tectonics that will cause significant alterations or even total reversal of the stress field and any attendant rotation of original fractures and faults as part of this dynamic stress evolution of the future potential CO_2 reservoir - caprock system. In Table 1 we summarise how basin types may be susceptible to problems or unsuitable for a geomechanical facies type of classification.

We can conclude from the above that, for the most part, there is insufficient regularity imparted by tectonic setting to discriminate and group basins (i.e. reservoir - caprock systems targeted for CO_2 sequestration) and undertake any commercial risk appraisal solely on this basis.

However, particularly for long, regular passive margins and foreland basins, critical information for appraising a CCS site is inherent in the tectonic setting of basin formation and should therefore have the potential to better quantify business costs. We can therefore additionally conclude that there is potential here for extracting process control information for THMC coupled processes modelling from a detailed, statistically robust study of documented reservoirs from long, regular passive margins and foreland basins. The need for prior site specific or otherwise localised geological information is clear in all general cases, however. This need is further illustrated in section 8, below, in the three examples of CCS projects.

examples of different coupled processes for different reservoir types

From the analysis previously, it can be seen that there are many causes of seal damage. Factors include fracture aperture, deformation or fault-slip or collapse induced by the high injection pressure, and the convective flow or heat transport induced by temperature changes, and the new formed minerals caused by the geochemical reaction. Because different locations and histories of the reservoir will influence, or be influenced by, different THMC processes, the link between reservoir setting and couplings of the processes is particularly of interest.

Typical types of reservoirs can be described in extensional margins and passive margins. Here two types are considered; one reservoir is located in an extensional basin and the other is in a passive margin.

Example 1 - extensional basin

Extensional basins are often characterized by faulted margins with tilted horst and terrace systems developed on both listric and planar normal faults. Structural elements of the margins are offset by lateral transfer ramps and folds which allow complex integrated subsidence to occur along the basin margin [51].

Generally, hydraulic properties are permeability/conductivity and the thermal properties are temperature gradient, heat capacity and thermal conductivity. For this kind of fractured/faulted basin, the safety of deep CO_2 reservoirs is concerned with the structural settings which dominate any groundwater flow and heat transport. Hydraulic pressure and temperature increase significantly with depth and will act on the faults and fractures and induce mechanical instability (stick-slip) or stable sliding.

The hydraulic conductivity in the fracture system is relevant to fracture aperture as shown in equation 5. Fluid density and flow dynamic viscosity are fundamental parameters for both fluid flow and heat transport. They strongly depend on the temperature and pressure. In the aquifer storage, the thermal process performs through the heat transporting and thermal stress adding on the rock and aquifer. Heat transport via the vectors of advection and convection, depends on the heat conductivity which relates to the liquid density, heat capacity, and thermal diffusivity, all of which are functions of pressure and temperature.

Under high pressure and temperature, the stability of any fault or fracture will be affected greatly because of stress distribution changes induced by the hydraulic pressure and thermal stress. Thermal stress is assumed to operate in the opposite direction to normal tectonic stress. They both influence the rock mechanical performance. The thermal stress induced in a rock due to cooling was noted in equation (3) assuming non-viscous flow in the rock. The initial seal of the reservoir alters by either hydraulically fracturing the caprock or by trigging slip on pre-existing faults. Excessively high pressures can fracture the formation, reactivate faults, damage the well facility, or create leakage pathways, and in so doing defeat the purpose of the sequestration project. Generally, analytical shear-slip analysis is based on injection principal stress magnitudes and orientations, but the inflation of a reservoir during injection should be taken into consideration. Under high temperature, the elasticity and plasticity of the reservoir rock will change because of the thermal contraction and extension. The inflation of the reservoir is induced by the thermal fracturing because of the thermal stress and heat transport. If we take the inflation of the reservoir into consideration, any fault will be easier to fail, even if the effective normal stress decreases just a little. It should be noted that the injection pressure should be well controlled in practice to avoid causing sudden fault slip during the sequestration process. For the deep active faulted reservoir, it is clear that the parameters of fluid and fracture system play important roles in coupling the hydraulic, thermal and mechanical processes.

The phenomenon of fault "reactivation" or any slip on an existing discontinuity (as opposed to elastic shear fracture of an intact rock) remains an issue. In particular, this is likely to be a fundamental mechanism behind reservoir "hysteresis" that may impinge on storage security in mature (produced, depleted or exhausted) oil and gas fields. Some degree of structural damage to the caprock and reservoir is likely to be caused by hydrocarbon production. This damage arises during extraction of the gas and/or oil as well as during repeated pumping in of water, lighter gasses or other phases for secondary and enhanced oil and gas recovery. The removal, addition and re-distribution of these phases within the reservoir during its production lifetime, as part of established reservoir engineering practises, frequently results in attendant changes in (pore fluid) pressure. This manipulation of phases may well be accompanied by caprock movement (either passive collapse or dynamic rupture), slip on reservoir (compartment) faults and / or new fault genesis. This potentially poses a major challenge to re-using depleted hydrocarbon reservoir despite the obvious attraction that they should

"automatically" offer a storage reservoir with a predictable level of caprock integrity and so readily-quantifiable business risk.

Example 2 – passive margin basin

In the passive margin basin, protracted terrigenous sediment supply via fluctuating energy of transport results in a good quality, lower permeability sediments, providing a thick regional seal. Ottway, on the passive margin basin in Australia as an example, and utilises an ideal stratigraphic system, especially typical transgressive formations, to trap CO_2 [52, 53].

According to the Kozeny-Carman equation (eq. 7), in many rocks and sediments, permeability and porosity have a strong positive correlation. The relationship between permeability and porosity can depend on the material, for example, clays, clay rich material, and volcanic tuffs. The existing porosity is not interconnected and therefore does not contribute to the permeability of the porous medium.

In deep geothermal CO_2 storage fields, these parameters must reflect the interaction between heat transfer and fluid flow in aquifer. They are in varied response to the pressure and temperature. Different rock types demonstrate different stress-permeability relationships as illustrated in Figure 8. This figure shows experiment data of permeability versus effective confining stress from laboratory tests on shale, granite and low-permeability sandstone. The heat transport happens when the permeability is pertinent, and the temperature gradient is also a factor to force the heat flow. Studies concluding that heat transport is conduction dominated typically infer limiting permeability values of <10-17m2 to <10-15m2, depending on the geometry and dimensions of the system [54].

Because of the multiple types of sediment media typically present in a passive margin basin, there is greater scope for CO_2 dissolution into the formation water, allowing a range of CO_2-water-rock interactions. These alter the mineralogy and potentially alter the physical aspects of the rock. Mineral dissolution may lead to migration of fine clay minerals and sand grains, or precipitation of new minerals, either of which can block or occlude the porosity and permeability of the reservoir rock. Therefore, the geochemical process will give a major role here.

Chemical reactions depend on the chemical composition of the storage formation minerals and on the pH changes of the resident brine due to CO_2 dissolution. Both aspects can influence the hydraulic properties of the storage formation by inducing changes in the pore size distribution. Different reservoirs each with their own mineralogy will have different rates of reaction with CO_2 and different kinds of resulting new minerals. For example, the feldspars are dominantly alkali, which have a very slow reaction rate, and the rock fragments are metamorphic (quartz and mica dominated), which also have a very slow reaction rate or are inert to CO_2 dissolution. In a high permeability reservoir, the mineralogy of the formation is typically quartz-rich with a minor component of feldspar, clays or occasionally rock fragments. These minerals all have relatively low rates of reaction with CO_2, and would not result in any major mineralogical trapping of CO_2. However, reservoirs containing substantial amounts of reactive clays (i.e. chlorite, berthierine), nontypical cement phases (i.e. glauconite, laumontite), fine-grained feldspars and fine-grained rock fragments (i.e. ferromagnesium minerals) all react readily due to the lower pH resulting from the CO_2 dissolution.

Examples of three reservoir types

Example 1 – Sleipner, nominally extensional

The offshore gas field Sleipner in the mid- to eastern edge of the Viking Graben System of the North Sea produces condensate hydrocarbon from an upper Jurassic reservoir. The Sleipner project is the first commercial application of storage in a deep saline aquifer in the world and is injected into a sand layer called the Utsira formation which is a highly elongated sand reservoir, extending for more than 400km from north to south and between 50and 100km from east to west.

The Utsira sand is a major regional saline aquifer, which is only sparsely faulted and ranges smoothly in depth from 550-1500m, the sand thickness is locally about 300m and the regional top seal is a thick mudstone. The caprock succession overlying the Utsira reservoir is hundred metres thick and variable and can be divided into three main units: the lower, the middle and the upper seals. The Lower Seal, formerly known as the Shale Drape, forms a shaly basin-restricted unit some 50-100m thick. The Middle Seal mostly comprises prograding sediment wedges of Pliocene age, dominantly shaly in the basin centre, but coarsening into a sandier facies both upward and towards the basin margins. The Upper Seal is of Quaternary age, mostly glacio-marine clays and glacial tills [55] (Chadwick et al. 2004; [56, 57].

The Utsira formation (Tables 2 and 3) consists of largely uncemented fine-grained sand, with medium and occasional coarse grains. Porosity estimates of the Utsira formation core based on microscopy range generally from 27% to 31%, locally up to 42% and range 35%-42% based on geophysical logs [55]. The overlying mudrock seal is grey clay and silt or silty-clay. The pore throat diameter is 14–40 nanometres, which is empirically converted to predict capillary entry pressures of 2–5.5 MPa, enabling a CO_2 column of several hundred meters thickness to be trapped [58].

Example 2 - Miller extensional & rotated half-graben

The Miller Field (Fig. 9) is located at the western margin of the north-south–trending South Viking Graben in UKCS blocks 16/7b and 16/8b. The South Viking Graben is a half graben fault which is bounded against the west basement of the Fladen Ground Spur. Late Jurassic rifting and subsidence in the graben led to deposition of submarine fan systems which constitute the reservoirs in the Brae-Miller. The Miller reservoir sequence comprises Upper Jurassic submarine fan sandstones of the Brae Formation which were sourced from Devonian sandstones at the Fladen Ground Spur to the west. The fan deposits form the distal part of an extensive syn-rift submarine fan in the late Jurassic rifting of the South Viking Graben. The Brae Formation generally comprises a fining-upwards sequence [56].

Near the western margin, the Brae Formation sandstones consist of thick units of mud- and sand-supported conglomerates and coarse-grained sandstones at the North, Central, South and East Brae Fields. Further eastwards in the Miller and Kingfisher fields, these sandstones prograde into medium-to fine-grained mid-and distal-fan deposits.

The Miller reservoir sandstones are composed of three main lithofacies. Clean, fine to medium-grained, well-sorted quartzose sandstone is the dominant lithology. The sandstone is subarkosic to sublithic in composition and is interpreted to have been transported by, and deposited from sand-rich, high-density, low-efficiency turbidity currents. The second lithofacies, thinly bedded alternations of sandstone and mudstone, are usually interbedded with the clean sandstones. This facies is considered to be the deposits of low-density turbidity currents. The third lithofacies is isolated mudstones locally interbedded within the main part of the reservoir. The mudstones represent normal background sedimentation at margins of the fan system, or during periods of non-deposition within the fan [59].

Example 3 - Krechba, In Salah

The In Salah Gas Project, located in Algeria, is a major CCS project like Sleipner. The CO_2 is separated from natural gas produced from three fields of Krechba, Reg, and Teguentour, and is injected into underground saline aquifer of Carboniferous age through three adjacent wells. The Krechba site, within the In Salah gas field, is currently the world's largest onshore CO_2 storage site. The reservoir is overlain by more than 900 m of low permeability Carboniferous mudstones, which forms a significant barrier to flow. The storage unit is at 1880m depth with 20 metres thick and an initial pressure of 175 bars and a temperature of 93°C.

Rutqvist [60] simulated the actual CO_2 injection in a three-dimensional model around one horizontal injection well, and conducted sensitivity studies to determine the cause and mechanisms of the uplift. Iding and Ringrose [61] focused on fault and fracture properties at Krechba, evaluating the impact of fractures on the long-term performance of the In Salah CO_2 storage site. Onuma and Ohkawa [62] detected surface deformation related with CO_2 injection by DInSAR at In Salah.

Lessons drawn from the three reservoir types

In all three of the reservoir types examined, there are geomechanical facies elements to the reservoir imparted by the overall tectonic setting basin, as well as by the site-specific sedimentary layering and structural architecture. However, as is seen in the Sleipner / Miller comparison, both reservoir caprock systems are in the North Sea, part of the overall terrestrial rift network, yet Miller, being located close to a major bounding normal fault (that later becomes partly inverted) is stratigraphically and geodynamically influenced throughout its basin depositional history by this macro-tectonic settings. Therefore, as we noted in section 7, for the various tectonic settings of basin types, the need for prior information to illuminate such differences in the regional tectonic settings is clear in all cases. We therefore recommend the use of prior local geological knowledge [e.g., 63], on a site by site basis, in the current use, and ongoing refinement of, the THMC coupled processes modelling.

Discussion

Presently, CO_2 storage is a relatively new discipline that, for most of the World's countries, is still in a pre-commercial pilot or proof-of-concept phase. We suggest that during the present transition from this proof-of-concept phase to a commercially established school of techniques and thus better defined business sector, the goal of better defining geomechanical facies up and down the basin setting hierarchy (from 100's km long tectonic margin scales to 10's m scale sedimentary layering architecture) will become a core part of best practices. This will reduce and/or significantly further quantify the business risk in assessing the suitability of, and guide the workflow design for, site appraisal and injection and monitoring strategy. This work has not attempted to present a commercially-ready, finished workflow that guides operators through the appraisal, screening and early steps of project planning. We have, however, presented the first trials of devising a geomechanical facies approach as part of an appraisal process that incorporates commercial risk for caprock integrity at earlier stages that are implicit in most existing proposed methodologies. Crucially, by using the THMC coupled processes approach to extract the pertinent geomechanical facies information from CO_2 storage sites globally, operators can greatly accelerate this process by integrally co-screening and appraising caprock security along with capacity and injectivity. Existing knowledge for parts of the THMC processes for a given facies type will allow the unknown values for a wide range of parameters to be calculated &/or inferred, even if only a few are known initially. An optimal balance of prior knowledge with a THMC coupled processes modelling should provide a straightforward commercially-deployable geomechanical facies approach to screening and appraisal for reservoir capacity and caprock security.

Conclusion

The injection and storage of CO_2 in deep brine formations is related to coupled thermo-hydro-mechanical-chemical processes. The coupled processes operating on the top seal and reservoir determine the integrity of caprock which play a pivotal role of the security of the geological storage. Using a THMC coupled processes approach in storage site appraisal and, after site selection, workflow design, is more beneficial than considering individual parts of the system alone. A geomechanical facies approach at the regional and macro-tectonic hierarchical levels of passive margin and intercontinental rift settings, despite the limitations examined, can provide a wealth of process control information on the THMC coupled processes, particularly when combined with the application of prior geological knowledge. This has clear potential to quantify at early stages, and therefore reduce the commercial risk in planning of CO_2 storage and measuring and costing caprock - reservoir security.

Acknowledgements

This work is partly supported by EU FP7 Project Mustang funding to the University of Edinburgh. We thank reviewers, and numerous members of the SCCS group and the Project Mustang partners and advisors for open discussion and sharing of ideas.

References

[1] IEA. IEA-International Energy Agency, Prospects for CO2 Capture and Storage. Paris: IEA/OECD; 2004. p. 249.
[2] Bachu S, Adams JJ. Sequestration of CO2 in geological media in response to climate change: capacity of deep saline aquifers to sequester CO2 in solution. Energy Conversion and Management. 2003;44(20):3151-75.
[3] Li X, Wei N, Liu Y, Fang Z, Dahowski R, Davidson C. CO2 point emission and geological storage capacity in China. Energy Procedia. 2009;1(1):2793-800.
[4] Bachu S. Screening and ranking of sedimentary basins for sequestration of CO2 in geological media in response to climate change. Environmental Geology. 2003;44(3):277-89.
[5] Benson SM, Cole DR. CO2 sequestration in deep sedimentary formations. Elements. 2008;4(5):325.
[6] Kaldi G-P. Kaldi and Gibson-Poole, 2008 J.G. Kaldi and C.M. Gibson-Poole, Storage Capacity Estimation, Site Selection and Characterisation for CO2 Storage Projects, Cooperative Research Centre for Greenhouse Gas Technologies, Canberra (2008) CO2CRC Report No. RPT08-1001. 2008.
[7] Plasynski S, Litynski J, McIlvried H, Srivastava R. Progress and new developments in carbon capture and storage. Critical Reviews in Plant Sciences. 2009;28(3):123-38.
[8] Arts R, Chadwick A, Eiken O, Thibeau S, Nooner S. Ten years' experience of monitoring CO2 injection in the Utsira Sand at Sleipner, offshore Norway. First break. 2008;26:65-72.
[9] Chadwick. A. Chadwick, R. Arts, C. Bernstone, F. May, S. Thibeau and P. Zweigel, Best practice for the storage of CO2 in saline aquifers, British Geological Survey Occasional Publication vol. 14, Keyworth, Nottingham (2008) ISBN 978-0-85272-610-5, p. p. 267. 2008.
[10] Bradshaw J, Bachu S, Bonijoly D, Burruss R, Holloway S, Christensen NP, et al. CO2 storage capacity estimation: Issues and development of standards. International Journal of Greenhouse Gas Control. 2007;1(1):62-8.
[11] Goodman A, Hakala A, Bromhal G, Deel D, Rodosta T, Frailey S, et al. U.S. DOE methodology for the development of geologic storage potential for carbon dioxide at the national and regional scale. International Journal of Greenhouse Gas Control. in press;In Press, Corrected Proof.
[12] Neele F, Hendriks C, Brandsma R. Geocapacity: economic feasibility of CCS in networked systems. Energy Procedia. 2009;1(1):4217-24.

[13] Nakanishi S, Mizuno Y, Okumura T, Miida H, Shidahara T, Hiramatsu S. Methodology of CO2 aquifer storage capacity assessment in Japan and overview of the project. Energy Procedia. 2009;1(1):2639-46.
[14] Poulsen NE. Potential for permanent geological storage of CO 2 in China: the COACH project. Geological Survey of Denmark and Greenland Bulletin. 2010;20:95-8.
[15] McDermott CI, Lodemann M, Ghergut I, Tenzer H, Sauter M, Kolditz O. Investigation of coupled hydraulic-geomechanical processes at the KTB site: pressure-dependent characteristics of a long-term pump test and elastic interpretation using a geomechanical facies model. Geofluids. 2006;6:67-81.
[16] Tenzer H, Park C-H, Kolditz O, McDermott C. Application of the geomechanical facies approach and comparison of exploration and evaluation methods used at Soultz-sous-Forêts (France) and Spa Urach (Germany) geothermal sites. Environmental Earth Sciences. 2010;61(4):853-80.
[17] Rutqvist J, Stephanson O. The role of hydromechanical coupling in fractured rock engineering. Hydrogeology Journal. 2003;11:7-40.
[18] Pruess K, Garcia J. Solutions of test problems for disposal of CO2 in saline aquifers. Earth Sciences Division, Lawrence Berkeley National Laboratory, Berkeley, CA 94720, U.S.A.; 2002. p. 44.
[19] Rutqvist J, Birkholzer J, Tsang CF. Coupled reservoir-geomechanical analysis of the potential for tensile and shear failure associated with CO2 injection in multilayered reservoir-caprock systems. International Journal of Rock Mechanics and Mining Sciences. 2008;45(2):132-43.
[20] Rutqvist J, Wu Y-S, Tsang C-F, Bodvarsson G. A modeling approach for analysis of coupled multiphase fluid flow, heat transfer, and deformation in fractured porous rock. International Journal of Rock Mechanics and Mining Sciences. 2002;39(4):429-42.
[21] Rutqvist J, Chijimatsu M, Jing L, Millard A, Nguyen TS, Rejeb A, et al. A numerical study of THM effects on the near-field safety of a hypothetical nuclear waste repository--BMT1 of the DECOVALEX III project. Part 3: Effects of THM coupling in sparsely fractured rocks. International Journal of Rock Mechanics and Mining Sciences. 2005;42(5-6):745.
[22] Morris JP, Detwiler RL, Friedmann SJ, Vorobiev OY, Hao Y. The large-scale geomechanical and hydrogeological effects of multiple CO2 injection sites on formation stability. International Journal of Greenhouse Gas Control. 2011;5(1):69-74.
[23] Chiaramonte L, Zoback MD, Friedmann J, Stamp V. Seal integrity and feasibility of CO 2 sequestration in the Teapot Dome EOR pilot: geomechanical site characterization. Environmental Geology. 2008;54(8):1667-75.
[24] Streit JE, Hillis RR. Building geomechanical models for the safe underground storage of carbon dioxide in porous rock. In: Gale J, Kaya Y, editors. Greenhouse gas control technologies : proceedings of the 6th International Conference on Greenhouse Gas Control Technologies. Kyoto, Japan: Pergamon; 2002. p. 495-500.
[25] Pruess K, Doughty C. Thermal single-well injection-withdrawal tracer tests for determining fracture-matrix heat transfer area. 35th Workshop on Geothermal Reservoir Engineering. Stanford, Ca, USA: Lawrence Berkeley National Laboratory; 2011.
[26] McDermott CI, Randriamanjatosoa AL, Tenzer H, Kolditz O. Simulation of Heat Extraction from Crystalline Rocks: The Influence of Coupled Processes on Differential Reservoir Cooling. Geothermics. 2006;35:321-44.
[27] Pruess K. On CO 2 fluid flow and heat transfer behavior in the subsurface, following leakage from a geologic storage reservoir. Environmental Geology. 2008;54(8):1677-86.
[28] Watson MN, Gibson-Poole CM. Reservoir selection for optimised geological injection and storage of carbon dioxide: a combined geochemical and stratigraphic perspective In: DOE/NETL editor. Conference Reservoir selection for optimised geological injection and storage of carbon dioxide: a combined geochemical and stratigraphic perspective, vol. 2.
[29] Rutqvist J, Tsang CF. A study of caprock hydromechanical changes associated with CO 2-injection into a brine formation. Environmental Geology. 2002;42(2):296-305.
[30] Rutqvist J, Tsang CF. Coupled hydromechanical effects of CO2 injection. Developments in Water Science. 2005;52:649-79.
[31] Hassanzadeh H, Pooladi-Darvish M, Keith D. Modelling of Convective Mixing in CO Storage. Journal of Canadian Petroleum Technology. 2005;44(10):43-50.

[32] Bielinski A, Kopp A, Schütt H, Class H. Monitoring of CO2 plumes during storage in geological formations using temperature signals: numerical investigation. International Journal of Greenhouse Gas Control. 2008;2(3):319-28.
[33] Pruess K, Spycher N. ECO2N-A fluid property module for the TOUGH2 code for studies of CO2 storage in saline aquifers. Energy Conversion and Management. 2007;48(6):1761-7.
[34] McDermott C, Bond A, Wang W, Kolditz O. Front Tracking using a Hybrid Analytical Finite Element Approach for Two Phase Flow applied to Supercritical CO2 Replacing Brine in a Heterogeneous Reservoir and Caprock. Transport in Porous Media. in press;in press.
[35] Wang W, Kosakowski G, Kolditz O. A parallel finite element scheme for thermo-hydro-mechanical (THM) coupled problems in porous media. Computers & Geosciences. 2009;35(8):1631-41.
[36] McDermott CI, Kolditz O. Geomechanical model for fracture deformation under hydraulic, mechanical and thermal loads. Hydrogeology Journal. 2006;14:487-98.
[37] Heiland J. Laboratory testing of coupled hydro-mechanical processes during rock deformation. Hydrogeology Journal. 2003;11(1):122-41.
[38] Tsang CF. linking thermal, hydrological, and mechanical processes in fractured rocks 1. Annual review of earth and planetary sciences. 1999;27(1):359-84.
[39] Bruand A, Prost R. Effect of water content on the fabric of a soil material: an experimental approach. European Journal of Soil Science. 1987;38(3):461-72.
[40] Davies J, Davies D. Stress-dependent permeability: characterization and modeling. SPE Journal. 2001;6(2):224-35.
[41] Spycher N, Pruess K, Ennis-King J. CO2-H2O mixtures in the geological sequestration of CO2. I. Assessment and calculation of mutual solubilities from 12 to 100 C and up to 600 bar. Geochimica et cosmochimica acta. 2003;67(16):3015-31.
[42] Bachu S, Bonijoly D, Bradshaw J, Burruss R, Holloway S, Christensen NP, et al. CO2 storage capacity estimation: Methodology and gaps. International Journal of Greenhouse Gas Control. 2007;1(4):430-43.
[43] Hornung J, Aigner T. Reservoir and aquifer characterization of fluvial architectural elements: Stubensandstein, Upper Triassic, southwest Germany. Sedimentary Geology. 1999;129(3-4):215-80.
[44] Hornung J, Aigner T. Reservoir architecture in a terminal alluvial plain: An outcrop analogue study (upper triassic, southern Germany) Part II: Cyclicity, controls and models. Journal of Petroleum Geology. 2002;25(2):151-78.
[45] Klingbeil R, Kleineidam S, Asprion U, Aigner T, Teutsch G. Relating lithofacies to hydrofacies: Outcrop-based hydrogeological characterisation of Quaternary gravel deposits. Sedimentary Geology. 1999;129(3-4):299-310.
[46] Liu K, Paterson L, Wong P, Qi D. A sedimentological approach to upscaling. Transport in Porous Media. 2002;46(2-3):285-310.
[47] Rea J, Knight R. Geostatistical analysis of ground-penetrating radar data: A means of describing spatial variation in the subsurface. Water Resources Research. 1998;34(3):329-39.
[48] Stephens M. Architectural element analysis within the Kayenta Formation (Lower Jurassic) using ground-probing radar and sedimentological profiling, southwestern Colorado. Sedimentary Geology. 1994;90(3-4):179-211.
[49] Shatsky NS. Essay of tectonics of Volga-Urals oil-bearing region and adjacent parts of the western slope of southern Urals. Moscow, USSR Izd. Moskovskogo Obshchestva Ispytately Prirody; 1945. p. 78.
[50] Einsele G. Sedimentary basins: evolution, facies, and sediment budget: Springer Verlag, 2000.
[51] Gibbs A. Structural evolution of extensional basin margins. Journal of the Geological Society. 1984;141(4):609.
[52] Sharma S, Cook P, Berly T, Lees M. The CO2CRC Otway project: overcoming challenges from planning to execution of Australia's first CCS project. Energy Procedia. 2009;1(1):1965-72.
[53] Sharma S, Cook P, Jenkins C, Steeper T, Lees M, Ranasinghe N. The CO2CRC Otway Project: Leveraging experience and exploiting new opportunities at Australia's first CCS project site. Energy Procedia. 2011;4:5447-54.
[54] Manning C, Ingebritsen S. Permeability of the continental crust: Implications of geothermal data and metamorphic systems. Reviews of Geophysics. 1999;37(1):127-50.

[55] Chadwick R, Zweigel P, Gregersen U, Kirby G, Holloway S, Johannessen P. Geological reservoir characterization of a CO2 storage site: The Utsira Sand, Sleipner, northern North Sea. Energy. 2004;29(9-10):1371-81.
[56] Eiken O, Ringrose P, Hermanrud C, Nazarian B, Torp TA, Høier L. Lessons learned from 14 years of CCS operations: Sleipner, In Salah and Snøhvit. Energy Procedia. 2011;4:5541-8.
[57] Torp TA, Gale J. Demonstrating storage of CO2 in geological reservoirs: the Sleipner and SACS projects. Energy. 2004;29(9-10):1361-9.
[58] Haszeldine RS. Deep geological CO 2 storage: Principles reviewed, and prospecting for bio-energy disposal sites. Mitigation and Adaptation Strategies for Global Change. 2006;11(2):369-93.
[59] Lu J. CO2 interaction with aquifer and seal on geological timescales: the Miller oilfield, UK North Sea, Ph.D. Thesis. Edinburgh, Scotland: The University of Edinburgh, 2008.
[60] Rutqvist J, Vasco DW, Myer L. Coupled reservoir-geomechanical analysis of CO2 injection and ground deformations at In Salah, Algeria. International Journal of Greenhouse Gas Control. 2010;4(2):225-30.
[61] Iding M, Ringrose P. Evaluating the impact of fractures on the long-term performance of the In Salah CO2 storage site. Energy Procedia. 2009;1(1):2021-8.
[62] Onuma T, Ohkawa S. Detection of surface deformation related with CO2 injection by DInSAR at In Salah, Algeria. Energy Procedia. 2009;1(1):2177-84.
[63] Wood R, Curtis A. Geological prior information and its applications to geoscientific problems. Geological Society, London, Special Publications. 2004;239(1):79.

FIGURES

NB *Colour figures are intended for colour reproduction on the Web and, unless page charges are prohibitive, also in print.*

FIGURE CAPTIONS

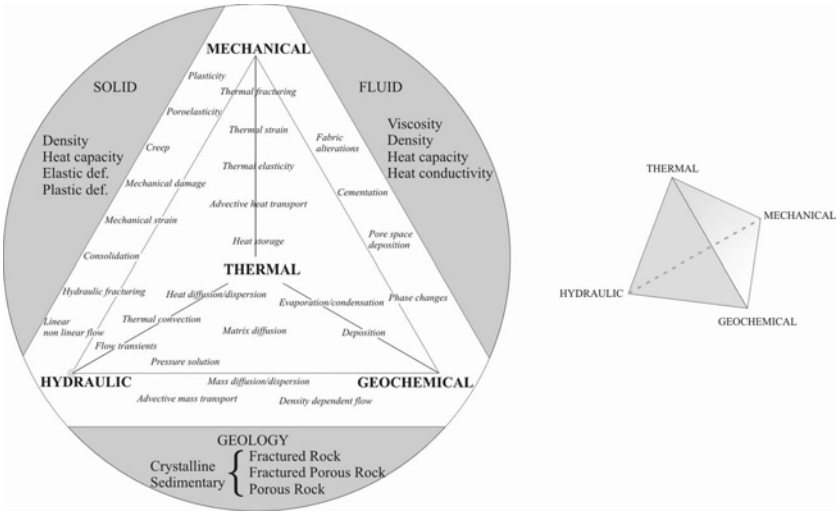

Figure 132 Tetrahedron (3-simplex) plot of the four nodes of the THMC coupling processes and the potential spectrum of reciprocal interaction and feedback amongst these processes.

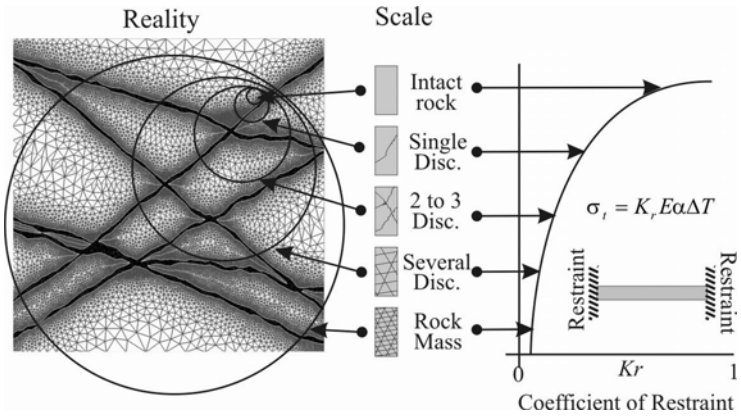

Figure 133 Conceptual model of fracture and scale issues in modelling. Shown is variation in co-efficient of restraint for thermal stress considerations of density of fracture in a single geological media.

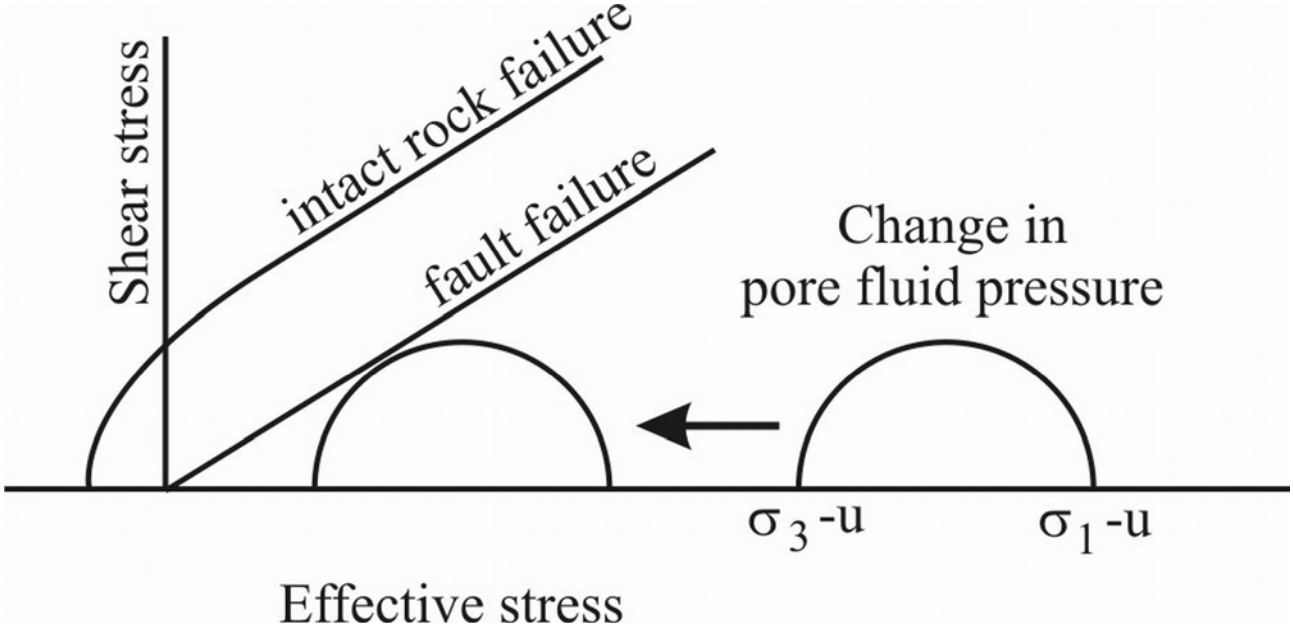

Figure 134 Effects of pore fluid pressure on effective. 3a, stress a Mohr circle for the two dimensional stress tensor allows graphical resolution of shear and normal stress values to be resolved on a fault (new fracture &/or dynamic rupture) and a pre-existing fault (frictional shear slip) before and after an increase in fluid pressure. Angles and magnitudes intensionally unspecified. 3b, example of fracture population disrtibuition with respect to an prevailing stress field with calculations of pore fluid pressure contoured for isobaric values for changing σ_1/σ_3 ratios.

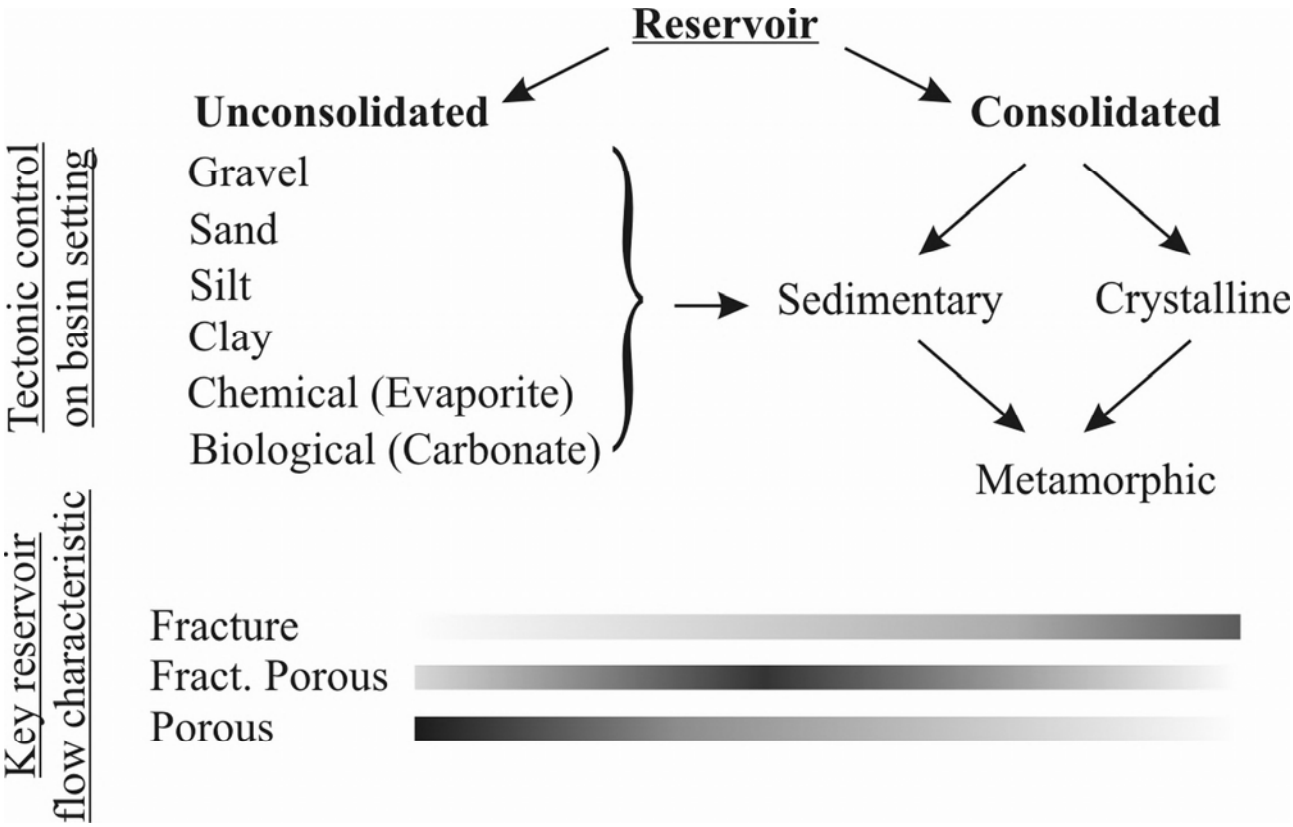

Figure 135 Tectonic settings of basin types for reservoirs. 4a, basin type classification based upon plate tectonic kinematics. 4b, summary of media types that may be present and respective dominant reservoir flow characteristics

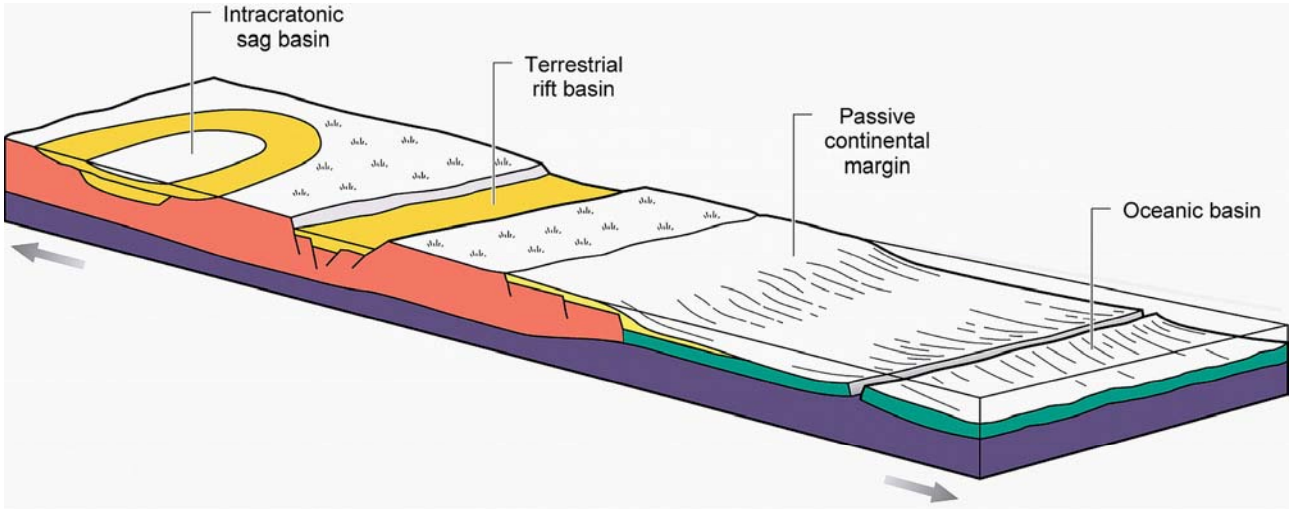

Figure 136 Schematic illustration of basin setting architecture of the upper lithosphere for extensional systems

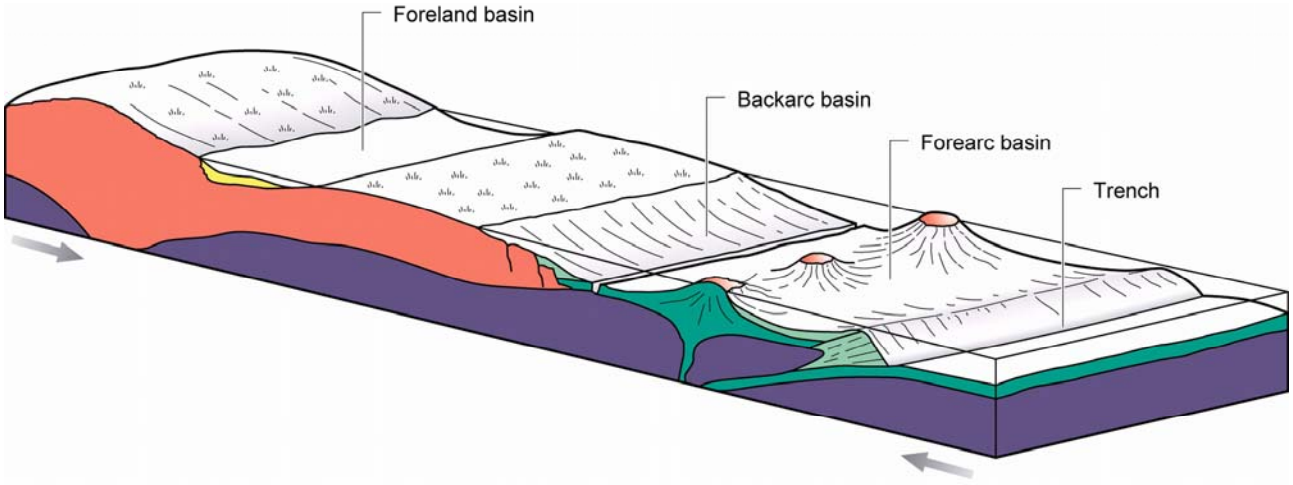

Figure 137 Schematic illustration of basin setting architecture of the upper lithosphere for convergent systems

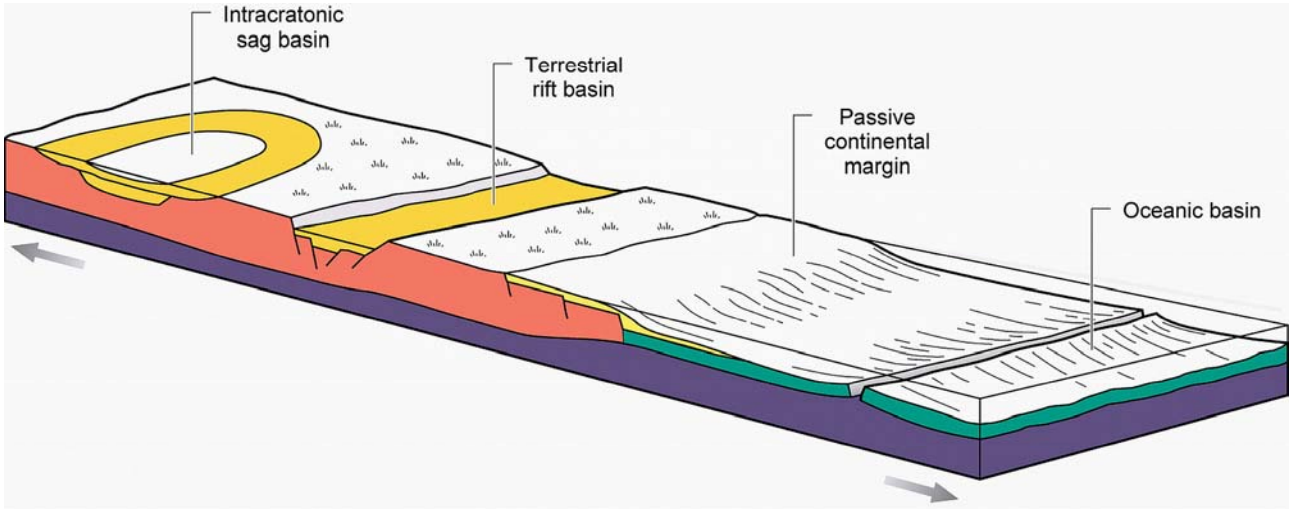

Figure 138 Schematic illustration of basin setting architecture of the upper lithosphere for Strike-Slip Systems

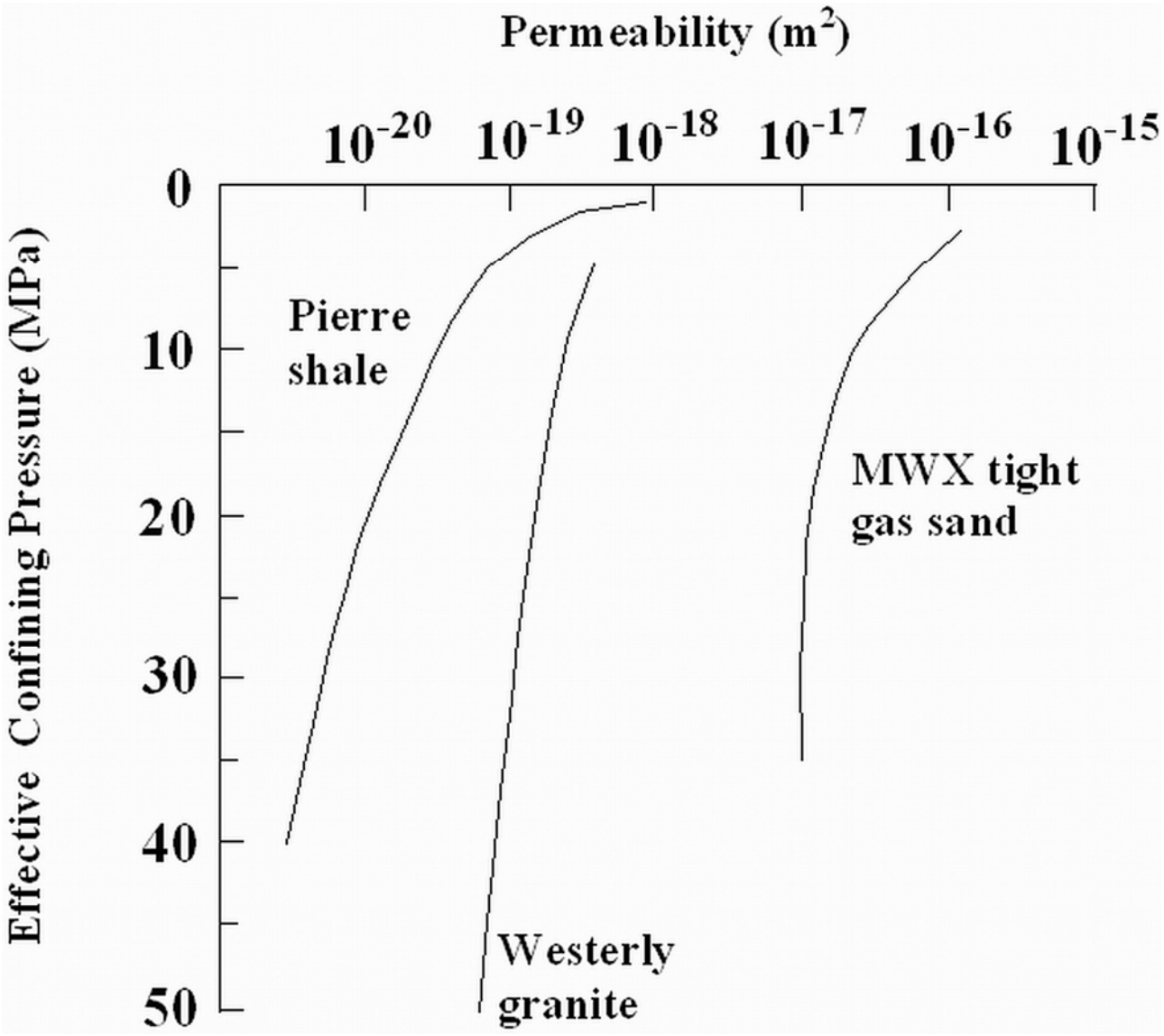

Figure 139 The relationship between permeability and pressure in three kinds of rock (Datapoints after: Brace et al., 1968; Kilmer et al., 1987; Neuzil, 1986; Rutqvist and Stephanson, 2003)

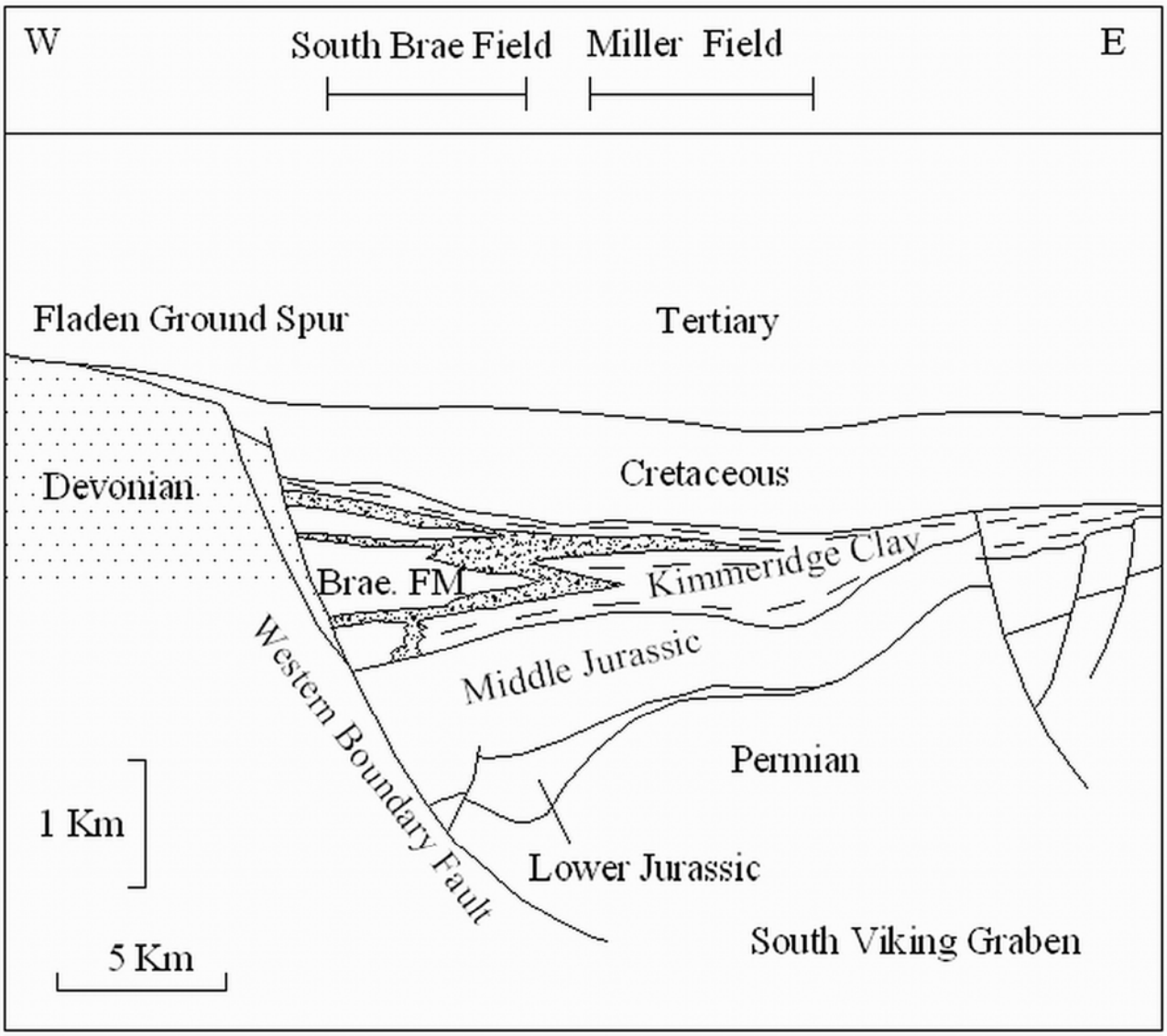

Figure 140 Schematic cross section of the Miller CO_2 storage site (after Lu 2008)

TABLES

Basin Type	**Susceptibility to problems**						
	Storage opportunity	Preservation potential	Major rotation	Uneconomic location	risk of major orogenesis modification	Predictive geometry?	Risk of overprint or destruction
Extensional systems							
Oceanic basin	poor	poor	possible	yes	high	poor	high
Passive continental margin	good	fair	unlikely	no	mid	fair	mid
Terrestrial rift basin	fair	good	unlikely	no	low	poor	mid
Convergent systems							
Trench	poor	poor	likely	yes	high	poor	mid
Forearc basin	fair	fair	possible	sometimes	high	poor	mid
Backarc basin	fair	fair	possible	sometimes	mid	fair	mid
Foreland basin	good	good	unlikely	no	low	fair	mid
Wrench systems							
Strike slip pull apart basin	poor	poor	likely	no	mid	poor	high

Table 25 Overview of basin types susceptible to problems or unsuitable for geomechanical facies type classification

Generalized properties of the Utsira Sand from core and cuttings.Mineral percentages based on whole-rock XRD analysis				
		Mineral(%)		
Grain size	Porosity	Quartz	Calcite	K-feldspar
Fine(medium)	35%-40%(27-42%)	75	3	13
Permeability	Sand/shale ratio	Albite	Aragonite	Mica and others
1-3 Darcy	0.7-1.0 (0.5-1.0)	3	3	3

Table 26 General properties of the Utsira Sand

Generalized properties of Utsira caprocks, based on analysis of cuttings										
			Mineral(%)							
Sand (>63um)	silt(2-63um)	clay(<2um)	Quartz	K-spar	Alb	Calc	Mica	Kaol		
0-5%	49-60%	45-55%	30	5	2	3	30	14		
CEC meq/100g	TOC(%)		Smect	Chlor	Pyr	Gyr	Hal	sylv	bar	
6.0-20.2	0.68-1.28		3	1	1	1	2	1	5	

Table 27 General properties of the Utsira Caprock